November 2014

Short and Long-term Performance of a Skewed Integral Abutment Prestressed Concrete Bridge

Rami Bahjat
University of Massachusetts Amherst

Short and Long-term Performance of a Skewed Integral Abutment Prestressed Concrete Bridge

A Thesis Presented

by

Rami Ameer Bahjat

Submitted to the Graduate School of the

University of Massachusetts Amherst in partial fulfillment

of the requirements for the degree of

MASTER OF SCIENCE IN CIVIL ENGINEERING

September 2014

Civil and Environmental Engineering

Short and Long-term Performance of a Skewed Integral Abutment Prestressed Concrete Bridge

A Thesis Presented

by

Rami Ameer Bahjat

Approved as to style and content by:

_____
Sergio F. Breña, Chairperson

_____
Scott A. Civjan, Member

_____
Richard N. Palmer, Department Head
Civil and Environmental Engineering

ACKNOWLEDGEMENTS

I would like to express my appreciation to my supervisor Dr. Sergio F. Breña who guided me through my research and academic studies at University of Massachusetts Amherst with continuous support, patience, and motivation. His experience and advice helped me to accomplish this study successfully.

Beside my advisor, I would like to thank Dr. Scott A. Civjan my committee member, who helped my gaining much of the knowledge I have today.

Foremost, I thank my wife Shahad, who has sacrificed a lot for me and chose to support and encourage me through my master's studies and life. Thanks to my son Ryan who made me smile when I was depressed.

Last but not the least, I would like to thank my parents Ameer Bahjat and Thikra Yousif for being the reason behind what I became today, who have always kept me happy at the expense of their happiness.

ABSTRACT

SHORT AND LONG-TERM PERFORMANCE OF A SKEWED INTEGRAL ABUTMENT PRESTRESSED CONCRETE BRIDGE

SEPTEMBER 2014

RAMI AMEER BAHJAT, B.S., UNIVERSITY OF TECHNOLOGY
M.S., UNIVERSITY OF MASSACHUSETTS AMHERST

Directed by: Professor Sergio Breña

This study presents the behavior of a precast skewed integral abutment bridge (IAB) using the recently developed NEXT-F Beam section in particular. In order to understand the bridge response, a 3-dimensional finite element model of a bridge (Brimfield Bridge) was developed to examine the thermal effect on the response of the bridge structural components. Eighteen months of field monitoring including abutments displacements, abutment rotations, deck strains, and beam strains was conducted utilizing 136 strain gauges, 6 crackmeters, and 2 tiltmeters. The behavior of the NEXT beams during construction was examined by conducting hand calculation considering all factors that could affect strain readings captured by strain gauges embedded in the 6 beams. Parametric analysis and model validation were conducted considering the effect of soil conditions, distribution of thermal loads, and the coefficient of thermal expansion used for the analyses. Using the validated model, the effect pile orientation was investigated. All the results and illustration plots are presented in detail in this study. As a result of this study, the behavior of the NEXT beams during construction was explained. Long term behavior of the bridge was also explained using field data and FE model. Furthermore, it was concluded that the coefficient of thermal expansion of concrete and temperature variation along the bridge depth and transverse direction can have a significant effect on the strain

readings and calculated response, respectively. Lastly, it was found that orienting piles with their web perpendicular on the bridge centerline or with their web perpendicular to the abutment centerline will result in small ratio of moment demand to moment capacity.

TABLE OF CONTENTS

LIST OF TABLES

Table Page

LIST OF FIGURES

Figure Page

CHAPTER 1

INTRODUCTION

1.1 Motivation

Many studies have been conducted recently on the behavior of integral abutment bridges (IABs) and their response under thermal load, yet most of these studies focused on straight IABs and only some considered skewed IABs. However, the long and short term behavior of skewed IABs using NEXT beam (Northeast Extreme Tee beam)sections in the superstructure under thermal loading is not understood yet owing to the novelty of the NEXT beam section, which was recently developed by PCI North-East, and it was used for the first time in the Commonwealth of Massachusetts to replace the Brimfield Bridge. For the sake of determining the live load distribution factor and understanding the long term behavior under thermal effect, the bridge was instrumented with strain gauges and displacement transducers as well as tiltmeters. Through field data provided by this instrumentation, and the development of a finite element model (FE model), the behavior of such a bridge will be studied to fully understand the response and performance. This study will provide guidance on the behavior of skew IABs and those using NEXT beam in particular, the effect of soil conditions and other factors on the bridge, and the best pile orientation.

1.2 Background

1.2.1 Integral Abutment Bridges

Bridges with continuous deck and abutments built monolithically with the superstructure and supported on flexible piles are called Integral Abutment Bridges (IABs). The main purpose of constructing this type of bridge is to avoid using costly deck expansion joints and sliding bearings at abutments (Integral Abutment Bridge Design Guidelines 2nd edition 2008 by VTrans Integral Abutment Committee). IABs can be single or multiple spans that are typically supported by a single row of piles driven under abutments walls. In Massachusetts the piles are aligned such that their web is perpendicular to the abutment wall to give higher flexibility. By making the abutments and superstructure continuous and monolithic, the bridge acts as a single unit. Thus, IABs accommodate thermal movements directly through the transfer of thermally-induced loads throughout the continuous structural system. Figure 1-1 shows the details of a typical integral abutment section in Massachusetts.

In many states in the U.S, IABs have become the preferred choice for moderate spans, yet each department of transportation (DOT) has different design and construction methods for these bridges. Different DOTs impose limits to the maximum span length and skew angle for IABs. These design limitations are meant to be conservative, which poses a barrier hindering design of IABs with longer spans, larger angle of skew, and different soil conditions (Civjan et al. 2007).There are still uncertainties associated to the design of IABs; such as the magnitude of soil pressure generated behind abutments and next to piles, especially during thermal expansion (Faraji et al. 2001).

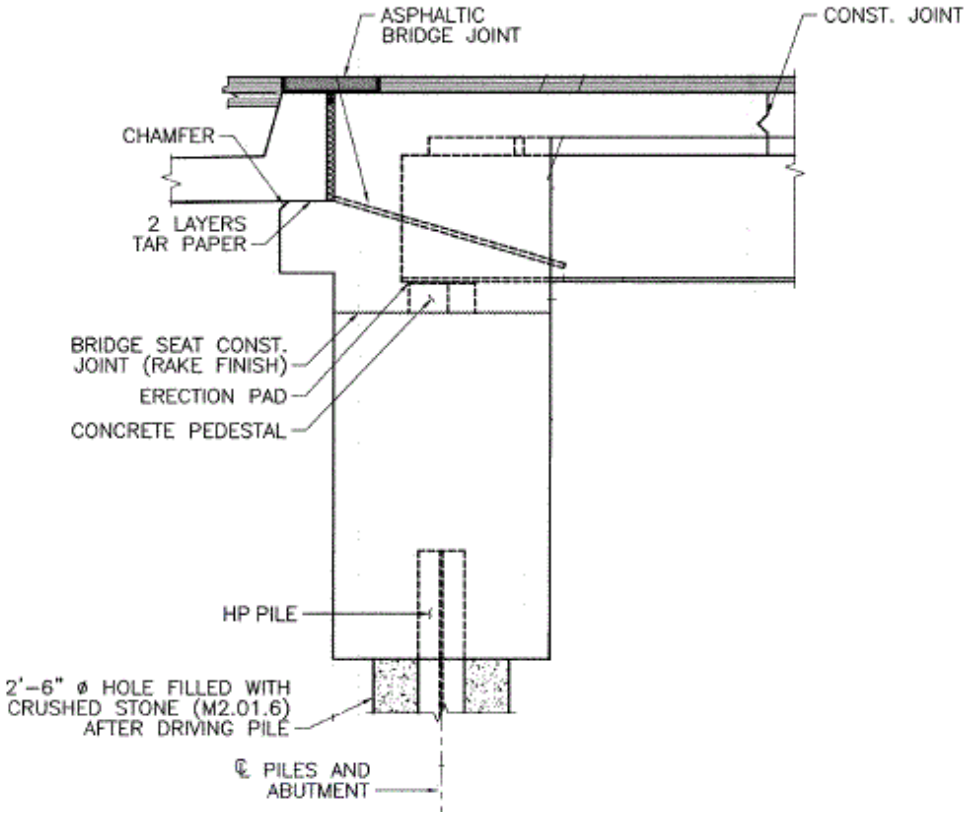

Figure 1-1: Integral Abutment Details in Massachusetts

1.2.2 Advantage of Integral Abutment Bridges

The main purpose of constructing IABs is to eliminate expansion joints. Unlike bridges with expansion joints, IABs offers initial and life-cycle cost saving since no installation and maintenance expenses of the expansion joints are required. Also, since only one row of piles is typically used, the construction of such bridges is faster and simpler (Hassiotis et al. 2005). Due to the absence of massive footings in IABs, bridge replacement process using integral bridges are often easier than non-IAB structures as they can be constructed behind the existing foundation of the old bridge without any need for extra excavations (Hassiotis et al. 2005). Furthermore, IABs are preferred in structures at regions with high seismic activity since they increase capacity during seismic events (FHWA 1986). Other advantages can also be gained

such as better ride experience and a larger end-span ratio in continuous bridge as they resist uplift caused by dead loads (Hassiotis et al. 2005).

1.2.3 Types of Jointless Bridges

IABs can be classified into three types,

- full integral
- semi-integral
- deck extension

The first type is characterized by abutments built monolithically with the superstructure and supported by one row of flexible piles. In this type, the deck is continuous with no expansion joints. Figure 1-2 and 1-3 show abutment details of this type of bridge and a view from within the span of an integral abutment bridge after finishing construction, respectively.

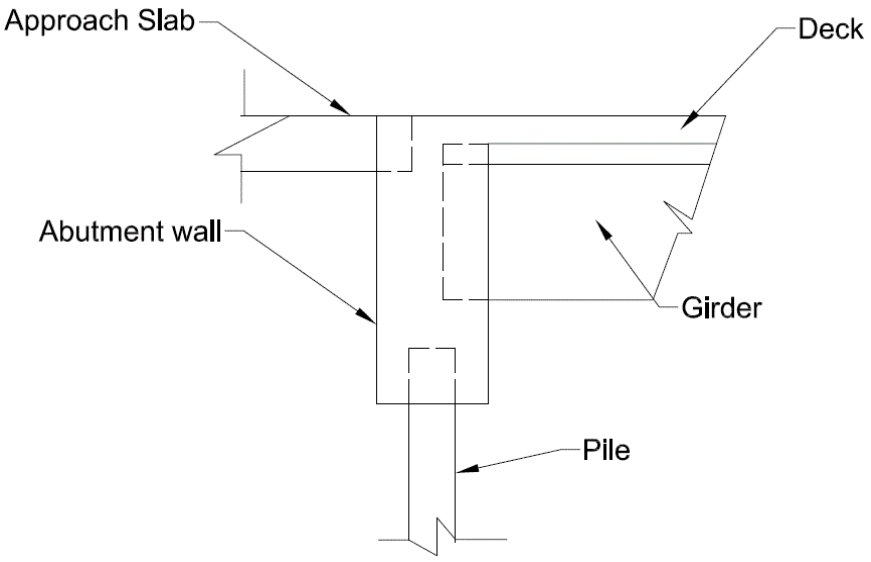

Figure 1-2: Full Integral Abutment Details

Figure 1-3: Full Integral Abutment after Construction

The second type (semi-integral), in which beams are supported on bearing elements, such as elastomeric pads, on top of the abutments. The superstructure is cast monolithically with backwalls that overhang from the deck behind the abutments. (Figure 1-4). Therefore the bridge deck is constructed without joints, but the superstructure/substructure does not act monolithically.

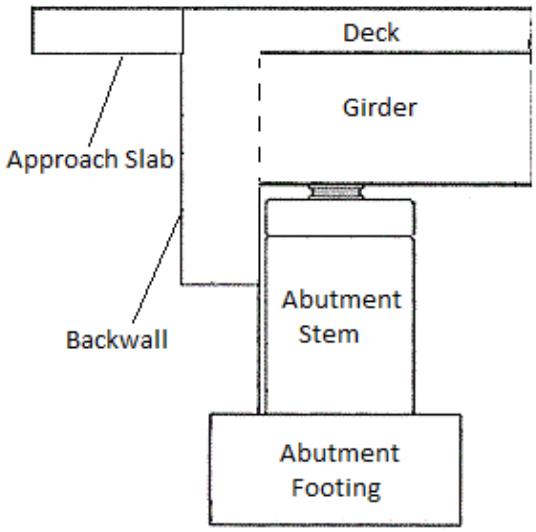

Figure 1-4: Semi-Integral Abutment Details

A deck extension bridge is constructed by extending the deck slab over the abutment backwall toward the adjacent approach pavement. Beams in the superstructure are not embedded into the abutment wall (Figure 1-5).

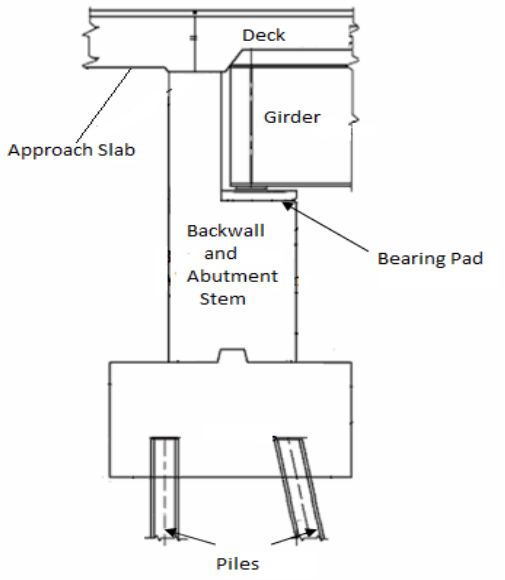

Figure 1-5: Extension Deck Abutment Details (Vermont DOT Integral Bridge Design Guidelines)

As in any other bridge, full integral abutment bridges can be classified according to geometry of their superstructure into three types:

- straight IABs
- skew integral abutment bridges
- curved integral abutment bridges

When the substructure of an integral abutment bridge makes a 90 degree angle with the road alignment and the superstructure then it is a straight IAB. A skew integral abutment bridge is a bridge with substructure makes any other angle with the line perpendicular to the road alignment as shown in Figure 1-6.

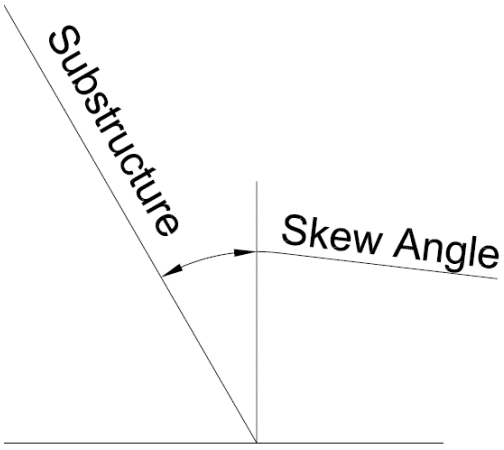

Figure 1-6: Skew Angle

Like typical bridges, IABs can also be classified according to number of spans, specifically as single or multiple spans.

1.3 Literature Review

The behavior of IABs is not yet fully understood due to many factors that contribute to their behavior. Important factors that can affect IABs behavior are soil properties of backfill and pile foundation, soil-structure interaction, bridge geometry, and superstructure type and material.

An IAB constructed using a newly developed NEXT beam section is of interest as it combines a new structural system with IAB design. Because of the novelty of this section in bridge engineering, no past studies have been performed regarding the long-term behavior under thermal effects of straight or skewed IABs with NEXT beam superstructures. The main purpose of developing such a section, according to the *Guide Line for Extreme Tee Beam (NEXT Beam) 1st Edition 2012*, which is presented by PCI, is to go with the Federal Highway Administration's philosophy of accelerated bridge construction by giving a better degree of consistency

among DOTs, engineers, and industry of the Northeast with respect to planning, designing, fabricating, and constructing. Moreover, the design of the NEXT Beam allows them to support utilities along the length of the bridge. By making stem dimensions constant and using magnetic side forms with the ability of using them for various beam widths, fabrication costs were reduced (Gardner and Hodgdon 2013). According to the *Guideline for Extreme Tee Beam (NEXT Beam) 1st Edition 2012,* there are two types of NEXT beam sections. The first one is NEXT D Beam which has a full-depth flange, on which a membrane and wearing surface can be field-applied, which makes it ready for traffic immediately after finishing construction. The second type is NEXT F Beam which has a partial-depth flange that can be used as the framework for the concrete deck. The dimension of the NEXT beam can be adjusted in order to be used in different span length and width. Figures 1-7 and 1-8 show the general shape of type D and F NEXT beam, respectively.

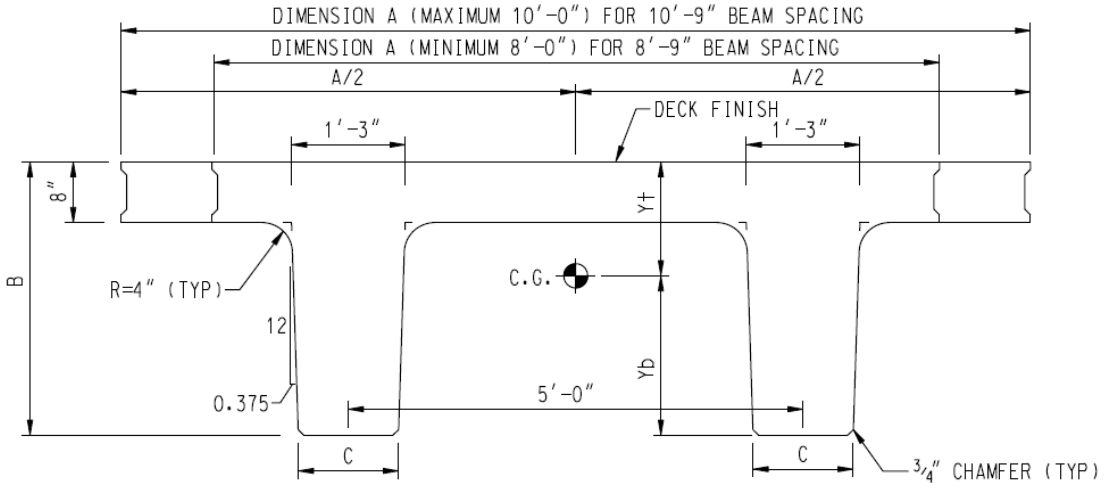

Figure 1-7: NEXT D Beam General Shape (Guideline for Extreme Tee Beam (NEXT Beam) 1st Edition 2012) Used by Permission

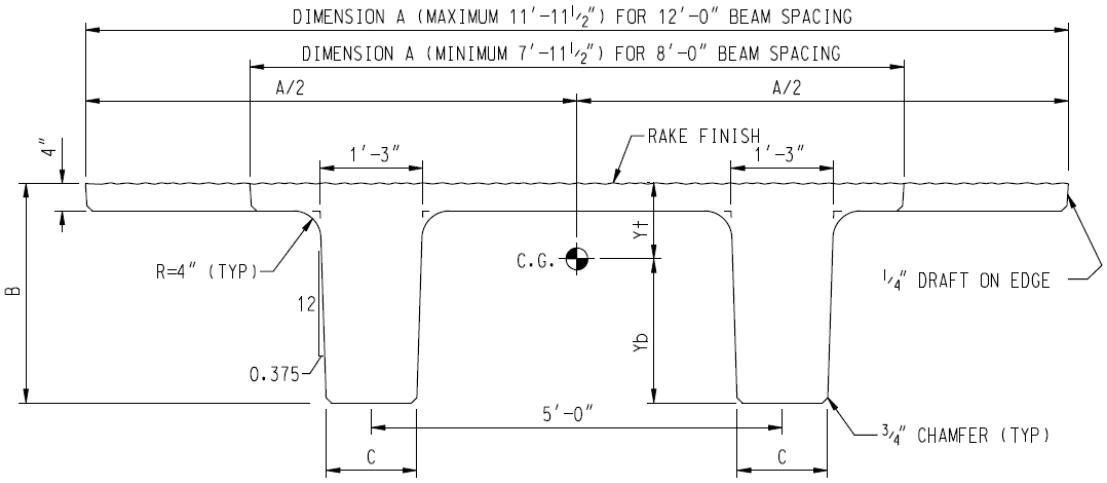

Figure 1-8: NEXT F Beam General Shape (Guideline for Extreme Tee Beam (NEXT Beam) 1st Edition 2012) Used by Permission

A review of past studies related to IAB behavior is necessary prior to modeling and analyzing the NEXT beam IAB discussed in this thesis, to allow behavioral comparisons to be drawn. There were many studies published discussing the behavior of IABs, yet for the sake of this research, only some of which were chosen as they introduce aspects of interest to this research.

William et al. 2012 investigated the response of a skew integral abutment bridge under thermal loading. A 3-dimensional finite element model was developed for a three-span steel beam integral bridge in West Virginia, which was instrumented with 232 sensors in order to capture its long-term behavior. The bridge has a skew angle of 35^{o} degrees and a total length of 44.8 m (146.9 ft) with a central span length of 14.78 m (48.5 ft) and end spans length of 15.24 m (50 ft). A plan view of the bridge is shown in Figure 1-9.

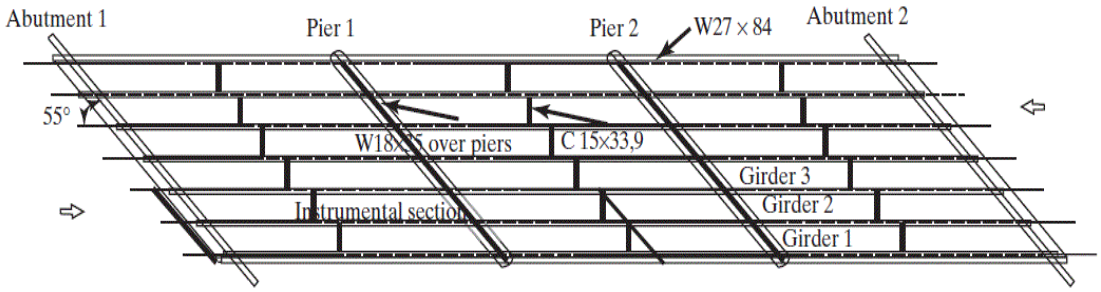

Figure 1-9: Plan View of Evansville Bridge (William et al. 2012) Used by Permission

The abutments were supported on 16 HP 12x53 piles oriented with their weak axes parallel to the abutment alignment. As a result of this study, it was found that resisting movement induced by temperature change will induce axial stress and permanent compression in the beams, even with the way the piles were oriented emphasizing on considering P-Δ analysis in analyzing IABs. It was also found that the angle of skew has a minimal effect on this axial stress. A paramedic study was conducted using same conditions including the applied temperature but with different skew angle. The authors noticed that the lateral displacement at the ends of bridge increased with larger skew angles, and that lateral displacement was not proportional to temperature change. Moreover, the bending stress in the steel beams was not affected significantly by changing the skew angle.

Faraji et al. 2001developed a full 3-dimensional finite element model of an IAB taking into account the nonlinear soil response under temperature loading. Figure 1-10 shows Bemis Road Bridge Elevation.

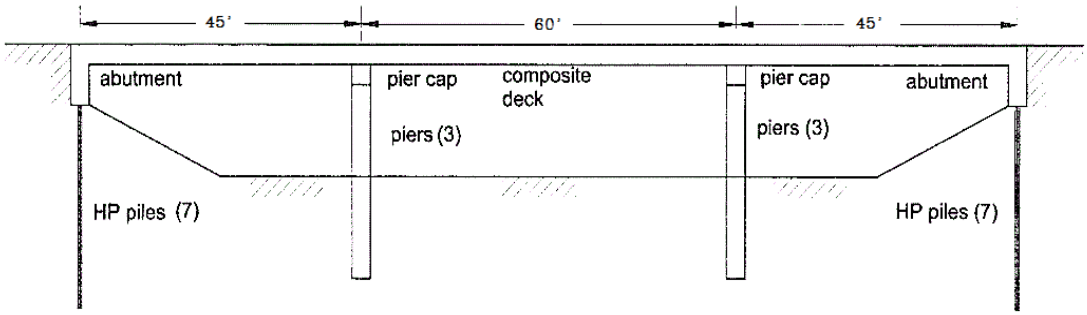

Figure 1-10: Elevation View of Bemis Road Bridge (Faraji et al. 2001) "With permission from ASCE"

In order to model the nonlinear response of the soil, the authors utilized uncoupled Winkler springs. By using the P-y curve method suggested by the American Petroleum Institute (API, 1993), the authors were able to define force-deflection relationship of the soil surrounding piles. The force-deflection relationship of springs representing backfill soil at a given node on the model for the abutments was estimated using Equation 1-1.

$$F = K\sigma_v' wh \qquad \text{Eq. 1-1}$$

Where:

F= lateral soil spring resistance force,

K= lateral earth pressure coefficient,

σ_v'= effective vertical earth pressure,

w= width of tributary area of abutment element,

h= height of the tributary area of abutment element,

Figure 1-11 shows the north abutment wall and plies under it of Bemis Road Bridge with springs distribution as it showed in Faraji et al. (2001).

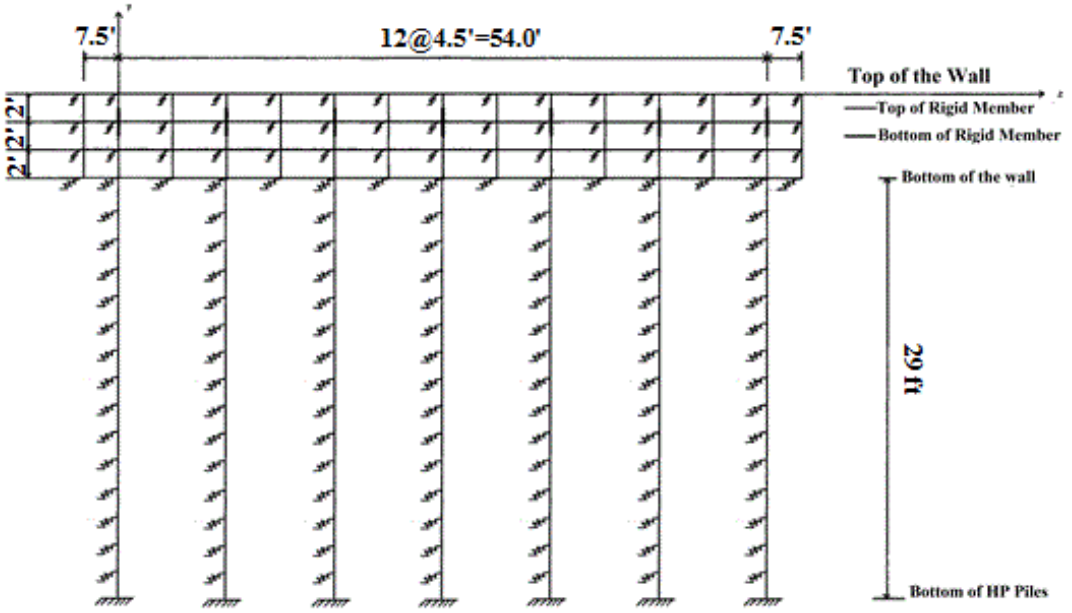

Figure 1-11: North Abutment and Piles of Bemis Road Bridge (Adopted from Faraji et al 2001)

As a result of applying an increment in temperature of 80^{o} F (26.67^{o} C) along with evaluating soil compaction level, it was noticed that the peak axial forces and bending moments in piles increased by a factor of 2 when varying from dense to loose soil conditions. Thus, the research team concluded that the soil compaction level behind the abutment is likely to significantly influence the response of the bridge. For soil conditions around the piles, however, the results showed little variation between loose and dense conditions, which indicated that soil conditions surrounding the piles do not affect the behavior of the bridge as much.

Bonczar et al. (2005) conducted a parametric study to investigate the seasonal behavior of IABs using a three- span instrumented bridge in Orange, Massachusetts as a prototype. The bridge was instrumented with strain gauges, movement sensors, and cell pressures behind the abutments (85 gauges total). An elevation view of the bridge is shown in Figure 1-12

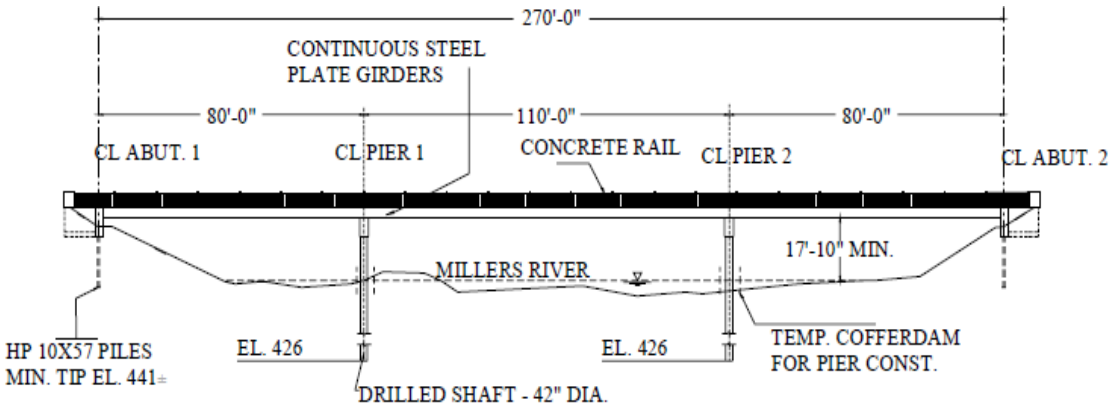

Figure 1-12: Elevation View of Orange Bridge, MA (Civjan et al. 2007) "With permission from ASCE"

The authors developed a 3-Dimensional FE model as well as 2-dimensional model. In order to define force-deflection relationships of pile springs, P-y curves were constructed using the procedure suggested by the American Petroleum Institute (API, 1993). Furthermore, defining the force-deflection curve for a given node on the abutment, after having the abutment meshed, was estimated using Equation 1-1 given previously.

In this study, the influences of loose and dense backfill soil were investigated as well as upper and lower bound restraint conditions surrounding the top 10 ft (3 m) of abutment piles. Piles in this bridge were driven into a 10-ft long pre-drilled hole that was filled with pea stone after pile driving. This in fact is a typical new procedure MassDOT started to follow to minimize the soil interaction around the top of piles. The researchers also considered two different soil-spring curves, one given in NCHRP "*Manuals for the Design of Bridge Foundations*" (1991) and the other using the *Massachusetts Highway Department Bridge Manual* (2005). The study took into account modification of wall spring curves with respect to relative wall displacement (δ/H), and changes in the passive earth pressure coefficient (K_p) near the top or

bottom of the abutments. It was found that the displacement of the abutment measured at beam centroid was not influenced by soil conditions, but the displacement that occurs at the bottom of the abutment, pile moments, and abutment rotation was strongly influenced by soil conditions. The research team reported that the most critical case for moment at the top of the piles is when upper bound pea stone properties being used whereas lower bound pea stone will give the least critical case when used with a dense abutment backfill. In terms of passive pressure, it was found that the highest passive pressure would occur at the base of the abutment when modeling dense backfill and lower pea stone properties. Field data and FE modeling indicate that the potential for pile yielding diminishes after the first year as the pile restraint decreases due to soil loosening. The results of using soil-spring curves given by NCHRP "*Manuals for the Design of Bridge Foundations*" (1991) and *Massachusetts Highway Department Bridge Manual* (2005) showed that both methods give response values that are within the range of values measured in the field. It was concluded that due to the change in soil properties under cyclic seasonal loads, the design assumptions used for this type of bridge are conservative.

A seven-year study including field monitoring of four IABs in the state of Pennsylvania was conducted by Kim et al. (2012). The objective was to record valuable long term data of the 4 bridges so it would be a good reference for future researchers who investigate the behavior of IABs. A weather station in central Pennsylvania was chosen to start collecting data since August 2002. The collected data from the weather station included solar radiation, temperature, rainfall, wind speed, and wind direction. A 3-dimensional FE models as well as 2-dimensional models were developed for these bridges along with archiving the long-term data. The first bridge (No.109), which consists of 4 spans that give the bridge an overall length

of 420 ft (128 m), was instrumented with 64 gauges; a similar number of instruments was used for the second and third bridges (No. 203 and 211 respectively) although the total length of the second bridge is 172 ft (52.4 m) with 3 spans only, and the third one is a single span bridge with114 ft (34.7m) total length. The fourth bridge (No. 222) is a single span bridge, and has a total span length of 62 ft (18.9 m), was instrumented with 48 gauges. The instrumentation of these bridges include extensometers for abutment displacement, pressure cells for backfill pressure, tiltmeters for abutment and beam rotations, beam strain gauges for beam moment and axial force, pile strain gauges for pile moment and axial force, and sister-bar gauges for approach slab strain. The research team reported the seven-year monitoring results including mean, maximum, and minimum envelopes, from which it was found that the response of all four bridges is within design limits. Furthermore, in the design of beams, the bending moment and axial force induced by thermal loading must be considered. Also, it was concluded that the temperature in the superstructure can be taken similar to the ambient temperatures since negligible differences were captured between the two.

Frosch and Lovell (2011) investigated the long term behavior of IABs and the effect of the skew. Three IABs were instrumented and monitored to observe and understand their behavior. The results of the field monitoring were used to calibrate the analytical models to capture the long term behavior. Then, a single-span, quarter – scale IAB was constructed and tested to get a better understanding on the behavior of highly skewed IABs. Using the knowledge gained from both field and laboratory investigations, the authors conducted a parametric analysis to determine the effects of possible parameters on the behavior of IABs. Finally, based on the analysis of the parametric study, geometric guidelines were developed. The authors concluded that

shrinkage of the concrete deck causes net inward movement of the bridge (contraction). The research states that a gap forms behind the abutment based on the fact that the lateral earth pressure reduces to approximately zero. They also found that the maximum lateral pile demand occurs as a result of contraction. Another conclusion states that because of the skew, rotation of the abutment and transverse movement of the structure occurs. Moreover, it was found that the largest longitudinal and transverse displacement occurs at the acute corner.

A recent research by Olson et al. (2013) investigating the potential of expanding the use of IABs in Illinois. An extensive 3- dimensional parametric study has been performed, complemented by field monitoring of two recently constructed bridges. It was concluded that a stiffer superstructure would restrain abutment rotation about its longitudinal axis. Therefore, the abutment remains nearly vertical during thermal expansion or contraction of the bridge deck in these cases. Because the abutment is almost vertical, the thermal movement of the superstructure must be almost fully accommodated at the pile heads. On the other hand, a more flexible superstructure permits rotation of the abutment, and some of the thermal deck displacement is accommodated by abutment rotation. In the case of the studied bridge, the moments are not severe at the pile head. Figure 1-13 illustrates the difference in pile response during thermal expansion of stiff and flexible superstructures. As a result of the parametric study it was concluded that concrete shrinkage could influence maximum pile stresses in some IAB configurations as it cause the bridge to displace inwardly in addition to the contraction induced by thermal loading.

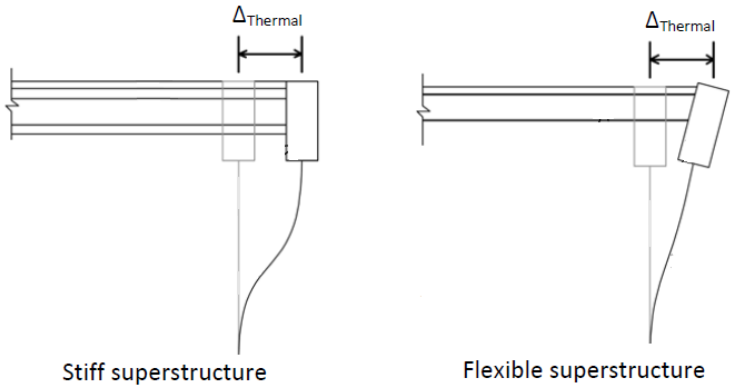

Figure 1-13: Effect of Superstructure Stiffness on the Moment at the Pile Head (Adopted from Olson et al. 2013)

The authors concluded that the way the HP piles are being oriented in Illinois (their web is perpendicular to the abutment alignment) is inappropriate in skewed bridges because they permit excessive weak-axis bending, so they suggested to orient the piles with their web parallel to the bridge longitudinal global axis regardless of skew. Furthermore, the researchers recommend the use of compacted granular backfill behind the abutments due to the fact that the passive pressures of the backfill are beneficial to piles resisting thermal expansion in bridges with skew less than 45 degrees.

1.4 Scope and Objectives

The objective of this thesis is to understand the long-term behavior of skewed IABs in which precast NEXT Beam section was used in their superstructure. Hence, field monitoring of Brimfield Bridge along with detailed 3-dimensional FE model were used in order to achieve this objective. Since the long-term behavior of IABs is essentially governed by thermal loading, the FE model of the Brimfield Bridge primarily focuses on investigating the thermal effect. Another important aspect that is lacking in general from the literature is the inclusion of data during construction of IABs, an aspect that is particularly important for prestressed concrete bridges such as

the NEXT beam chosen for this thesis. FE models were validated using field data. Models were changed to better approximate field data by varying soil properties, thermal load distribution, and assumed coefficient of thermal expansion. The effect of pile orientation on abutment base rotational restraint was also investigated by changing the way piles are oriented relative to the abutment centerline.

CHAPTER 2

BRIMFIELD BRIDGE DESCRIPTION AND INSTRUMENTATION

2.1 Introduction

The existing Brimfield Bridge (Figure 2-1) crossing Mill brook on Route-19 (Figure 2-2), was built in 1951 and scheduled to be replaced by a new IAB. The goal was to construct a new bridge using accelerated bridge technologies to minimize the impact of construction activities on site. Hence, beams of the NEXT beam section (Figure 1-8) were utilized in the superstructure of the new bridge owing to the advantages of this type of beam sections as stated in Chapter 1

Figure 2-1: Existing Brimfield Bridge

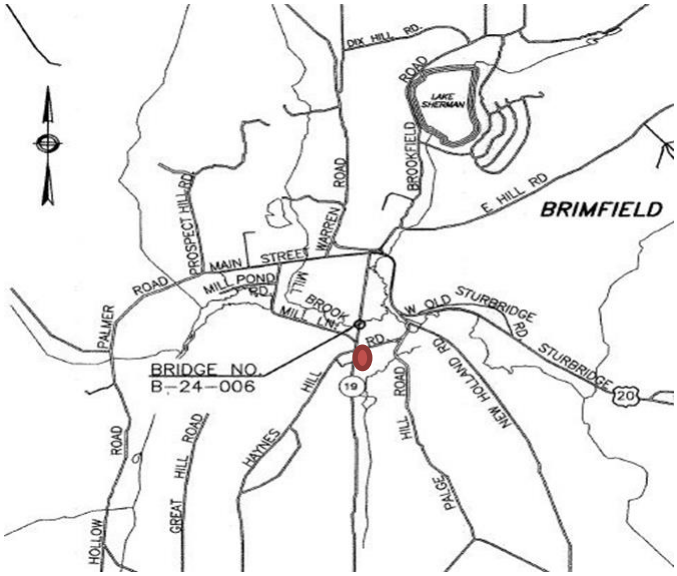

Figure 2-2: Brimfield Bridge Location

The replacement bridge has a 30 degree skew angle. Furthermore, the bridge was widened and lengthened compared with the existing bridge to accommodate new geometric requirements. The new length of the bridge is 65 ft (19.8m) and the total width is 48.5 ft (14.8m). Figures 2-3, 2-4, and 2-5 show the plan view, transverse section, and elevation view of Brimfield Bridge.

The replacement bridge was constructed in two phases. During each phase, three NEXT beams were installed starting with beams 6, 5, and 4 and then beams 3, 2, and 1. After finish installing the NEXT beams at each phase, concrete deck was poured along with the abutments. Figures 2-6 and 2-7 show the construction procedure during the first phase.

The new bridge was instrumented with strain gauges and displacement transducers to collect data on the long term behavior. Field data is used to monitor the actual behavior and calibrate the FE model, giving the advantage to establish parametric studies to develop recommendations for expanding NEXT beam use in bridges.

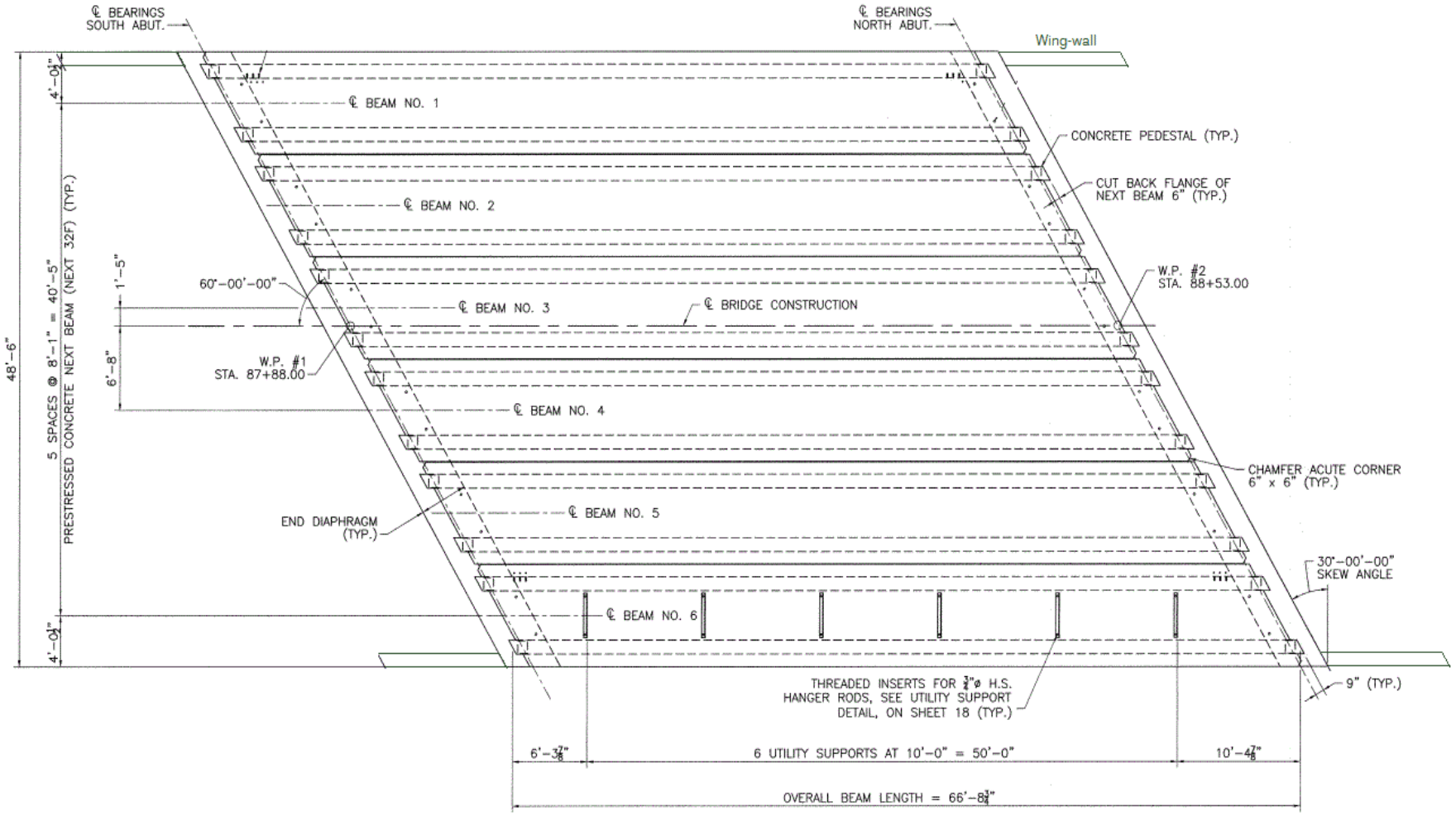

Figure 2-3: Plan View of Brimfield Bridge

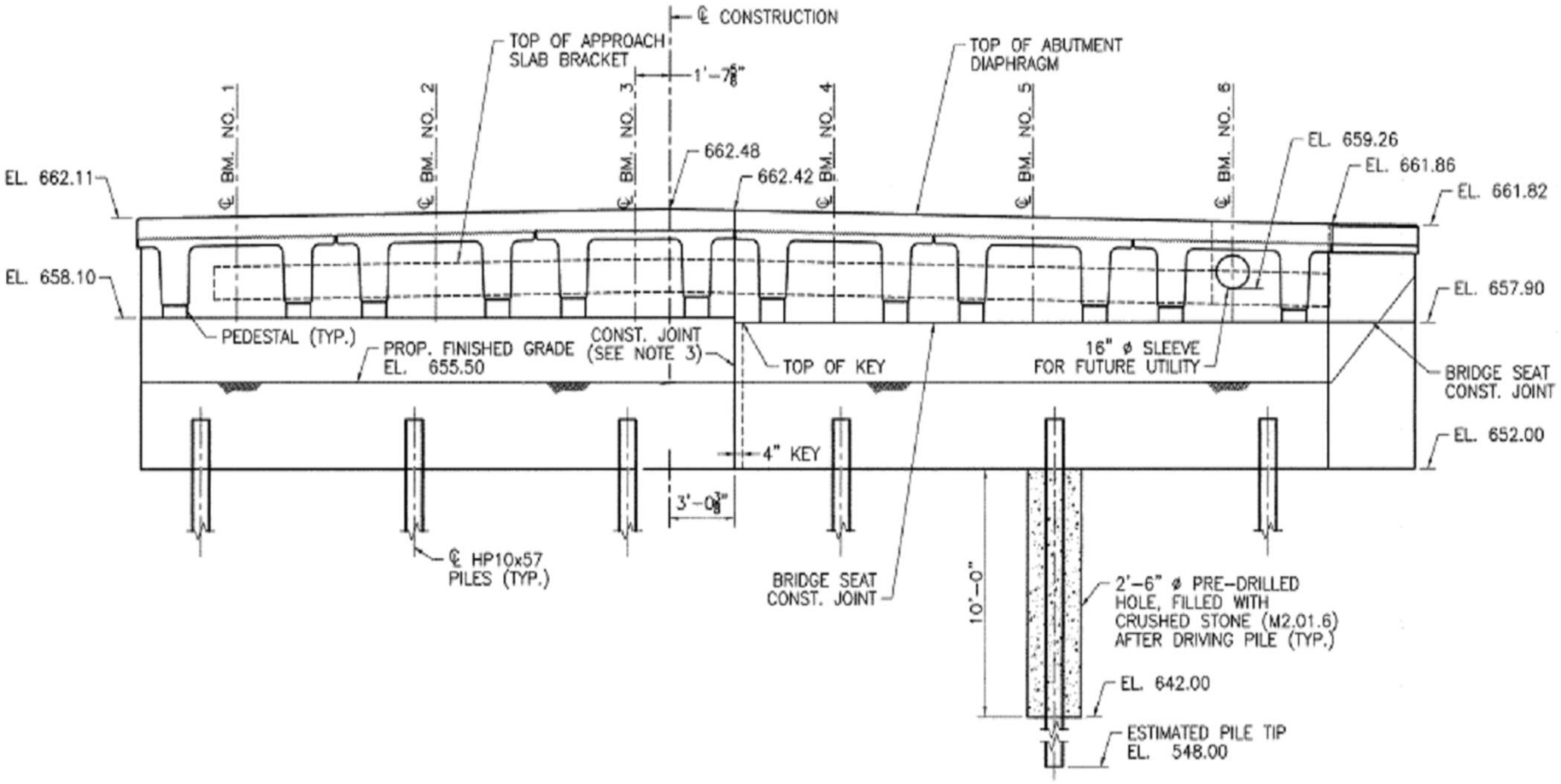

Figure 2-4: Transverse Section (North Abutment)

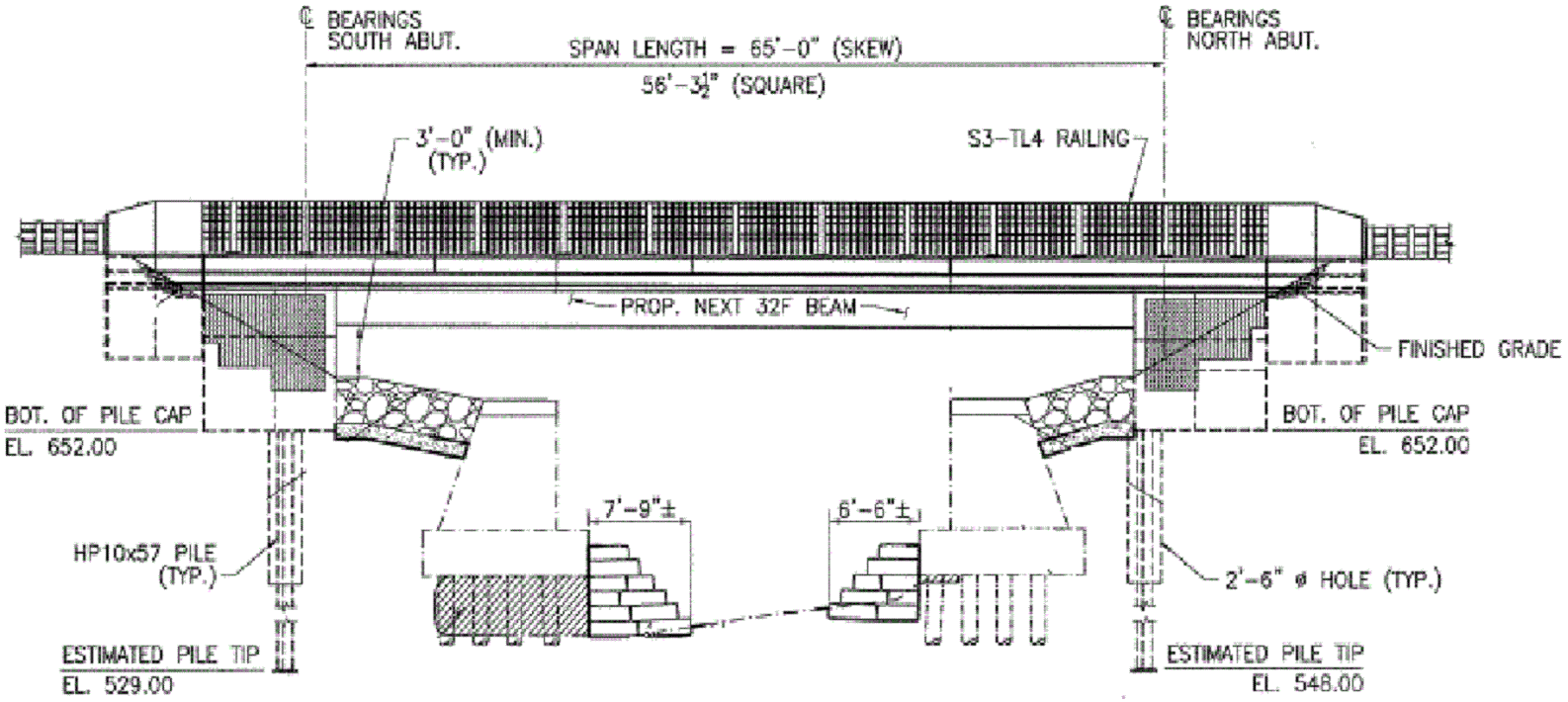

Figure 2-5: Elevation View of Brimfield Bridge

Figure 2-6: Beams 6, 5, and 4 Placed on the Abutments during Phase 1

Figure 2-7: Casting the Concrete Deck (Phase 1)

2.2 Brimfield Bridge Superstructure

2.2.1 Precast/Prestressed Beams

NEXT 32F section was utilized in the superstructure of Brimfield Bridge. The properties of the NEXT beam cross section utilized in the Brimfield Bridge are illustrated in Figure 2-8 and listed in Table 2-1.

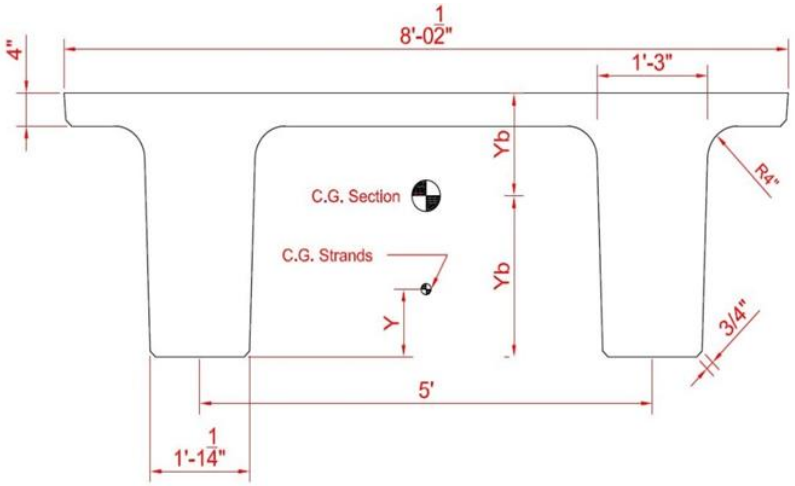

Figure 2-8: NEXT Beam Section Used in Brimfield Bridge

Table 2-1: NEXT Beam Section Properties Used in Brimfield Bridge

Property	Variable	Magnitude
Area	A	1183.84 (in.^{2}) 763766(mm^2)
Moment of Inertia	I_g	115936 (in.^{4}) 48256*10^6(mm^4)
Depth	D	32 (in) 812.8 (mm)
Distance from Top to C.G	Y_t	12.45 (in) 316.3 (mm)
Distance from Bottom to C.G	Y_b	19.54 (in) 496.3 (mm)
Distance from Bottom to C.G of Strands	Y	8.22 (in) 208.8 (mm)
Eccentricity	e	11.3 (in) 288.7 (mm)

The total length of each beam is 66'-8 3/4" (20.3 m). Six NEXT beams were used at an even spacing of 8'-1" (2.46 m) including a 0.5-in (12.7 mm) longitudinal beam joint. As a result, the bridge total width is 48'-6" (14.8 m) as shown in the plan view of the bridge in Figure 2-3 and as well as in Figure 2-4, which shows a transverse section of the bridge. The bridge has two travel lanes each 12 ft (3.6576 m), and two shoulders. Beams were erected onto bearing pads at the top of cast in place lower abutment sections. Continuity was then achieved by embedding the ends of the beams during casting of the deck and the remaining top portion of the abutments at both ends of the bridge. The distance between pads centerlines is 65 ft (19.8 m) and between abutments interior faces is 63 ft (19.2m) as shown in Figure 2-5. Thirty six 7-wire strands with an area of 0.217 were used in the NEXT beams as shown in figure 2-9.

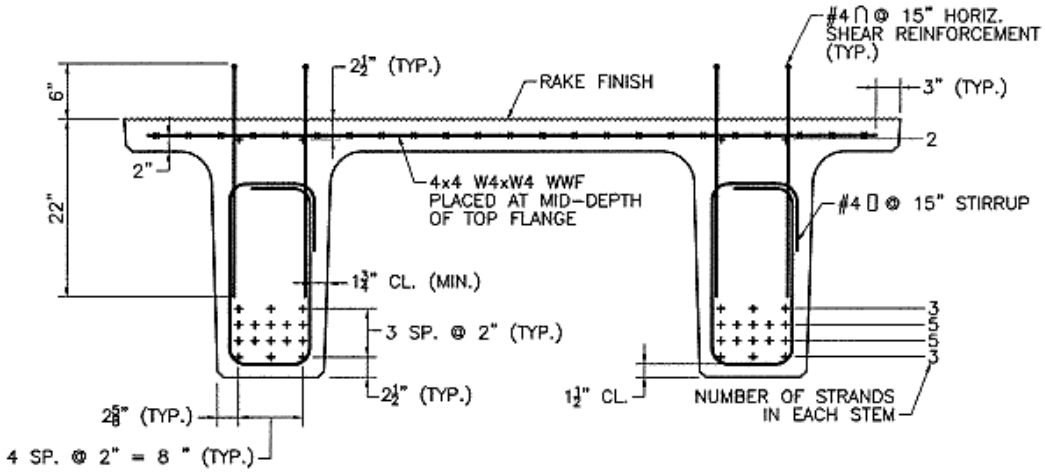

Figure 2-9: Strands Distribution and other Reinforcement Details

2.2.2 Concrete Deck and Wearing surface

The deck used in Brimfield Bridge consists of a cast-in-place reinforced concrete with thickness of 8 in. (200 mm). It was cast monolithically with the abutments. A concrete nominal compressive strength of 4000 psi (28 MPa) was used

in casting the deck. A 5'-6" wide (1.6764 m) sidewalk was located on the east side of the bridge whereas a safety curb was built on the west side as shown in Figure 2-7.

The wearing surface of Brimfield Bridge has a thickness of 3.5 in. (8.89 cm) and it consists of 1 3/4" (4.445 cm) hot mix asphalt (HMA) modified course over 1 3/4" (4.445 cm) HMA dense binder.

2.3 Brimfield Bridge Substructure

The foundation of Brimfield Bridge consists of two abutments, four wing walls (two for each abutment), and 12-HP piles (six under each abutment). The average height of the abutments is 10.283 ft (3.1 m), their variable height accommodates drainage and differences in grading at bridge ends (Figure 2-4).

The thickness and width of the abutments are 4 ft (1.22 m) and 48.5 ft (14.8 m), respectively. Each abutment is supported on six-HP10X57 steel piles. The interior four piles are evenly spaced at 10 ft (3 m); the distance between the centerline of the exterior piles and the edge of the abutment differs in each side of the abutment. The distance between the abutment side and the centerline of the exterior pile at the east and west sides of the south and north abutments, respectively, is 4'-17/8"(1.3 m) from the edge. The exterior piles at the west and east sides of the south and north abutments, respectively, are located 1'-10 1/8" (0.562 m) from the edge. The tops of piles are embedded 2 ft (0.6 m) into the bottom of abutments and the estimated driven length is 104 ft (31.6992 m) into the ground. The piles are oriented so that their weak axes are parallel to the abutment wall to minimize resistance to bending during thermal induced deformations. The top 10 ft (3.0 m) of the piles are driven into a pre-drilled hole with diameter equal to 2'-6" (0.762m) that was backfilled with crushed stone after driving piles. Figures 2-10 and 2-11 show details of the abutments at the

south and north sides of the bridge, respectively. Both the height and the length of the four wing walls is 10 ft (3.0 m) with a thickness of 1'-7 7/8" (0.5 m). Wing-walls are integral with the abutments and they make an angle of 60 degrees with the abutments alignment as shown in Figures 2-10 and 2-11.

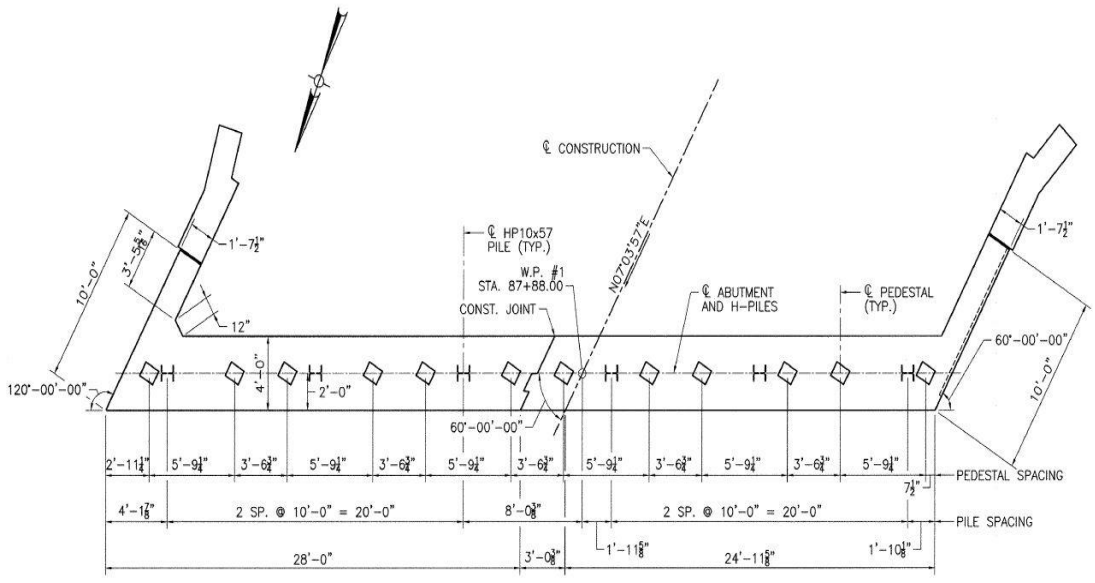

Figure 2-10: South Abutment Details

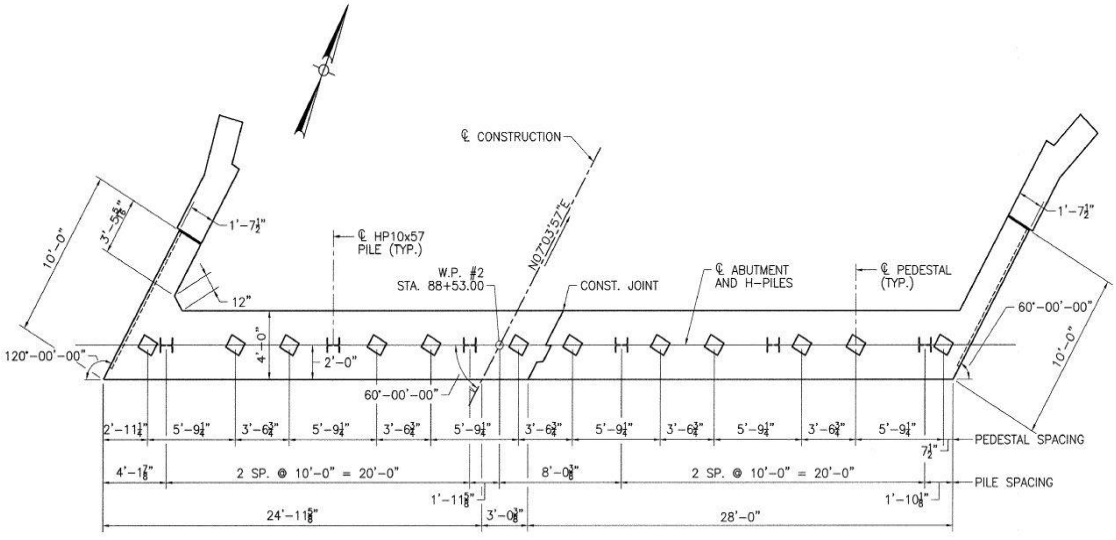

Figure 2-11: North Abutment Details

2.4 Bridge Instrumentation

2.4.1 Strain Gauges

A total of 138 strain gauges were used in the Brimfield Bridge superstructure. Strain gauges were labeled using two numbers separated by a hyphen. The strain gauges oriented in the longitudinal and transverse directions of the bridge. The distribution of strain gauges was planned to capture the most important deformations that reflect the behavior of the bridge. Beams one and two were instrumented at mid-span and at sections located one-third and two-thirds into the beam span. Figure 2-12 shows the sections selected for strain gauge instrumentation in the bridge superstructure.

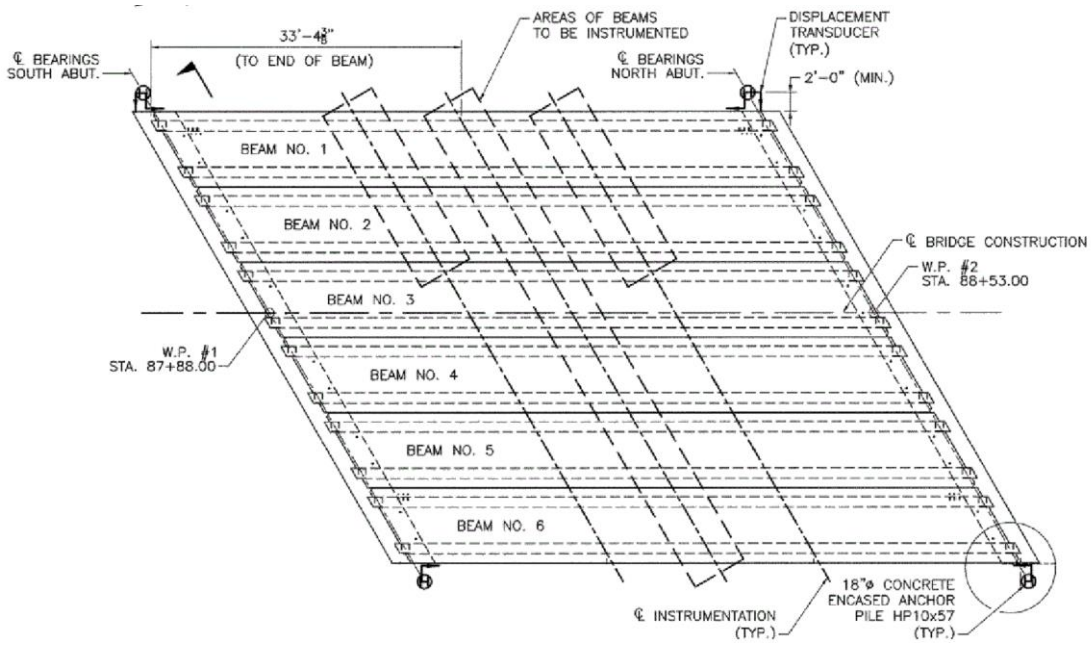

Figure 2-12: Brimfield Bridge Instrumentation

All beam cross-sections were instrumented using a similar pattern of strain gauges. Small differences in depth of the gauges resulted during construction. The longitudinal strain gauges near the bottom of the deck were installed directly above

strain gauges installed in beam flanges. An evaluation of composite action between the deck and the beams was possible with this configuration.

The first number in the gauge designation corresponds to the beam number; the second number represents gauge number used in the beam. Because of the different number of cross-sections instrumented in each beam, the total number of gauges varied per beam. Strain gauges embedded in the concrete deck were identified with the letter D after the gauge number. Figure 2-13 illustrates the locations of the strain gauges throughout the cross-section of a beam and deck. Table 2-2 lists the gauge depths and numbers for all beams and instrumented cross-sections.

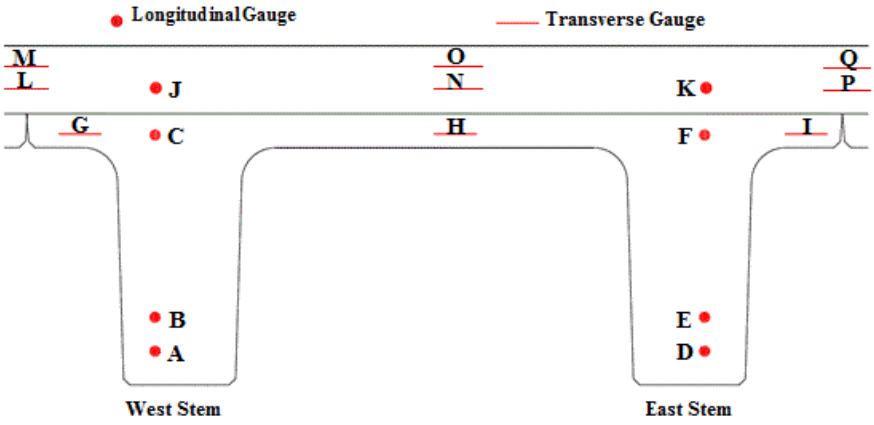

Figure 2-13: Generic Strain Gauge Locations inBeam Cross-section

Table 2-2: Details of Strain Gauge Locations

Position in Cross Section*	Field Numbering Scheme**	Gauge Direction	Gauge Depth from the Bottom of the Beam(in.)	Nominal Gauge Depth from the Bottom of the Beam (in.)
A	1-1 (1/3 span)	Longitudinal	3.75	2.5
	1-9 (Mid-span)	Longitudinal	4	2.5
	1-17 (2/3 span)	Longitudinal	4	2.5
	2-1 (1/3 span)	Longitudinal	3.5	2.5
	2-9 (Mid-span)	Longitudinal	3.75	2.5
	2-18 (2/3 span)	Longitudinal	3.625	2.5
	3-1 (Mid-span)	Longitudinal	3.5	2.5

	4-1 (Mid-span)	Longitudinal	4.25	2.5
	5-1 (Mid-span)	Longitudinal	4	2.5
	6-1 (Mid-span)	Longitudinal	3.785	2.5
B	1-2 (1/3 span)	Longitudinal	8.25	6
	1-10 (Mid-span)	Longitudinal	8.25	6
	1-18 (2/3 span)	Longitudinal	8.25	6
	2-2 (1/3 span)	Longitudinal	8.25	6
	2-10 (Mid-span)	Longitudinal	8.125	6
	2-19 (2/3 span)	Longitudinal	8.125	6
	3-2 (Mid-span)	Longitudinal	8.125	6
	4-2 (Mid-span)	Longitudinal	8	6
	5-2 (Mid-span)	Longitudinal	7.785	6
	6-2 (Mid-span)	Longitudinal	8	6
C	1-5 (1/3 span)	Longitudinal	29.5	30.5
	1-13 (Mid-span)	Longitudinal	29.5	30.5
	1-21 (2/3 span)	Longitudinal	29.5	30.5
	2-7 (1/3 span)	Longitudinal	29.5	30.5
	2-14 (Mid-span)	Longitudinal	29.5	30.5
	2-23 (2/3 span)	Longitudinal	29.5	30.5
	3-6 (Mid-span)	Longitudinal	29.5	30.5
	4-6 (Mid-span)	Longitudinal	29.5	30.5
	5-6 (Mid-span)	Longitudinal	29.5	30.5
	6-5 (Mid-span)	Longitudinal	29.5	30
D	1-3 (1/3 span)	Longitudinal	3.75	2.5
	1-11(Mid-span)	Longitudinal	4	2.5
	1-19 (2/3 span)	Longitudinal	4	2.5
	2-3 (1/3 span)	Longitudinal	3.75	2.5
	2-11 (Mid-span)	Longitudinal	3.75	2.5
	2-20 (2/3 span)	Longitudinal	3.5	2.5
	3-3 (Mid-span)	Longitudinal	3.5	2.5
	4-3 (Mid-span)	Longitudinal	4	2.5
	5-3 (Mid-span)	Longitudinal	3.785	2.5
	6-4 (Mid-span)	Longitudinal	3.625	2.5
E	1-4 (1/3 span)	Longitudinal	8	6
	1-12 (Mid-span)	Longitudinal	8	6
	1-20 (2/3 span)	Longitudinal	8	6
	2-4 (1/3 span)	Longitudinal	8.125	6
	2-12 (Mid-span)	Longitudinal	8.125	6
	2-21 (2/3 span)	Longitudinal	8.125	6
	3-4 (Mid-span)	Longitudinal	8.25	6
	4-4 (Mid-span)	Longitudinal	7.75	6
	5-4 (Mid-span)	Longitudinal	8.125	6
	6-3 (Mid-span)	Longitudinal	8	6

F	1-7 (1/3 span)	Longitudinal	29.5	30.5
	1-15 (Mid-span)	Longitudinal	29.5	30.5
	1-23 (2/3 span)	Longitudinal	29.5	30.5
	2-5 (1/3 span)	Longitudinal	29.5	30.5
	2-16 (Mid-span)	Longitudinal	29.5	30.5
	2-25 (2/3 span)	Longitudinal	29.5	30.5
	3-8 (Mid-span)	Longitudinal	29.5	30.5
	4-8 (Mid-span)	Longitudinal	29.5	30.5
	5-8 (Mid-span)	Longitudinal	29.5	30.5
	6-6 (Mid-span)	Longitudinal	29.5	30.5
G	2-8 (1/3 span)	Transverse	29.5	30.5
	2-13 (Mid-span)	Transverse	29.5	30.5
	2-22 (2/3 span)	Transverse	29.5	30.5
	3-5 (Mid-span)	Transverse	29.5	30.5
	4-5 (Mid-span)	Transverse	29.5	30.5
	5-5 (Mid-span)	Transverse	29.5	30.5
H	1-6 (1/3 span)	Transverse	29.5	30
	1-14 (Mid-span)	Transverse	29.5	30
	1-22 (2/3 span)	Transverse	29.5	30
	2-6 (1/3 span)	Transverse	29.5	30
	2-15 (Mid-span)	Transverse	29.5	30
	2-24 (2/3 span)	Transverse	29.5	30
	3-7 (Mid-span)	Transverse	29.5	30
	4-7 (Mid-span)	Transverse	29.5	30
	5-7 (Mid-span)	Transverse	29.5	30
I	1-8 (1/3 span)	Transverse	29.5	30.5
	1-16 (Mid-span)	Transverse	29.5	30.5
	1-24 (2/3 span)	Transverse	29.5	30.5
	2-17 (Mid-span)	Transverse	29.5	30.5
	3-9 (Mid-span)	Transverse	29.5	30.5
	4-9 (Mid-span)	Transverse	29.5	30.5
	5-9 (Mid-span)	Transverse	29.5	30.5
J	1-1D (1/3 span)	Longitudinal	33.75	33.5
	1-7D (Mid-span)	Longitudinal	34	33.5
	1-13D (2/3 span)	Longitudinal	33.5	33.5
	2-1D (1/3 span)	Longitudinal	34	33.5
	2-7D (Mid-span)	Longitudinal	33.75	33.5
	2-13D (2/3 span)	Longitudinal	33.375	33.5
	3-1D (Mid-span)	Longitudinal	34	33.5
	4-3D (Mid-span)	Longitudinal	34	33.5
	5-3D (Mid-span)	Longitudinal	33.75	33.5
	6-3D (Mid-span)	Longitudinal	34.5	34
K	1-4D (1/3 span)	Longitudinal	34	33.5

	1-10D (Mid-span)	Longitudinal	33.75	33.5
	1-16D (2/3 span)	Longitudinal	33.5	33.5
	2-4D (1/3 span)	Longitudinal	34	33.5
	2-10D (Mid-span)	Longitudinal	33.375	33.5
	2-16D (2/3 span)	Longitudinal	33.375	33.5
	3-4D (Mid-span)	Longitudinal	33.75	33.5
	4-6D (Mid-span)	Longitudinal	33.75	33.5
	5-6D (Mid-span)	Longitudinal	34.25	33.5
	6-4D (Mid-span)	Longitudinal	34.5	33.5
L	4-1D (Mid-span)	Transverse	33.5	33.5
	5-1D (Mid-span)	Transverse	33.5	33.5
	6-1D (Mid-span)	Transverse	34	33.5
M	4-2D (Mid-span)	Transverse	37	38
	5-2D (Mid-span)	Transverse	36.5	38
	6-2D (Mid-span)	Transverse	36.5	38
N	1-2D (1/3 span)	Transverse	33.75	34
	1-8D (Mid-span)	Transverse	33.75	34
	1-14D (2/3 span)	Transverse	33.75	34
	2-2D (1/3 span)	Transverse	34	34
	2-8D (Mid-span)	Transverse	33.5	34
	2-14D (2/3 span)	Transverse	33.75	34
	3-2D (Mid-span)	Transverse	34	34
	4-4D (Mid-span)	Transverse	33.75	34
	5-4D (Mid-span)	Transverse	34	34
O	1-3D (1/3 span)	Transverse	36.75	38
	1-9D (Mid-span)	Transverse	36.75	38
	1-15D (2/3 span)	Transverse	36.625	38
	2-3D (1/3 span)	Transverse	36.5	38
	2-9D (Mid-span)	Transverse	36.5	38
	2-15D (2/3 span)	Transverse	36.75	38
	3-3D (Mid-span)	Transverse	37	38
	4-5D (Mid-span)	Transverse	33.75	38
	5-5D (Mid-span)	Transverse	36.5	38
P	1-5D (1/3 span)	Transverse	33.75	33.5
	1-11D (Mid-span)	Transverse	34.25	33.5
	1-17D (2/3 span)	Transverse	33.5	33.5
	2-5D (1/3 span)	Transverse	33.75	33.5
	2-11D (Mid-span)	Transverse	34.25	33.5
	2-17D (2/3 span)	Transverse	34	33.5
Q	1-6D (1/3 span)	Transverse	36.75	38
	1-12D (Mid-span)	Transverse	36.75	38
	1-18D (2/3 span)	Transverse	36.5	38
	2-6D (1/3 span)	Transverse	36.75	38

	2-12D (Mid-span)	Transverse	36.75	38
	2-18D (2/3 span)	Transverse	37	38
*** Refers to generic gauge position in beam cross section (Figure 2-12)**				
**** The field numbering scheme follows beam number-gauge label**				

Gauges were embedded in the beams during fabrication and in the deck prior to casting of concrete in the field. All strain gauges are Geokon model 4200 vibrating wire gauges. Figure 2-14 shows a strain gauge attached longitudinally at the bottom group of strands in a beam.

Figure 2-14: Longitudinal Strain Gauge Attached to Strands

2.4.2 Crackmeters

To capture the longitudinal and transverse displacement of abutment walls, Brimfield Bridge was also instrumented using crackmeters at the right and left side of each abutment. These crackmeters measure displacements relative to a reference pile (HP10x57) which is assumed to be stationary. Four crackmeters were installed to capture movement in the longitudinal direction of the bridge; two crackmeters were installed at the west side of the abutments to measure movement in the transverse

direction of the bridge. Figure 2-12 shows the placement of crackmeters used at the abutments.

Crackmeters were attached to 2 by 2 by 0.25 in. (51x 51x 6.4 mm) angle, which was attached to HP steel piles driven at a 2 ft (0.61 m) distance from each side of the abutments (Figure 2-15 and 2-16). These piles provide a reference point considered assumed to not be affected by abutment movement. Crackmeters were installed at different depth from the top of the sidewalk as shown in Table 2-3.

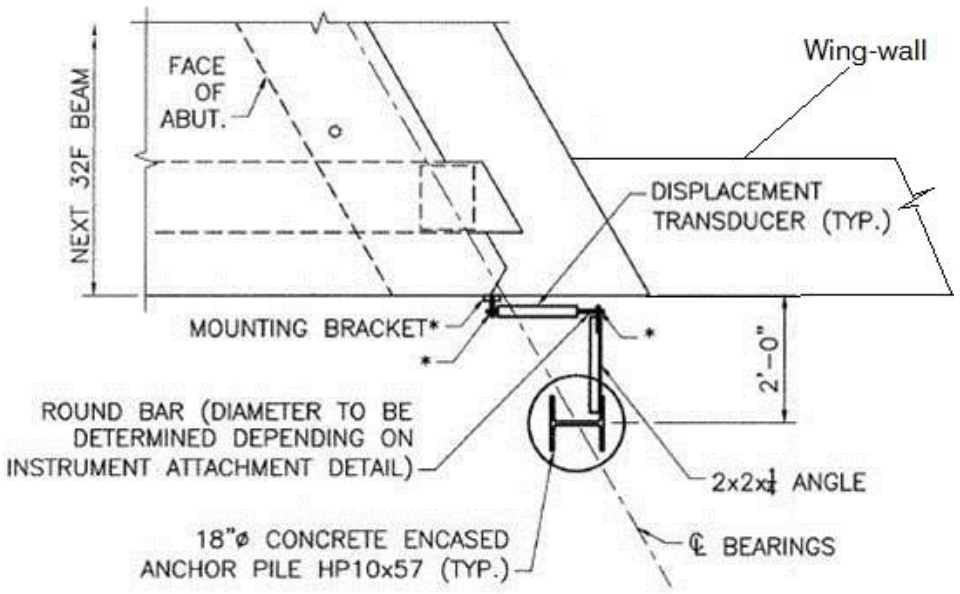

Figure 2-15: Crackmeter Location Details

Figure 2-16: Picture of Crackmeter Installation on Abutment

Table 2-3: Crackmeters Height

Abutment	Crackmeter Location	Depth from Top of the Sidewalk in. (mm)
South	Acute Corner	50 (1270)
South	Obtuse Corner	46.5(1181)
North	Obtuse Corner	49.5(1257)
North	Acute Corner	45.5(1155.7)

2.4.3 Tiltmeters

In order to capture the rotation of the abutments, one tiltmeters was installed at the center of each abutment wall at the interior side. Figure 2-17 shows a tiltmeter after being installed before installing the protective box.

Figure 2-16: Tilt-meter Right after Being Installed

2.5 Summary

In this chapter, precise details about the Brimfield Bridge were given. Instrumentation details were also shown in this chapter including the location, distribution, and depth of each strain gauge as well as the places and details of other instrumentation, crackmeters and tilt-meters.

CHAPTER 3

FIELD DATA

3.1 Introduction

Data obtained using the instrumentation described in Chapter 2 is presented in this chapter. The data was used to understand the short-term and long-term behavior of the bridge. Short-term data was used to understand the live-load distribution of NEXT beam components in an IAB. This chapter will focus on data collection, data correction, and data interpretation during construction and long- term monitoring. Live load testing of this bridge was studied recently in order to evaluate the live load distribution factor and reported elsewhere (Singh (2012)). Plots illustrating strain, temperature, displacement, and rotation data were generated to investigate the behavior of the entire bridge and individual components.

3.1 Data Collection

During construction, data were collected in three stages starting at the time when beams were cast until deck and abutments were hardened. The three stages, dates of each reading, and a briefly description of the readings are given in Table 3-1. Given the construction sequence, three of the six beams remained in the precasting plant yard for almost one year, so strain readings taken during this period reflect strains induced by shrinkage and creep of concrete.

Table 3-1: During Construction Data

Stage	Beam No.	Date	Description
Inside the plant	1,4	4/26/2011	20 hours after pouring concrete
		4/26/2011	10 minutes after de-tensioning
	2,3	4/22/2011	20 hours after pouring concrete
		4/22/2011	10 minutes after de-tensioning
	5,6	4/28/2011	20 hours after pouring concrete
		4/28/2011	10 minutes after de-tensioning
Outside the plant	1,4	4/26/2011	Beam is supported at 3' (0.91 m) from its ends
		4/28/2011	
		5/26/2011	
		8/5/2011	
	2,3	4/22/2011	
		4/26/2011	
		4/28/2011	
		5/26/2011	
		8/5/2011	
	5,6	4/28/2011	
		5/26/2011	
		8/5/2011	
Beam is placed on the Abutments	1,2,3	3/22/2012	After placing beam on the Abutments
		4/10/2012	After pouring the deck and Abutments
	4,5,6	8/11/2011	After placing beam on the Abutments
		9/13/2011	After pouring the deck and Abutments

A live-load test was conducted at the end of construction (05/24/2012). Long term monitoring started right after the end of the live-load test (12:30 pm on 05/24/2012) and the acquisition rate was set at 2 hours throughout the long-term monitoring period which is still continuing.

3.2 Data Correction

Actual measured strains in beams and in the concrete deck are determined by applying a temperature correction to the data logger readings in accordance with Equation 3-1 given by the strain gauge manufacturer. This accounts for different thermal expansion properties of the concrete elements and steel wire in the vibrating wire gages used in the project. Thus, only mechanical strains which can be directly related to stresses in the elastic range of material behavior will be presented.

$$\mu_{true} = (R_1 - R_0)\, B + (T_1 - T_0)\,(C_1 - C_2) \qquad \text{Eq.3-1}$$

Where,

R_1 = current strain reading (Tensile if positive)

R_0= reference strain reading (Tensile if positive)

B= 0.975 (Batch calibration factor)

C_1= coefficient of expansion of steel, 12.2 μ/°C

C_2= coefficient of expansion of concrete

T_1= temperature measured at current time

T_0= temperature measured at the time of reference reading.

The coefficient of thermal expansion of concrete C_2, as noted above, can vary significantly depending on the aggregate used, water/cement ratio, and relative humidity. Further discussion in Section 5.3.3 concentrates on how different values for the coefficient of thermal expansion affect data correction and FE model validation. Also, the measured strains include not only load related effects but also strains that induced by creep and shrinkage.

The reference reading that is used to correct data during construction is the one that was taken after 20 hours from casting the beams since by that time the concrete was hardened. The reference reading for long term data was chosen right after the end of the load test.

Temperature correction was applied to crackmeter and tiltmeter readings as well to account for changes in wire tension due to the expansion and contraction of

the wire under thermal changes. The following formula (Equation 3-2) was utilized to correct crackmeter readings

$$D_{corrected} = ((R_1-R_0)*G + (T_1-T_0)*K) \quad \text{Eq.3-2}$$

Where,

G = linear gauge factor in inches/digit (from the supplied calibration sheet. Each crackmeter have a slightly different value of G)

K= thermal coefficient calculated using Equation 3-3

$$K = ((R_1 * M)+B) * G \quad \text{Eq.3-3}$$

Where,

M= multiplier given by the Manufacturer (0.000192)

B= constant (0.669)

The following Equation 3-4 was used in order to correct tiltmeter readings for temperature

$$\Delta\theta = ((R_1 - R_0)G + K(T_1-T_0) \quad \text{Eq.3-4}$$

Where,

G= calibration factor in degrees/digit (from the supplied calibration sheet)

K= 0.5G

3.3 Data Taken throughout Construction

In order to understand the strain readings in beams during construction, strain calculations were conducted taking into account all factors that might contribute

to the values of these readings. Thus, beam self-weight, creep in concrete, shrinkage in concrete, and prestressing force losses were considered as discussed next. The initial prestressing force applied was 45.29 kip (201.46 KN) per strand which gives a total prestressing force of 1630 kip (7252KN) on each beam.

3.4.1 Loss Calculations

Two different specifications (AASHTO LRFD 2010 and PCI 6th edition) were considered to calculate prestress losses in the beams. Both specifications include four sources that induce losses that might occur after the application of the prestressing force, which are shrinkage, creep, elastic shortening, and strand relaxation, yet each uses a different calculation to predict the same type of losses.

Calculation of prestress losses using the refined estimate of losses in AASHTO LRFD 2010 was used to determine the value of losses in this study. A particular advantage of using this method despite its higher level of complication is that values can be determined as a function of time, which is more appropriate in this research since strains were taken at different times during construction. Prestress loss formulas given in the PCI 6th Edition only provide loss estimates in for a single time (long-term) and do not allow calculation of loss evolution with time.

3.4.1.1 Prestress Losses Due to Shrinkage

In order to estimate prestressing stress losses due to concrete shrinkage at different stages, Equation 3-5 given in AASHTO LRFD 2010 was used.

$$\Delta f p_{SR} = \epsilon_{sh} E_p K_{id} \qquad \text{Eq. 3-5}$$

Where,

E_p= modulus of elasticity of prestressing steel,

K_{id} = transformed section coefficient that accounts for time-dependent interaction between concrete and bonded steel in the section (Equation 3-6)

$$K_{id} = \frac{1}{1+\frac{Ep\ Aps}{Eci\ Ag}\left(1+\frac{Ag\ e^2}{Ig}\right)*\{1+0.7\Psi(ti,td)\}} \quad \text{Eq. 3-6}$$

ε_{sh} = concrete shrinkage strain of beam between the time of transfer and deck placement, which was estimated using Equation3-7,

$$\epsilon_{sh} = K_s\ K_{hs}\ K_f\ K_{td} * 0.48*10^{-3} \quad \text{Eq. 3-7}$$

K_s= factor for the effect of the volume-to-surface ratio of the component as shown below

$$K_s = (1.45 - 0.13(V/S)) \geq 1.0 \quad \text{Eq. 3-8}$$

K_{hs}= humidity factor for shrinkage (%), Equation 3-9,

$$K_{hs} = (2.00 - 0.014\ H) \quad \text{Eq. 3-9}$$

K_f= factor for the effect of concrete strength (Equation 3-10),

$$K_f = \frac{5}{1+f'c} \quad \text{Eq. 3-10}$$

K_{td}=time development factor (Equation 3-11),

$$K_{td} = \frac{t}{61-4f'c+t} \quad \text{Eq. 3-11}$$

e_{pg} = eccentricity of prestressing force with respect to centroid of beam,

$\Psi_{b(tf,\ ti)}$ = beam creep coefficient at final time due to loading introduced at transfer (Equation 3-12),

$$\Psi_b = 1.9\ K_s\ K_{hc}\ K_{td}\ t_i^{-0.118} \quad \text{Eq. 3-12}$$

t_d = age at deck placement,

t_i = age at transfer,

A_g = gross area of precast section,

A_{ps} = area of prestressing steel,

e = eccentricity of prestressing force with respect to centroid of gross beam section,

I_g = moment of inertia of gross precast section,

E_{ci} = modulus of elasticity of concrete at transfer or at time of load application, was estimated by using Equation 3-13,

$$E_{ci} = 33\ K_1\ W_c^{1.5}\ \sqrt{f'ci} \qquad \text{Eq. 3-13}$$

K_1=1,

W_C= weight of concrete, which was taken from field test as shown in Table 3-2

$f_{'ci}$= concrete strength at release. Table 3-2

Table 3-2: Quality Control Report (May12-2011)

Casting date	Air Temp.	Conc. Temp.	Slump spread	Unit weight	Air content	Strength at release	7 day strength	ID
04/21/11	64	78	23	141.36	7.5	9408	11050	2
	64	78	23	141.36	7.5	9944	11385	3
04/25/11	64	82	24	143.36	5.5	8760	9454	4
04/25/11	64	82	25	142.2	6	8437	9973	1
04/27/11	70	85	24	145.38	4.6	8886	10504	5
	70	85	24	145.36	4.6	9468	10665	6

In order to predicted losses at different stages, necessary assumptions were made. For instance, it was assumed that t_d (time at deck placement) is equal to the age

at the time when losses are being estimated. Furthermore, in the calculation of the humidity factor K_{sh} at each stage, an average value was used, which represents the humidity that has been experienced by the beams before each reading. This would lead to more accurate results than using the average yearly humidity given in AASHTO 2010. Since the beams were cast in a different place then moved to the site, the humidity of both places was considered. Also, the factor accounting for the effect of concrete strength was calculated at each stage using different concrete strength depending on time the readings were taken as will be discussed later in Section 3.4.2

3.4.1.2 Prestress Losses Due to Creep

Equation 3-14 represents the equation given in AASHTO LRFD 2010 to estimate prestressing stress losses due to creep. The equation can be used to calculate losses at each stage during construction.

$$\Delta f_{pcr} = \frac{E_p}{E_{ci}} f_{cgp} \Psi_{b(td,ti)} K_{id} \qquad \text{Eq. 3-14}$$

t_i= age at which curing was stopped.

f_{cgp}= sum of concrete stresses at the center of gravity of prestressing tendons due to the prestressing force as well as self-weight at the sections of maximum moment. It was found using Equation 3-15

$$f_{cgp} = P_i\,[1/A_t + e_t^2/I_t] - (M_g\, e_t)/I_t \qquad \text{Eq. 3-15}$$

Where,

P_i= initial prestressing force (before losses),

M_g= moment due to self-weight,

e_t= eccentricity of prestressing force with respect to centroid of transformed beam section

A_t= transformed section area.

I_t= transformed moment of inertia,

Due to the differences in unite weight of each beam mix as shown in Table3-2, the maximum moment calculated for each beam differed among beams. Transformed section properties were used in calculating f_{cgp}, which account for the existence of strands.

3.4.1.3 Prestress Losses Due to Elastic Shortening

When calculating concrete stresses using transformed section properties, the effects of losses and gains due to elastic deformations are implicitly accounted for (AASHTO LRFD 2010). Thus, no additional calculations to account for elastic shortening losses are needed as long as transformed section properties are used.

3.4.1.4 Prestress Losses Due to Strand Relaxation

Equation 3-16 is the equation given in AASHTO LRFD 2010 to estimate prestressing force losses due to strand relaxation. These losses were calculated at each stage during construction.

$$\Delta f_{pRL} = \frac{fpt}{Kl}\left(\frac{fpt}{fpy} - 0.55\right) \qquad \text{Eq. 3-16}$$

Where,

Kl= 30 for low relaxation strands,

f_{pt} = stress in prestressing steel immediately after transfer,

f_{py}= yield stress of the prestressing steel.

3.4.2 Strain Calculations Due to Prestressing Force and Beam Self-weight

In order to calculate the strain and compare it with the field data during construction, stress calculations had to be conducted first. The prestressing force generates both axial force and moment in beams so Equation 3-17 was used to calculate the stress under initial presstressing force (before losses) and moment induced by self-weight.

$$\sigma_{b1,t1} = -\frac{P_i}{A_t} \pm \frac{P_i\, e\, y}{I_t} \mp \frac{M_g\, y}{I_t} \qquad \text{Eq. 3-17}$$

Transformed section properties were used to compute stresses in the cross section to avoid calculation of elastic shortening losses as discussed previously. Change in stress due to losses were subtracted or added depending on the location in the cross-section (top or bottom). Moment due to self-weight was calculated assuming that beams were simply supported on a span equal to the beam length after application of the prestressing force as beams tend to camber right after applying this force. A special consideration in moment calculations was taken at the stage when beams were placed on temporary supports located 3 ft (0.91 m) from their ends outside the plant. To account for prestressing force losses on concrete stress, Equation 3-18 was used as shown below.

$$\sigma_{b2,t2} = \pm\,(\Delta fp_{RL} + \Delta fp_{cr} + \Delta fp_{SR})\frac{Aps}{Ag}\left(1+\frac{Ag\, eg\, yb}{Ig}\right) \qquad \text{Eq. 3-18}$$

The results obtained from Equation 3-17 at each stage were added to the results obtained by Equation 3-18 to determine the total load related stress. Consequently, the load induced strains at each stage were estimated using Hook's Law (Equation 3-19)

$$\text{Strain}=\frac{Stress}{E_c} \qquad \text{Eq. 3-19}$$

Here, different moduli of elasticity of concrete were used in calculating load related strains at each stage. Modulus was estimated from concrete compression strength, using Equation 3-20, as the compressive strength in concrete typically increases with time, which was estimated using Equation 3-20 given in ACI-209R-92.

$$f'_{ct}=\frac{t}{a+\beta.t}\ f'_{c28} \qquad \text{Eq. 3-20}$$

Where,

f'_{ct}= required compressive strength at different age

t= age in days

f'_{c28}= 28-day compressive strength

a and β = constants depend on curing and cement type.

3.4.3 Calculated Strain Due to Creep and Shrinkage

Creep and shrinkage in concrete affect the strain at throughout the depth of beams. Since shrinkage in concrete can vary throughout the section depth, no calculations were made as no approximate prediction of shrinkage can be determined as it can vary throughout the section, yet it has small effect on the results. Creep strain calculations were conducted using Equation 3-21 given by Branson (1977).

$$C_t=\frac{creep\ strain}{initial\ strain}=\left(\frac{t^c}{d+t^c}\right) C_u \qquad \text{Eq. 3-21}$$

Where

C_t= creep coefficient,

C_u=ultimate creep coefficient,

c and *d*= constants,

By applying C_u= 2.35(for standard conditions) along with using correction factors of 0.8 for both humidity and volume to surface ratio *V/S*, and using a value of 0.6 and 10 for the constants c and d respectively, C_t was found. Having C_t multiplied by the initial strain due to self-weight and initial prestressing force only, creep strain at the required stages was found. Summing the strain results from different components gave the total strain at the top and the bottom of each beam. An example shows strain calculations is represented in Appendix A

3.4.4 Beams Behavior during Construction

After determining the calculated and measured strain for each stem at each stage in all beams, these were compared at a point of given depth. The center of gravity of strands in each stem was chosen to be used as a point of comparison.

Field data showed that the strain in most cases varied linearly with depth and due to having three readings along the depth of the beam the strain profile consisted of two different slopes as shown in Figure 3-1 and in Appendix C, yet it is important to put in mind that there are limitations on knowledge about the exact strain distribution given that the strain was measured at three points only throughout the depth. The calculated strain, on the other hand, was assumed to vary linearly with depth. In order to establish simple comparison between data, results were reported and plotted at the center of gravity of the strands.

After finding the strain at the top and bottom of the beam, the strain at the center of gravity of the strands, located 8.22 in. (208.8 mm) from bottom of the

beams, was found. In order to estimate the measured strain at the center of gravity of the strands without neglecting the departure from linearity of strains at different depths, the procedure illustrated in Figure 3-2 was followed. Two values were calculated at the center of gravity of the strand: one was calculated using the data measured at the top strain gauge and at the bottom assuming that strains varied linearly between these values; the second method used strain values measured at bottom and middle gauges or top and middle gauges. By taking the average of these two values, an approximation was achieved for the strain at the center of gravity of strands (Figure 3-2). Figures 3-3 to 3-12 show plots of the strains determined at center of gravity of strands from field and calculated data. Strains are shown for each stage selected during construction and each instrumented section within each beam. The three stages shown in these figures are illustrated in Table 3-1

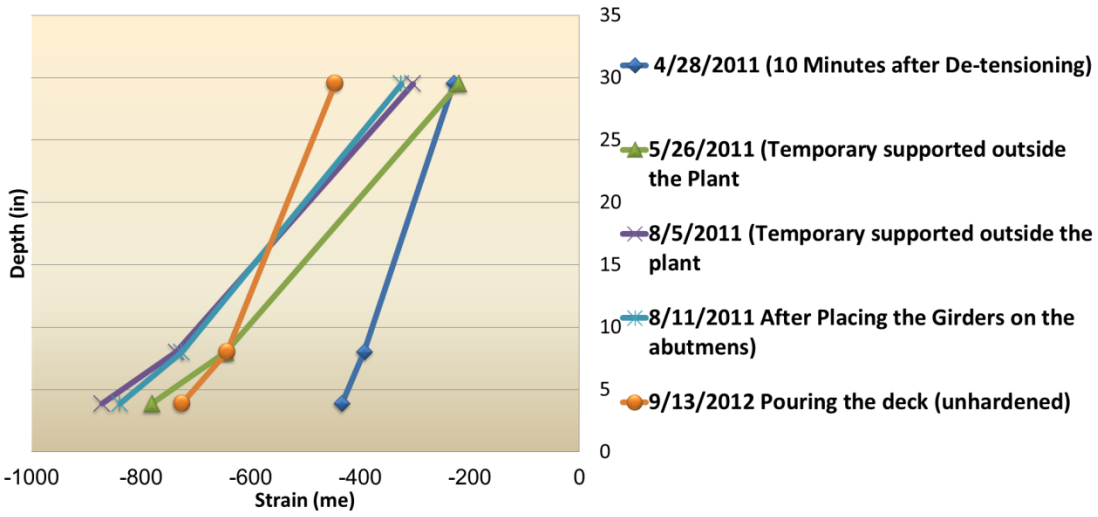

Figure 3-1: Sample of Measured Strain Variation with Depth

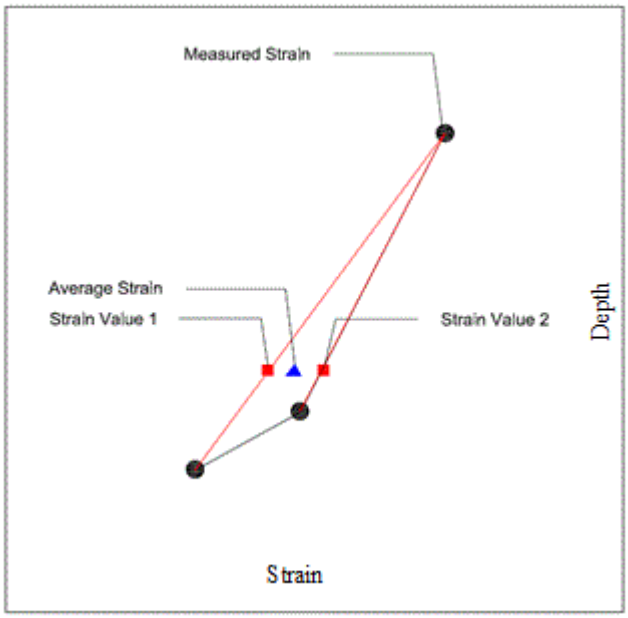

Figure 3-2: Example of Calaulating Stain at Strands Center of Gravity

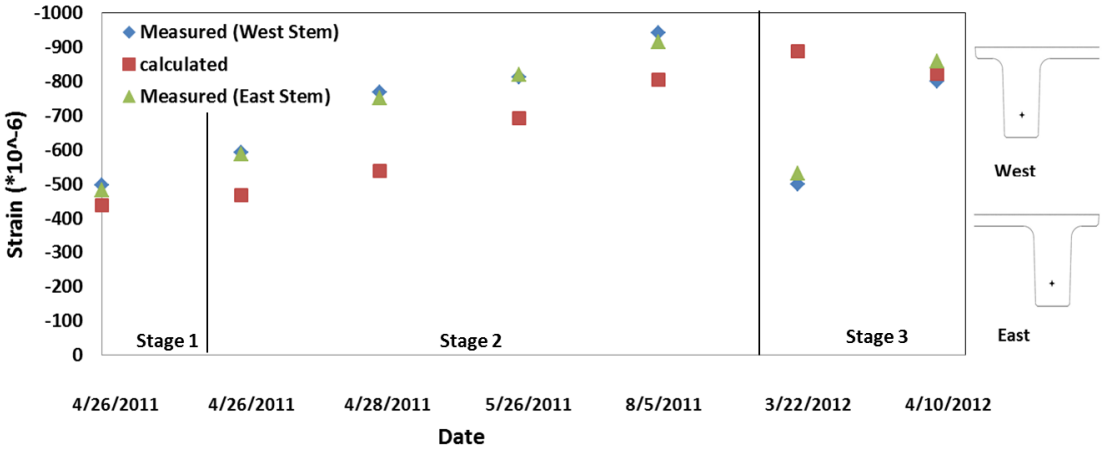

Figure 3-3: Calculated Vs. Measured Strains at Different Dates (Beam 1-1/3 span)

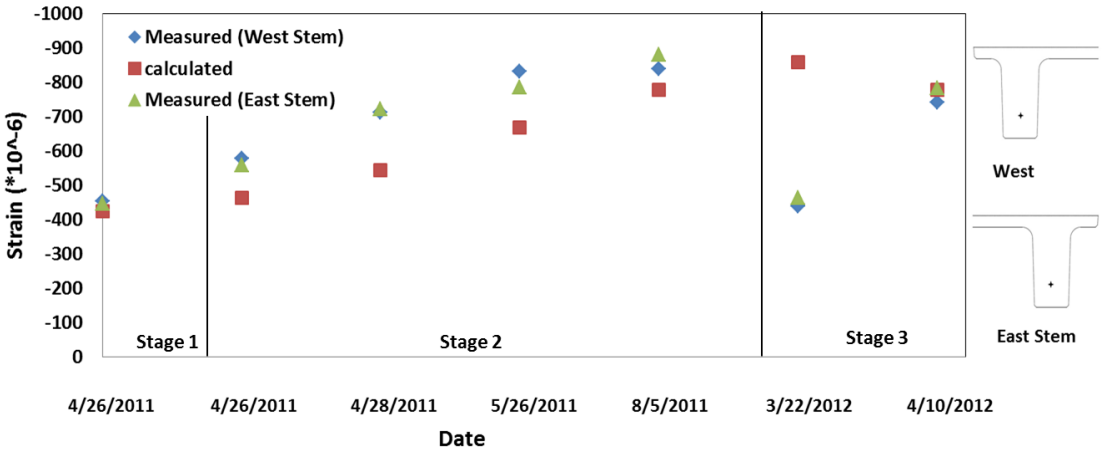

Figure 3-4: Calculated Vs. Measured Strains at Different Dates (Beam 1 mid-span)

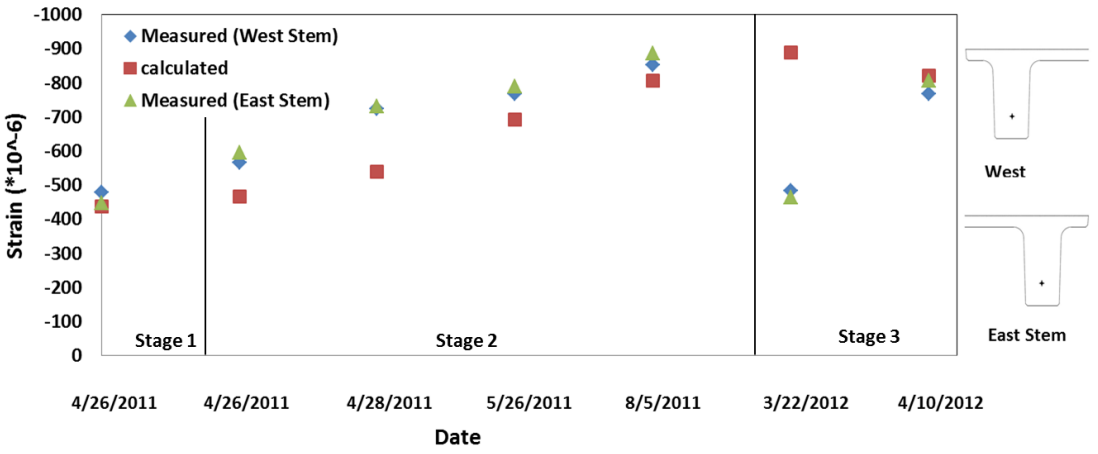

Figure 3-5: Calculated Vs. Measured Strains at Different Dates (Beam 1-2/3 span)

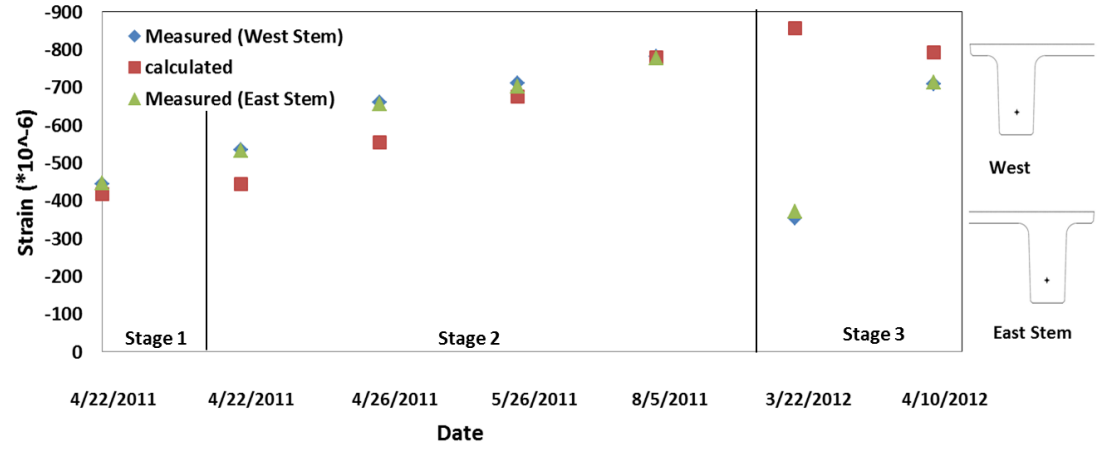

Figure 3-6: Calculated Vs. Measured Strains at Different Dates (Beam 2-1/3 span)

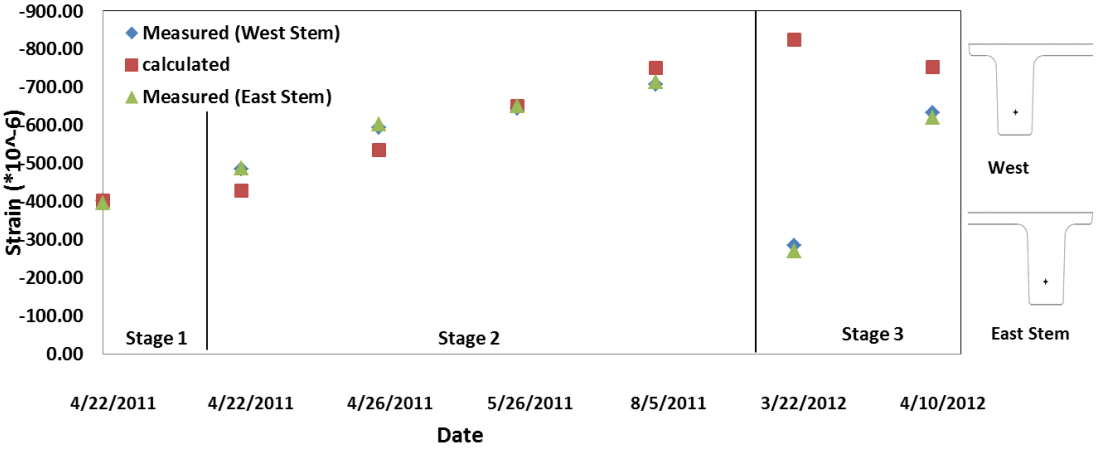

Figure 3-7: Calculated Vs. Measured Strains at Different Dates (Beam 2 mid-span)

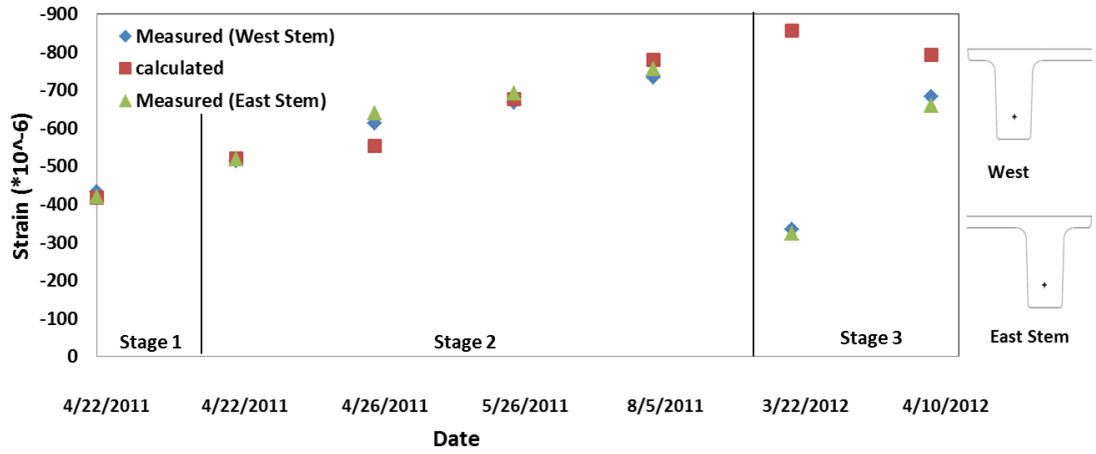

Figure 3-8: Calculated Vs. Measured Strains at Different Dates (Beam 2-2/3 span)

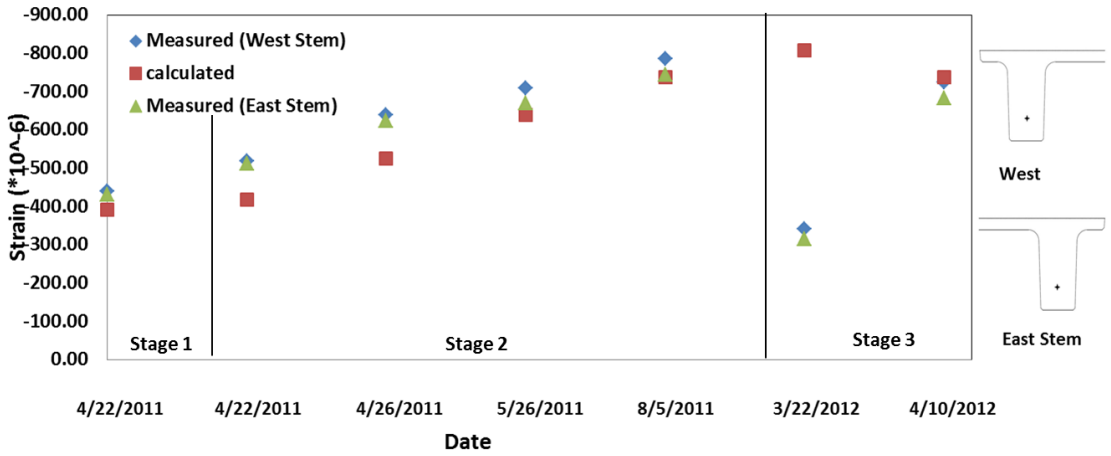

Figure 3-9: Calculated Vs. Measured Strains at Different Dates (Beam 3 mid-span)

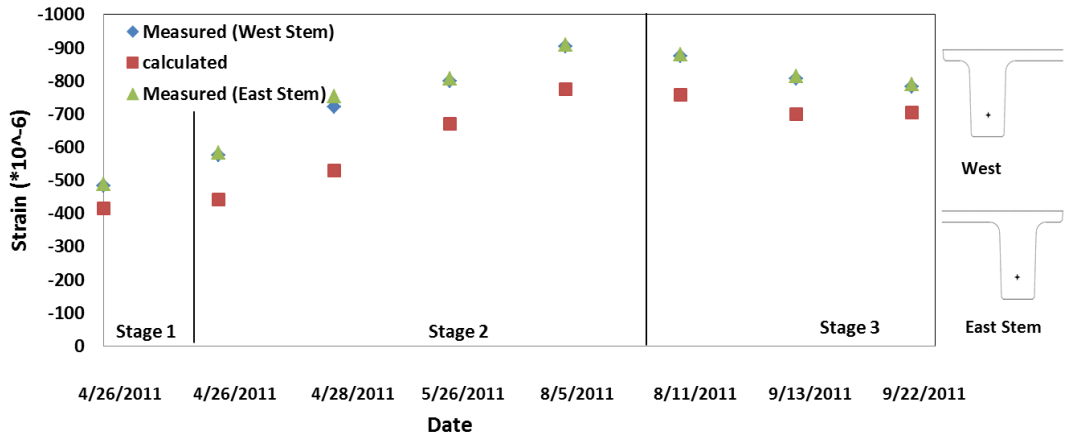

Figure 3-10: Calculated Vs. Measured Strains at Different Dates (Beam 4 mid-span)

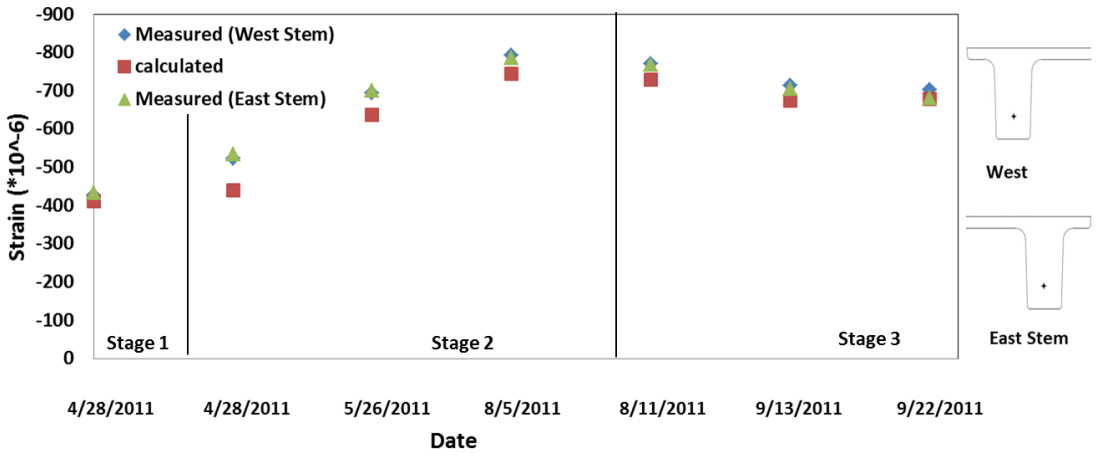

Figure 3-11: Calculated Vs. Measured Strains at Different Dates (Beam 5 mid-span)

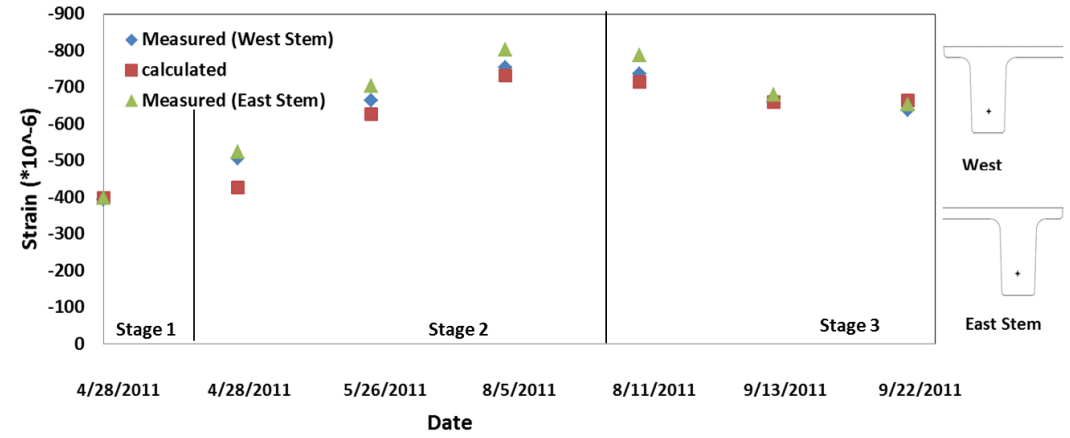

Figure 3-12: Calculated Vs. Measured Strains at Different Dates (Beam 6 mid-span)

It can be seen that calculated and measured strains follow the same trend except the readings taken for beams 1, 2, and 3 on 3/22/2012, when the beams were placed on the abutments, show a departure from the general trend observed at other stages. Since the readings taken before and after that date in these beams, as well as readings taken for other beams match the trend expected, the data taken for that date is not considered reliable. The small difference in measured and calculated strains at other dates may be due to shrinkage and error embedded in the equations used and assumptions.

Throughout the construction stages, no tensile strain readings were measured at the extreme fibers. This behavior is not surprising given the large prestressing

force in the beams and the small magnitude of applied external forces (self-weight). The maximum compressive strain captured during construction was 920 με and since strain gauges capture the deformation induced by creep and shrinkage as well as the strain generated by loading, this value doesn't represent the net compressive strain due to loading. The estimated maximum load related strain at the same stage was found equal to 411 με.

Stress limit given in AASHTO LRFD 2010, which suggests that during similar conditions the limit for design considerations is $0.45f'_c$ (874 με) was satisfied in comparison with the maximum strain captured at time of de-tensioning (first stage Table 3-1) (551 με).

3.5 Long- term Behavior

Understanding the long-term behavior of the integral abutment bridge in this research was limited to understanding effects of thermal changes. In this section the behavior of each component that was instrumented will be discussed in relation to the change in temperature observed throughout 18 months of monitoring that has taken place since the bridge construction was completed in 05/22/2012. Due to a battery malfunction in the data loggers, data collection was interrupted on11/26/2013 and restarted on 06/06/2014.

3.5.1 Temperature Fluctuation

The ambient temperature, which was recorded using the thermistors associated with the shaded tiltmeters, has ranged from 11^{o}F (-11.7^{o}C) to 83^{o}F (28.3^{o}C) according to 18 month monitoring. With a reference temperature at the end of construction of 68^{o}F (20^{o}C), the maximum positive change in temperature was 11.5 ^{o}F (6.4 ^{o}C) and 14.4^{o}F (8 ^{o}C) during year one and year two summer, respectively. The maximum

negative change in temperature was -57.3^{o}F (-31.8^{o}F) and it occurred in January 2012. The maximum temperature recorded by a weather station at Westover Air Reserve Base / Metropolitan Airport located approximately 26 miles (42 Km) from the bridge at the same date of the reference temperature was 79^{o}F (26.7^{o}C). At the dates when the maximum increase in temperature occurred, the highest temperatures recorded by this weather station were 91^{o}F (32.7^{o}C) and 92^{o}F (33.3^{o}C) in year one and year two summer, respectively. The temperature recorded by the weather station at the date when the maximum decrease in temperature occurred was 18^{o}F (-7.8 ^{o}C). As a results, the temperature measured by tiltmeter thermistors were always less by about 10^{o}F (5.5 ^{o}C) than those recorded by the weather station. However, the changes in temperature with regards to the reference temperature are about the same in both. Figure 3-13 shows the ambient temperature captured throughout the 18 months. Each gauge used in the Brimfield Bridge has an internal thermistor. This allowed having temperature readings at the location of each instrument in the bridge components that were instrumented. Reference temperatures for each gauge were slightly different. The fluctuation of the readings recorded by these thermistors has shown that the distribution of temperature not only varies with the depth of the superstructure, but also with the other 2 dimensions of it. Moreover, the ambient temperature is always less than that recorded at the deck in warm seasons and more in cold seasons. Figures 3-14 and 3-15 show temperature gradient throughout the superstructure for extreme readings taken in summer during day time and extreme reading in winter taken before the data logger battery malefaction in year one during day time, respectively.

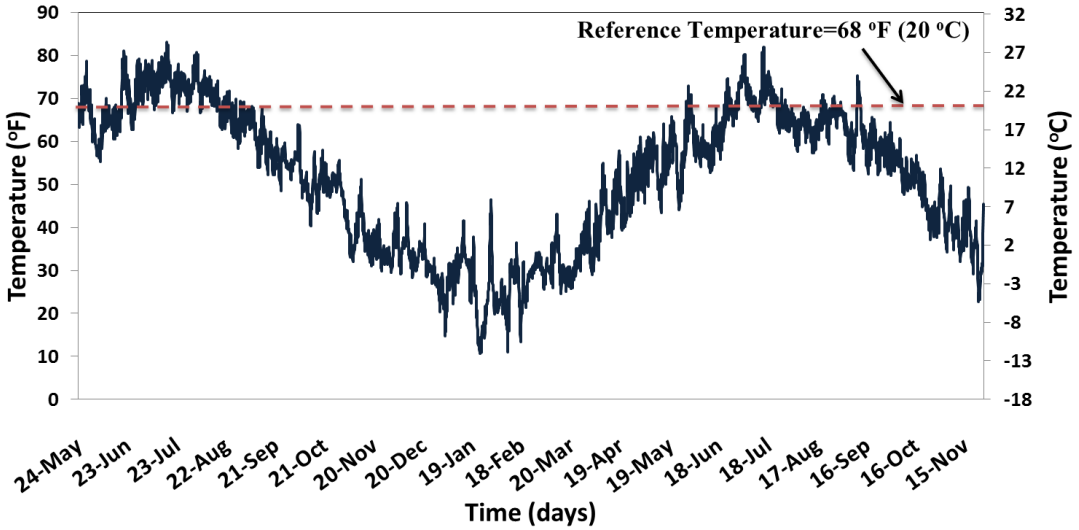

Figure 3-13: Ambient Temperature

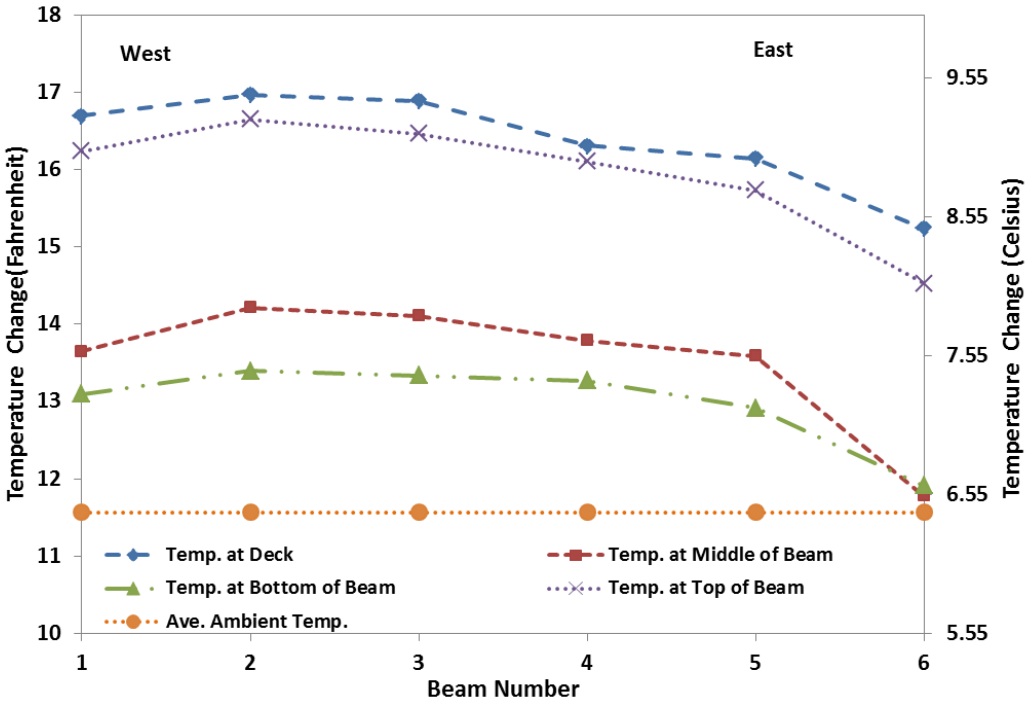

Figure 3-14: Temperature Gradient and Ambient Temperature Taken at a Certain Date in the Summer

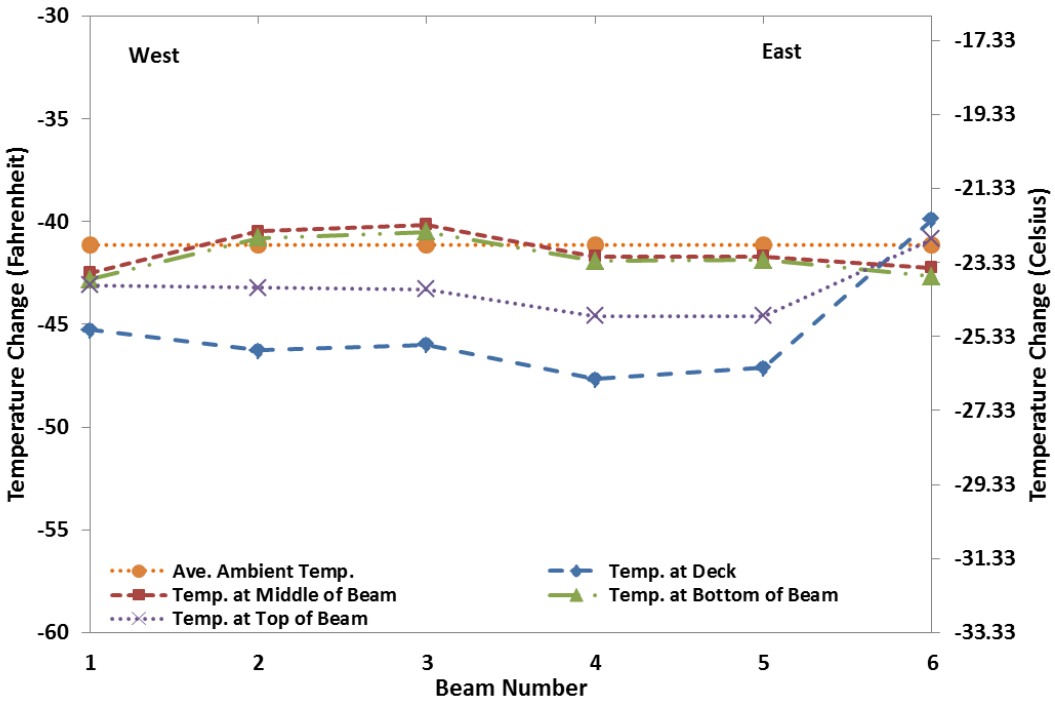

Figure 3-15: Temperature Gradient and Ambient Temperature Taken at a Certain Date in the Winter

3.5.2 Abutment Displacements

Crackmeter readings showed that abutment displacements are as expected according to the temperature changes experienced by the bridge. For instance, both abutments displaced inwardly during winter 2012-2013 as the bridge superstructure contracted and displaced outwardly during summer 2012. Plotting crackmeter data showed that the displacement at the obtuse corner of the north abutment was more than that occurred at the acute corner during winter. At the obtuse corner of the south abutment, on the other hand, displacement was more than at the acute corner. The transverse displacement of the north abutment was larger than that at the south abutment. The bridge, therefore, has not only contracted longitudinally during the winter season, but it has also experienced minimal in-plane rotation. Differences in soil pressures acting on the 30 degree skewed abutments may be a contributing factor for the observed displaced configuration. Both longitudinal and transverse

displacements are small during winter with a maximum displacement at the top of the abutment of 0.176 in (4.5 mm). Figure 3-16 shows a plan view of the exaggerated displaced shape of the bridge during the winter.

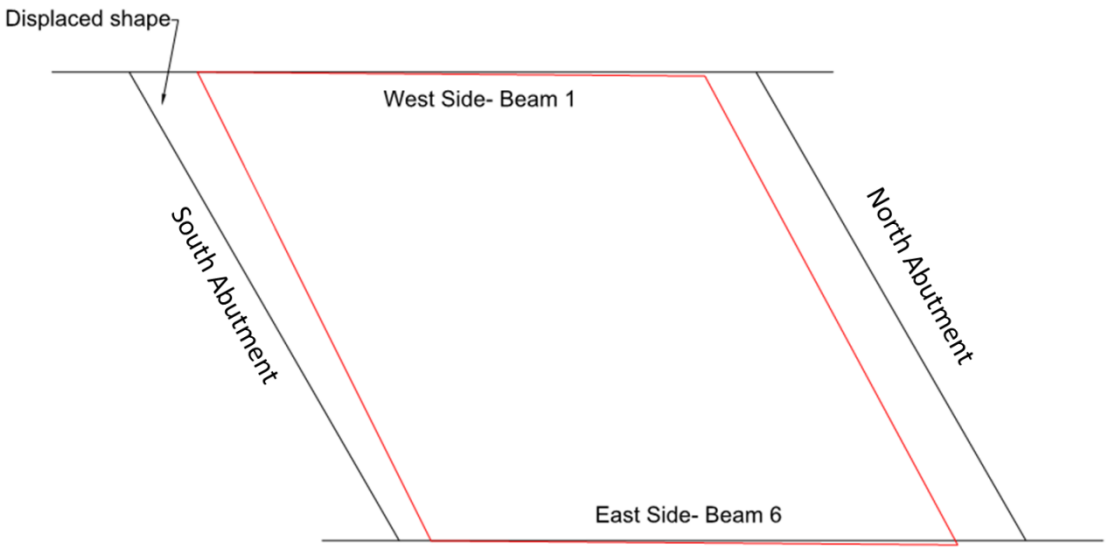

Figure 3-16: Displaced Shape During the Winter

The exaggerated displaced shape of the bridge experienced during summer 2012 is shown in Figure 3-17.

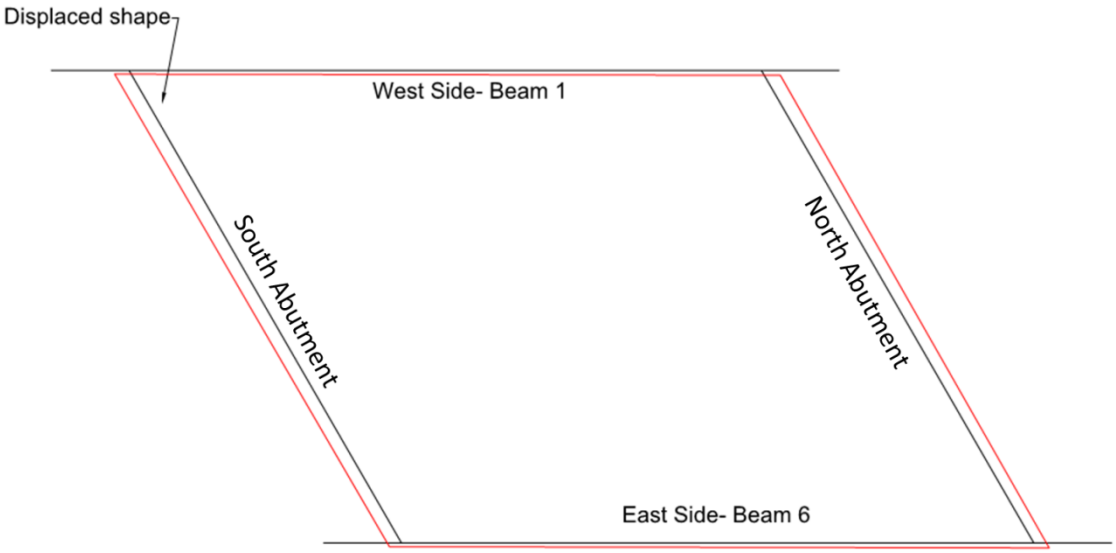

Figure 3-17: Displaced Shape During Summer

From Figure 3-17, it can be seen that the west side of both abutments have moved outward (toward backfill) more than the east side, which indicates that beam 1 extended more than beam 6 during summer 2012, yet the difference is negligible. Displacement values, however, were smaller in magnitude during summer than those that occurred during winter as the change in temperature from the reference temperature during winter was higher. Figures 3-18 to 3-23 show plots of displacement data taken at the location of the crackmeters in order to provide a general understanding of the behavior of the abutments and the bridge.

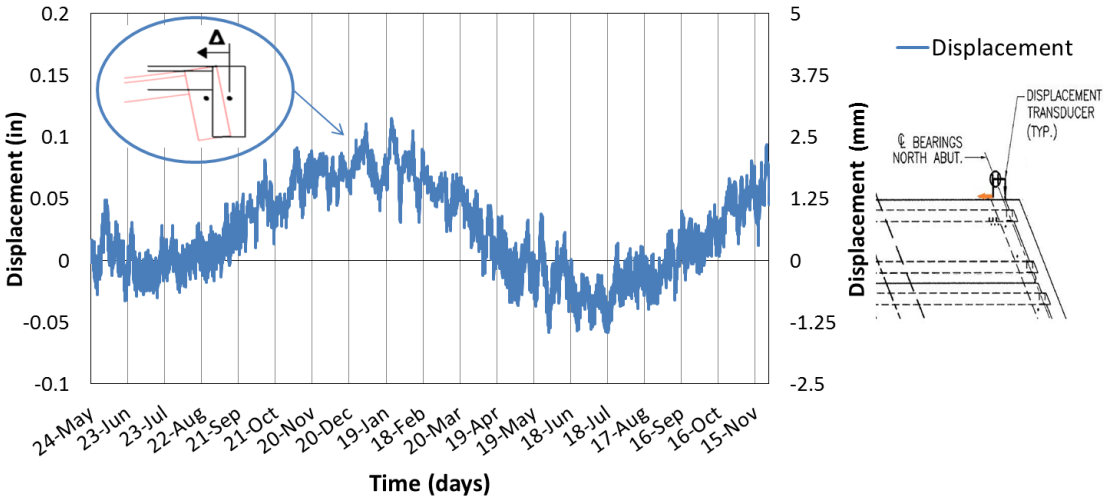

Figure 3-18: Longitudinal Displacement at the West Side of the North Abutment

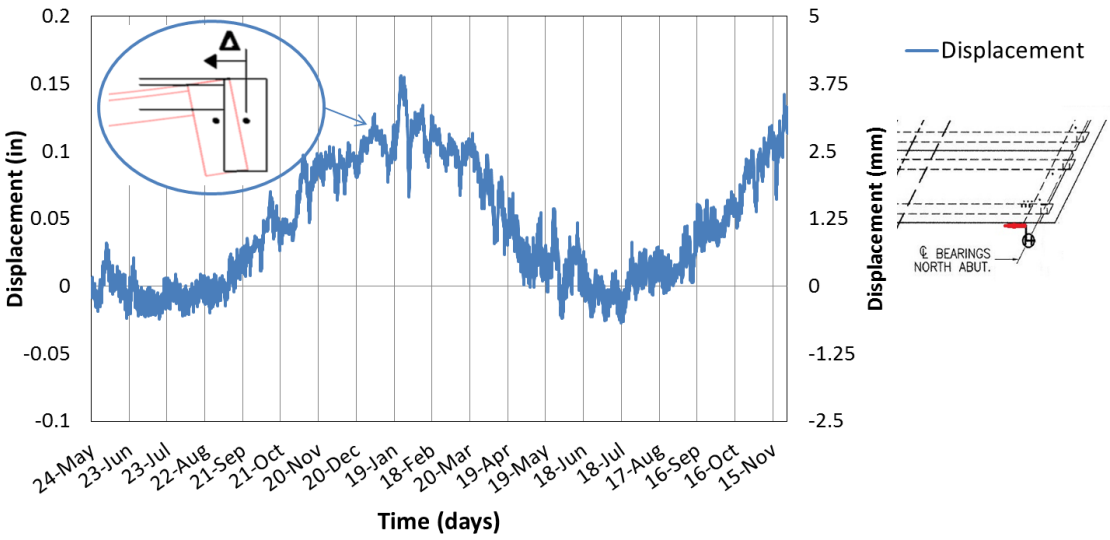

Figure 3-19: Longitudinal Displacement at the East Side of the North Abutment

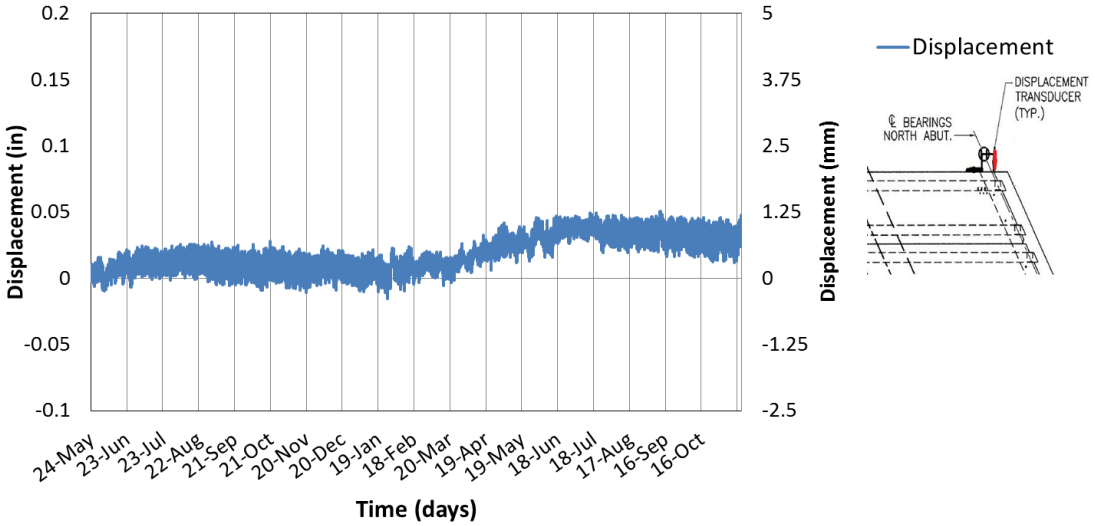

Figure 3-20: Transverse Displacement of the North Abutment

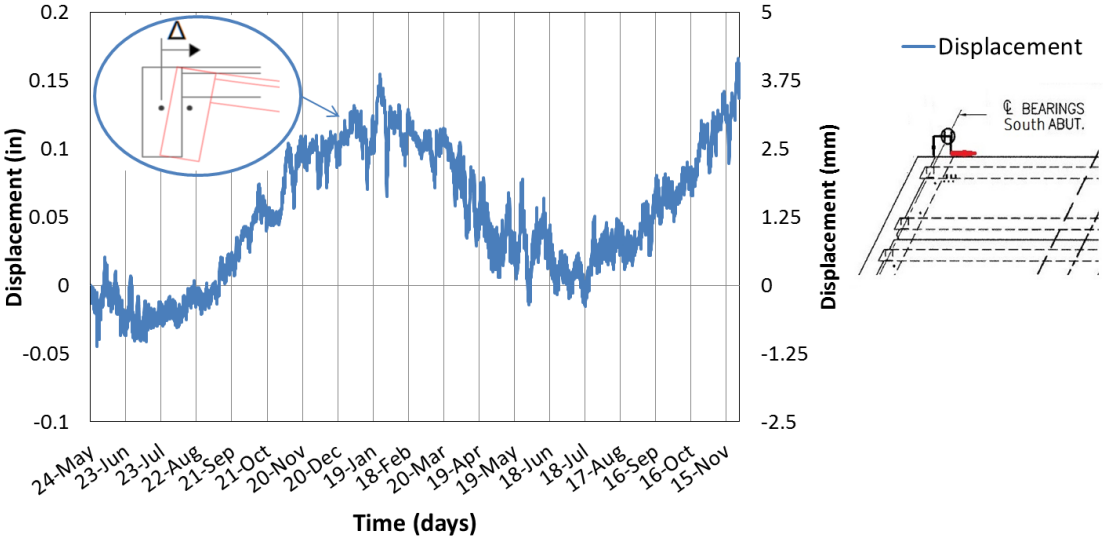

Figure 3-21: Longitudinal Displacement at the West Side of the South Abutment

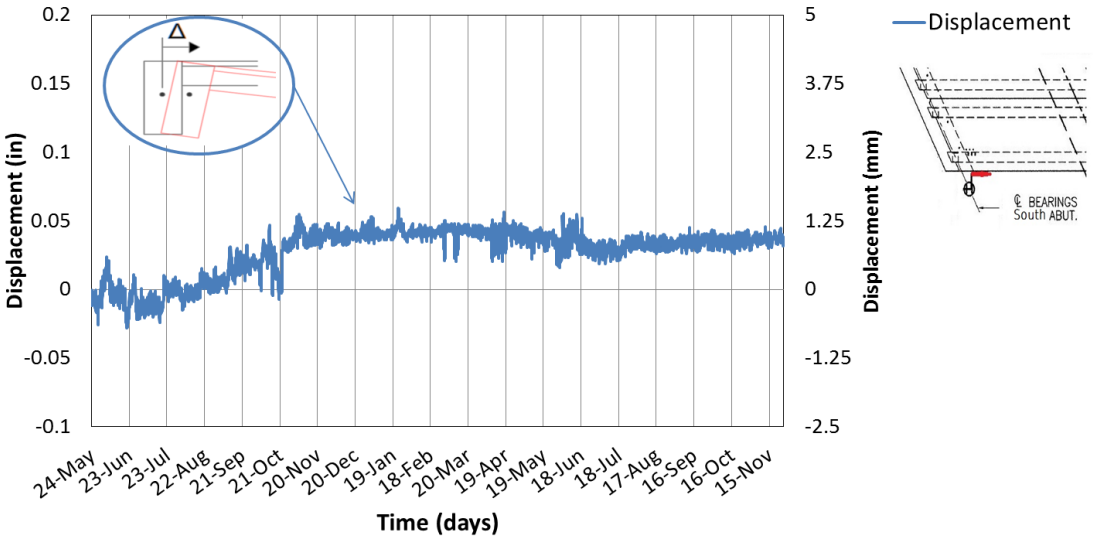

Figure 3-22: Longitudinal Displacement at the East Side of the South Abutment

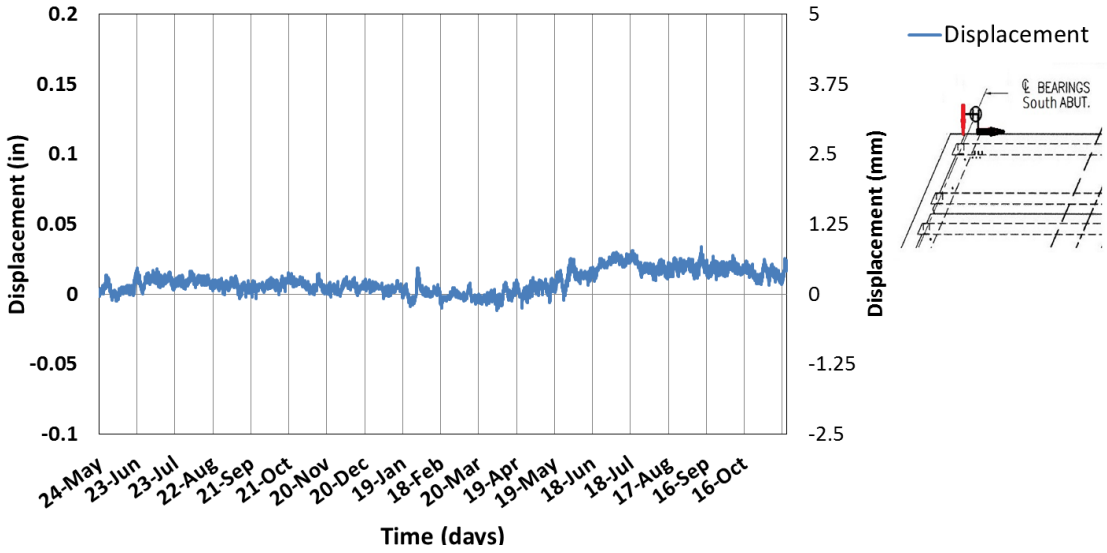

Figure 3-23: Transverse Displacement of the South Abutment

In order to be able to compare between the displacements measured at each abutment side, displacement readings along with rotation readings were utilized to estimate the displacement at the top and the bottom of each abutment. Since the bridge is on a skew, it is expected that the displacements occurring at the acute corner of the south abutment would be almost the same as that occurs at the north abutment acute corner. Likely, the displacements occurs at the obtuse corners of the bridge matches each other. By plotting the temperature versus displacement at the top and

bottom of the abutments for both years, it was found that the south abutment has moved toward the superstructure during the second year (Figure 3-24). The crackmeter installed at the acute corner of the south abutment (south east side, Figures 3-24 and 3-25), however, showed a shift in displacement readings after winter 2013. Similar shifting but smaller occurred at the north west corner in year one. The displacement at the north abutment has generally increased in the warmest days of year two. During winter of year two, the upstream side of the north abutment (obtuse corner) had more displacement than what was recorded during year one, yet the downstream side (acute corner) has displaced less than what occurred in year two winter. Figures 3-24 and 3-25 show the yearly change in displacement at the top and bottom of each abutment sides, respectively.

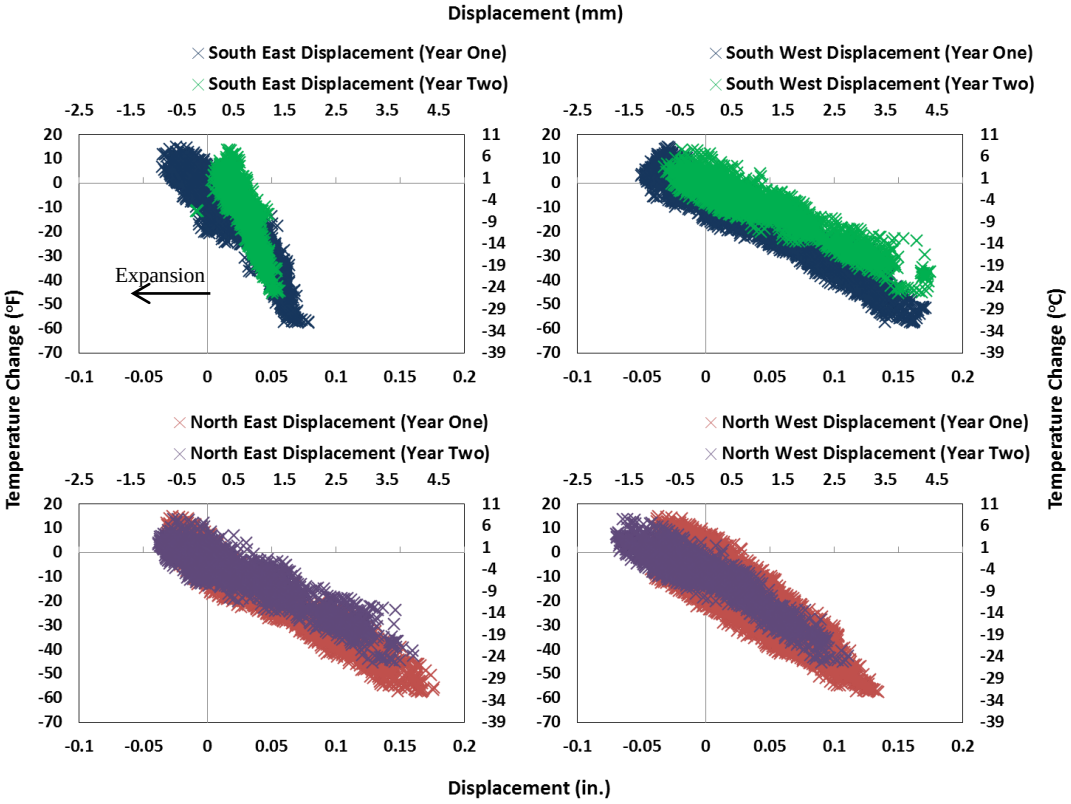

Figure 3-24: Yearly Change in Abutment Top Displacement

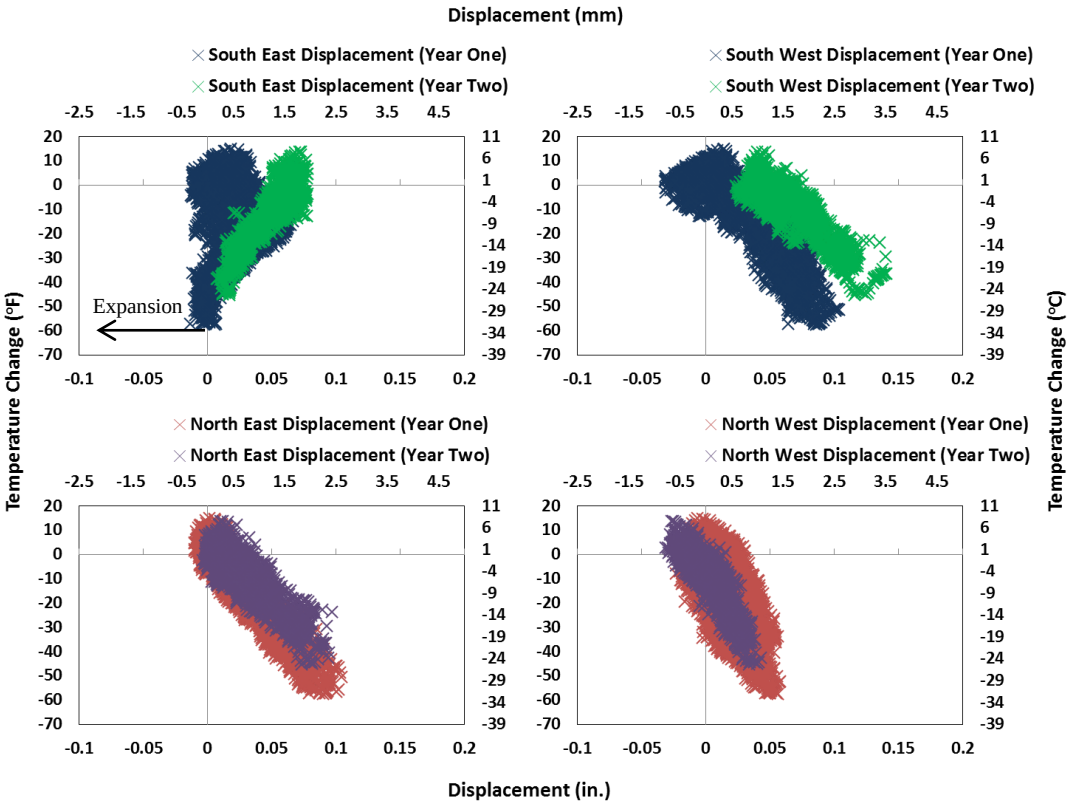

Figure 3-25: Yearly Change in Abutment Bottom Displacement

3.4.3 Abutment Rotations

Tiltmeter readings showed that the rotation of both abutments followed the change in temperature in terms of direction. As the temperature increases, the abutments experienced negative rotation, which indicates that the abutments rotate toward the backfill; positive rotation occurs during winter as the abutments rotate inward because of temperature decrease. The maximum rotation occurred in winter 2012 at the north abutment with a value equal to 0.076 degrees. Figures 3-26 and 3-27 show the field data with a sketch illustrating the rotation.

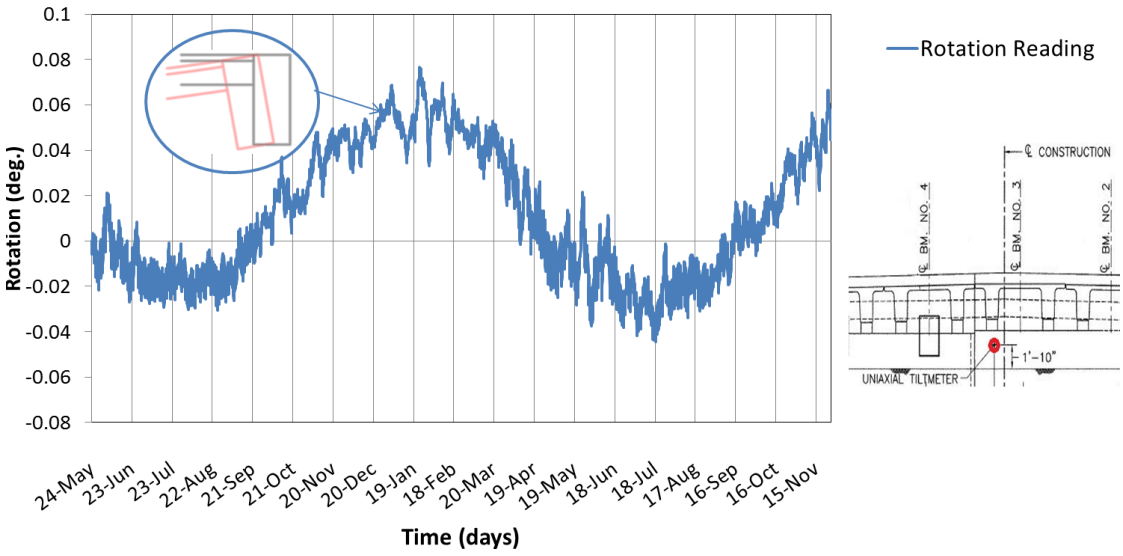

Figure 3-26: North Abutment Rotation

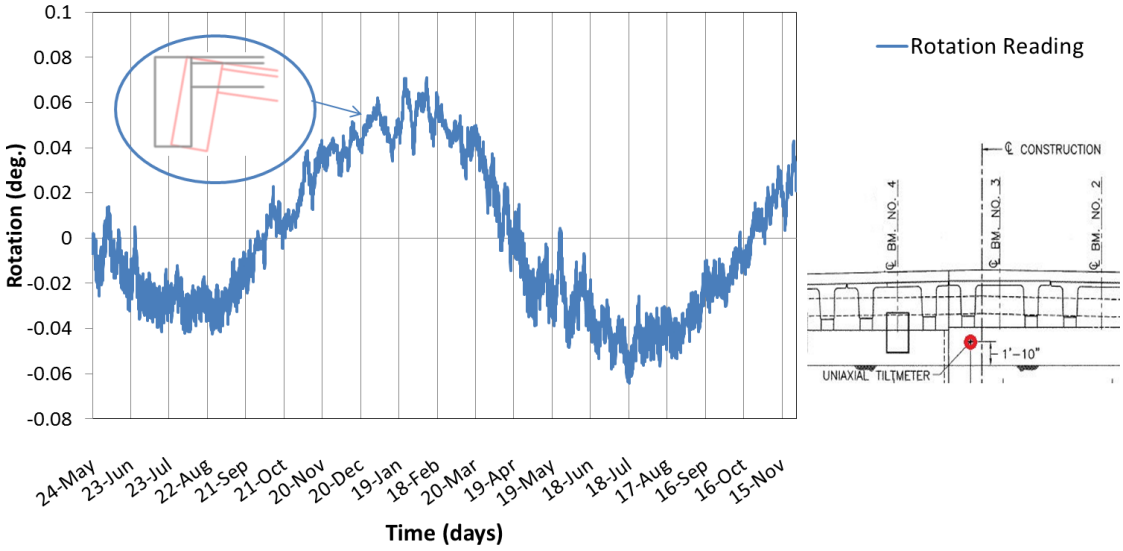

Figure 3-27: South Abutment Rotation

By plotting the temperature versus rotation of the two years (Figure 3-28), it was found that both abutments had more rotation in summer of year two than in year one. During cold days of the second year, on the other hand, the south abutment rotated less whereas north abutment rotated more.

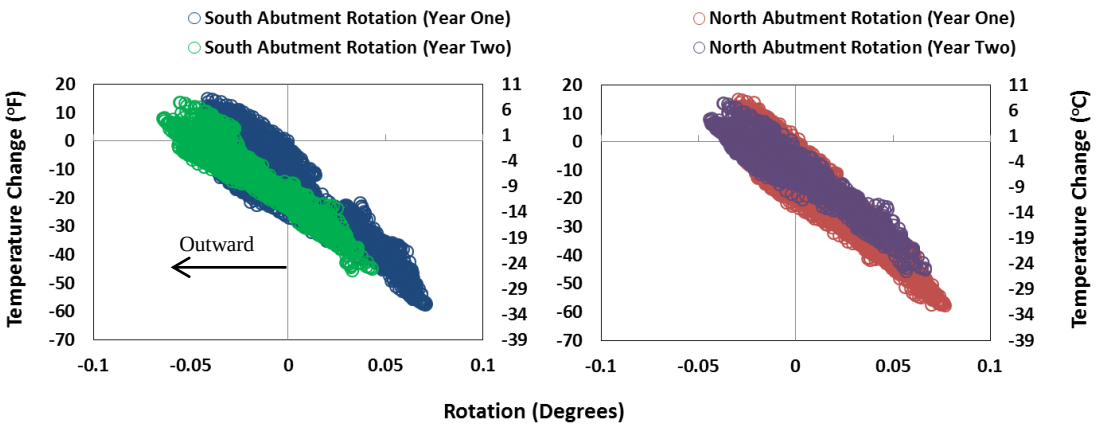

Figure 3-28: Yearly Change in Abutments Rotation

3.5.4 Strain Measured in the Concrete Deck

The longitudinal strains measured in the concrete deck throughout the 18 months were compressive. This could be as a result of the fact that the deck was cast in place and the creep and shrinkage effects from the deck are controlling behavior. During winter, the longitudinal gauges (1.5-2 in. from deck bottom) captured increasing in the compressive strain, which indicates that the bridge superstructure is contracting and thus concaving upward. Moreover, compressive strain was captured in the concrete deck during summer with magnitudes less than those that appeared during winter, indicating that the superstructure concaved downward in such a small amount that did not change the strain at the deck level into tension. Figure 3-29 shows the expected deflected shape of the bridge.

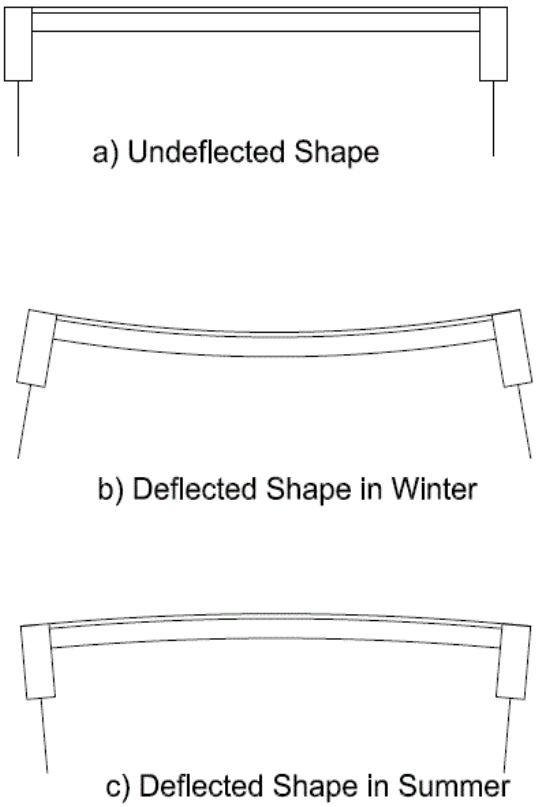

Figure 3-29: Deflected Shape during Different Seasons

Figures 3-30 to 3-35 show the plotted field data for the strain gauges embedded in the concrete deck at mid-span of each beam. As it can be seen, there is missing data between December, 2012 and February, 2013 in some of these plots as one of the data loggers malfunctioned due to a battery loss. The blue series in these plots represents strain readings at the west stem while the red series represents strain readings at the east stem.

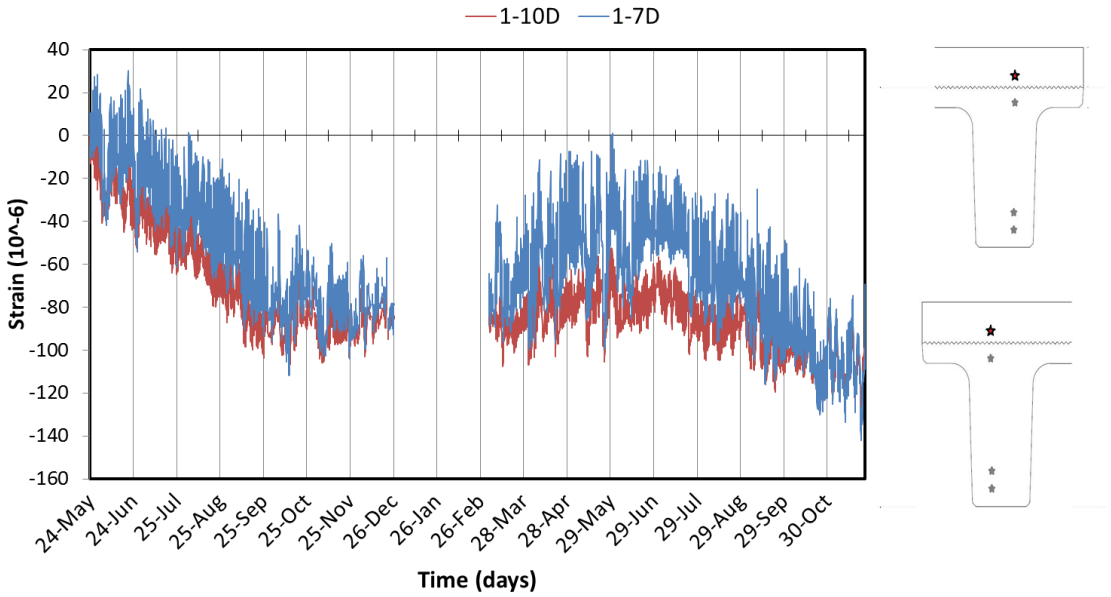

Figure 3-30: Strain Reading of Deck Gauges above Beam 1 (Mid-Span)

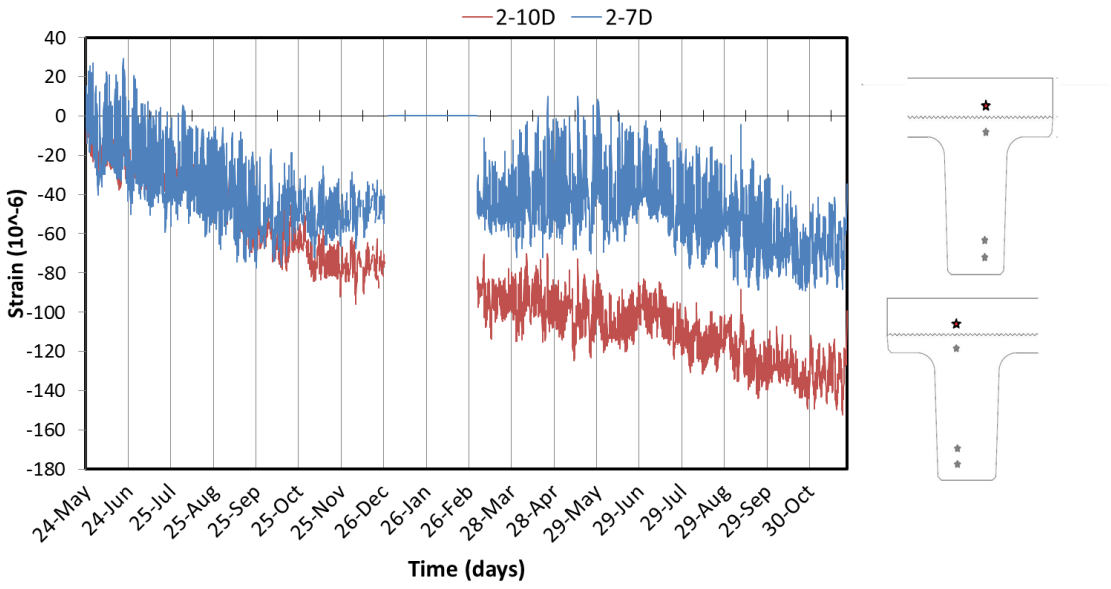

Figure 3-31: Strain Reading of Deck Gauges above Beam 2 (Mid-Span)

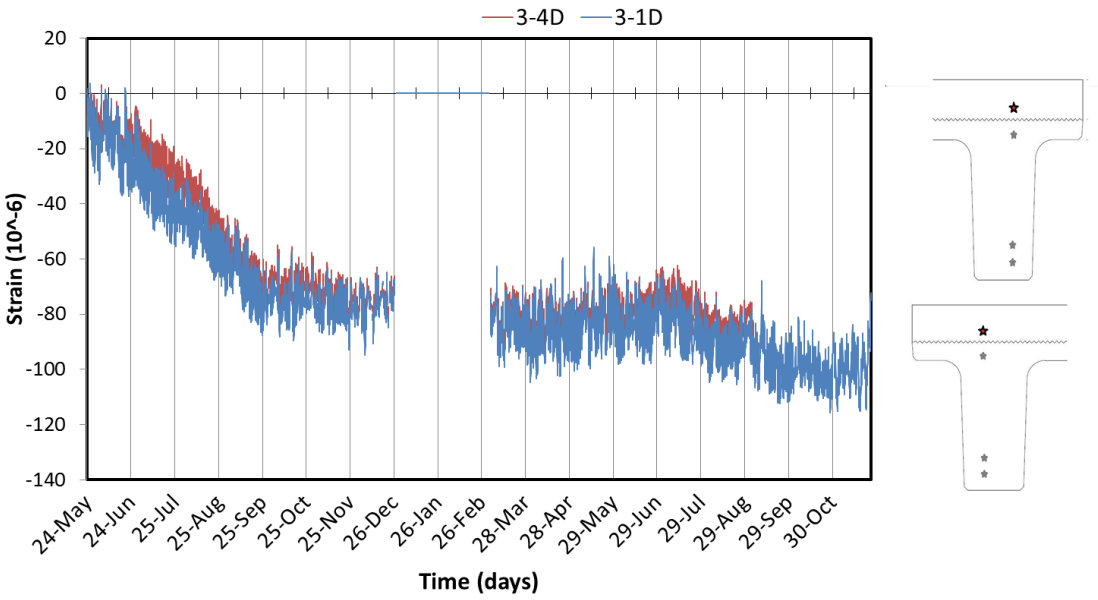

Figure 3-32: Strain Reading of the Deck's Gauges above Beam 3 (Mid-Span)

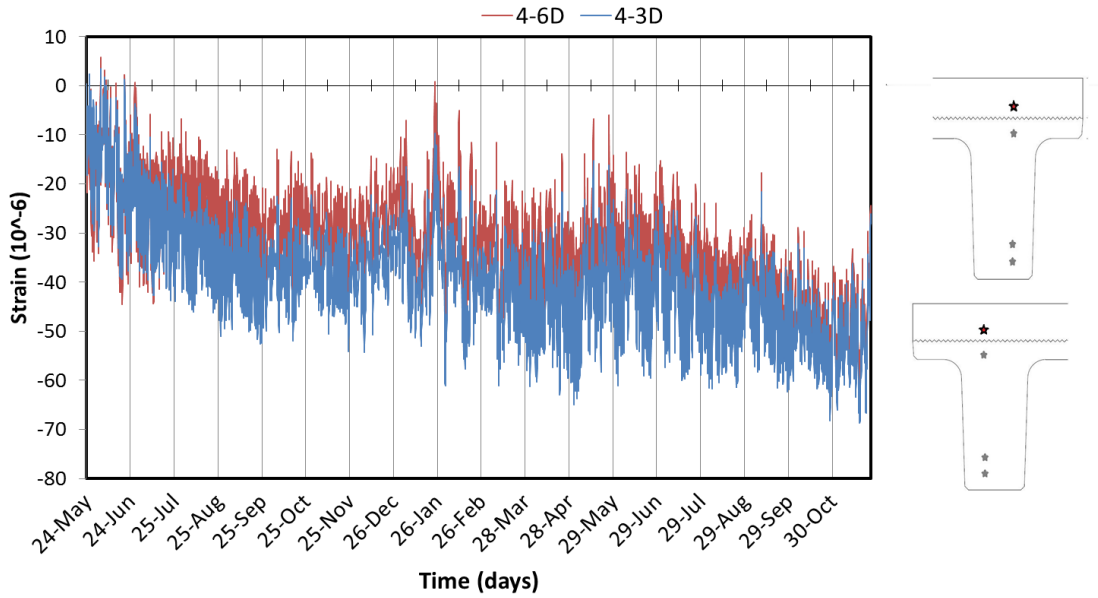

Figure 3-33: Strain Reading of the Deck's Gauges above Beam 4 (Mid-Span)

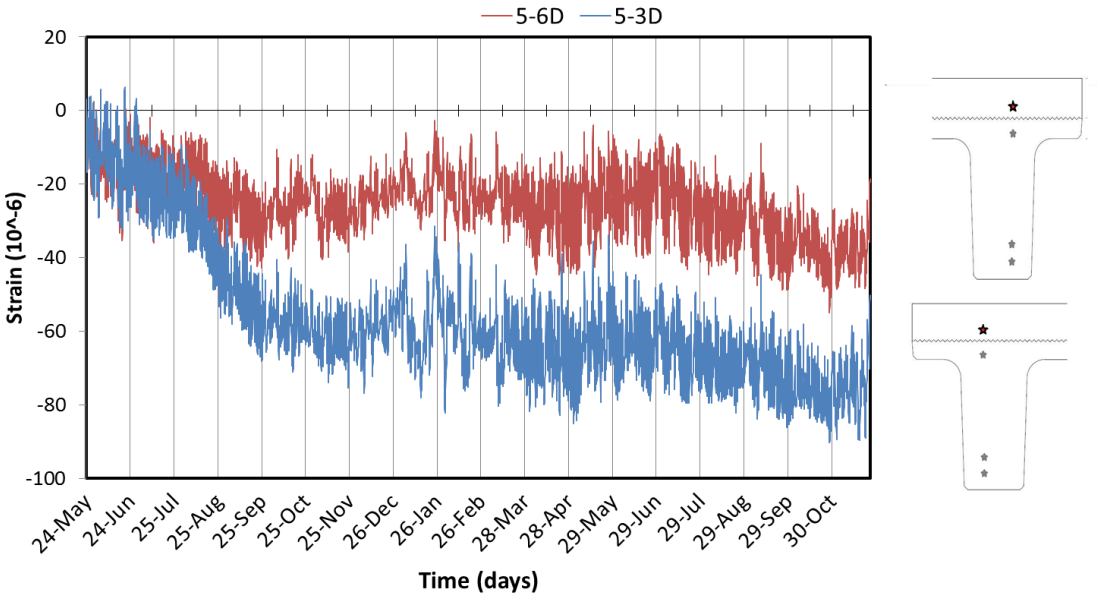

Figure 3-34: Strain Reading of the Deck's Gauges above Beam 5 (Mid-Span)

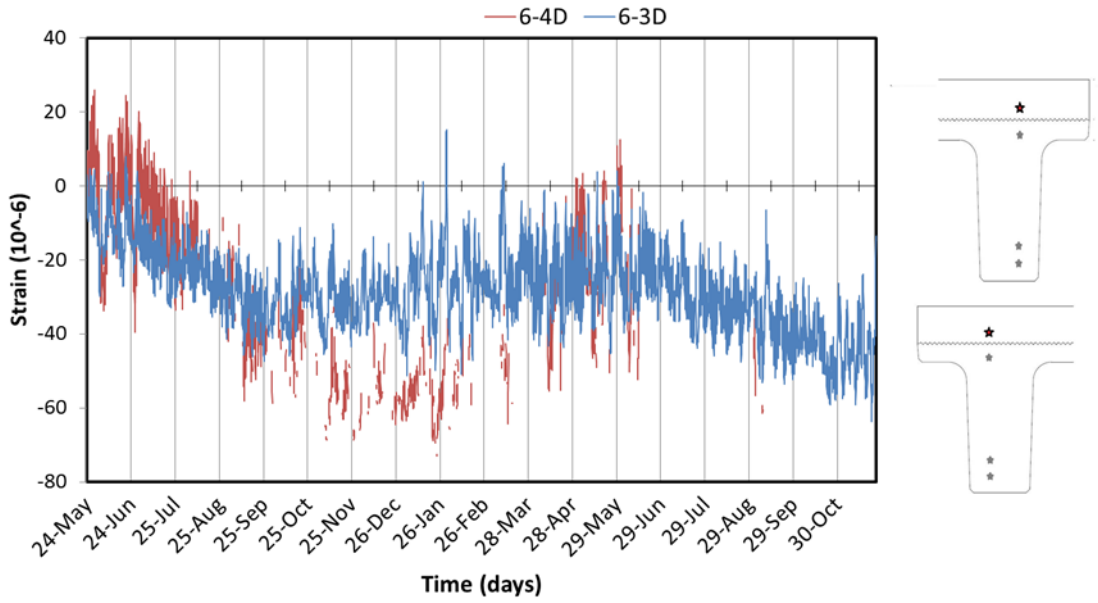

Figure 3-35: Strain Reading of the Deck's Gauges above Beam 6 (Mid-Span)

The plots above clearly show that there are some differences in the magnitude of the strain between the two gauges in the deck overlying each beam, yet beams 2 and 5, and 6 had larger differences. These differences could be as a result of the temperature gradient along the transverse direction of the superstructure due to radiation.

3.5.5 Strain Measured in Beams

Strain readings of the gauges installed at the top of beams 1, 2, and 3 showed the same trends as those recorded in the concrete deck, yet differences in strain values were noticed as the concrete deck is under the effect of creep and shrinkage (Figures 3-36 to 3-38). Strain readings of the gauges at the top of beams 4, 5, and 6 showed a similar behavior to that captured in the concrete deck with almost the same values as shown in Figures 3-39 to 3-41. This behavior is due the fact that the concrete deck was cast on beams 4, 5, and 6 several months before the deck was cast on beams 1, 2, and 3 and had already undergone shrinkage and creep effect the same time beams 4, 5, and 6 did. The consistency of readings with depth confirms the composite action assumed in the design.

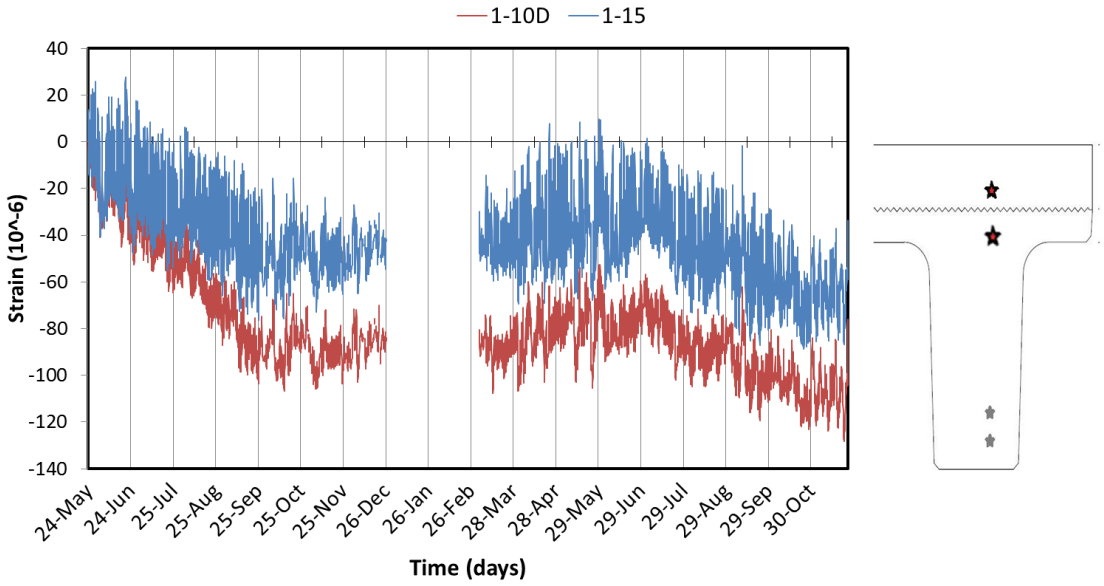

Figure 3-36: Comparison between Strain Readings at the Top Gauge of the West Stem in Beam 1 and Strain Readings in Deck above It (Mid-Span)

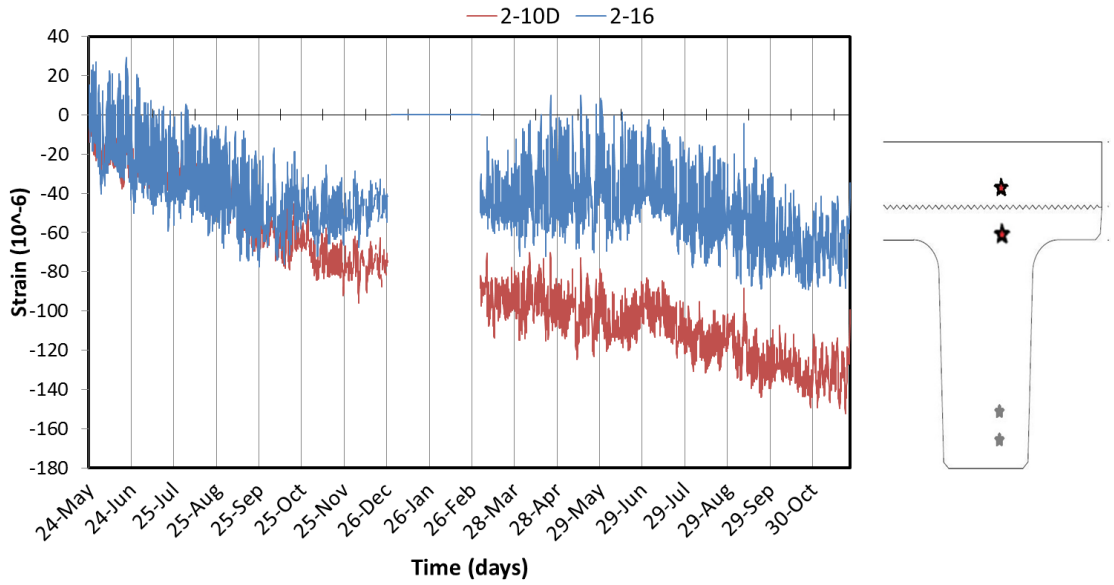

Figure 3-37: Comparison between Strain Readings at the Top Gauge of the West Stem in Beam 2 and Strain Readings in Deck above It (Mid-Span)

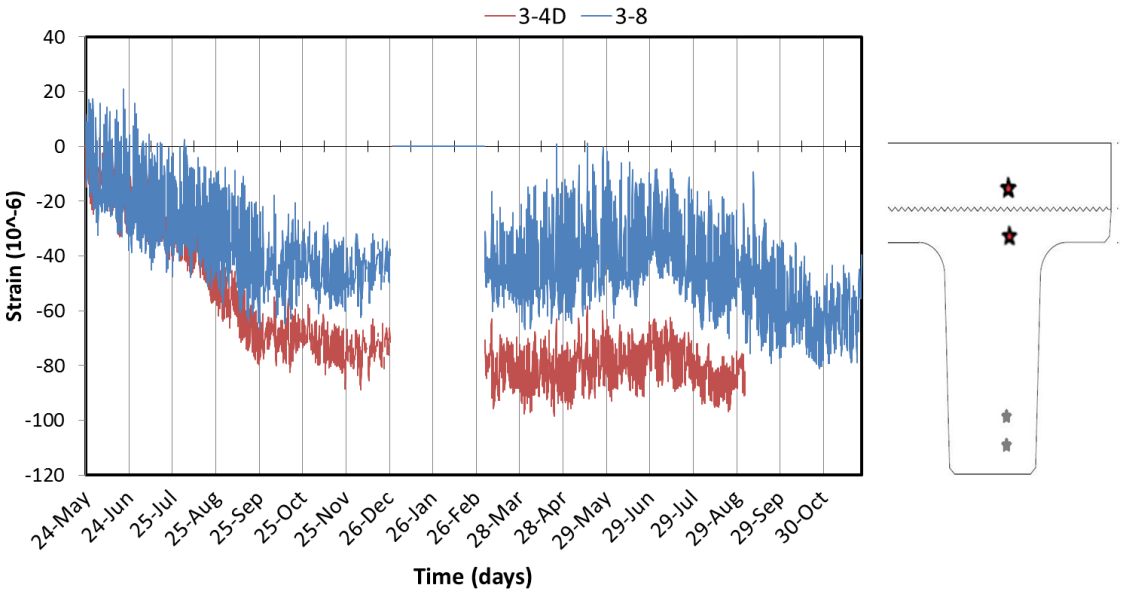

Figure 3-38: Comparison between Strain Readings at the Top Gauge of the West Stem in Beam 3 and Strain Readings in Deck above It (Mid-Span)

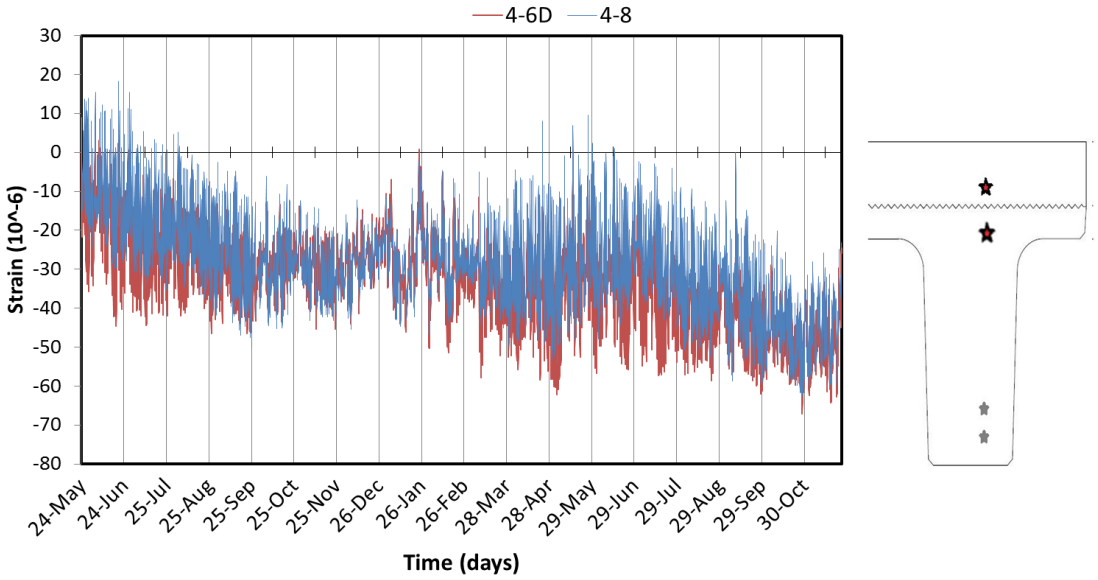

Figure 3-39: Comparison between Strain Readings at the Top Gauge of the West Stem in Beam 4 and Strain Readings in Deck above It (Mid-Span)

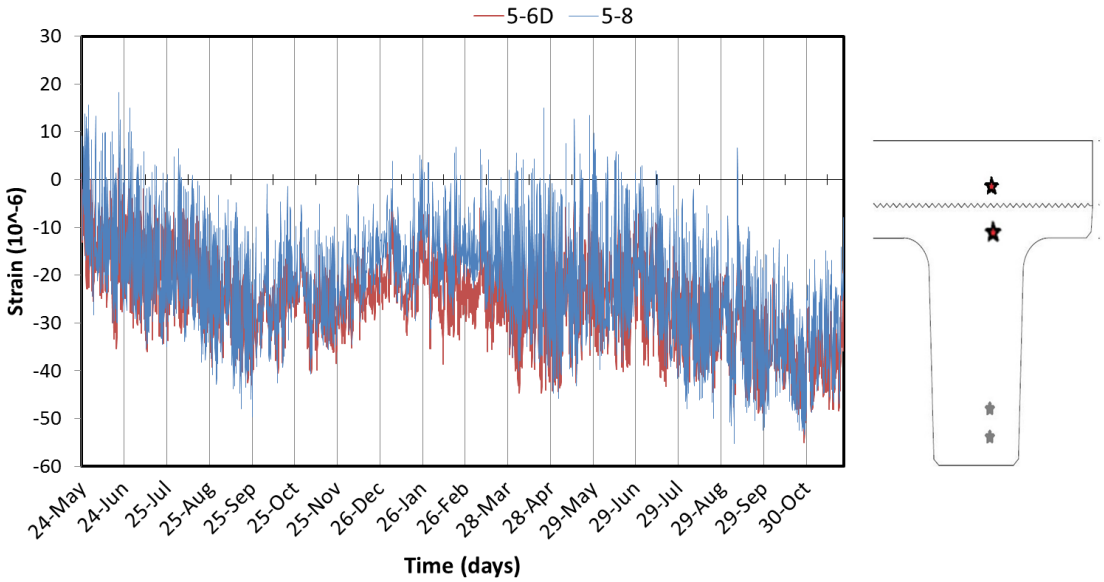

Figure 3-40: Comparison between Strain Readings at the Top Gauge of the West Stem in Beam 5 and Strain Readings in Deck above It (Mid-Span)

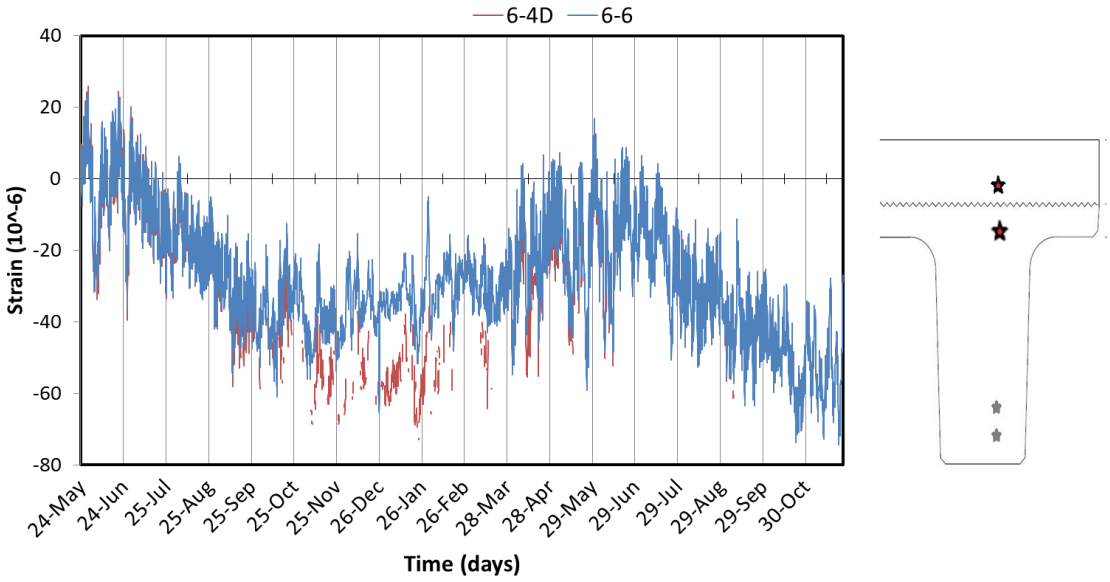

Figure 3-41: Comparison between Strain Readings at the Top Gauge of the West Stem in Beam 6 and Strain Readings in Deck above It (Mid-Span)

Figures 3-42 to 3-47 show strain readings at the top of each beam stem at mid-span. The blue and red series in these plots represent the strain readings at the west and east stems, respectively.

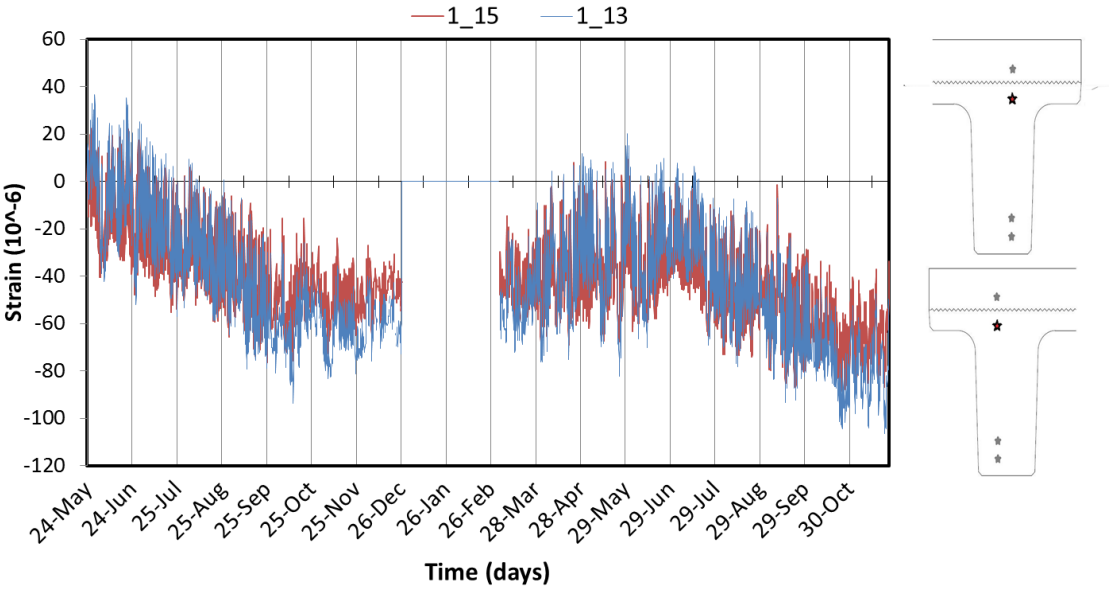

Figure 3-42: Strains at the Top Gauges of Beam 1 (Mid-Span)

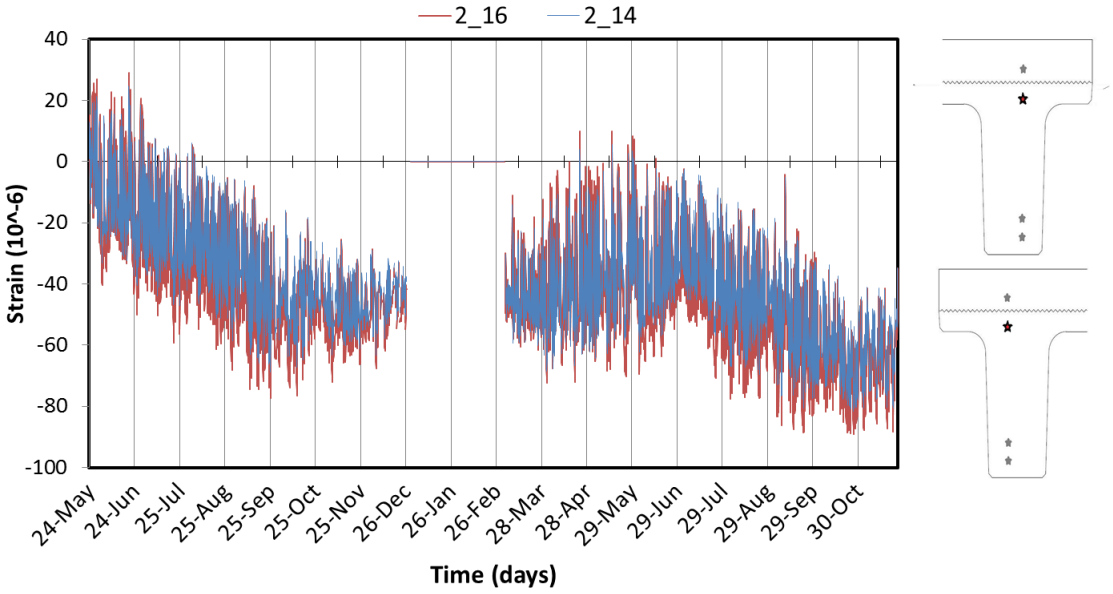

Figure 3-43: Strain at the Top Gauges of Beam 2 (Mid-Span)

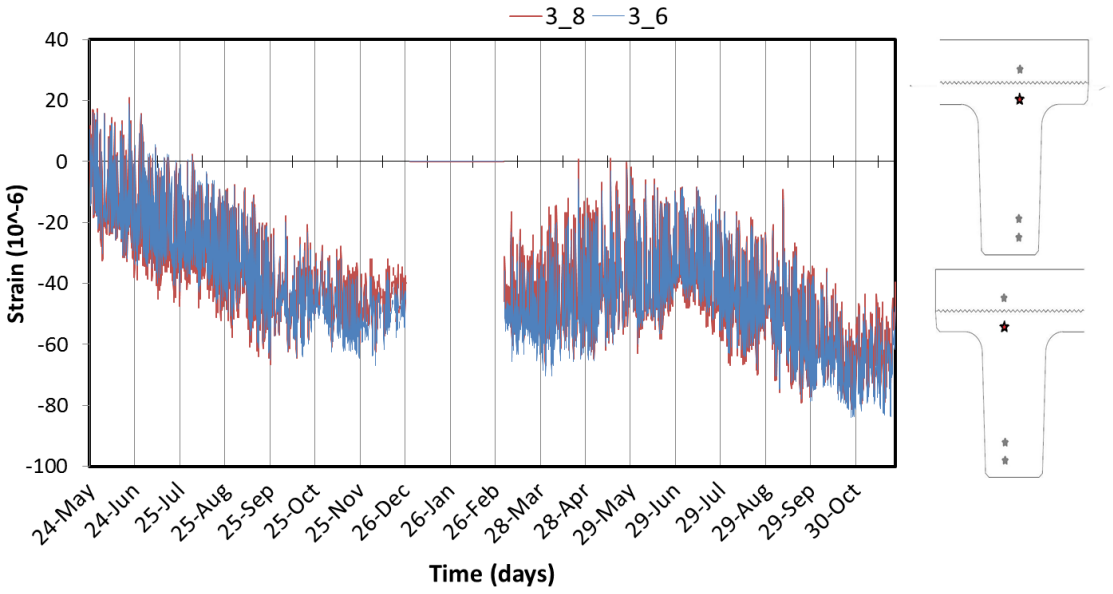

Figure 3-44: Strains at the Top Gauges of Beam 3 (Mid-Span)

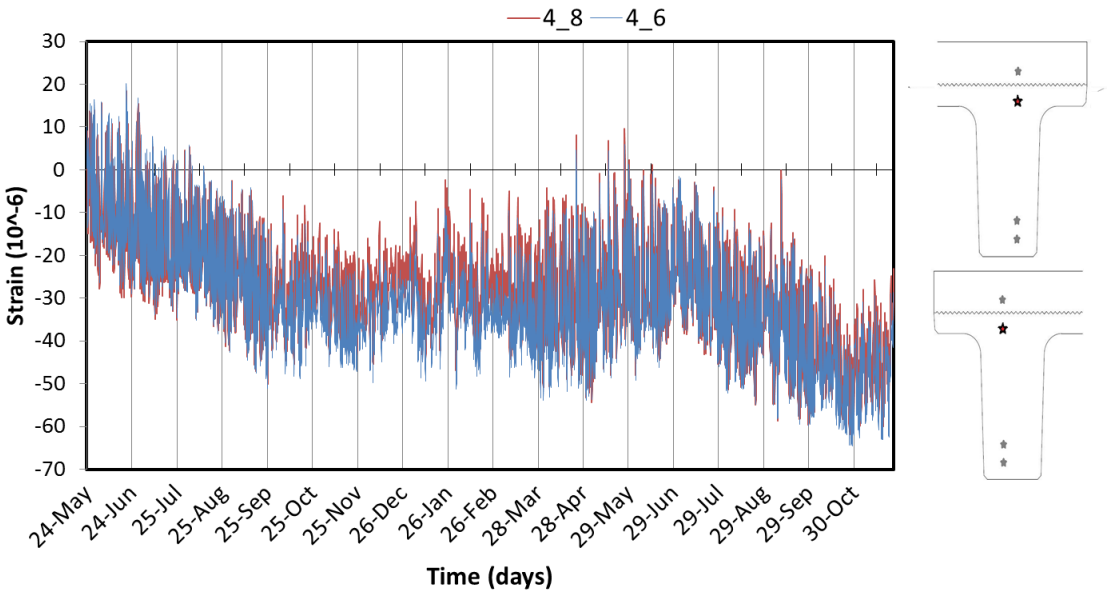

Figure 3-45: Strains at the Top Gauges of Beam 4 (Mid-Span)

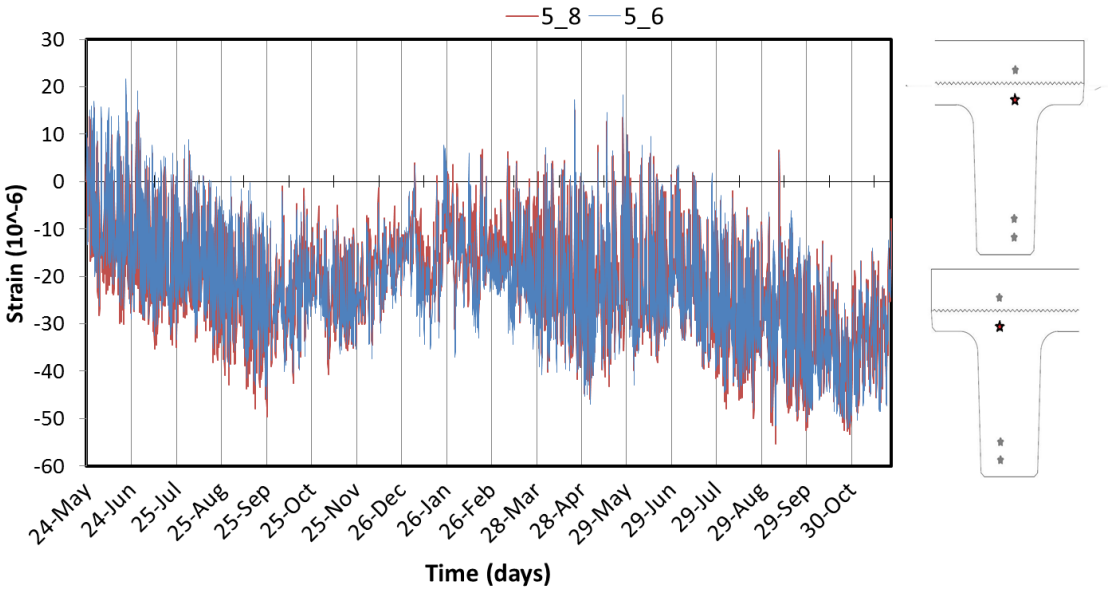

Figure 3-46: Strains at the Top Gauges of Beam 5 (Mid-Span)

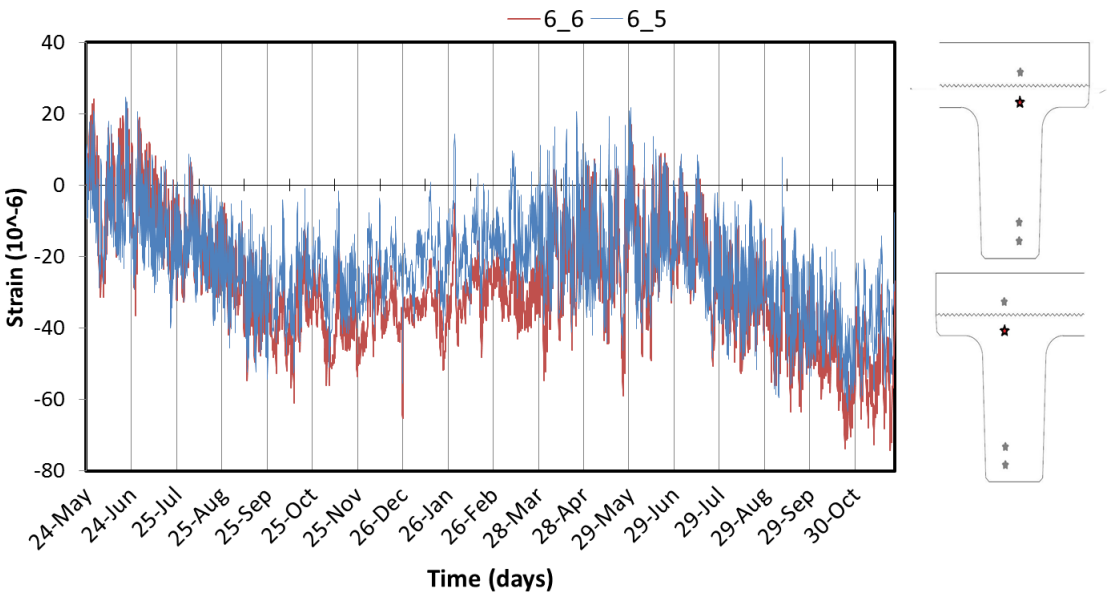

Figure 3-47: Strains at the Top Gauges of Beam 6 (Mid-Span)

Strain readings that were recorded throughout the 18 months by gauges near the bottom of beams showed similar trends to each other. By plotting the field data for those gauges, it was confirmed that the superstructure is deflecting as expected due to different seasons (Figure 3-29). The west stem in beam 6 showed the same trend as the others, yet with larger tensile strain. This behavior may be explained by the sidewalk acting compositely with the deck and beam at that location. Figures 3-48 through 3-53 show the strains at the bottom of both stems in all beams. The blue series in these plots represents the strain readings at the west stem whereas the red series represents readings at the east stem.

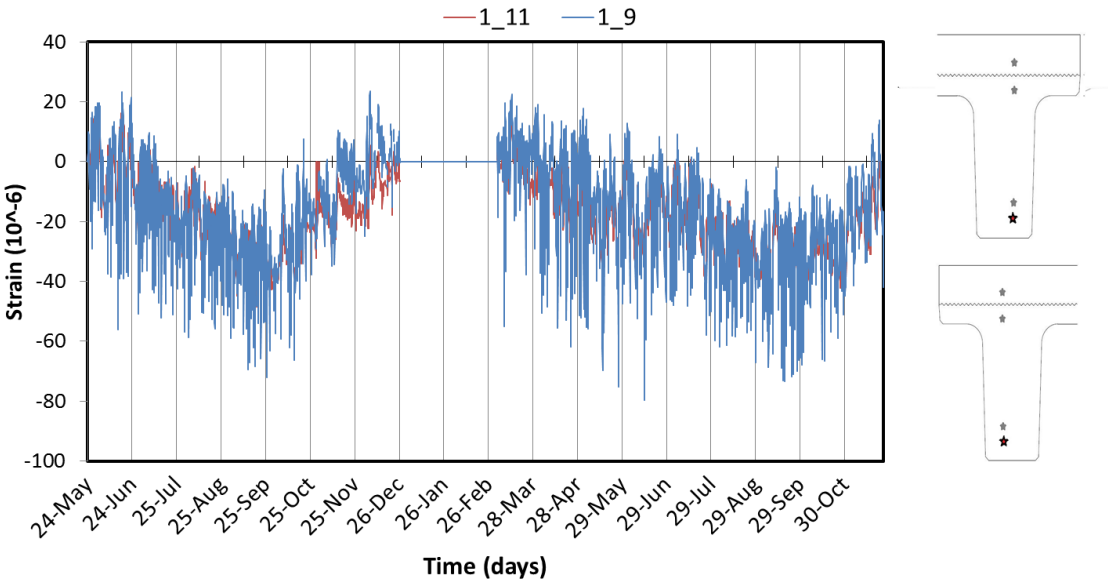

Figure 3-48: Strain at the Bottom Gauges of Beam 1 (Mid-Span)

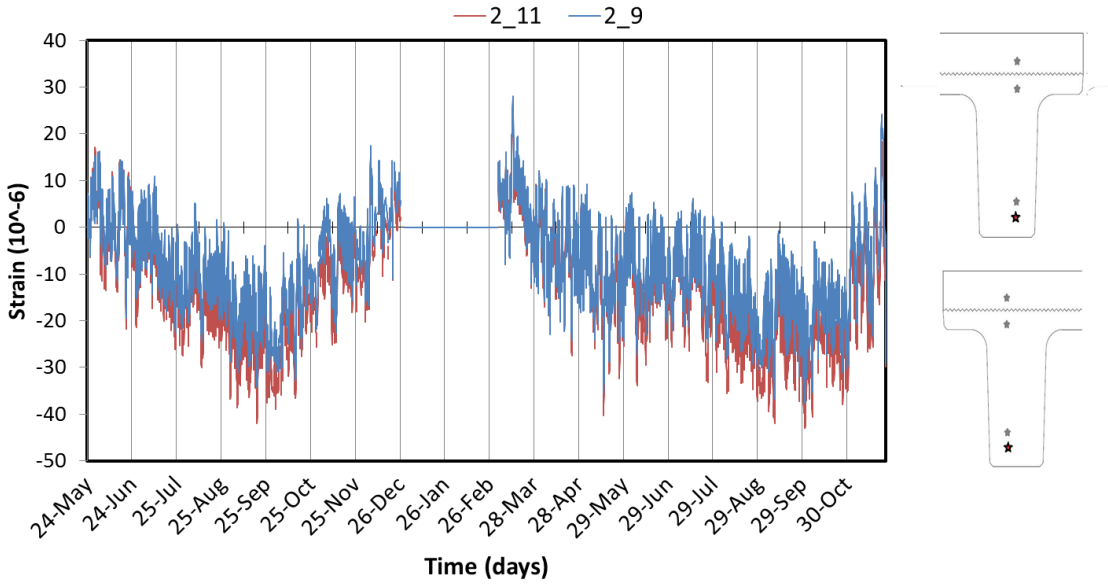

Figure 3-49: Strain at the Bottom Gauges of Beam 2 (Mid-Span)

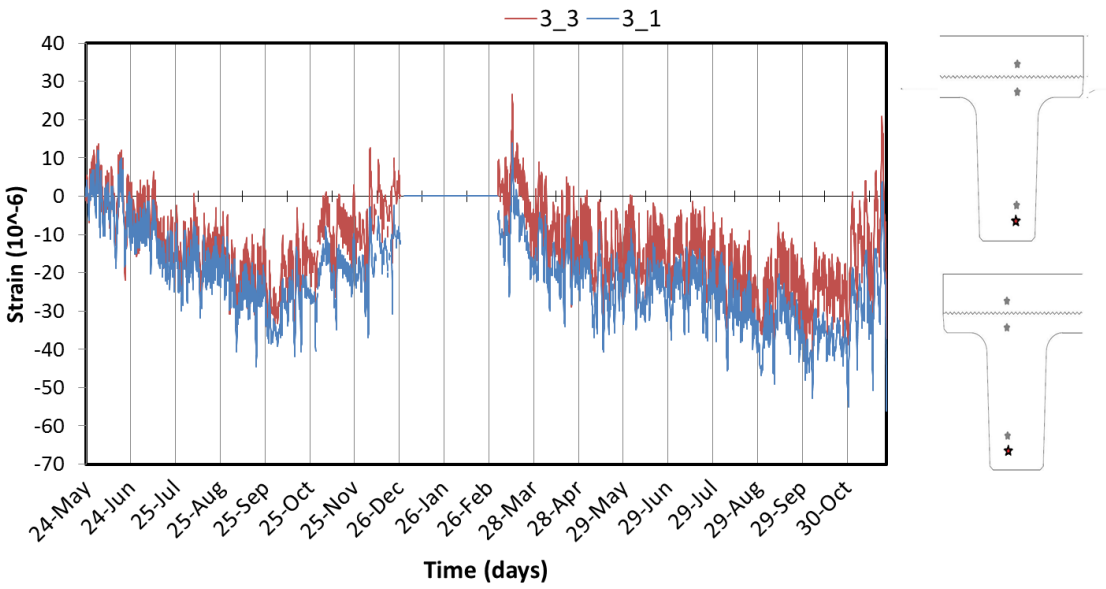

Figure 3-50: Strain at the Bottom Gauges of Beam 3 (Mid-Span)

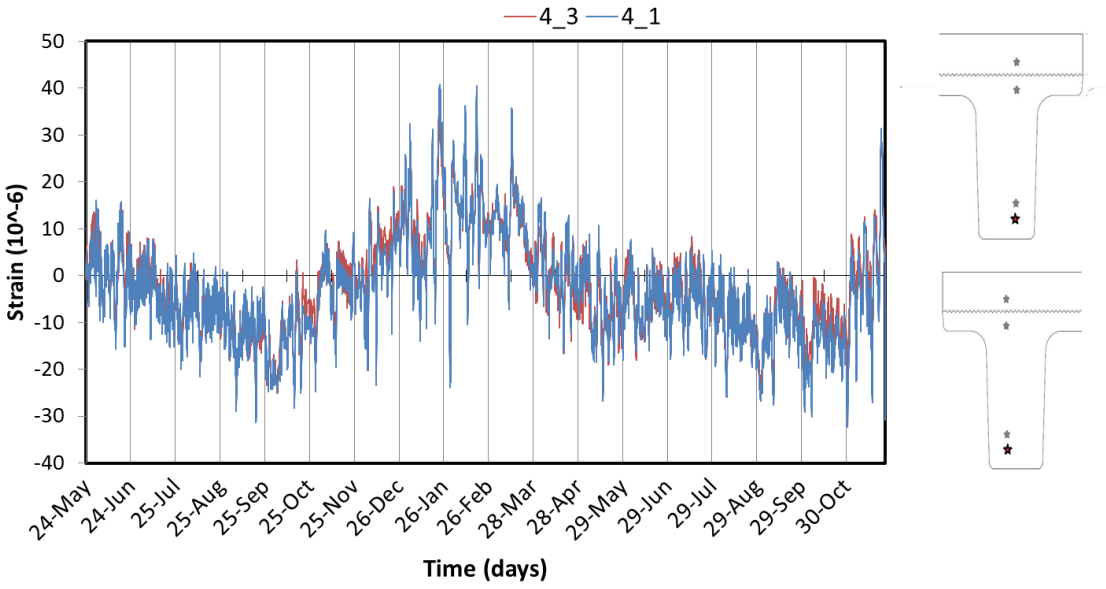

Figure 3-51: Strain at the Bottom Gauges of Beam 4 (Mid-Span)

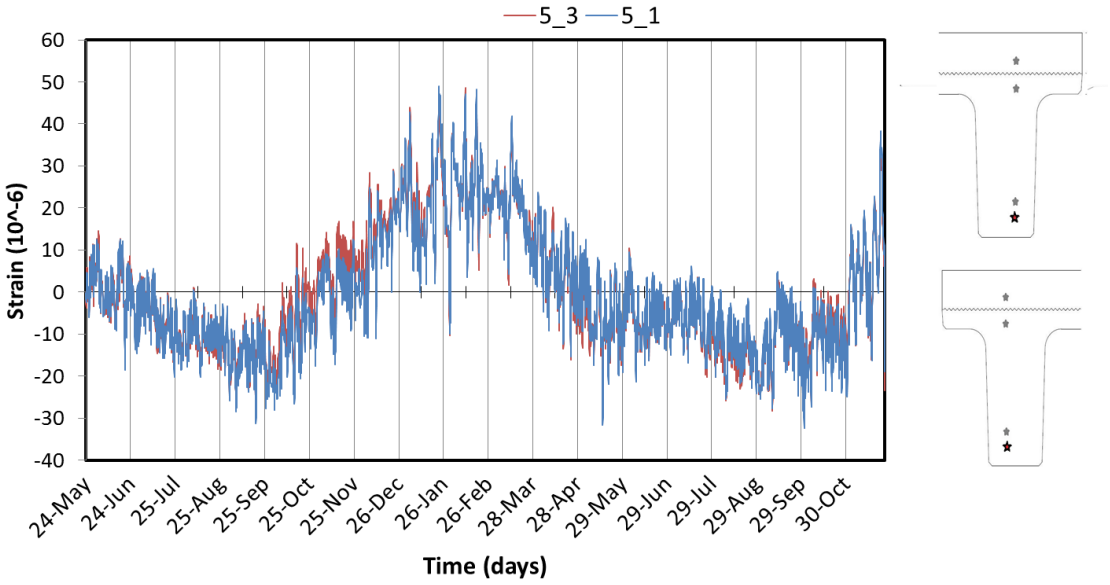

Figure 3-52: Strain at the Bottom Gauges of Beam 5 (Mid-Span)

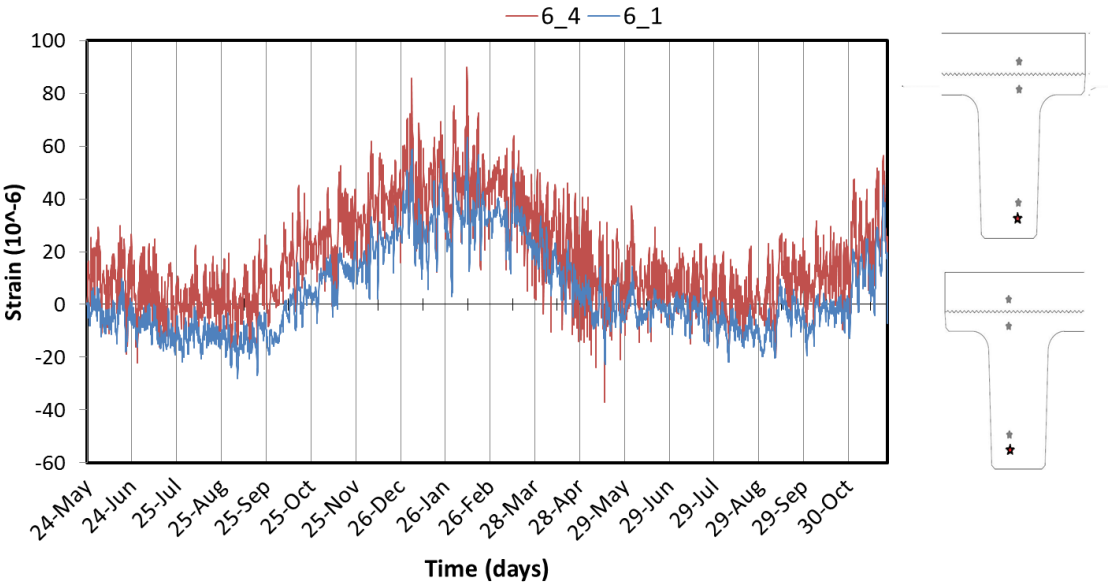

Figure 3-53: Strain at the Bottom Gauges of Beam 6 (Mid-Span)

The plots above show that the maximum compressive stress calculated using Hook's Law assuming elastic section properties did not exceed 0.6 Ksi (4.13 MPa). The maximum tensile stress did not exceed 0.5 ksi (3.44 MPa).

3.6 Summary

In this chapter the process of collecting and correcting field data was illustrated. The calculation of losses, creep, and other factors that would explain the data during construction were shown as well. Also, a comparison between the calculated and measured strain for data during construction was presented. Temperature fluctuation and thermal distribution captured throughout the 18 month monitoring were also explained and shown in plots. Long term behavior of each component that was instrumented in the Brimfield Bridge was explained with field data plotted .

CHAPTER 4

FINITE ELEMENT MODELING

4.1 Introduction

A finite element model of the Brimfield Bridge was developed using SAP2000. A detailed description and the assumptions made in order to build this model are given in this chapter. The model was chosen to be 3-dimensional as it is believed that the level of detail is more accurate given the complex behavior of IABs as well as to understand the effects of skew.

Field data collected for 18 month as well as live load test data was used in calibrating the FE model. As a result, a better understanding was gained on how precast skew IABs behave and the factors that might affect the design of such bridges. An understanding of the long term behavior of the novel NEXT beams used in the Brimfield Bridge is desired, and their effect on the behavior of the entire bridge is needed. Figure 4-1 shows the finite element model of the Brimfield Bridge.

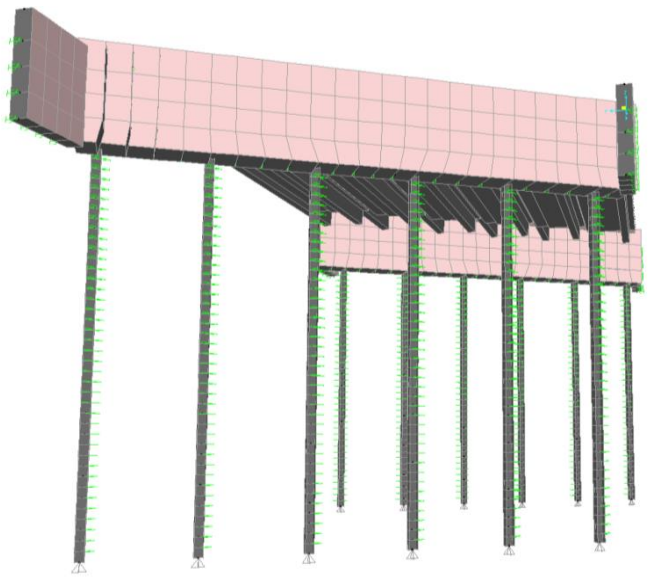

Figure 4-1: Finite Element Model of Brimfield Bridge

4.2 Bridge Superstructure Modeling

The concrete deck of the Brimfield Bridge was modeled by utilizing 4- node thin-shell elements with six degrees of freedom per node, three rotational and three translational. The modulus of elasticity was based on a nominal concrete compressive strength f'_c = 4,000 psi for the deck.

The deck was manually meshed by dividing the shell-element into 32 elements in the longitudinal direction of the bridge and 24 elements in the transverse direction, resulting in a width to length ratio of one for these shell elements.

The *Section Designer* feature in SAP2000 was used in order to create the NEXT Beam frame element cross-section. The overall width of the beam was assumed to be 8'-1"(2.4638 m) instead of the actual width 8'- 1/2" (2.4511m) to account for the longitudinal beam joints, which were assumed continuous with each beam. Slight differences in beam section properties were unavoidable when creating the NEXT beam section in SAP2000. Table 4-1 shows beam section properties for the actual beams and the section created using SAP2000.

Table 4-1: Actual and SAP2000 Section Properties

Property	Actual NEXT Beam	Section Designer	%
Area $in^2(m^2)$	1183.84 (0.7637)	1168 (0.75)	1.34
I_{3-3} $in^4(m^4)$	115936 (0.05)	115746 (0.05)	0.16
Y_b in(mm)	19.54 (490.6)	19.52 (495.9)	0.081
Y_t in(mm)	12.45 (310.6)	12.48 (316.9)	-2.01

The beams were modeled using two node frame elements with six degrees of freedom per node. The beams ends were offset 2 ft (0.61m) to edges of abutment to model a rigid zone at each end and ensure that these portions don't bend inside the abutments. Since the deck was designed to be fully composite with the beam, a master node located at the top of the flange was defined as the centroid of the beam; using the *Frame Insertion Point* option, the beams were offset 4 in. (101.6 mm) down accounting for the half-depth of the deck. Superstructure material properties that were used in the SAP2000 model are shown in Table 4-2.

Table 4-2: Material Properties Used in SAP2000 Model of Brimfield Bridge

Member	*Compressive Strength f'_c Ksi (MPA)	Modulus of Elasticity, E Ksi (MPA)	Poisson's Ratio, υ	Coefficient of Thermal Expansion, α $1/^oF$ ($1/^oC$)	Weight per Unit Volume, γ K/in^3 (kN/mm^3)
Beam	11.4 (78)	6312 (43519)	0.2	$6.5E^{-6}$ ($1.080E^{-5}$)	$8.391E^{-5}$ ($2.278E^{-8}$)
Deck	4 (28)	3604 (24849)	0.2	$6.5E^{-6}$ ($1.080E^{-5}$)	$8.681E^{-5}$ ($2.356E^{-8}$)
***Calculated using Equation 3-20**					

4.3 Abutment and Wing-Wall Modeling

Four-node thin- shell elements with six degrees of freedom per node were utilized in order to model abutment walls and wing-walls. Material properties used were identical to these used in modeling the concrete deck. Abutments were manually meshed not only to make sure that they will share the same nodes with the concrete deck, beams, and piles, but also to capture the full depth of the beams in order to add

rigid links as will be discussed later. Thus, abutment walls were divided into 4 rows, with 24 shell elements for each row as shown in Figure 4-2.

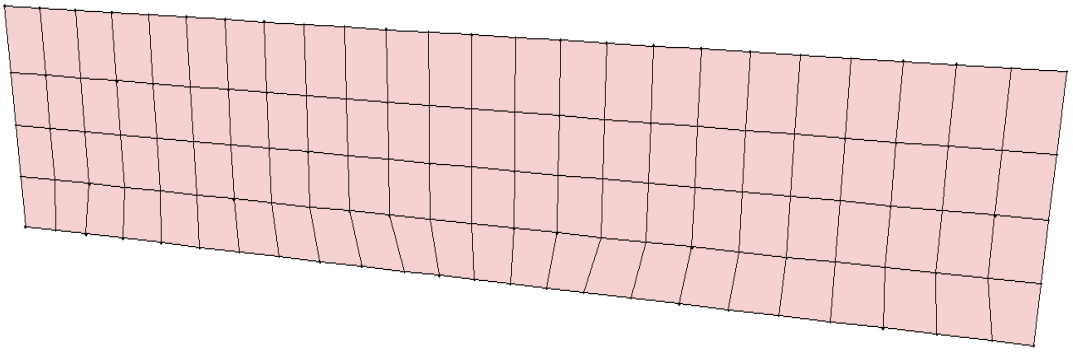

Figure 4-2: Abutment Wall Mesh

It's should be noted that the actual top level of the abutments was not modeled since they were modeled to the center of the concrete deck to share the same nodes. Owing to the existence of the approach slab, this assumption would not affect the results as there is no soil in the top 2 ft (0.61 m) that would generate pressure on the abutments. Rigid links were used to connect the composite beam sections to the abutments over the full beam depth in order to distribute beams forces along their depth rather than transfer them to one point at the beam-deck node (Bonczar et al. (2005)). Another group of rigid links were modeled on top of the abutments. These rigid links were utilized to provide the transverse stiffness of the beam-deck system across the abutment rather than just at the beam end joints. Rigid links are two-node elements with all degrees of freedom constrained to ensure the transfer of forces as well as moments. Figure 4-3 illustrates the distribution of these rigid links.

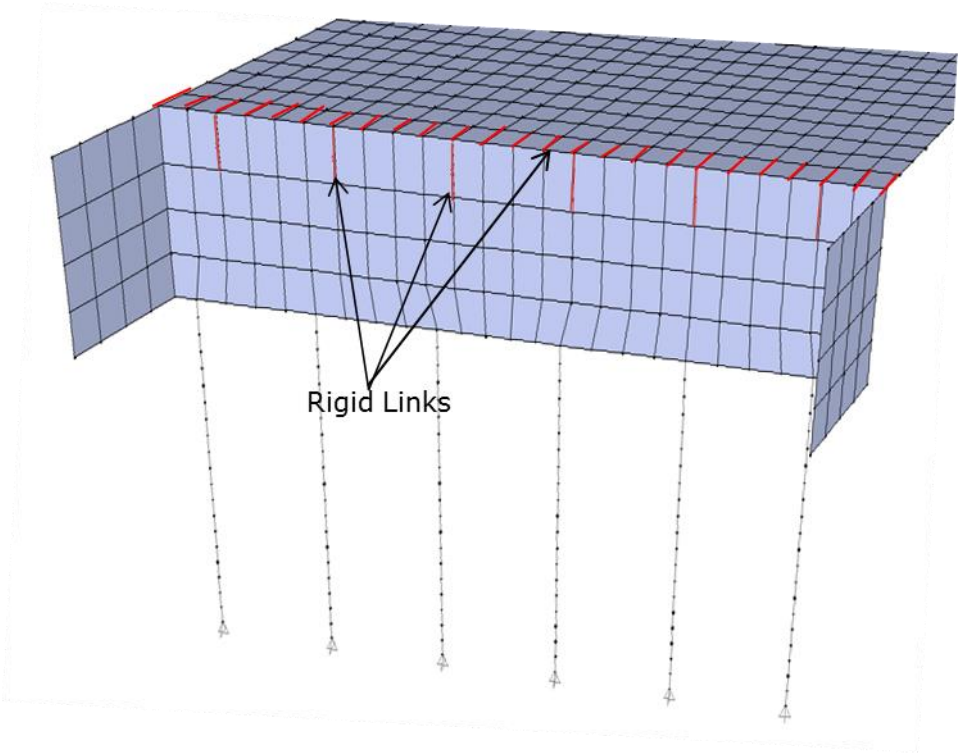

Figure 4-3: Distribution of the Rigid Links

Manual meshing was achieved by dividing the wing-wall shell elements into four rows, with four shell elements in each row. The length to width ratio of abutment and wing-wall shell elements did not exceed 1.48. The nodes of the abutments were constrained in order to reflect the rigid body behavior of the abutment. By constraining these nodes, all abutment elements would have the same rotation but not necessarily the same displacement.

4.4 Finite Element Modeling of Piles

In order to model the Brimfield Bridge piles, two-node frame elements with six degrees of freedom per node were used. The piles were made continuous at the connection point with the abutment and pin supported at the pile end tip. Although the estimated pile driven length was 104 ft (31.6992 m), only 40 ft (12.2 m) were modeled due to the negligible values of displacement and rotation at larger depth would be likely achieved. A later check showed that displacement beyond a depth of

17 ft (5.18 m) was minimal and can be neglected for this bridge and FE model assumptions made.

To represent the soil-structure interaction, piles were divided into 40 frame elements so non-linear springs could be attached to the piles every 1 ft (0.3048 m) to model the surrounding soil. A modification to the pile orientation was done in order to make the weak axis correspond to the actual pile orientation. Figure 4-4 shows pile details as they were modeled.

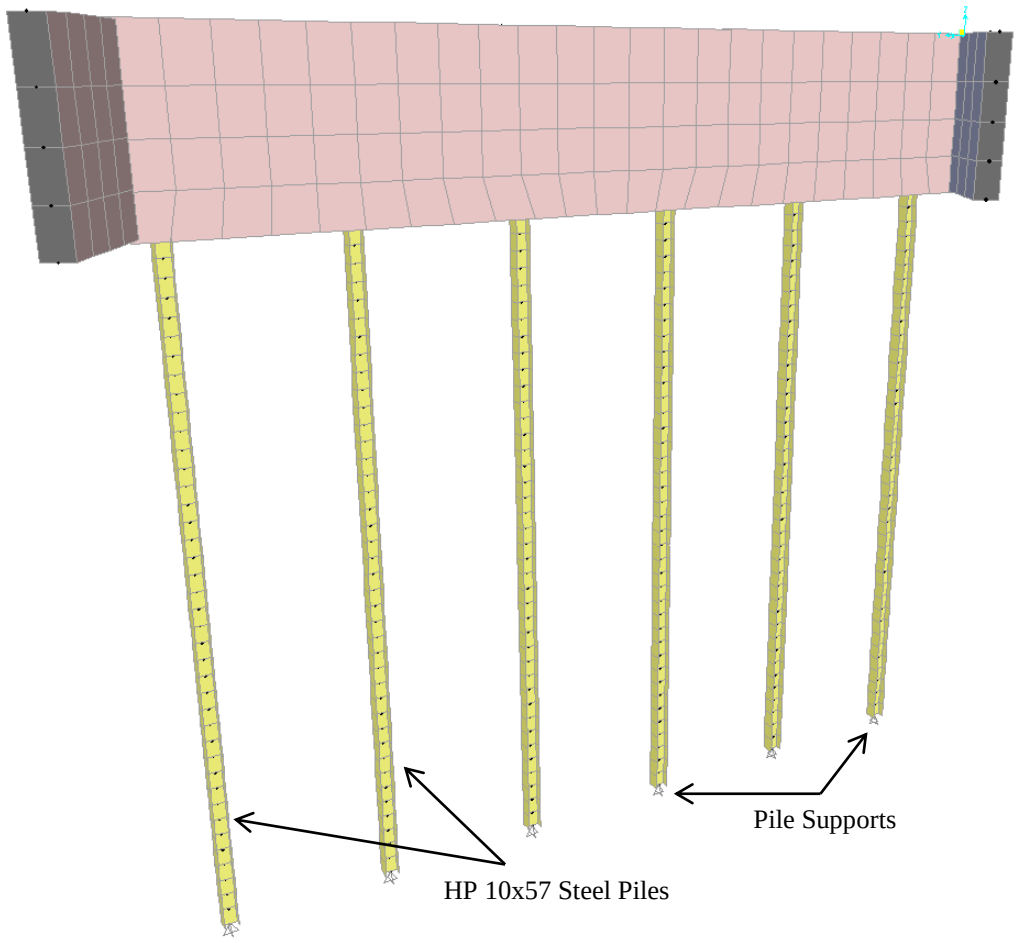

Figure 4-4: The Finite Element Modeling of Piles

4.5 Abutment and Wing-wall Springs

Abutments at the Brimfield Bridge were backfilled with a compacted mix of gravel and sand as is common practice by MassDOT. Figure 4-5 shows the backfill details behind abutments.

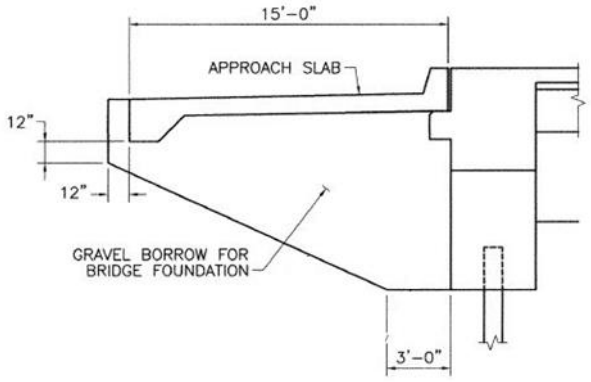

Figure 4-5: Backfill Details

Because the water table level is located below the abutment bottom at the north and south ends of the bridge, dry dense soil properties with a unit weight of 140 lb/ft^3 (22 KN/m^3) and a friction angle of 45 degrees were assumed when modeling the soil behind abutments and wing walls. Furthermore, medium-dense and loose soil properties were also considered to be used in calibrating the model, as needed. The unit weight utilized to represents the medium-dense soil was 125 lb/ft^3 (19.5 Kn/m^3) whereas for loose soil it was 110 lb/ft^3 (17 Kn/m^3). The friction angles assumed were 37 and 30 degrees for medium-dense and loose soil properties, respectively. These soils were modeled using non-linear Winkler springs to simulate the soil interaction. Spring distribution along abutments and wing-wall depth and width is shown in Figure 4-6.

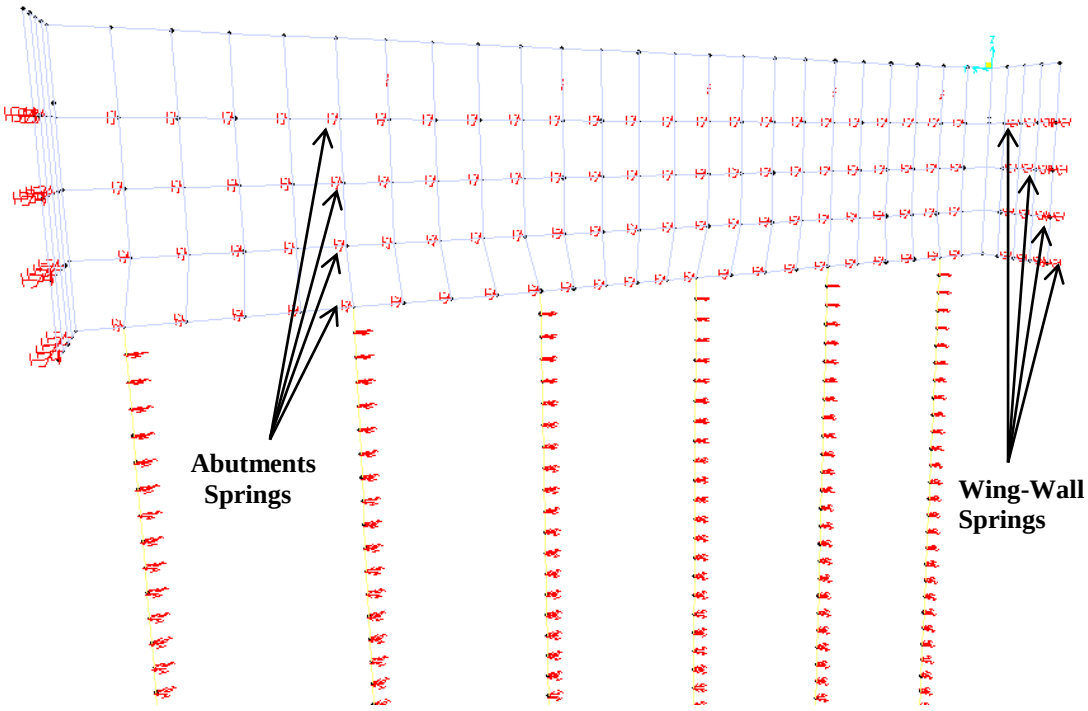

Figure 4-6: Springs Distribution on Abutments and Wing-Walls

Springs forces were estimated by multiplying the tributary area of each spring by the effective horizontal stress, which can be found by multiplying the vertical effective stress by the coefficient of lateral earth pressure. Hence, Equation 4-1 was used to define springs force at each level and/or at each different tributary area.

$$F = K\sigma_v' wh \qquad \text{Eq. 4-1}$$

Where:

F= lateral soil spring resistance force,

K= lateral earth pressure coefficient,

σ_v'= effective vertical earth pressure,

w= width of the tributary area,

h= height of the tributary area,

In the calculation of the effective vertical earth pressure, the depth of each spring was used after subtracting 2 ft (0.61 m) which represents the approach slab thickness.

Backfill soil will generate passive or active pressure depending on the movement of the abutments with thermal changes. As a result, both passive and active coefficients of lateral earth pressure were needed in order to define the non-linear force curve of each spring.

Lateral passive earth pressure for the compacted gravel borrow backfill was estimated according to the MassHighway Bridge Manual 2005 shown Equation 4-2.

$$K_p=0.43+5.7[1-e^{-190(\delta/H)}] \qquad \text{Eq. 4-2}$$

Where δ/H = relative wall displacement,

Equation 4-3 (Thompson 1999) was also used when non-compacted soil behind the abutment was considered for the sake of calibrating the models for the long term.

$$K_p=0.43+3.82[1-e^{-140.68(\delta/H)}] \qquad \text{Eq. 4-3}$$

In these equations, K_p values vary with the relative wall displacement, as seen in Figure 4-7 included in NCHRP 343 (1991) for different backfill soil properties.

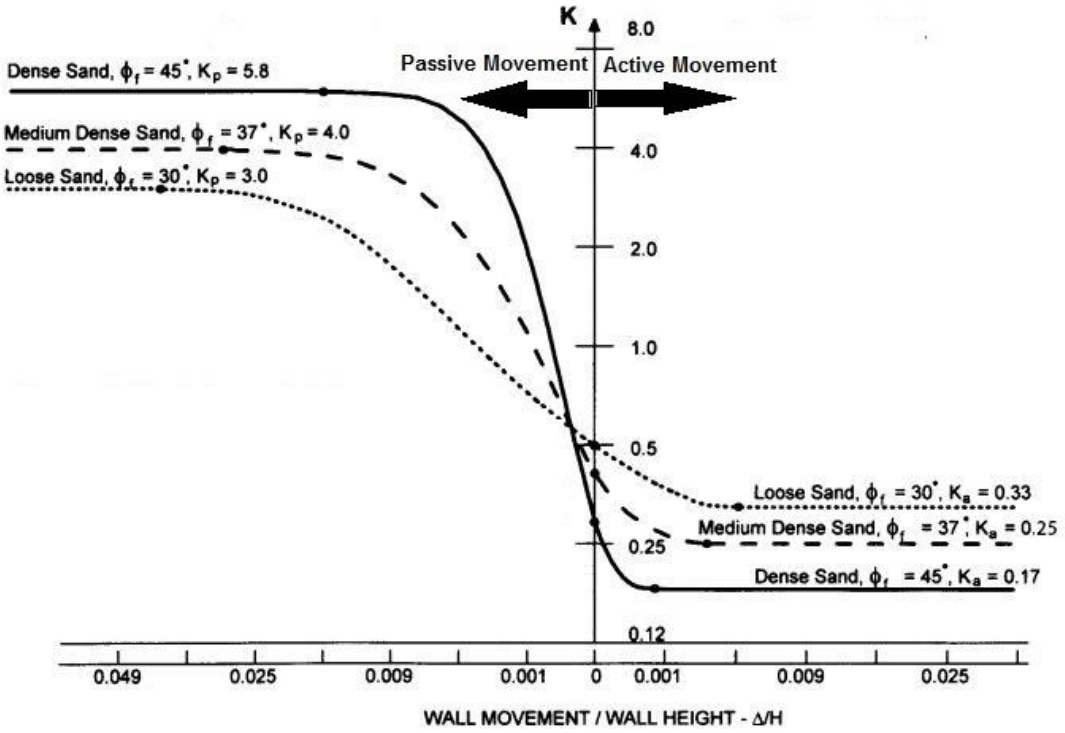

Figure 4-7: Passive Earth Coefficient for Different Soil Properties Depending on Wall Movement as Adopted from NCHRP 343 (1991)

By multiplying the relative wall displacement (δ_T /H) by the total soil height (H) behind the abutment, deflection values for the force-deflection curves were obtained. The active earth pressure coefficient was calculated according to Equation 4-4, given by MassHighway Bridge Manual (2005),

$$K_a = tan^2(45 - \frac{\varphi'}{2}) \qquad \text{Eq.4-4}$$

Where

φ_f= internal friction angle in degrees,

The calculated force-deflection curves for the three soil properties modeled are shown in Figures 4-8 to 4-10.

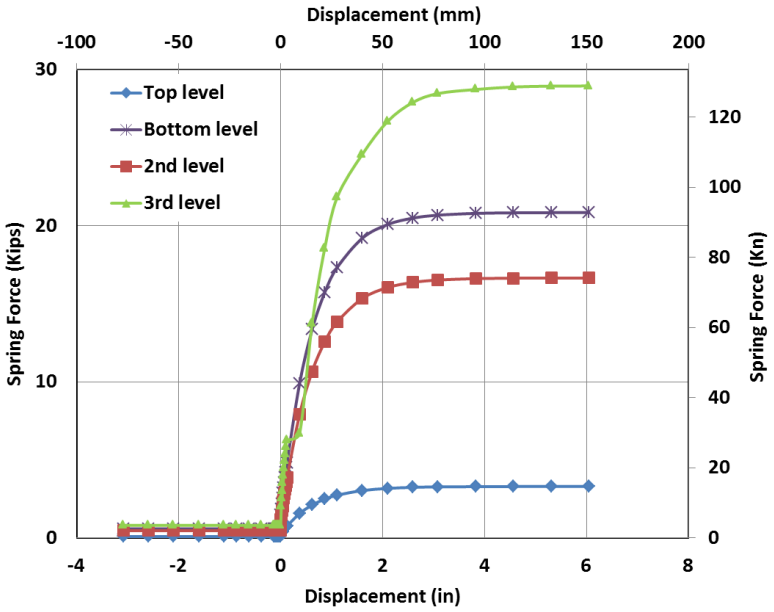

Figure 4-8: Force-Deflection Curves for Springs at Different Levels Assuming Dense Soil

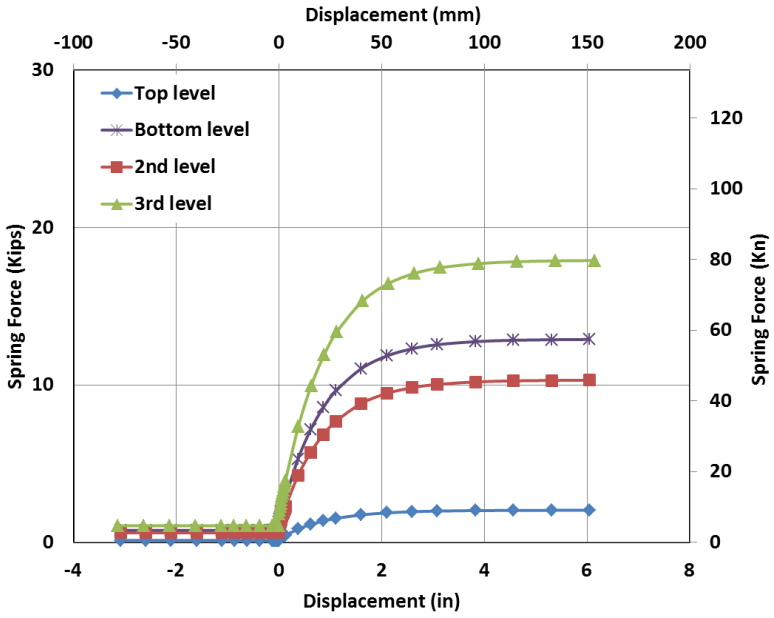

Figure 4-9: Force-Deflection Curves for Springs at Different Levels Assuming Medium-dense Soil

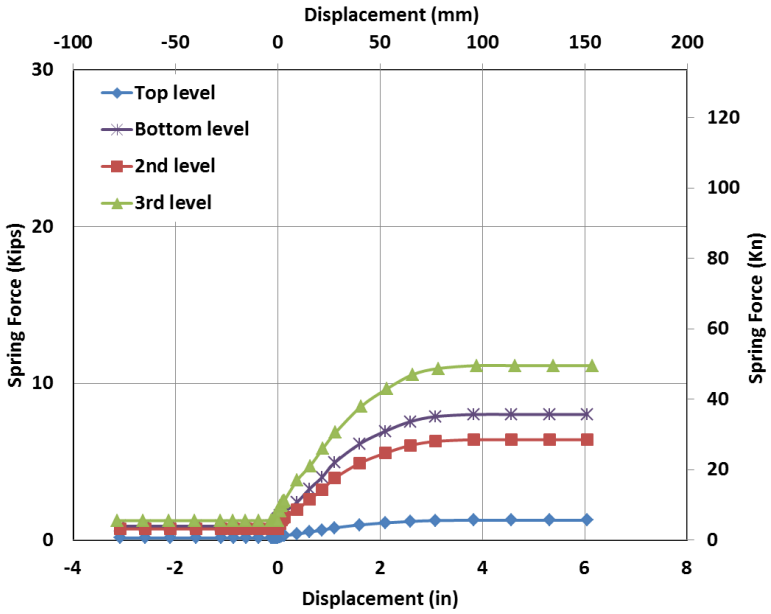

Figure 4-10: Force-Deflection Curves for Springs at Different Levels Assuming Loose Soil

These curves in Figures 4-8 to 4-10, however, were not modeled as shown above. This is as a result of the fact that FE programs wouldn't accept applying positive force while having negative displacement. Thus, the force-deflection curves were offset down an amount equal to the calculated active force. The active pressure effect was assumed to be included in the reference readings. The force-deflection curves were modeled are shown in Figures 4-11 to 4-13.

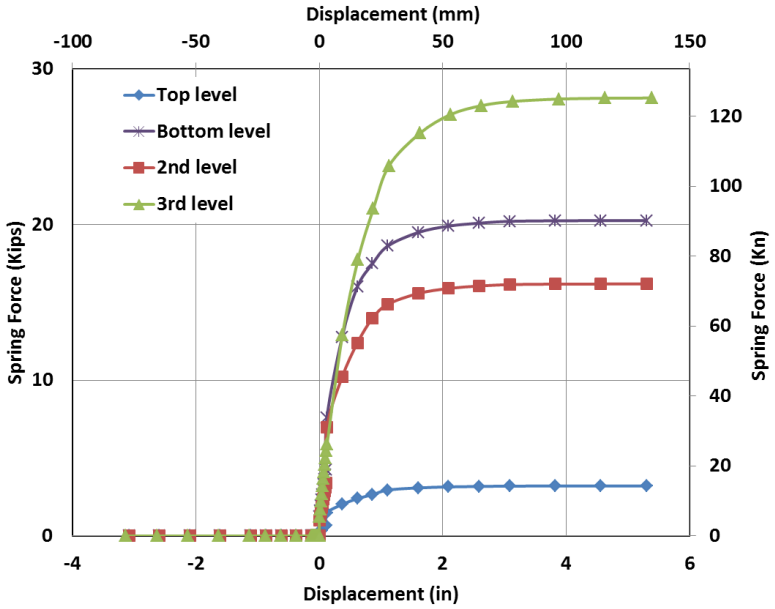

Figure 4-11: The Modeled Force-Deflection Curves for springs at Different LevelS Assuming Dense Soil

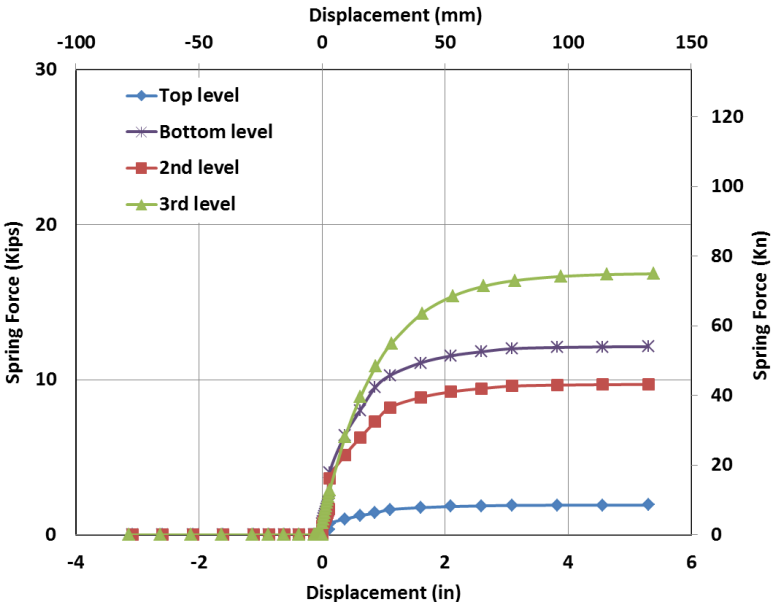

Figure 4-12: The Modeled Force-Deflection Curves for springs at Different LevelS Assuming Medium-dense Soil

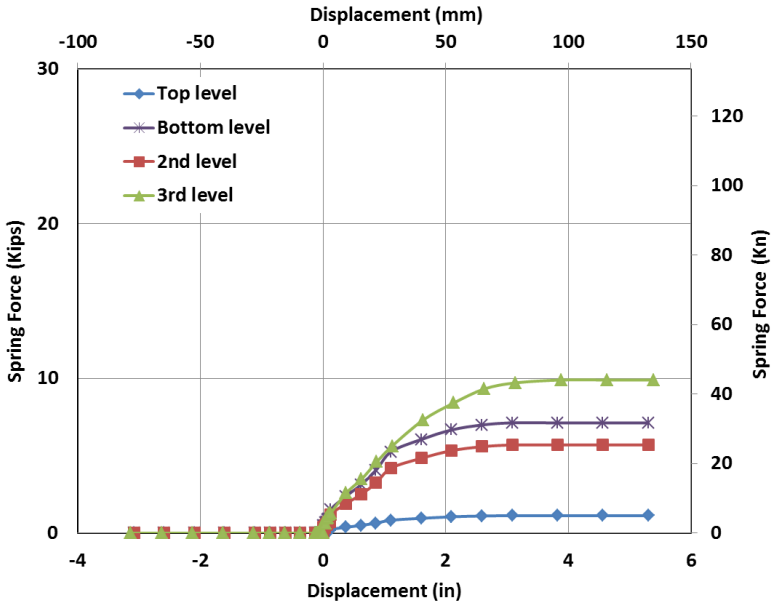

Figure 4-13: The Modeled Force-Deflection Curves for springs at Different LevelS Assuming Loose Soil

4.6 Wing-Wall Vertical Springs

Compression-only area springs in the vertical direction were modeled simulating the vertical bearing of the wing-walls as a foundation. Equation 4-5 was used to estimate springs stiffness which was adopted by ATC-40 (1996) from Gazetas (1991).

$$Kv = [\frac{GL}{1-\upsilon}](0.73+1.54\,(\frac{B}{L})^{0.75}) \qquad \text{Eq. 4-5}$$

Where

K_v = vertical stiffness of the foundation,

G = shear modulus of the soil,

υ = Poisson's ratio, 0.3 for dense soil.

L = length of the foundation,

B= width of the foundation,

This formula, however, was developed for a homogenous soil. As a result, dense soil properties were assumed similar to the properties used in the modeling of abutment and wing-wall non-linear horizontal springs.

Shear modulus was calculated according to Equation 4-6 which is adopted from Bolton et al. 1986.

$$G_{maz} = 1000 * K_{2max}\sqrt{\sigma_m'} \qquad \text{Eq. 4-6}$$

Where,

K_{2max} = soil modulus coefficient (up to 65 for dense sand)

σ_m' = 0.65 times effective vertical soil pressure for normally consolidated soils.

Figure 4-14 shows the vertical springs distribution on the wing-walls.

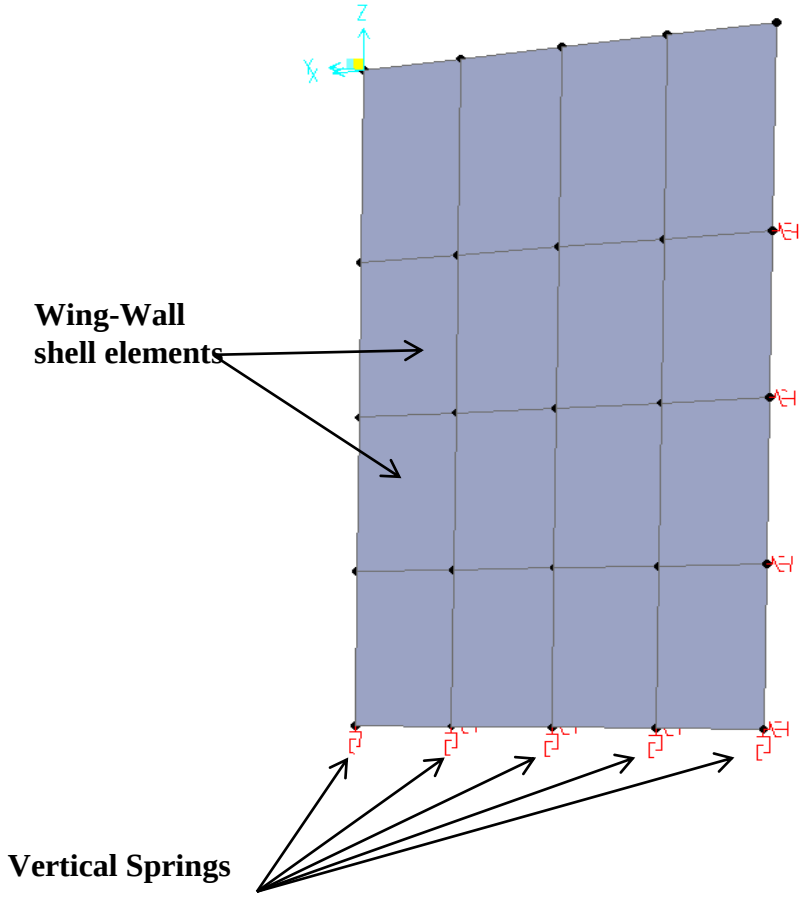

Figure 4-14: Vertical Spring Distribution under Wing-Walls

4.7 Pile Springs

The top 10 ft (3.048m) of the piles were driven into a pre-drilled hole with diameter equal to 2'-6" (0.762m) that was backfilled with crushed stone after driving the piles. Since the actual properties of crushed stone cannot be predicted accurately, spring calculations were made for two different submerged soil properties that were believed to represent bounds of actual behavior of the crushed stone the best. Soil properties that gave the best result during the calibration of the FE model were then chosen. Since crushed stone used to provide near zero soil resistance in this area after initial loading, removing soil springs at the top 10 ft (3m) will be considered along with other soil conditions illustrated above. Submerged medium-dense sand properties were used for the remaining length of the piles below the pre-drilled bore since the actual soil in field is medium-dense sand as shown in Figure 4-15. Table 4-3 shows soil properties that were used in modeling pile springs.

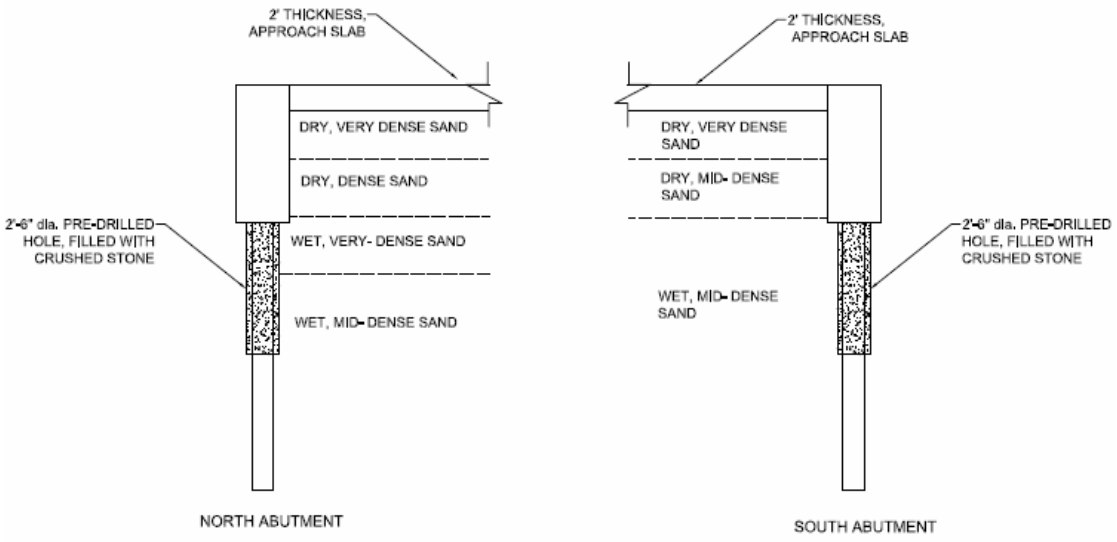

Figure 4-15: Soil Profile

Table 4-3: Soil Properties Used in Spring Calculations

Location	Soil Type	Submerged unit weight (γ') lb/ft^3 (KN/m^3)	modulus of subgrade reaction (k) lb/in^3 (KN/m^3)	Angel of internal friction Φ'
The top 10' (3.0 m) of the piles (option 1)	Loose	47.58 (7.475)	45 (122161)	30
The top 10' (3.0 m) of the piles (option 2)	Medium-dense	62.58 (9.83)	104 (28232.75)	37
The rest of piles depth	Medium-dense	62.58 (9.83)	104 (28232.75)	37

The spring at each segment of the pile was defined using the hyperbolic tangent method as defined in API 21st edition (2005). In this method, the force in each spring was calculated using Equation 4-7

$$F = A\,P_u\,tanh\left[\frac{k\,H}{A\,P_u}y\right]L_p \qquad \text{Eq. 4-7}$$

Where

F= Force in pile spring,

A= factor to account for cyclic or static loading condition, A= (3-0.8 $(\frac{H}{D})$) $\geq$ 0.9 for static loading

k= initial modulus of subgrade reaction, which can be found using Figure 4-16, given in API 21st edition (2005), as a function of internal friction φ'.

P_u= ultimate lateral bearing capacity at depth H,

H = soil depth from the top of the soil layer to the specified node,

y = the deflection along horizontal axis,

D=average pile diameter, which was taken as HP pile section depth,

L = length of pile segment,

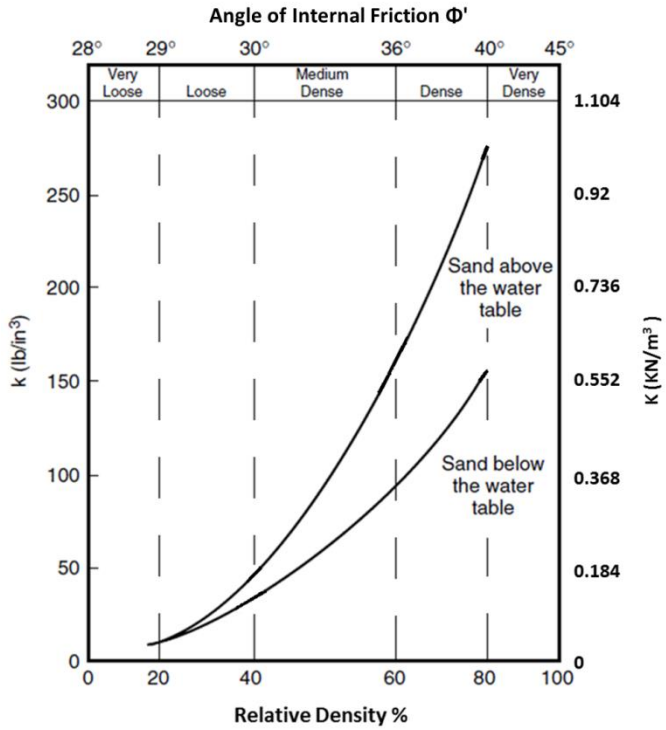

Figure 4-16: Initial Modulus of Subgrade Reaction as a Function of the Internal Friction Angle (Adopted from API 2005)

In order to calculate the ultimate lateral bearing capacity (P_u), API (2005) provides two equations and suggests using the smallest values given by these equations depending on the depth. Thus, Equations 4-8 and 4-9 were used to estimate the lateral bearing capacity at each spring level.

$$P_{u\ shallow} = (C_1\ H + C_2\ D)\ \gamma\ H \qquad \text{Eq. 4-8}$$

$$P_{u\ deep} = C_3\ D\ \gamma\ H \qquad \text{Eq. 4-9}$$

Where

γ = soil unit weight,

C1, *C*2, *C*3 = Coefficients determined from Figure 4-17, given in API (2005), as a function of φ',

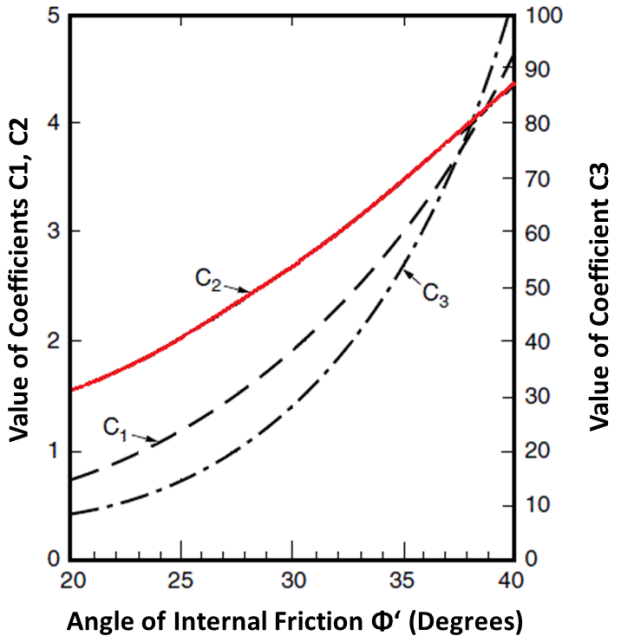

Figure 4-17: C1, C2, and C3 Coefficients as a Function of the Internal Friction Angle (Adopted from API 2005)

Having spring calculations ready, non-linear plastic links in SAP2000 were utilized to represent soil interaction after defining p-y curve for each single spring. Non-linear links were modeled in two orthogonal directions to account for the possible biaxial bending of the piles. Due to the fact that HP10x57 (metric equivalent) steel shape has a cross section depth d of 10 in. (254 mm) and a flange width of 10.22 in. (259 mm), same p-y curves were defined for both directions as there were no significant differences in spring forces. A proper adjustment for spring local axes was made to match pile local axes. Vertical soil resistance was not taken into account considering that end bearing piles were used in Brimfield Bridge. Figures 4-18 and 4-19 show the p-y curves for non-linear piles springs at different depths considering two different soil properties as discussed previously.

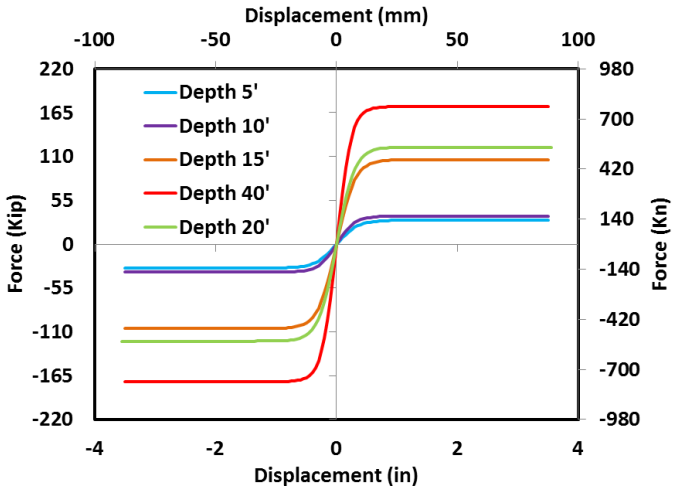

Figure 4-18: P-y Curves For Pile Springs Assuming Loose Soil Properties at the Top 10 ft (3.048 m) of Pile Depth

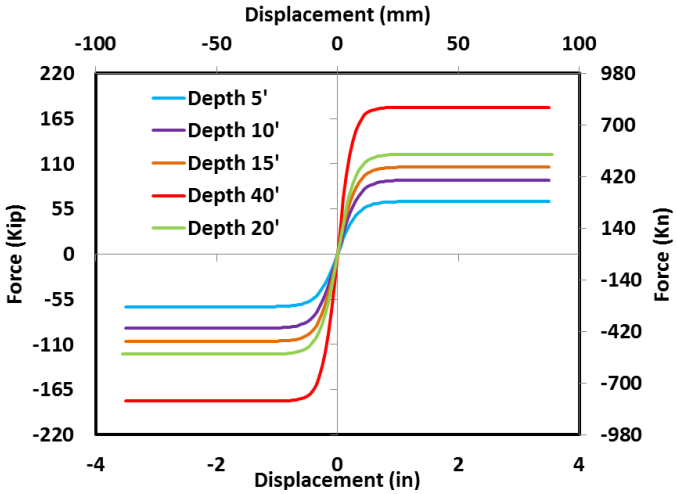

Figure 4-19: P-y Curves For Pile Springs Assuming Medium-Dense Soil Properties at the Top 10 ft (3.048 m) of Pile Depth

4.8 Summary

The Brimfield Bridge 3-Dimensional model was developed using SAP2000. Detailed information about the modeling of each component in the bridge, including model assumptions, soil backfill, and in-situ soil conditions were described in this chapter. Force- deflection curves of different soil conditions were developed for abutment, wing-wall and pile springs. The modeling of these curves in the FE model using non-linear springs was also illustrated in this chapter.

CHAPTER 5

FINITE ELEMENT MODEL VALIDATION AND INVESTIGATION OF KEY PARAMETERS AFFECTING BRIDGE BEHAVIOR

5.1 Introduction

After having the FE model of Brimfield Bridge created, model validation was conducted in order to obtain agreement with field data. Data from the load test, which took place at the end of construction, was used for initial validation of the model. The purpose of this validation was to check whether the FE results match field data at this stage (immediately after finishing construction). Long-term displacement and rotation data were subsequently utilized to validate the FE model accordingly for the first and second year. Since thermal load poses the main effect on the long-term behavior of the bridge, the validation of the model was done by applying thermal load only considering different temperatures occurred during the 18 months.

5.2 Initial Model Validation

Two load test configurations (configuration 7 and 8) were selected to validate the model initially. These were chosen because maximum moments are induced in the beams due to these configurations. Although load test results are not discussed as part of this thesis as mentioned before, the field data has been considered a good reference to be used for initial model validation. Configurations 7 and 8 truck positions are shown in Figure 5-1 and 5-2, respectively. Table 5-1 lists trucks dimensions and weights.

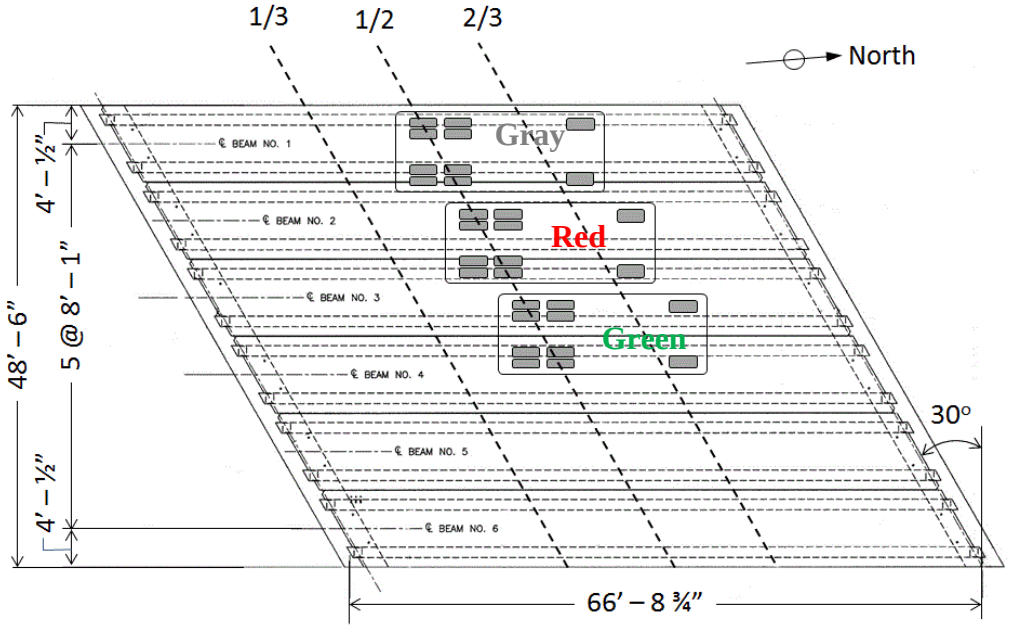

Figure 5-1: Configuration 7 Truck Positions

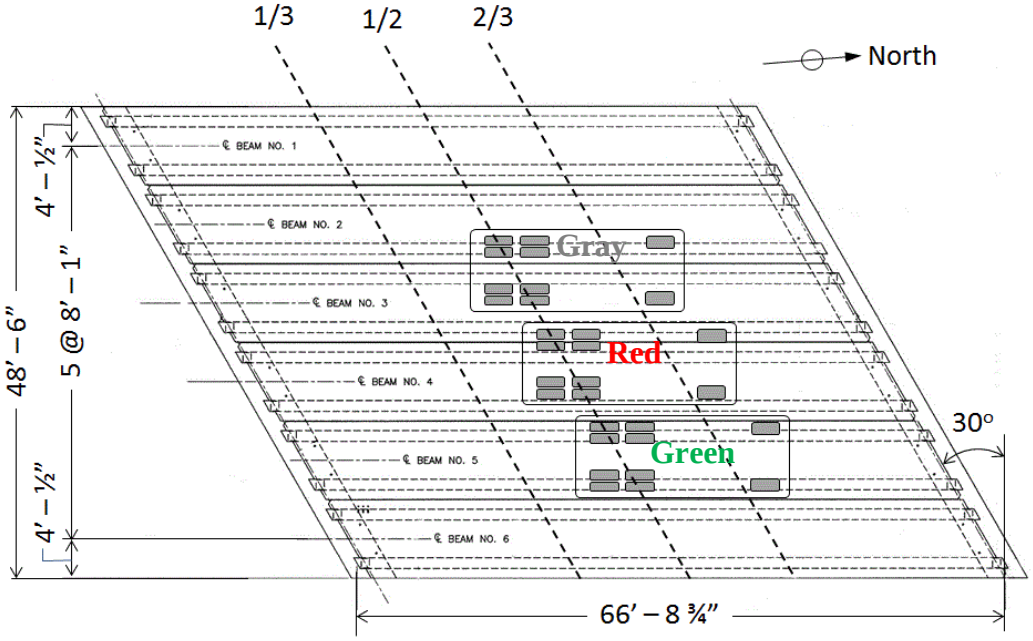

Figure 5-2: Configuration 8 Truck Positions

Table 5-1: Trucks Dimensions and Weights

Truck	Weight, lb (KN)		Distance, in. (m)			
	Rear Tandem	Front axle	Front to 1st rear	1st rear to 2nd rear	Rear axle width	Front axle width
Grey	56100(249.5)	24600(109.4)	199 (5)	54 (1.4)	72(1.8)	84(2.1)
Red	59740(265.7)	20540(91.3)	229(5.8)	55(1.4)	72(1.8)	84(2.1)
Green	56460(251.1)	20540(91.3)	204 (5.2)	51(1.3)	72(1.8)	84(2.1)

For this stage, two different soil conditions were investigated. The conditions were chosen based on the backfill used and the construction sequence that was followed for the bridge. The first soil properties considered soil behind the east half of the abutments corresponded to medium-dense soil (Section 4.5). The soil behind the west half of the abutments, on the other hand, was considered using dense properties (Section 4.5). The soil around the first 10 ft. (3.048m) of the piles were considered loose and medium-dense (Table 4-3) for the piles under the east half and west half of the abutment, respectively. The soil around the rest of the pile length was considered medium-dense. The reason behind choosing this pattern relates to the construction sequence followed for this bridge. The east half of the bridge was constructed 7 months before the west side. The assumption that was made here is that the soil behind the east side has become looser as the bridge has expanded and contracted during the 7 month period that it took for the bridge to be finished. Figure 5-3 illustrates the first soil conditions assumed.

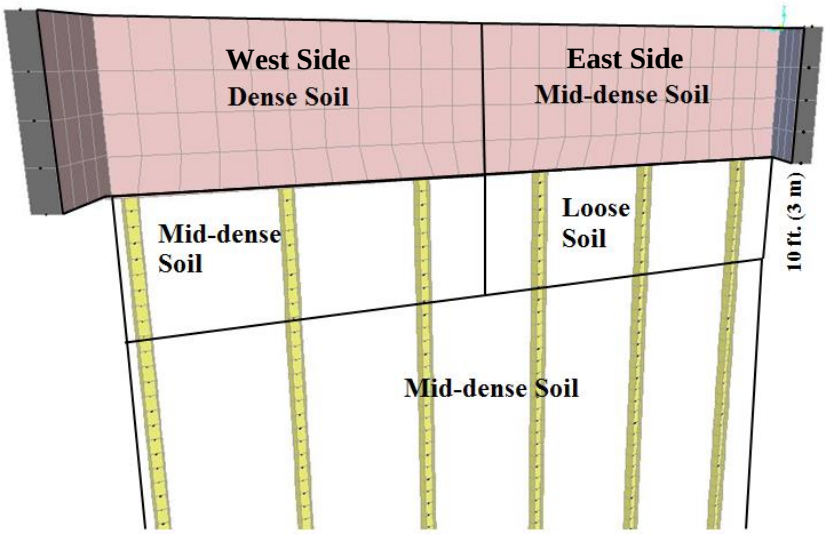

Figure 5-3: First Soil Condition Assumed

The second possible soil condition considered was that the soil behind the abutments is dense. The soil around the first 10 ft. (3.048 m) was assumed mid-dense. Similar to the first assumed soil condition, the soil around the rest of the piles was assumed medium-dense. The assumption made regarding this condition is that there had been no change in soil properties behind the east side of the abutments during the 7 month period. Considering no soil restrain at the top 10 ft (3 m) of piles was also investigated, yet the results were far from the measured once and they presented in Appendix D.

Owing to the fact that the concrete deck can develop cracking under shrinkage effects, a modification to the gross moment of inertia in two directions was applied. The cracked moment of inertia for the deck was assumed equal to 50% of the gross moment of inertia. The Section Cut option in SAP2000 was used to report the moments at the neutral axis of the composite section. On the other hand, new moment of inertia about the neutral axis that was extracted from the measured strain profile was used to calculate moments from strain readings Equation 5-1 was used in converting the strain data to moments.

$$M=\frac{\varepsilon EI}{c} \qquad \text{Eq. 5-1}$$

Where,

ε= Strain x 10^{-6},

E= Modules of elasticity,

I= Moment of Inertia of the composite section about the neutral axis,

c= Distance between the strain gauge and the neutral axis that was extracted from field data.

Figures 5-4 and 5-5 show comparisons between the moments that were obtained from field data and SAP2000 models. Table 5-2 show the ratio differences between moments resulted from the FE models and the measured moment.

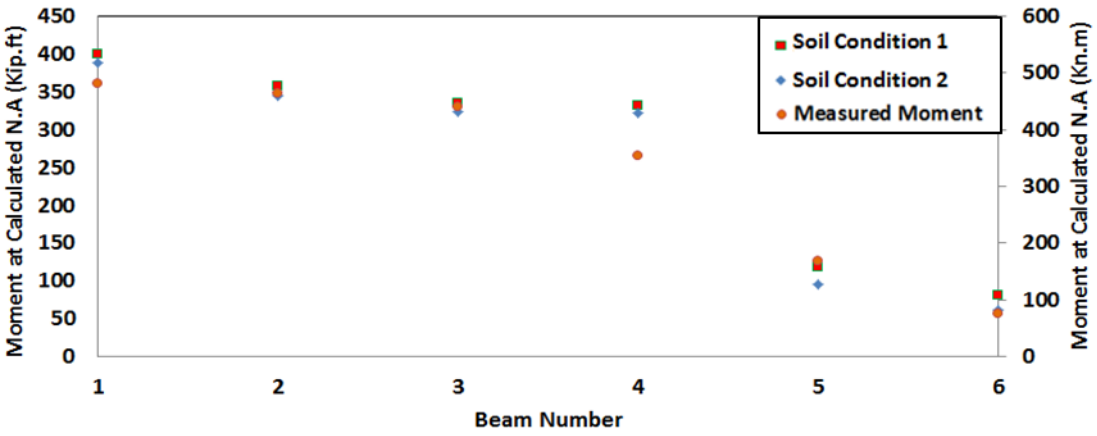

Figure 5-4: Comparison between Field and FE Models Results for Configuration 7

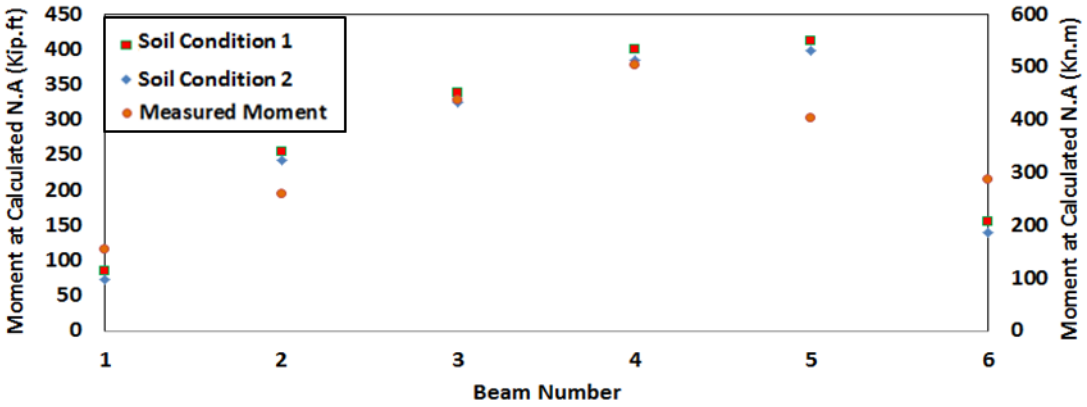

Figure 5-5: Comparison between Field and FE Models Results for Configuration 8

Table 5-2: Moment Values Resulted from The FE Models and Field Strain

Configuration	Moment Kip.ft (KN.m)						
	Beam	1	2	3	4	5	6
7	Soil Condition 1	399 (541)	357.6 (485)	334.4 (453)	332.5 (451)	117.5 (159)	80.6 (109)
	Soil Condition 2	387.7 (526)	344.8 (468)	323.8 (439)	322 (437)	95.3 (129)	61.7 (84)
	Measured	361.8 (491)	348.6 (473)	331 (449)	266 (361)	126 (171)	57 (77)
8	Soil Condition 1	85 (115)	254.6 (345)	338.3 (459)	399.7 (452)	412.9 (560)	154.8 (210)
	Soil Condition 2	74 (100)	242.4 (329)	325.5 (441)	385.7 (523)	398.2 (540)	139.4 (189)
	Measured	115.6 (157)	195.6 (265)	329.1 (446)	378.4 (513)	302.3 (410)	214.8 (291)

From the comparison made in the figures above and moment values in Table 5-2, it was concluded that in some of the beams the first assumption of soil properties corresponded better to measured values whereas the second assumption resulted in better results in the other beams. However, the same general moment trend was captured. Thus, the minor differences in moments values between the two assumptions gave indication of some soil effect. The FE results of configuration 7 showed an excellent agreement with the actual moments except for beam 4. This could be due to the approximation in the force location applied to the FE models. The results of the FE models showed a good agreement with the actual moments in terms of trend and values, yet for beams 5 and 6, the results were not approximating to the

measured ones. This is owing to the fact that in configuration 8 the trucks were closer to the sidewalk, which likely acts compositely with the concrete deck and beams.

5.3 Year One Model Validation and Parametric Analysis

The long term model validation was conducted by varying selected parameters, which helped identify the factors that affect the FE model results. Unlike the initial validation, the long-term calibration was based on abutment rotations and displacements captured during the 18 months of monitoring. The reason for choosing abutment movements and not beam strains to calibrate the long-term models was based on the observation that field-determined neutral axis locations kept changing. To better understand the bridge response, field data were divided into two separate years and the validation of the model was performed for each year considering different seasons. By separating the data, any changes in the bridge yearly behavior were isolated. Different parameters were investigated in this model validation and parametric analysis, including different soil conditions, thermal load application procedure, and value of coefficient of thermal expansion. The parameters were varied initially to achieve good results when compared with first year data. However, different soil condition patterns were also investigated to better match second year data. Data were available for the four seasons during the first year so the model was adjusted to match data for a wide range of temperatures found in these seasons. During the second year, however, only data during spring, summer and fall seasons were available due to a logger malfunction during winter. Only data collected during these three seasons were used to validate the year 2 model.

Parameters were varied sequentially to provide a closer match to measured data. Each parameter was varied within plausible ranges and the value that best approximated the measured data was fixed to examine the effects of the next

parameter in the sequence. However, other soil conditions such as removing soil spring at the top 10 ft (3m) of the piles, assuming loose soil behind the abutments, and making the soil behind the abutment and around the piles very dense were investigated, yet their results are not presented herein for the sake of having good data only presented clearly.

5.3.1 Effect of Soil Properties on Long-Term Thermal Response

The effect of soil properties on the FE model results was investigated by assuming four different soil conditions. These four conditions are shown in Table 5-3 below.

The first soil condition (A1 Table 5-3) considered for long-term evaluation was the first one selected during initial model validation using short-term load test results (Figure 5-3). This condition was initially assumed in the long-term evaluation as it was believed that changes in soil properties during the first year would be minimal.

The second soil pattern (A2 Table 5-3) investigated was assumed to represent soil loosening during the first year that the bridge was in service. Here, the assumption considers that the soil behind the abutments had become looser than what was assumed in the initial calibration.

Table 5-3: Soil Conditions Investigated in Studying the Effect of Soil Properties on Long-Term Thermal Response of the Bridge

Soil Condition		Description *
A1	Behind the abutments	Medium-dense soil properties assumed behind the east side of the abutments and dense properties behind the west side of the abutments
	Around the Piles	Loose soil properties assumed around the top 10 ft (3.048 m) of the piles which support the east side of the abutments and mid-dens properties were assumed around the piles that are supporting the west side of the abutments. The soil around the rest of the pile length was assumed to be medium-dense
A2	Behind the abutments	Loose soil properties assumed behind the east side of the abutments and medium-dense properties behind the west side of the abutments
	Around the Piles	Soil springs were removed at the top 10 ft (3.048 m) of the piles which support the east side of the abutments and loose properties were assumed around the piles that are supporting the west side of the abutments. The soil around the rest of the pile length was assumed to be medium-dense
A3	Behind the abutments	Dense soil properties assumed behind the abutments
	Around the Piles	Medium-dense soil properties assumed along the piles length
A4	Behind the abutments	Similar to condition A1
	Around the Piles	In representing soil conditions when extreme negative change in temperature over -41 ^{o}F(-22.8 ^{o}C), the top 3 ft (0.9 m) of the soil around the piles were made stiff to achieve freezing condition.
*** For the soil behind the abutments density details, see Section 4.5** *** For the soil around the piles density details, see Table 4-3**		

The third soil condition (A3 Table 5-3) considered was the same as the second condition chosen during initial model validation, especially since the results of this model showed almost the same results as the first condition model in the initial validation, yet it is expected to give higher abutment rotation when validating the model for temperature.

Lastly, the fourth soil condition (A4 Table 5-3) considered the fact that the top soil around the pile is frozen when having change in temperature exceeds -41 ^{o}F (-

22.8 ^{o}C) which correspond to freezing. As a results, the models that correspond to change in ambient temperature of -41 ^{o}F (-22.8 ^{o}C) and -57 ^{o}F (-31.7 ^{o}C) were the only two on which this condition was applied as these temperature were appeared between January and march (Selezneva and Hallenbeck (2008)). The soil behind the abutments as well as the soil around the rest of the pile length were chosen to be the same as soil condition A1, which resulted in better displacement and rotation results than the others (Figures 5-6 and 5-7). Moreover, soil condition A1 was also used to represent the soil during temperature increase and decrease of less than -41 ^{o}F (-22.8 ^{o}C). Displacement and rotation results of the fourth soil condition were presented separately than the first three conditions results and compared to those extracted from the first assumptions model.

In the investigation of the soil effect, ambient temperature was initially applied on the deck and beams considering no temperature gradient (MassHighway Bridge Manual 2005). The changes in ambient temperature applied were taken as the average of titltmeter thermistors readings located at each abutment. These changes in ambient temperature are shown in (Table 5-4). It should be noticed that maximum positive and maximum negative change in ambient temperature were used to represent summer and winter conditions. The coefficient of thermal expansion of the deck and beams was taken 5.5$\mu\varepsilon/°F$ (10 $\mu\varepsilon/°F$) as assumed in the MassHighway Bridge Manual (2005). Investigations on the effect of the temperature gradient and potential variations in coefficient of thermal expansion will be discussed in subsequent sections.

Table 5-4: Applied Temperatures

Average Ambient Temperature at Time of Construction ^{o}F (^{o}C)	Temperature Change Applied (^{o}F)	Temperature Change Applied (^{o}C)
68 (20)	11.5*	6.4*
	-18	-10
	-41	-22.8
	-57**	-31.7**
Highest positive change in temperature occurred in year one summer** * Highest negative change in temperature occurred in year one winter**		

Figures 5-6 shows the comparison between the displacements determined from FE models using different soil conditions and field data. The displacements are compared at the top and bottom of the south and north abutments at the obtuse and acute corners, respectively. Comparisons of the results at the acute corner of the south abutment and obtuse corner of the north abutment are shown in Appendix D. In this figure, A1, A2, A3 represent the first three soil conditions introduced above, respectively. Field data are indicated using hollow circles. All comparisons for the top and bottom displacements of the abutments were calculated using displacement data at crackmeter locations as their depth vary as listed in Table 2-3, and tiltmeter data. From tiltmeter readings, rotation was converted to displacement assuming rigid body rotation of the abutments.

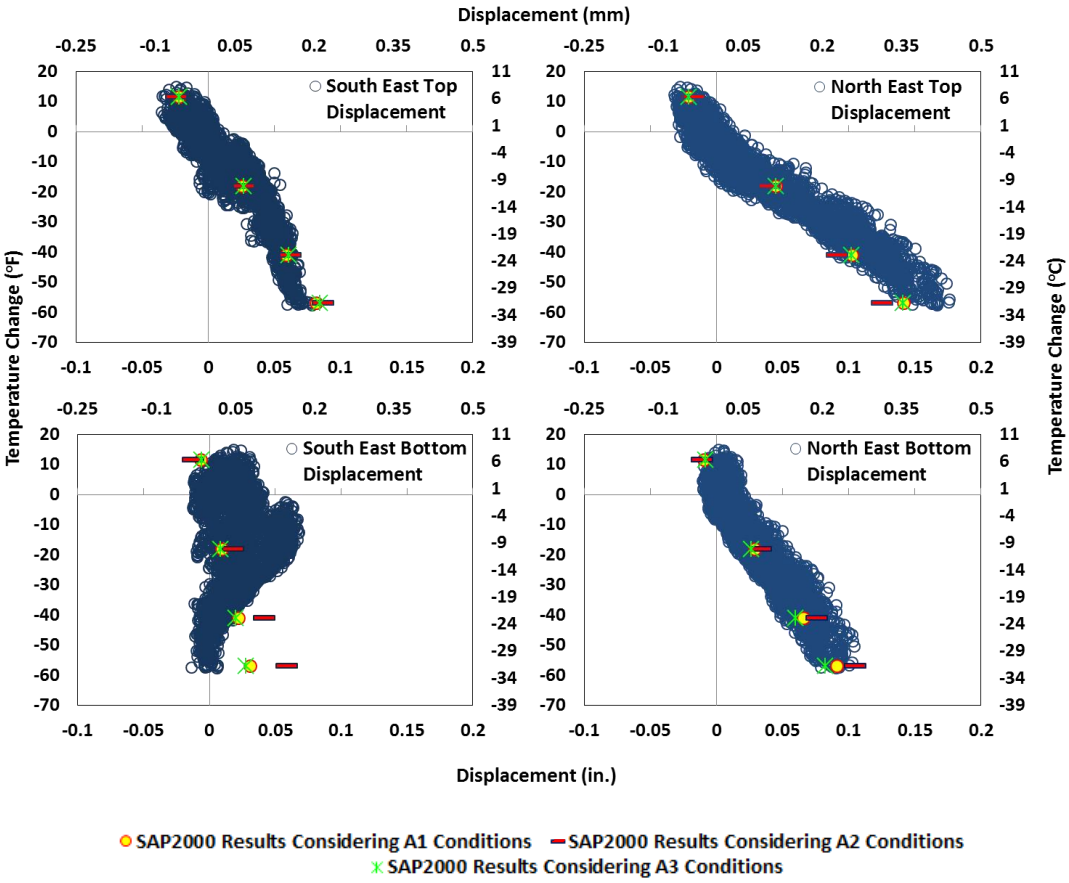

Figure 5-6: Comparison among FE Model Displacement Results of Different Soil Conditions with Regards to Field Data

The comparison between different assumed soil conditions and measured displacements (Figure 5-6) show that the first and third soil conditions resulted in almost the same displacement values and approached the range of valued measured in the field. On the other hand, the results assuming the second soil properties tended to show higher discrepancy from field data.

Figure 5-7 shows the comparison between abutment rotations determined in the different FE models and field data of the first three soil conditions.

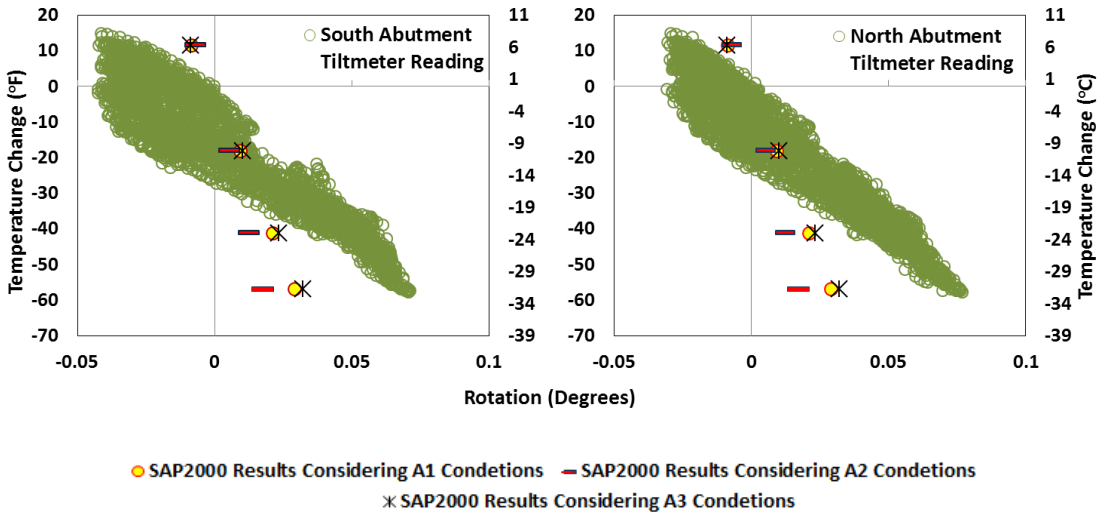

Figure 5-7: Comparison among Rotation Readings and FE Models Results of Different Soil Conditions with Regards to Field Data

Abutment rotations are shown in Figure 5-7. It can be observed that none of the three assumed soil conditions results matched field rotations, especially, when the change in temperature was negative (winter), with calculated differences as large as 60% lower. Rotation results for summer were marginally better in comparison with field data. The large discrepancies in calculated and measured rotations in cold season could potentially be attributed to the top few feet of soil surrounding the piles becoming frozen during winter. To confirm this theory, the soil springs at the top 3ft (1m) of the piles were replaced by springs with properties equal to those found at a 40ft (13m) depth when applying change in temperature larger than -41 ^{o}F (-22.8 ^{o}C). The depth of the soil selected to be considered freezing was based on an FHWA report (Selezneva and Hallenbeck (2008)). In this report the soil in Amherst, MA was analyzed for two years and it was found that the freezing condition starts in January and ends in March and the freezing depth is 3ft (1 m). The higher stiffness of the soil at the top of the piles was used to represent the freezing condition. Since calculated abutment displacement and rotation values when using the first and third soil conditions were approximately equal, first soil condition was chosen to be used in the

FE model to examine the effect of soil freezing. Figures 5-8 and 5-9 present the results assuming the top region of soil surrounding the piles was frozen during winter and spring. In these figures, A1, A4 represent the first and fourth soil conditions assumed.

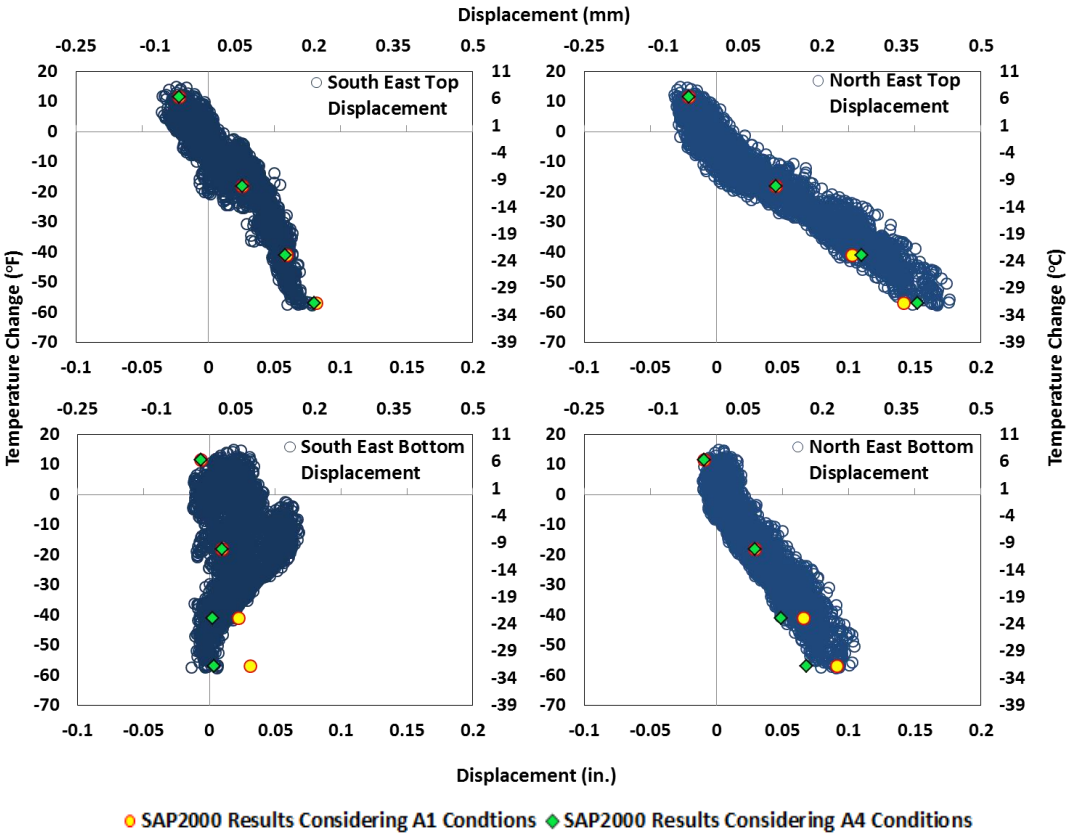

Figure 5-8: Comparison between FE Model Displacement Results of Conditions A1 and A4 with Regards to Field Data

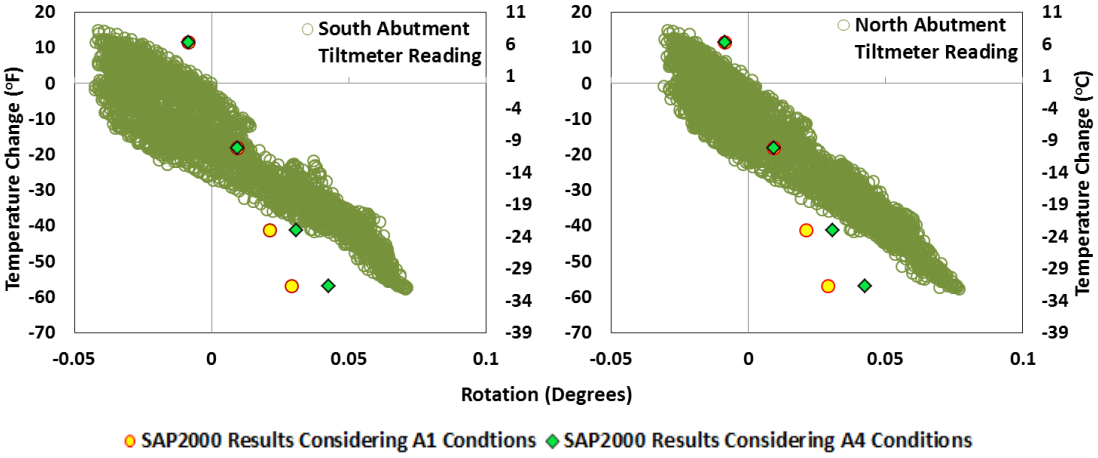

Figure 5-9: Comparison between FE Model Rotation Results of Conditions A1 and A4 with Regards to Field Data

By simulating the increase in stiffness of the top 3 ft (1 m) during the coldest days of the year (change in temperature larger than -41 ^{o}F (-22.8 ^{o}C)), displacement results have improved as it can be seen in most of the plots in Figure 5-8 when compared with the measured displacements that occurred at the bottom of the east side of the south abutment. Moreover, the calculated rotation increased by 20%, becoming 40% less than the measured rotation. The difference in calculated and measured rotations is still large, but the modification to soil condition around the piles improved the results. The fourth soil condition (A4) will therefore be utilized next in the analysis of effects of other parameters to provide better approximation to the actual data. Ultimately, the effect of soil condition can be significant in some cases especially, those involving different soil properties around the piles. The analyses conducted using different soil properties indicate that the assumed properties of soil around the piles is more significant than properties of backfill on the FE results.

5.3.2 Effect of Distribution of Thermal Loads

Figures 3-14 and 3-15 showed that temperature can vary substantially along the transverse direction of the bridge as well as through the depth of the composite beam section. Hence, in order to investigate the effect of temperature distributions in the transverse and vertical directions of the bridge superstructure, temperatures measured by thermistors in the deck and in the beams were used in the FE model to provide a distribution that better represented field conditions. Since frame elements were used to model the beams, it was not possible to apply different temperatures throughout the depth of the beam so the analysis conducted is not truly a thermal gradient analysis. Therefore, only the temperature recorded by thermistors located at the bottom level of strands in each beam was applied as the temperature change in

beams. As a result of this approximation in applying the temperature, beam rotations will likely be smaller than if a thermal gradient were used.

As discussed in Section 5.3.1, MassHighway Bridge Manual 2005 does not consider both the variation of temperature along the transverse direction of the bridge and with the depth of the superstructure. Also, no temperature in the abutments is considered in designing and analyzing IABs. Thus, two methods of applying thermal loads were investigated. In one method the ambient temperatures were applied to the entire bridge superstructure. The second method, on the other hand, involved using different temperatures as recorded in the deck and beams. In this method, temperature was applied on the visible parts of the abutments and wing-walls assuming that the rest of the abutments, which are buried, have no changes in temperature. Since there was no temperature record collected at the abutments but those taken by tiltmeter thermistors, ambient temperature was applied at the visible part of the abutments and wing-walls. The results of the second method model were then compared to the model that considered applying ambient temperature on both the deck and beams. Both models considered same soil conditions (A4), which showed better matching to field data as discussed in the previous section. The thermal expansion coefficient for the superstructure was taken as 5.5×10^{-6}/°F (10×10^{-6} /°C) as recommended in the MassHighway Bridge Manual (2005). Figures 5-10 and 5-11 compare the model abutment displacements and rotations with field data, respectively.

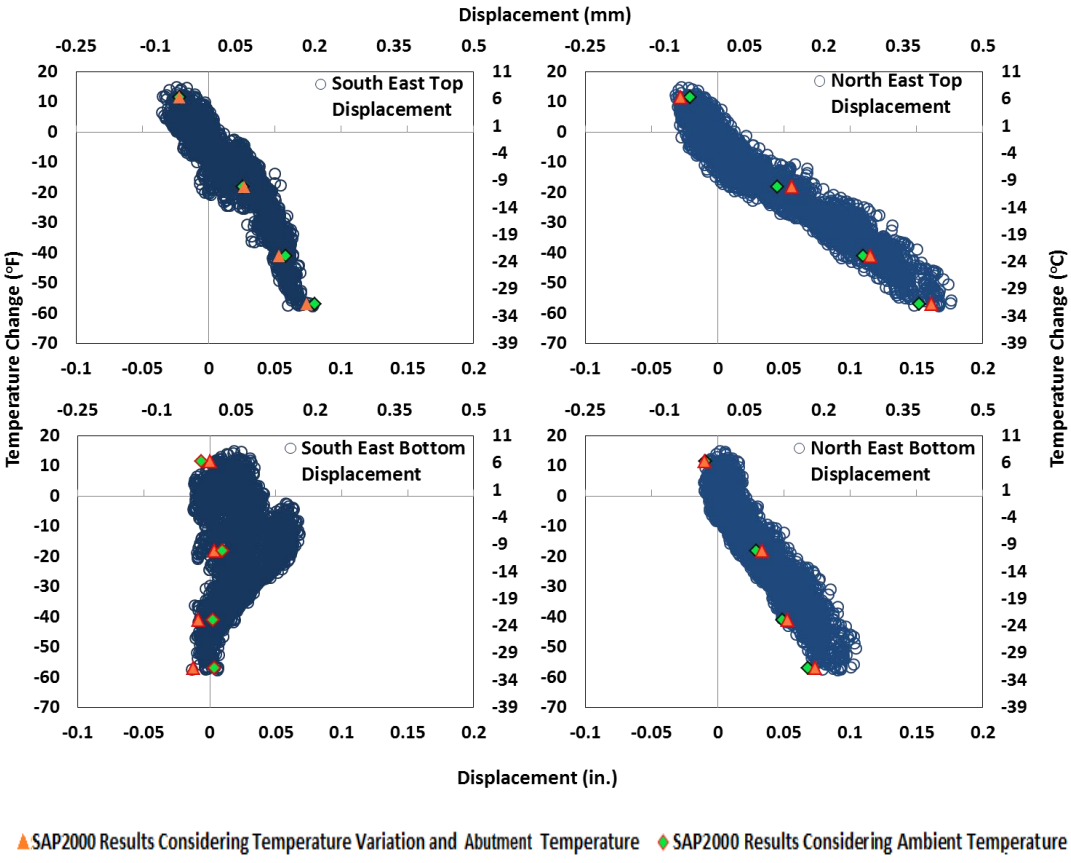

Figure 5-10: Comparison between FE Model Displacement Results due to Different Ways in Applying Thermal Loads

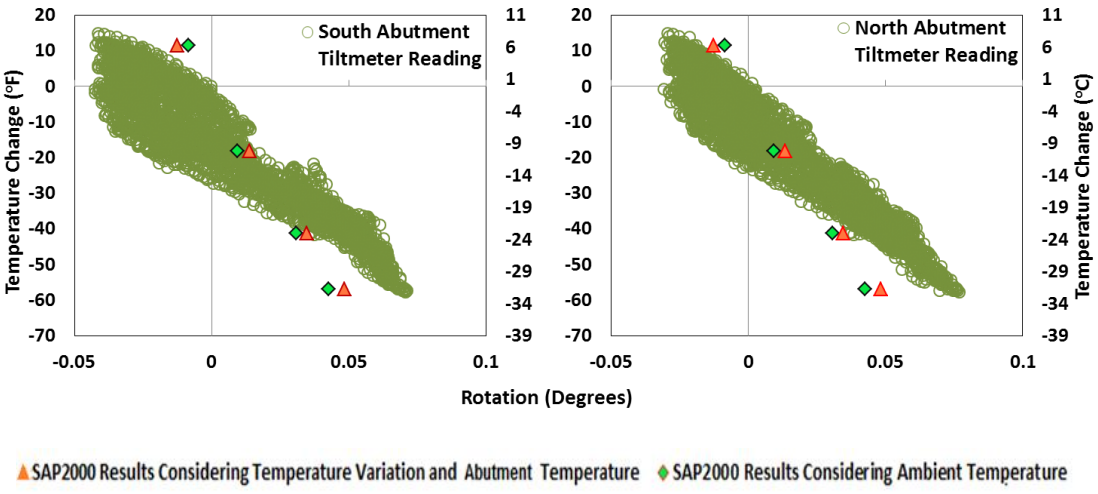

Figure 5-11: Comparison between FE Model Rotation Results due to Different Ways in Applying Thermal Loads

It can be observed that the model that considers the variation of temperature along the transvers direction of the bridge and between deck and beams brought

values of these parameters closer to the rotations and displacements measured in the field. Hence, this model was utilized in investigating other parameters as shown next.

5.3.3 Coefficient of Thermal Expansion Effect

The coefficient of thermal expansion of concrete (α) can vary significantly depending on the type of aggregate used in the mix, water/cement ratio, and relative humidity. According to AASHTO LRFD Bridge Design Specifications (2010) the coefficient of thermal expansion of normal weight concrete can range between 3 to 8 $\mu\varepsilon/°F$ (5.4 to 14.4 $\mu\varepsilon$/°C). This represents a threefold variation in a material constant that directly influences expansion and contraction of the superstructure. Since the thermal expansion coefficient is not typically determined in practice, three different values were utilized in this study to see their effect in matching strain data and calibrating the FE models. The first value considered was the one recommended by MassHighway Bridge Manual (2005), which is 5.5 $\mu\varepsilon/°F$ (10 $\mu\varepsilon/°C$). The second value corresponds to the value recommended in AASHTO LRFD Bridge Design Specifications (2010), which is 6.0 με/°F (10.8 με/°C). The third value was arbitrarily chosen to be high but within the reasonable range of concrete to increase the range of α investigated in this study (6.5 με/°F (11.7 με/°C)). The three values of α were used in the FE models and in the temperature correction applied to readings from each strain gauge.

The anticipated deflection shapes of the bridge during winter and summer are illustrated in Figure 3-28, which suggests that in winter the bottom of the beams are supposed to be in tension and the vice versa in summer. In Figure 5-12, corrected strain data taken near the bottom of one of the beams in the bottom and top strand layers are plotted for the three different assumed values of α. When correcting the data

using the value of α in the Massachusetts Highway Bridge Manual (2005), strain readings near the bottom of the beams were opposite of the anticipated deformed shape of the bridge. During winter, thermal strains near the bottom of the beams are expected to be tensile (positive) and compressive (negative) in summer, yet by using α of value of 5.5 με/°F (10.0 με/°C), compressive strain occurs in the winter and tensile strain in the summer (Figure 5-12(a)).

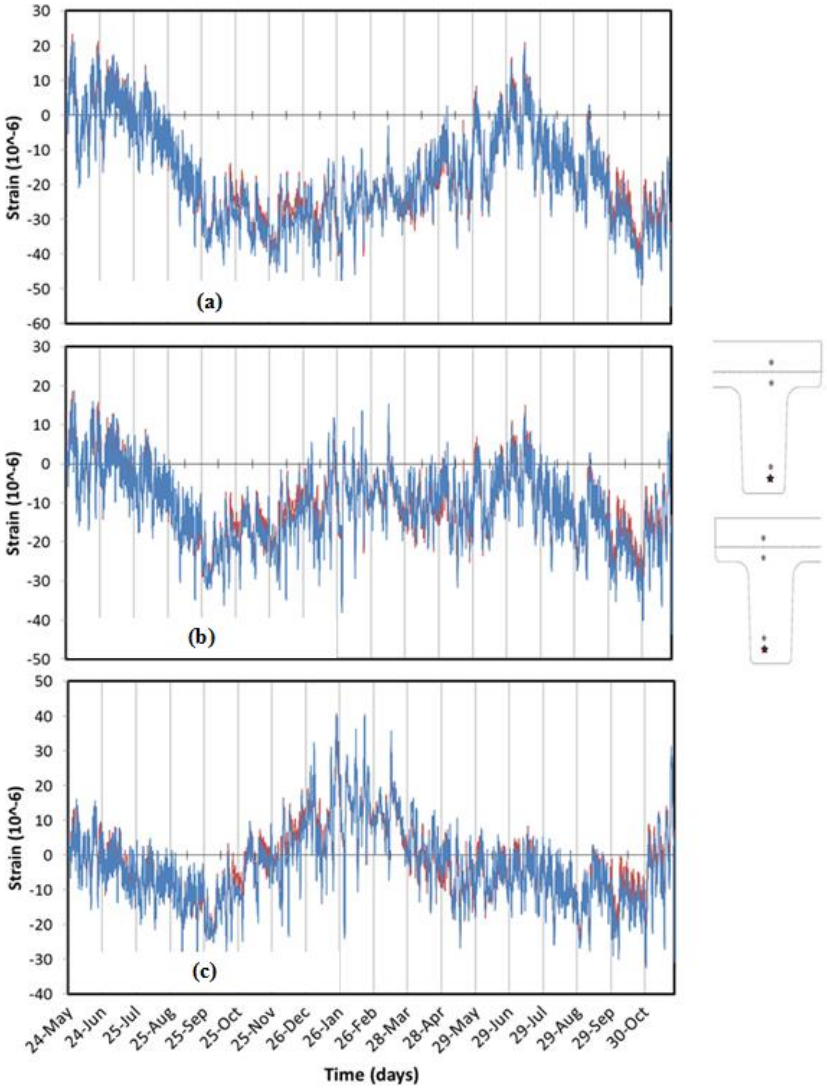

Figure 5-12: Corrected Strain Data by Using Different Values of Thermal Expansion Coefficient (a) 5.5 με/°F (10.0 με/°C) , (b) 6.0 με/°F (10.8 με/°C) , (c) 6.5 με/°F (11.7 με/°C)

When using the value of α in the AASHTO LRFD Specifications, the corrected strain readings near the bottom of the beams in the winter, spring, and part of the summer are negative values indicating compressive strain (Figure 5-12(b)).

The effects of correcting data using the highest assumed value of α are shown in Figure 5-12c. The corrected strain data showed a strong agreement with the deformed shape that corresponds with the rotation and displacement data of the abutments in different seasons (Figure 5-12(c)).

These three values of α were then tested in the FE models in order to determine the value that better matched the measured displacement and rotation response. Figures 5-13 and 5-14 show the comparison of abutment displacement and rotation, determined using the FE models with different α in comparison with measured data. By using the highest value of α equal to 6.5 με/°F (11.7 με/°C), the rotation results get closer to the field data as shown in Figure 5-14. Displacement results, however, showed that depending on the location, the three values can give good results, yet when using 6.5 με/°F (11.7 με/°C), displacement at more than 60% of the locations where results compared has improved. Nevertheless, at 60% of the rest of the locations, displacement results using the third value ((6.5 με/°F (11.7 με/°C)) had shown almost matching slope when compared to the field data slope, but with higher values. It is essential to understand that trying to match rotation results will lead to having some of the displacement results less matching and vice versa. Hence, a decision about how good the results are should take into consideration both results.

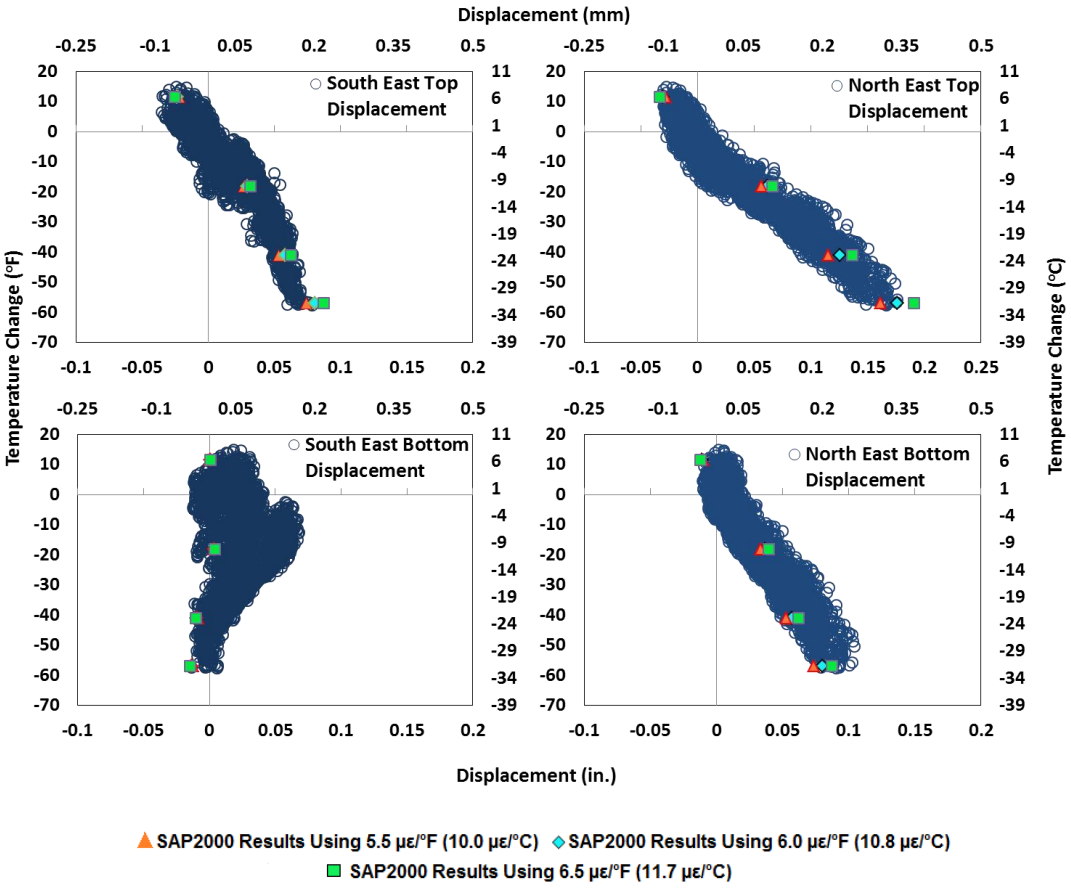

Figure 5-13: Comparison among FE Model Displacement Results due to Using Different Coefficient of Thermal Expansion with Regards to Field Data

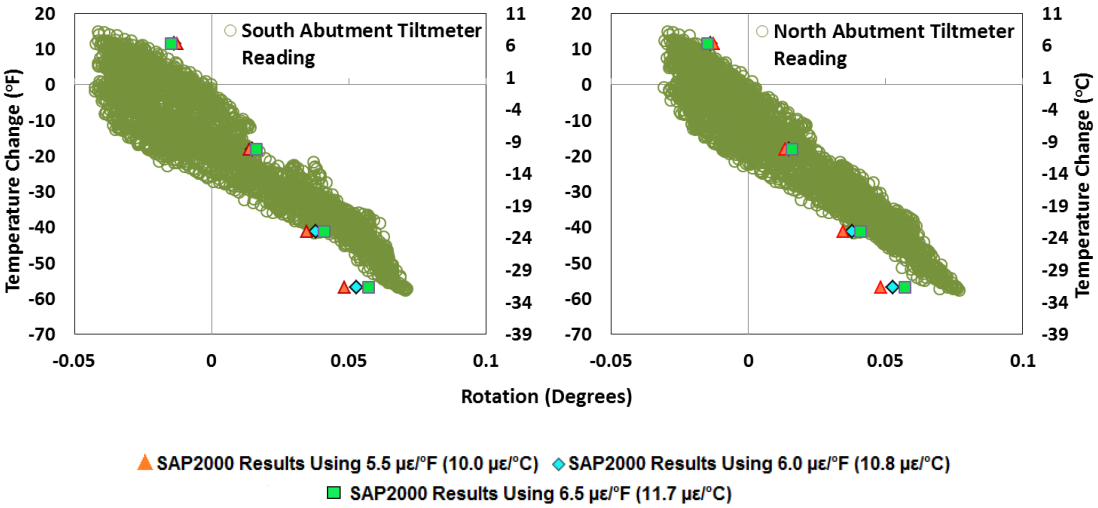

Figure: 5-14: Comparison among FE Model Rotation Results due to Using Different Coefficient of Thermal Expansion with Regards to Field Data

As a result of this investigation, it was concluded that the approximate α value that can be used in correcting strain data is 6.5 με/°F (11.7 με/°C) for this particular bridge. Hence, this value was used to re-correct strain readings for temperature and will be used in all FE models in this research next.

The total difference in calculated response between the initially assumed model and the validated model for year one after including effects of soil properties, application of thermal loading, and coefficient of thermal expansion is illustrated in Figures 5-15 and 5-16.

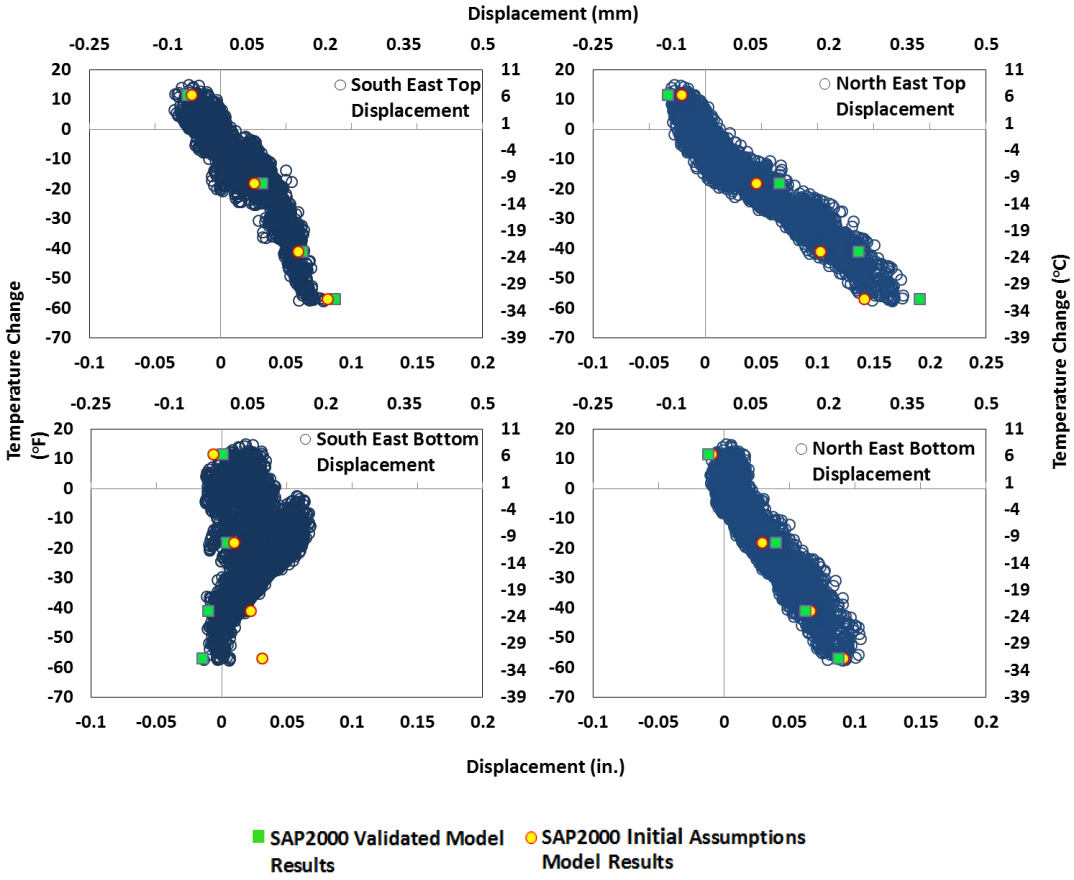

Figure: 5-15: Comparison between Initial Assumptions FE model and the Final Calibrated FE Model Displacement Results with Regards to Field Data

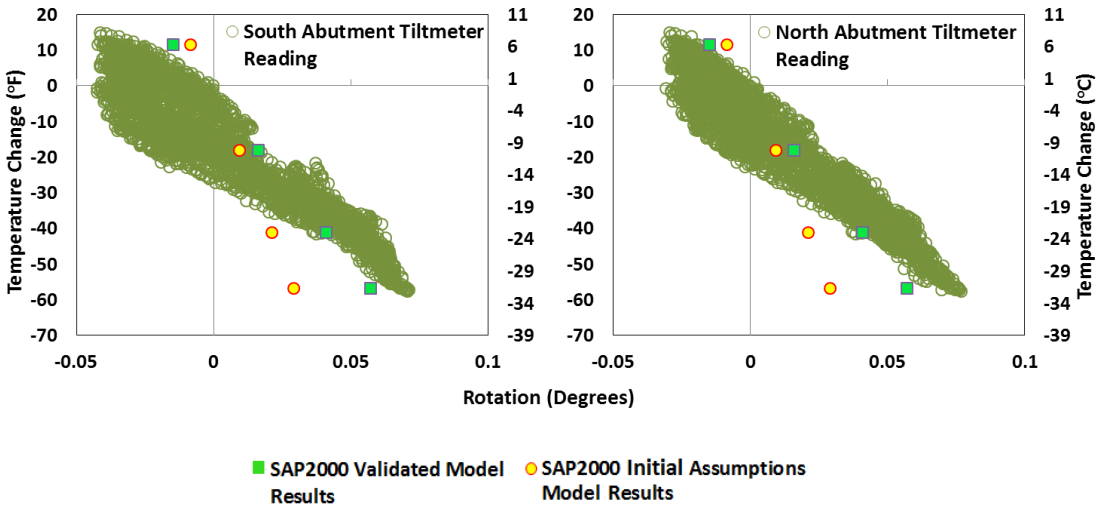

Figure: 5-16: Comparison between Initial Assumptions FE Model and the Final Calibrated FE Model Rotation Results with Regards to Field Data

Displacement results improved in value and trend at most of the abutment locations where results were reported and compared. Abutment rotation results have improved significantly. In Figure 5-16, the rotation increased to more than twice of the value calculated from the initial model. However, the slope of the data trend still does not match. The parameter evaluation study presented here highlights the importance and influence that these parameters have on the response of this type of IAB. The results presented here, however, are limited to this particular bridge for the site, construction, and seasonal conditions that were encountered during the first year of monitoring. These results cannot be extrapolated to other bridges with different conditions than those studied in this project.

5.4 Year Two Model Validation

Year two model validation was conducted after investigating all the parameters that affect the FE model results. In this validation, different soil conditions were utilized to reach a better approximation to field data. The purpose of having a validated model for year two was to determine the possibility of having any changes in soil properties, and to investigate if these changes led to the differences in

displacement and rotation values recorded in year two from those obtained in year one. These observed changes from year one to year two were discussed in Sections 3.5.2 and 3.5.3, and Figures 3-24, 3-25 and 3-28, in displacement and rotation experienced by the abutments. The same initial values and modeling conditions as used in the validated model for year 1 were used initially for year 2. Thermal loading was applied by considering temperature changes applied on the visible parts of abutments and wing-walls, frozen soil condition in the top of the piles was considered, and a coefficient of thermal expansion (α) equal to 6.5 με/°F (11.7 με/°C) was used. The soil conditions investigated in validating year two model are shown in Table 5-5 below.

Table 5-5: Soil Conditions Investigated in Validating Year Two FE Model

Soil Condition		Description *
A1-Y2	Behind the abutments	Similar to soil condition A1 Table 5-3
	Around the Piles	Similar to soil condition A1 Table 5-3
A2-Y2	Behind the abutments	Similar to soil condition A2 Table 5-3
	Around the Piles	Similar to soil condition A2 Table 5-3
A3-Y2	Behind the abutments	Similar to soil condition A2 Table 5-3
	Around the Piles	Medium-dense soil properties assumed along the piles length
*** For the soil behind the abutments density details, see Section 4.5** *** For the soil around the piles density details, see Table 4-3**		

The first soil condition (A1-Y1 Table 5-5) was assumed to investigate the ability of using the same model for different years. Second soil condition (A2-Y1 Table 5-5) was assumed to see whether the soil became looser than what it is used to in year 1. Third soil condition utilized in validating year two model considered the changes in rotation and displacement that took place as discussed in Sections 3.5.2 and 3.5.3 as the rotation in year two summer has increased as well as displacement in

during the winter and summer of year two. Due to the fact that the density of the soil around piles plays an essential role in affecting rotation results as proven in the parametric study presented previously, soil around piles were assumed to have medium-dense properties since the stiffer the soil is the larger rotation would be captured.

Figures 5-17 and 5-18 show a comparison between results of the three models with the measured field data. In these figures, A1-Y2, A2-Y2, A3-Y2 represent the three soil conditions discussed previously in this section. Temperature variation along the depth of the superstructure and the transverse direction of the bridge was applied on the three models. The temperatures were taken from the readings of the deck and girders thermistors in in year two.

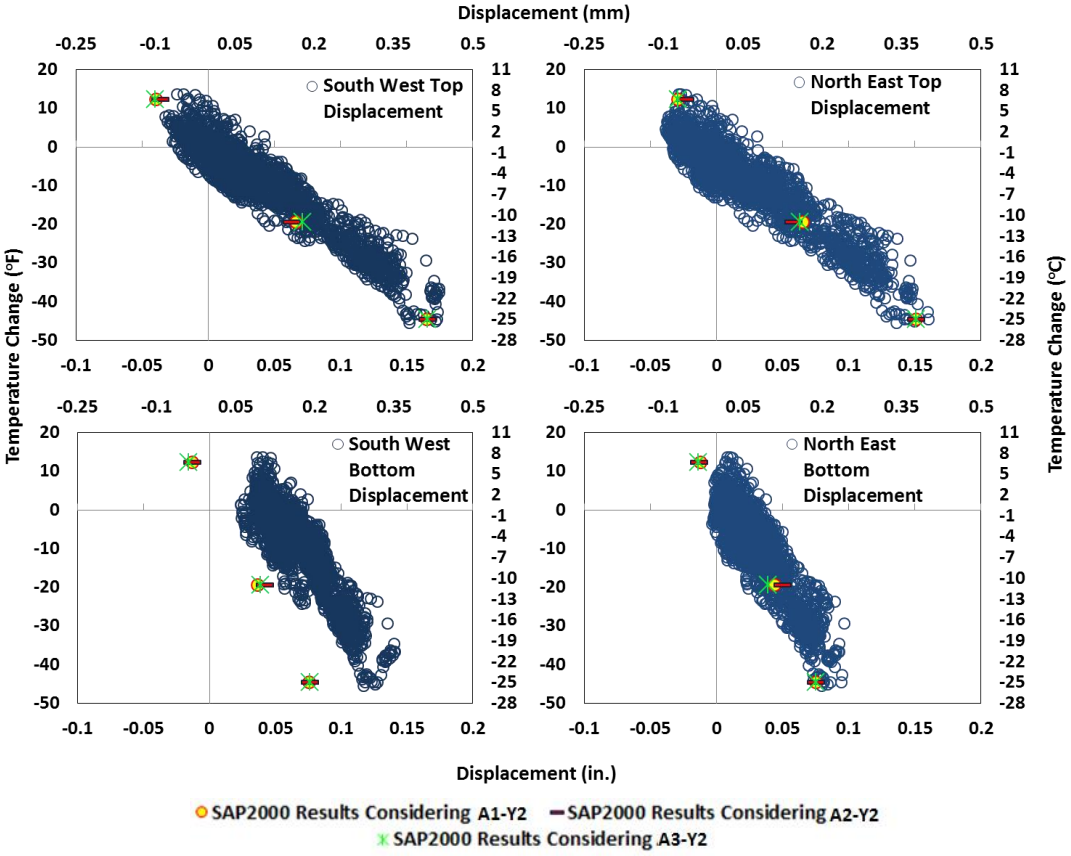

Figure: 5-17: Comparison among FE Model Displacement Results with Different Soil Conditions

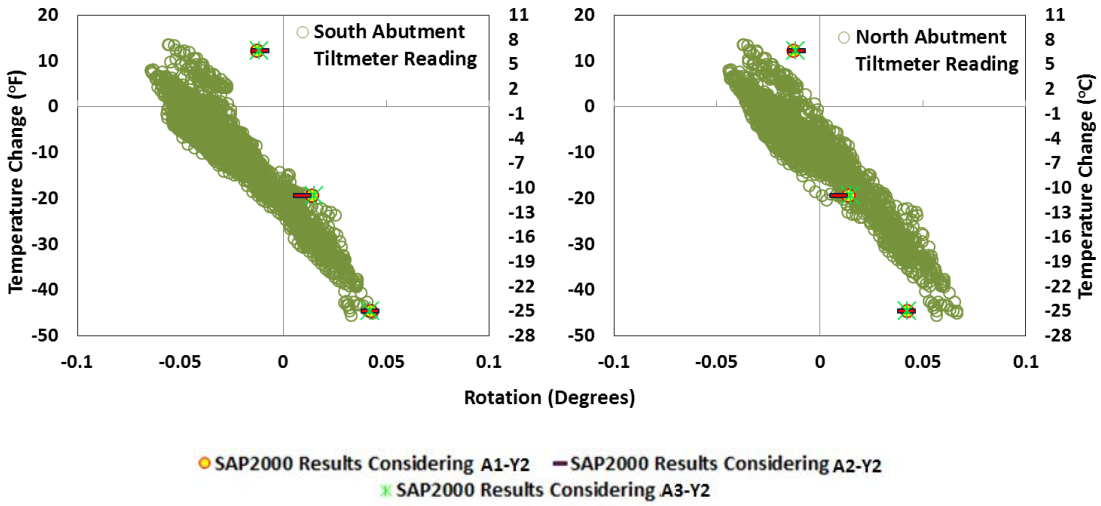

Figure: 5-18: Comparison of FE Model Rotation Results with Different Soil Conditions

Displacement results showed good agreement with field data. Even though these results were lower at the bottom of the west side of the south abutment than field data, the slope of them matched and, therefore, the general data trend matches well. The most important observation here is that all soil conditions resulted in almost the same values and gave similar trends (slope). Rotation results showed a better agreement with north tiltmeter readings, yet the results were lower than measured when temperature decrease and increase. Rotation results did not agree as well with south abutment tiltmeter readings in the summer. This could indicate the possibility of having a permanent rotation took place toward the backfill when the temperature increased. On the other hand, when applying decrease in temperature the results matched field data.

Data loggers stopped collecting data at the beginning of winter in year two. It could be possible that the soil around the top few feet of the piles had not yet frozen even though the ambient temperatures at that time were below freezing. Hence, another analysis was run for each soil condition without increasing the top soil stiffness to simulate unfrozen conditions. Figures 5-19 and 5-20 show the comparison of displacement and rotation results assuming that soil at top of piles had not frozen.

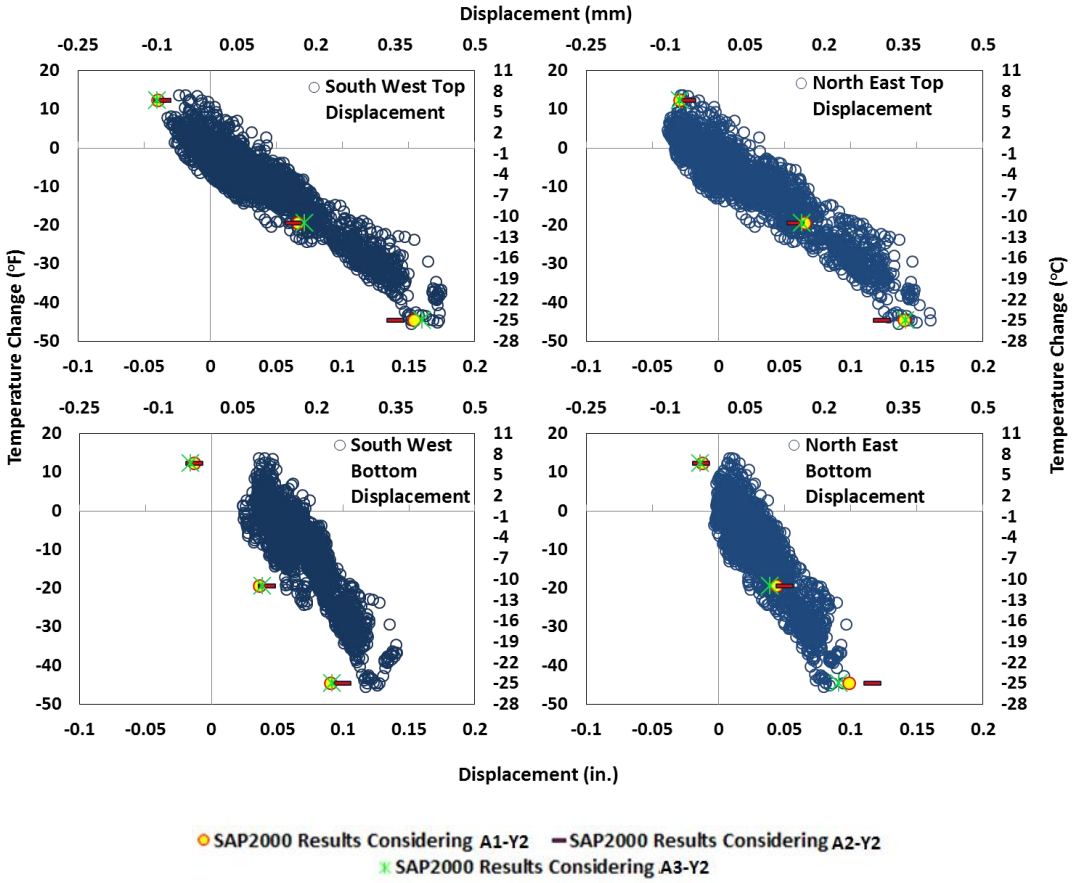

Figure: 5-19: Comparison of FE Model Displacement Results with Different Soil Conditions and Field Data – Unfrozen Soil

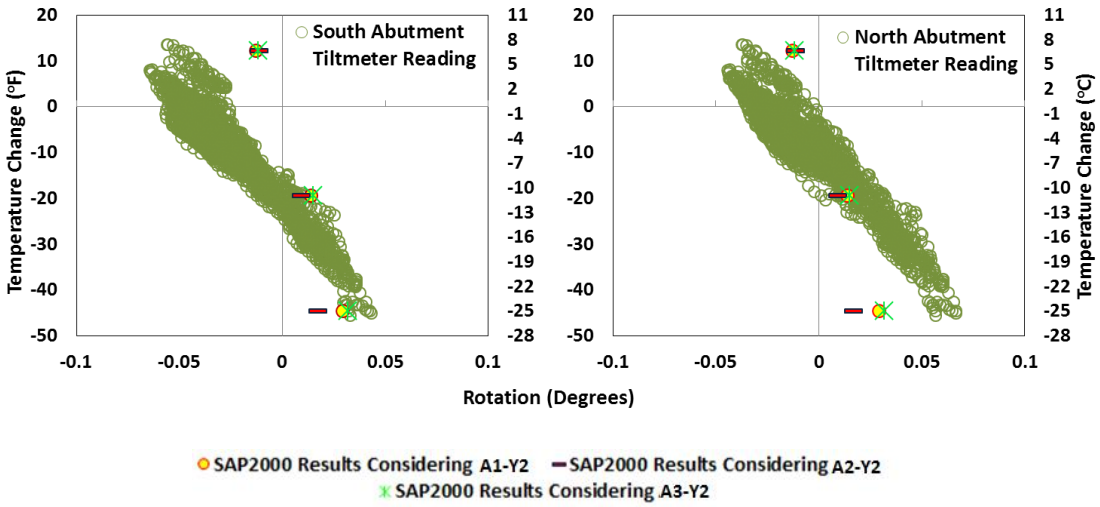

Figure: 5-20: Comparison of FE Model Rotation Results with Different Soil Conditions and Field Data – Unfrozen Soil

As shown in Figure 5-19, soil conditions A1-Y2 and A3-Y2 agreed reasonably with displacement data measured in the field. Similar to the displacement results, rotation values (Figure 5-20) calculated assuming A2-Y2 properties were the farthest from the measured data, it seems appropriate to assume the same soil conditions for both years in this case despite the observed differences in field data.

Displacement and rotation results of A1-Y2 model was utilized to establish the comparison between results of the two models, one considers freezing one does not. Figure 5-21and 5-22 show comparison between displacement and rotation results of these two cases, respectively.

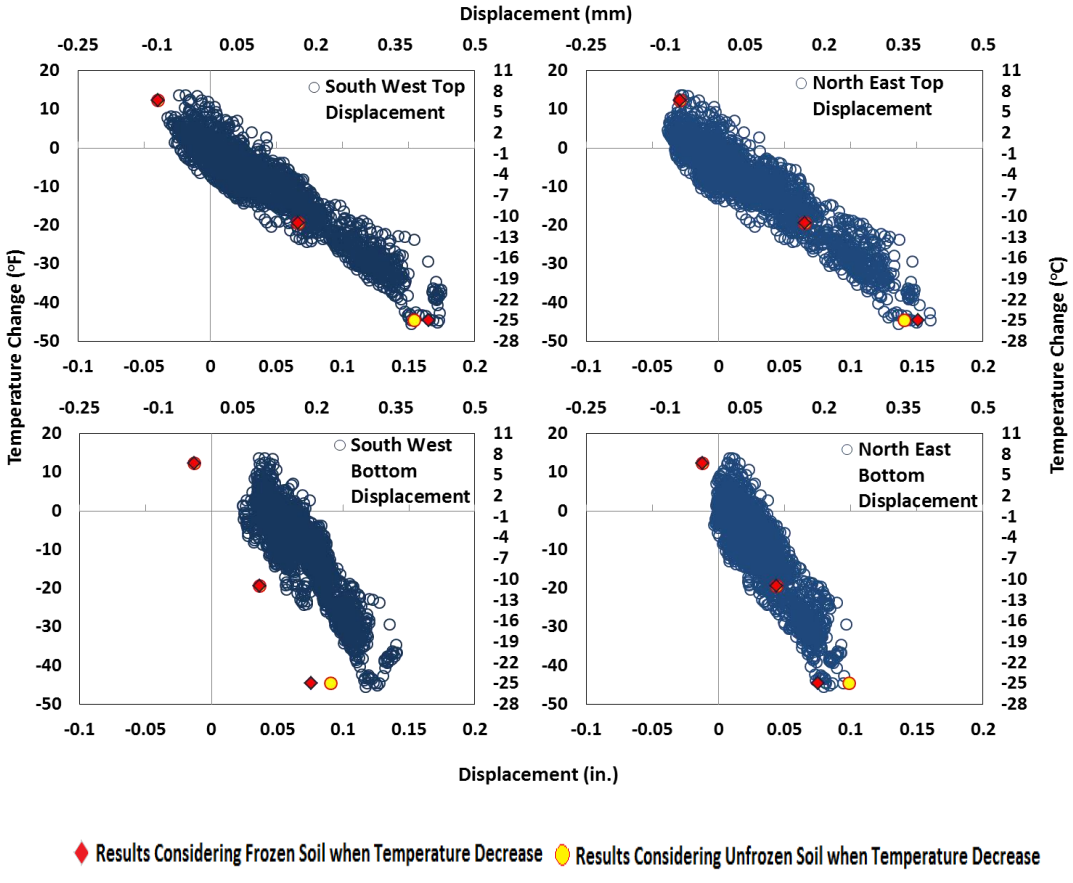

Figure: 5-21: Comparison between Displacements of FE Models Considering Two Top-of-Pile Soil Conditions: Frozen and Unfrozen

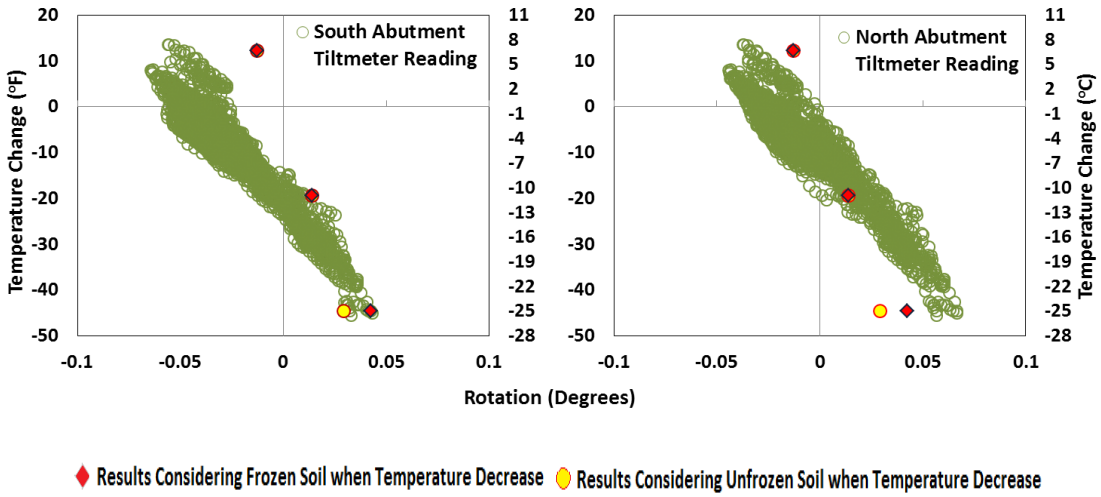

Figure: 5-22: Comparison between Rotation Results of Two FE Models One Considers Frozen Soil Condition in Winter and The Other Does not with Regards to Field Data

Displacement results of both cases were acceptable in general except at the acute corner of the north abutment as shown in Appendix D. The results at the acute corner when considering top-of-pile frozen soil resulted in a completely different trend from measured values. On the other hand, rotation results considering frozen soil condition at the very beginning of winter, at which the decrease in temperature was about -45 ^{o}F (-25 ^{o}C), were better matching field data.

Ultimately, there might be several effects other than soil conditions that lead to greater rotation at the south abutment than anticipated when temperature increased in year 2. In general, year one soil conditions could be assumed for year two as well. This indicates that the softer soil at one side of the abutment could be due to construction effects such as different soil compaction in phase 1 than phase 2 rather than loosening due to re-loading of soil as explained before.

5.5 Summary

In this chapter, FE model validation was presented. This validation was conducted for two periods: short-term and long-term performance. Short term performance was captured by matching the FE model results with live load test records. As a result, a soil condition that best reflected the measured data was chosen for initial calibration of the long-term models.

Variation of key parameters that affect the bridge response in the long-term was then conducted. The long-term validation of the model was done by fixing each parameter to the value that resulted in better results before proceeding to investigate the effect of other parameters. Different soil conditions were considered including the possibility of soil around the top 3 ft (1 m) of the piles frozen during winter. This was found to be a valid theory as rotation and displacement FE results better reflected the measured performance. The effect of thermal loading application procedure on the structure was also investigated. It was found that considering differences in thermal loading in deck and beams, and accounting for differences in temperatures in the transverse direction of the bridge led to better estimates of the bridge response. The effect of an appropriate value for the coefficient of thermal expansion (α) of concrete was also investigated by using three different values. The effect of α on strain data was first investigated. It was found that different values of α result in completely different strain readings when used in correcting raw strain data and, as a result, a completely different deformed shape of the bridge. FE model displacement and rotation results using different values of α were reported and compared with field data. Depending on FE results and strain data, the value of α was chosen to be the best that represents the actual bridge behavior. Since it is not customary to report α for the concretes used in bridge construction, different analyses using reasonable variations

from design values may be useful during design to ensure that the models reflect the anticipated deformed shape of the superstructure under different loading conditions.

Year two model validation was also discussed in this chapter. The validation of year two is limited from the summer to fall seasons because of a data logger failure in early winter. The primary purpose of validating the FE model with regards to year two field data was to investigate whether soil properties changed as a result of thermal cycling. It was concluded that it could be appropriate to assume the same soil conditions used for year one. It should be emphasized, however, that the data for year two is limited to two seasons. Monitoring the performance of this bridge for a longer period may result in different conclusions about soil behavior and changes in its properties, but at the same time, it is believed that there might be other factors that have not been considered in the parametric study herein may need further study such as considering the effect of creep and shrinkage.

CHAPTER 6

EFFECT OF PILE ORIENTATION ON CALCULATED RESPONSE OF THE BRIMFIELD BRIDGE

6.1 Introduction

The orientation of piles has an essential role on the way IABs behave. Abutment displacement, rotation, stresses developed in beams, and moments in piles vary because of pile orientation, particularly those IABs with long span or high skew angle. Most of the states including Massachusetts suggest orienting abutment piles to minimize rotational restraint with the pile web parallel to the abutment center axis line regardless of skew, whereas several Midwestern states suggest orientation in the other direction. Few studies have addressed the best orientation that could be used for IABs. However, the recommendations were not always the same. For instance, Najib et al. 2010, investigated the best pile orientation that could be utilized in a 2 span 200 ft (61 m) 60^o degree skewed IA bridge. The superstructure of the examined bridge consists of steel beams and concrete deck. The authors found that orienting the piles with their weak axis perpendicular to the bridge centerline will yield in less stress in piles. A recent research by Olson et al. (2013) showed that the best orientation for a 2 span 200 ft (61 m) 40^o skewed IAB with a superstructure consists of steel beams and concrete deck is pile weak axis parallel to the bridge centerline. Thus, it was essential to investigate the best orientation in relatively short span bridge with less skew angle and stiffer superstructure.

In this chapter, results from an investigation utilizing the calibrated model will be discussed in order to determine the effects on pile orientation on several response parameters including abutment displacement, rotation, and moment in piles.

The investigation considered four different pile orientations under the action of dead loads and thermal load as described in Section 5.3.2 and shown in Figures 6-1 and 6-2. These four orientations are described in Table 6-1 whereas Figure 6-3 shows the four considered pile orientations.

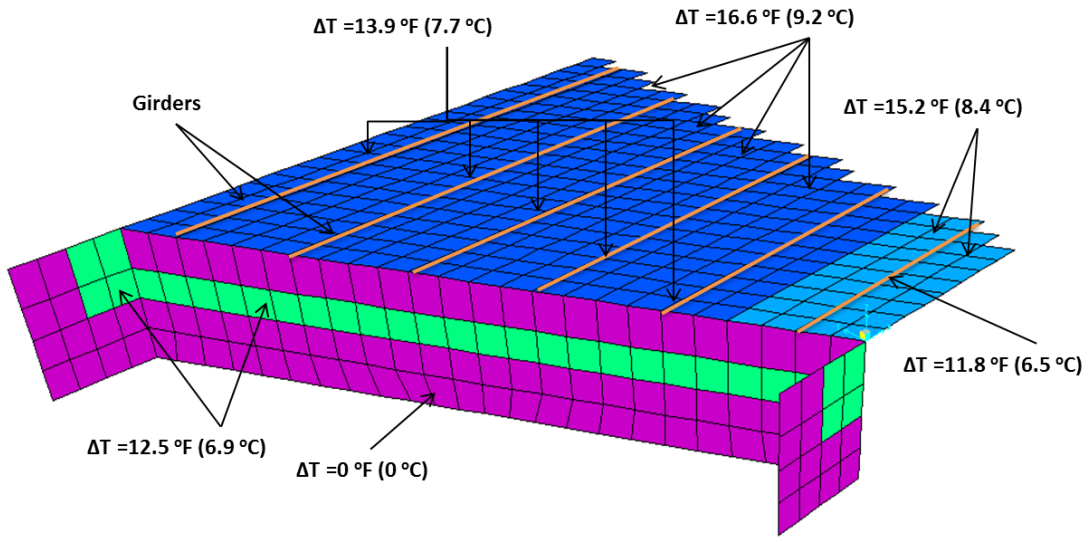

Figure 6-1: Temperature Increase Applied on the Model

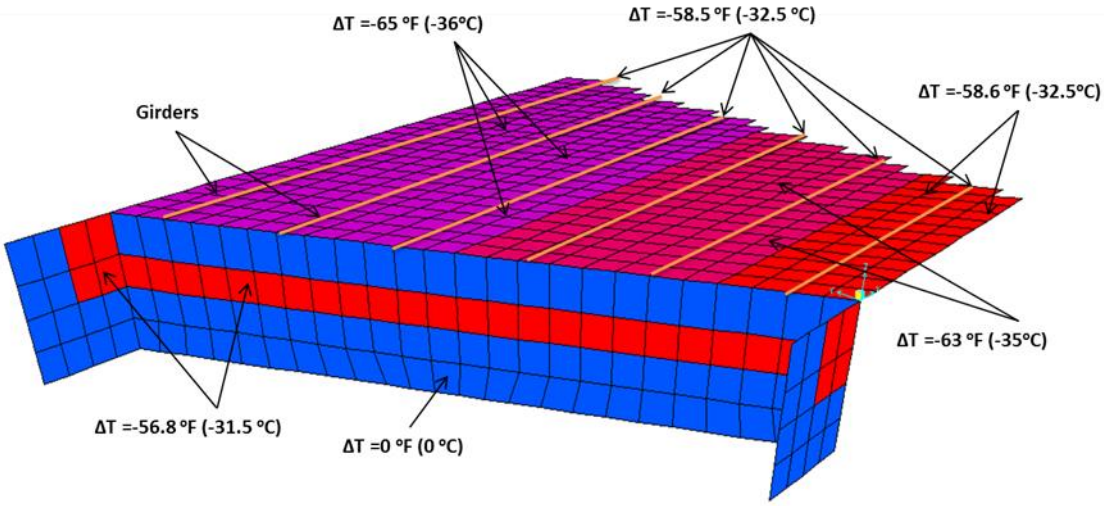

Figure 6-1: Temperature Decrease Applied on the Model

Table 6-1: Pile Orientations Analyzed

Orientation	Description
A	Pile web parallel to the abutment centerline
B	Pile web perpendicular to the abutment centerline
C	Pile web perpendicular to the road alignment
D	Pile web parallel to the road alignment

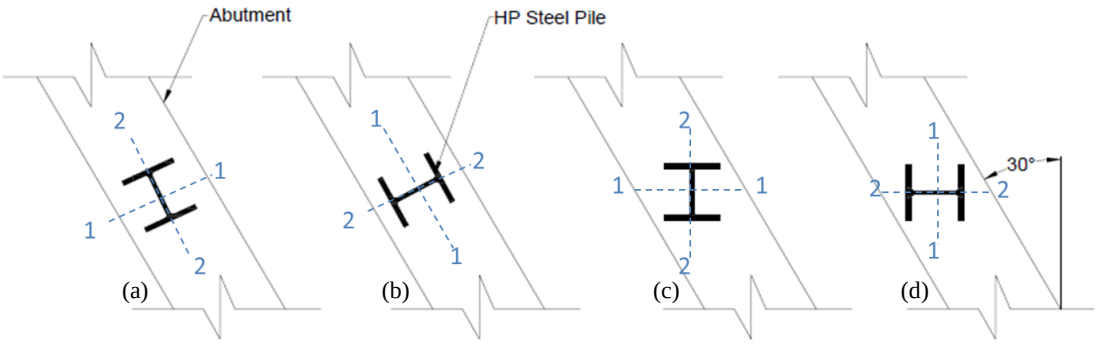

Figure 6-3: Pile Orientations Considered (a) Pile Web Parallel to Abutment centerline (b) Pile Web Perpendicular to Abutment centerline (c) Pile Web Perpendicular to Road Alignment (d) Pile Web Parallel to Road Alignment

6.2 Effect of Pile Orientation on Abutment Displacement

Orienting the piles as shown in Figure 6-3(b) and (d) provides higher rotational restraint than orienting piles as shown in Figure 6-3(a) and (c). However, the differences in displacement (translation and rotation) due to these four orientation patterns might not be as high when an IAB has a short span and/or small to moderate skew angle. Abutment displacements are largely governed by substructure stiffness and the length of the bridge because, for a given temperature change and coefficient of thermal expansion, the change in length of the superstructure is directly proportional to bridge length. Nevertheless, different transportation agencies have preferences on pile orientation regardless of bridge length and skew, to it was considered important to investigate the effect of pile orientation on displacement of the Brimfield Bridge to provide data that can be considered in future designs for

bridges similar to the Brimfield Bridge. Abutment displacement results obtained for each studied pile orientation were compared and discussed for the top and bottom of the acute and obtuse corners of the south abutment. Results of the north abutment displacements, which were not significantly different than those in the south abutment, are shown in Appendix E. Figures 6-4 and 6-5 show comparisons of longitudinal displacements of the south abutments from FE models of the Brimfield Bridge that incorporated different pile orientations. The results include dead loads and thermal changes. The temperature increase and decrease applied to the models were considered to vary along the transverse direction of the bridge and the depth of the superstructure and were the same as those applied in validating the model (Figures 6-1 and 6-2). Due to construction sequence of the bridge, beams and deck self-weights were calculated and added as a concentrated load on the abutment. Then, wearing surface, sidewalk, railing loads, and abutments weight were applied to the model. It should be noted that all loads applied on the model are not factored so that the actual behavior is captured.

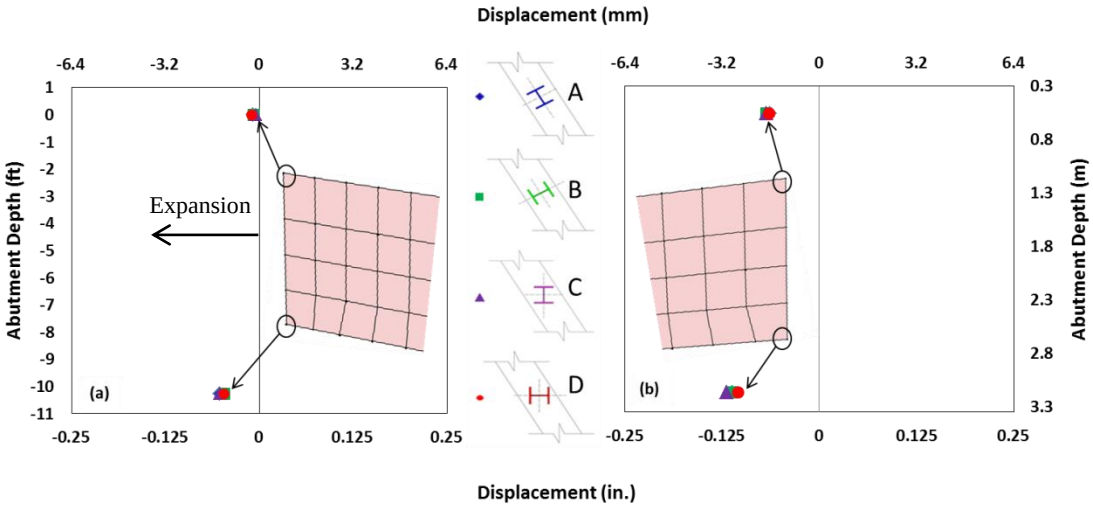

Figure 6-4: Longitudinal Abutment Displacements from Different Pile Orientations: Temperature Increase and Dead Load (a) Obtuse Corner (b) Acute Corner (South Abutment)

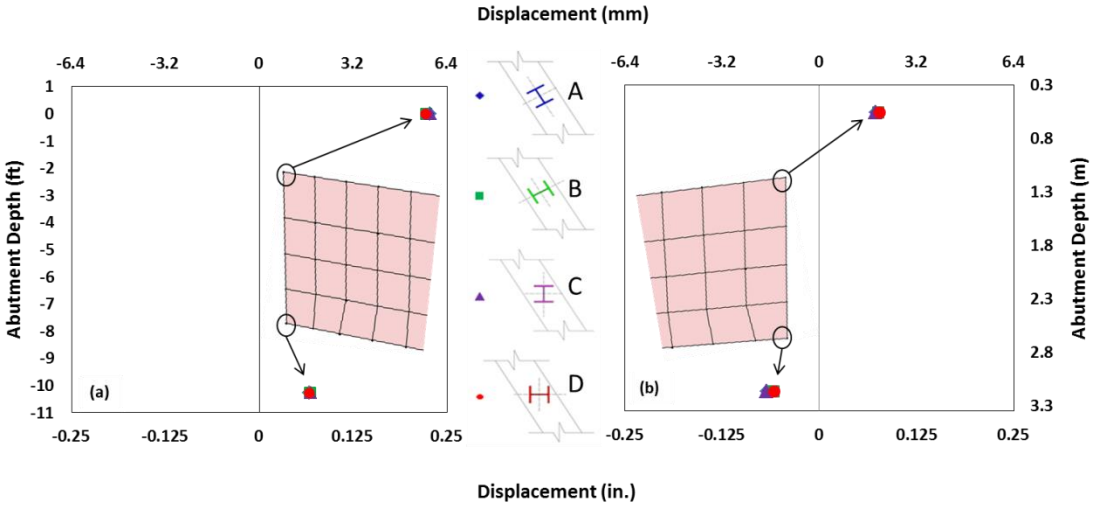

Figure 6-5: Longitudinal Abutment Displacements from Different Pile Orientations: Temperature Decrease and Dead Load (a) Obtuse Corner (b) Acute Corner (South Abutment)

Differences in longitudinal displacements of the abutments for the different pile orientations are hardly noticeable in Figures 6-4 and 6-5. One can conclude that in this case (Brimfield Bridge) the pile orientation does not affect the magnitude of displacements calculated at top and bottom of the abutments. However, this result would not extend to the moment demand in the piles caused by dead and thermal loading. The transverse displacements of the south abutment were also studied as shown in Figures 6-6 and 6-7. In these figures, the transverse displacement of the abutment is also not affected significantly by pile orientation. This confirms that the bridge movement in both directions is not controlled by pile orientation but rather the abutments conform to the displacements needed to accommodate the thermal load applied to the superstructure.

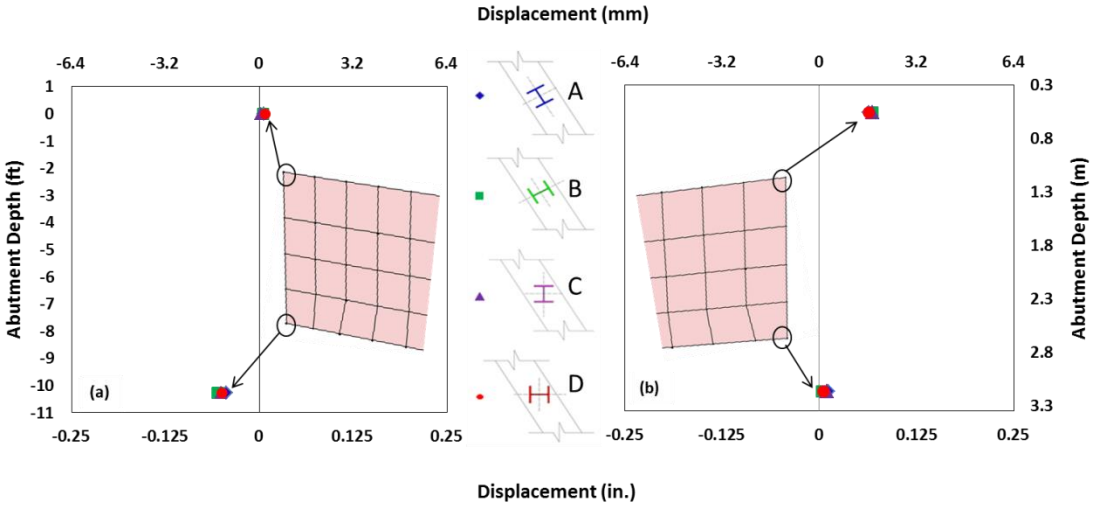

Figure 6-6: Transverse Abutment Displacements from Different Pile Orientations: Temperature Increase and Dead Load (a) Obtuse Corner (b) Acute Corner (South Abutment)

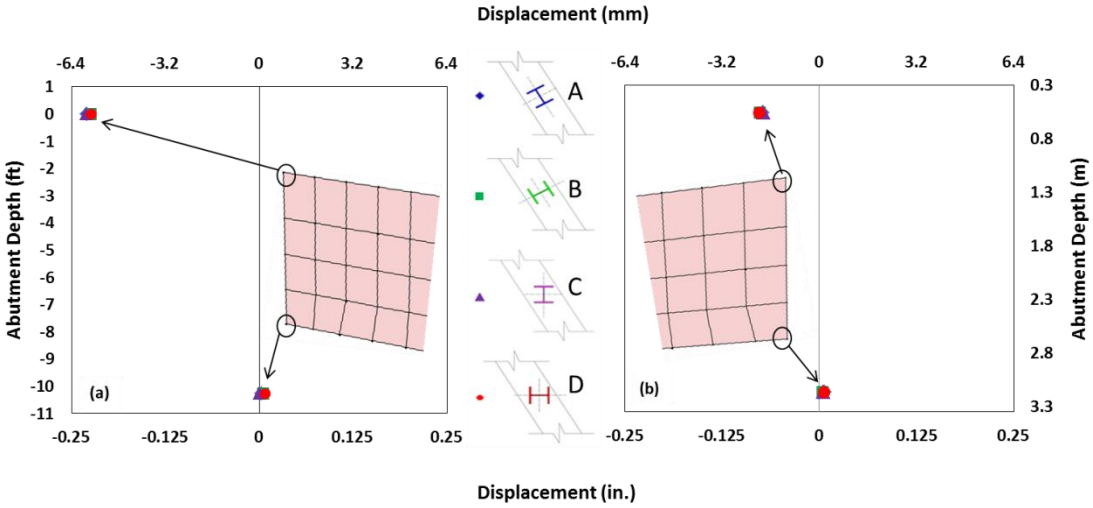

Figure 6-7: Transverse Abutment Displacements from Different Pile Orientations: Temperature Decrease and Dead Load (a) Obtuse Corner (b) Acute Corner (South Abutment)

6.3 Effect of Pile Orientation on Abutment Rotation

Although abutment rotation is not typically taken into account in the design of IABs, abutment rotations resulting from different pile orientations when applying same loading as in Section 6.2 were compared. Pile orientation has been identified as a parameter influencing abutment rotation to a larger extent than abutment displacement given that moment of inertia of piles ties directly to rotational restraint at the base of abutments. Figure 6-8 compares the rotations resulting from the four pile orientations reported at the south and north abutments.

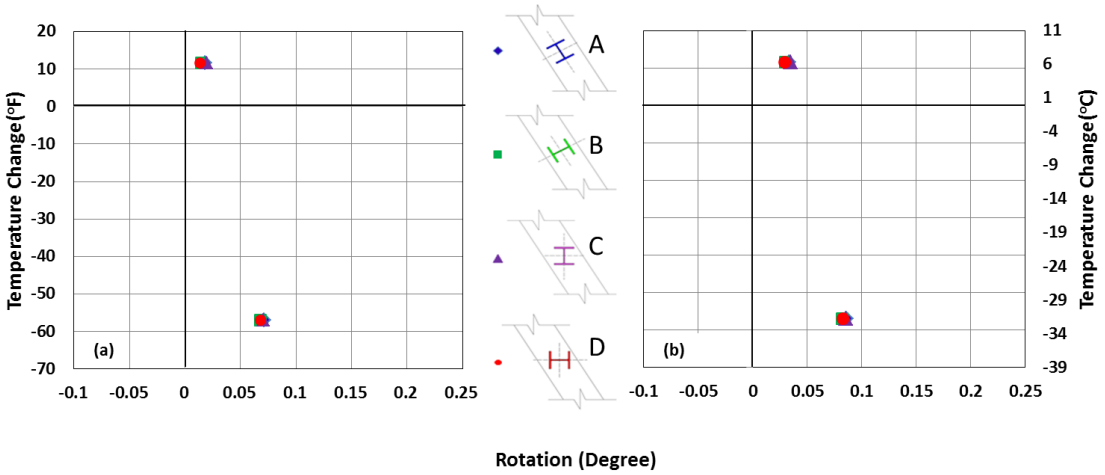

Figure 6-8: Rotation Results Due to Different Pile Orientation (a) South Abutment (b) North Abutment

Similar to displacement, rotation results of different pile orientations showed no noticeable variation in the Brimfield Bridge model. These results are in agreement with the nearly identical displacement values determined at top and bottom of the abutments as discussed before. A significant change in rotation as a result of pile orientation would cause the displacement at the bottom of abutments to change, since the imposed thermal deformation occurs at the abutment top. It is worth noticing that the rotation results here are positive when applying either a decrease or an increase in temperature. This is caused by the deformation imposed when applying dead loads to the model prior to application of thermal loading. Dead loads cause an inward rotation of the abutments that is not overcome by the magnitude of positive temperature change applied.

6.4 Effect of Pile Orientation on Pile Moments

Pile orientation plays an essential role in moment magnitude along piles. Due to having almost equal displacement and rotation values with different pile orientations, moments in piles will likely vary significantly because of changes in flexural stiffness. Comparison of pile moments were first conducted by computing

moments about axes oriented longitudinally (1-1) and transversely (2-2) relative to the abutment axes. These axes corresponded to the principal pile axes in two of the four configurations studied (A and B); for the other two configurations (C and D) the moments are computed about axes that are at 30 degrees from the pile principal axes (Figure 6-9). The moment about these axes is not to be used for design purposes but rather it is a quantitative description of the rotational restrain at the bottom of abutment. Figure 6-9 also illustrates the positive moment convention used to report pile moments.

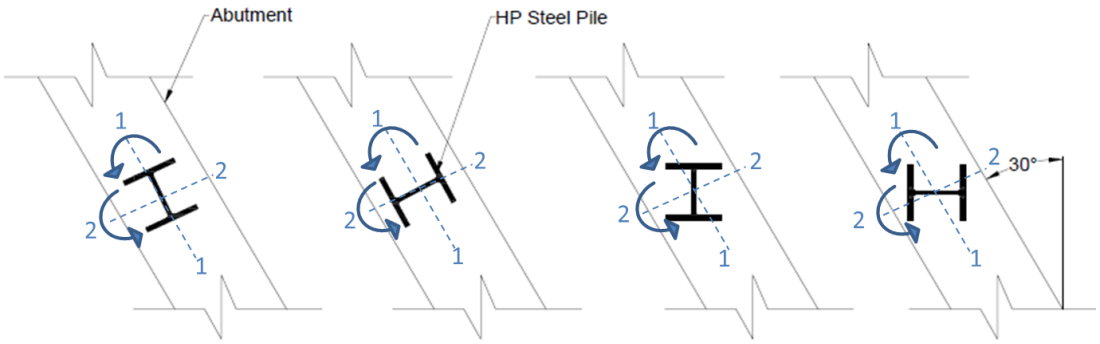

Figure 6-9: Calculated Moments About Abutment Axes

Figures 6-10 to 6-11 show the moment results about axis 1-1 when applying dead loads and increase in temperature. Figures 6-13 to 6-15 show pile moments about axis 1-1 that result from applying dead loads and decrease in temperature. In these figures, the moment results were plotted along the top 20 ft (6 m) of pile because moments below this position approach zero. These figures present the moments in piles supporting the south abutment only. Similar plots are given for the north abutment in Appendix E. Piles were numbered in these figures starting from the west side of the abutment, that is the exterior pile on the west side is Pile 1 and Pile 6 corresponds to the easternmost pile.

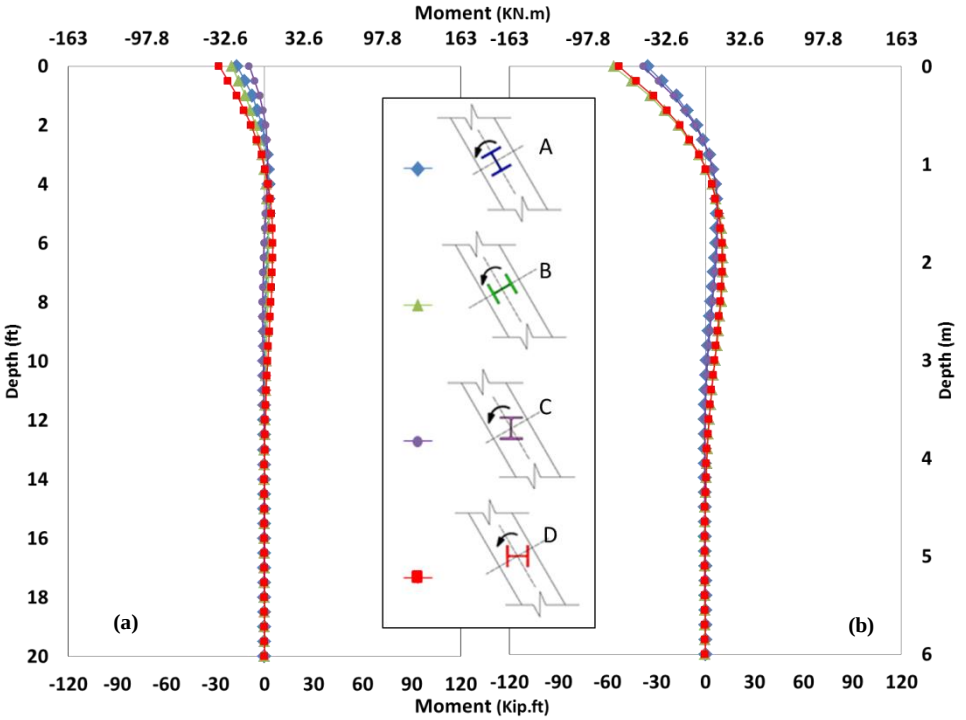

Figure 6-10: Moments in the Exterior Piles about 1-1 Due to Dead Load and Increase in Temperature (a) Pile 1 (b) Pile 6 (South Abutment)

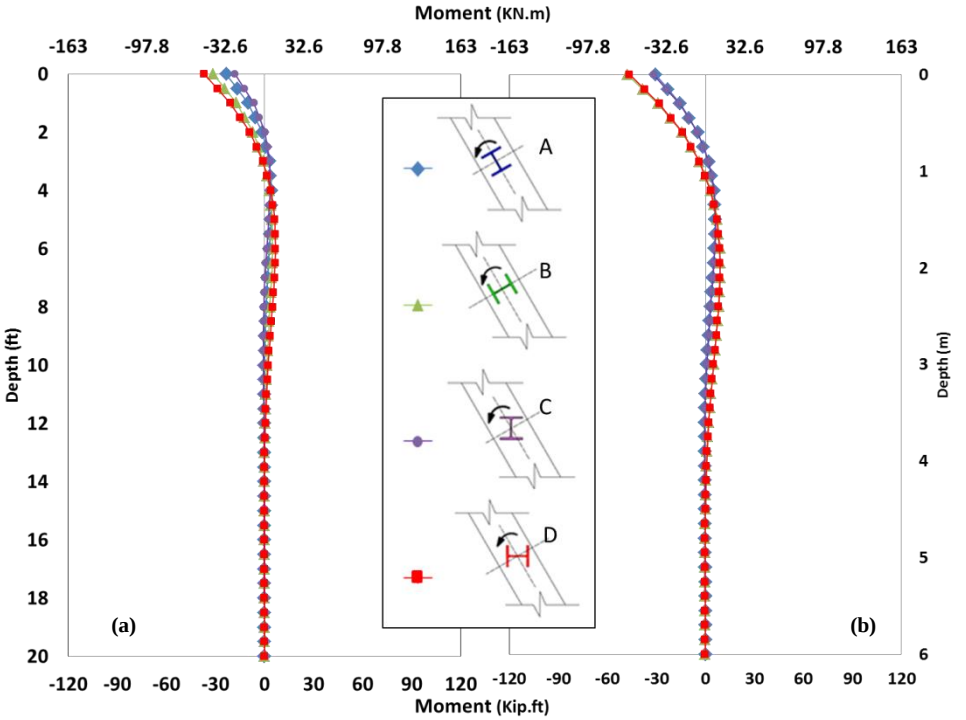

Figure 6-11: Moments in the Interior Piles about 1-1 Due to Dead Load and Increase in Temperature (a) Pile 2 (b) Pile 5 (South Abutment)

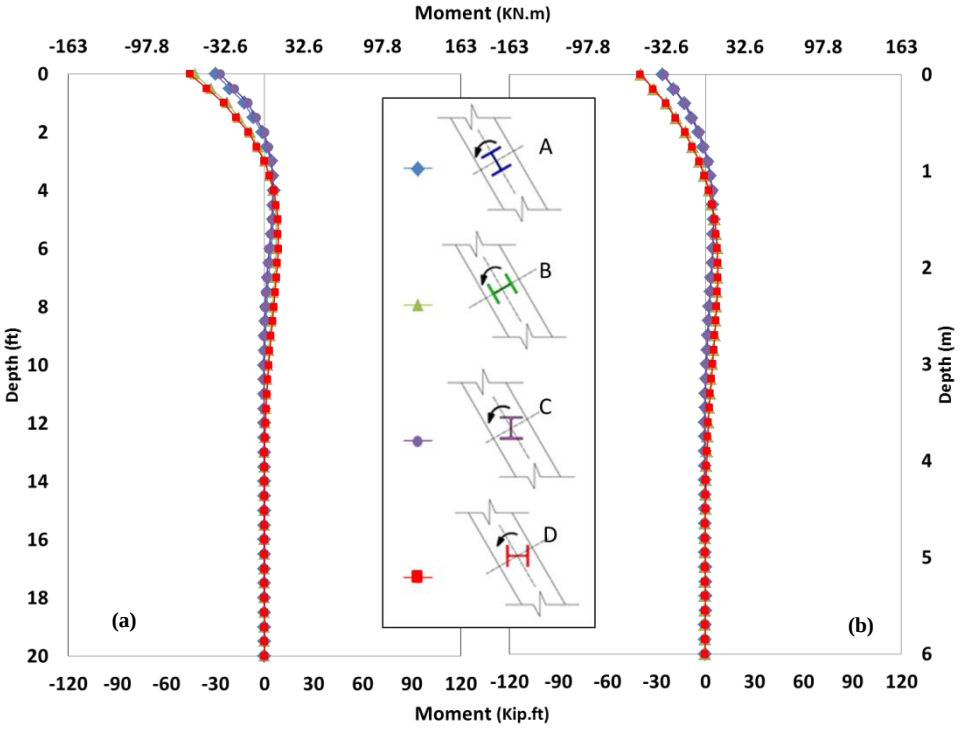

Figure 6-12: Moments in the Interior Piles about 1-1 Due to Dead Load and Increase in Temperature (a) Pile 3 (b) Pile 4 (South Abutment)

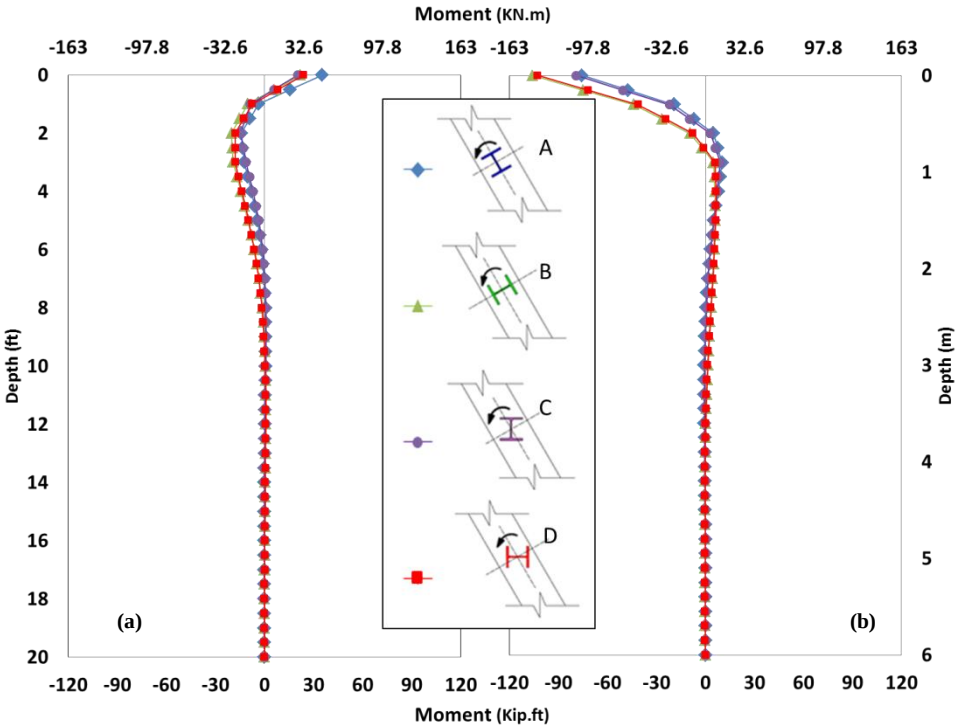

Figure 6-13: Moments in the Exterior Piles about 1-1 Due to Dead Load and Decrease in Temperature (a) Pile 1 (b) Pile 6 (South Abutment)

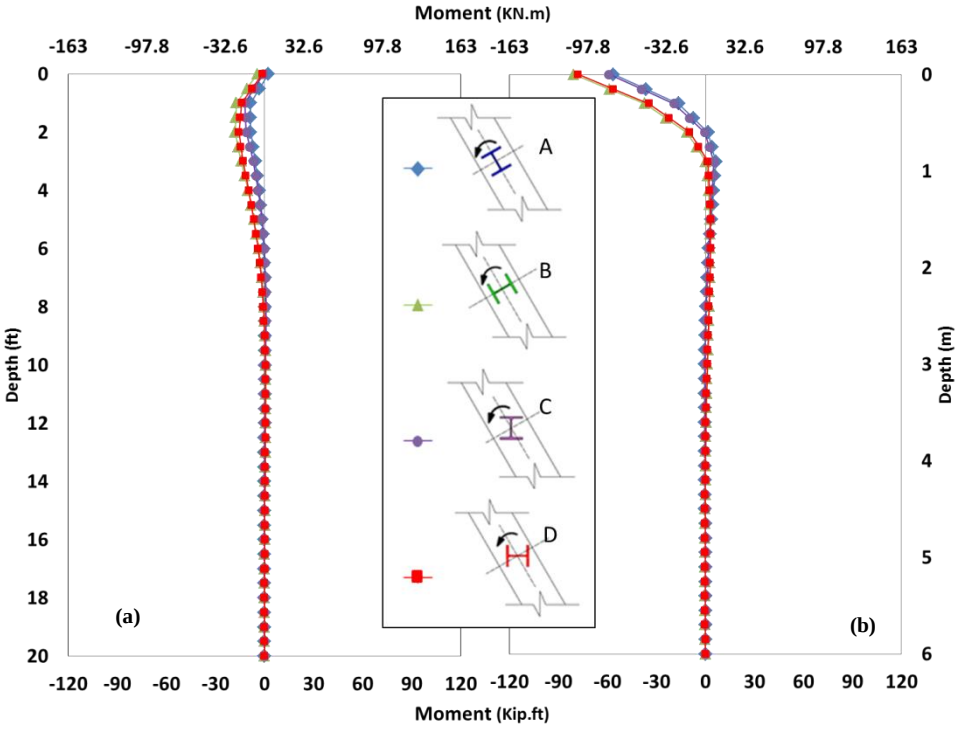

Figure 6-14: Moments in the Interior Piles about 1-1 Due to Dead Load and Decrease in Temperature (a) Pile 2 (b) Pile 5 (South Abutment)

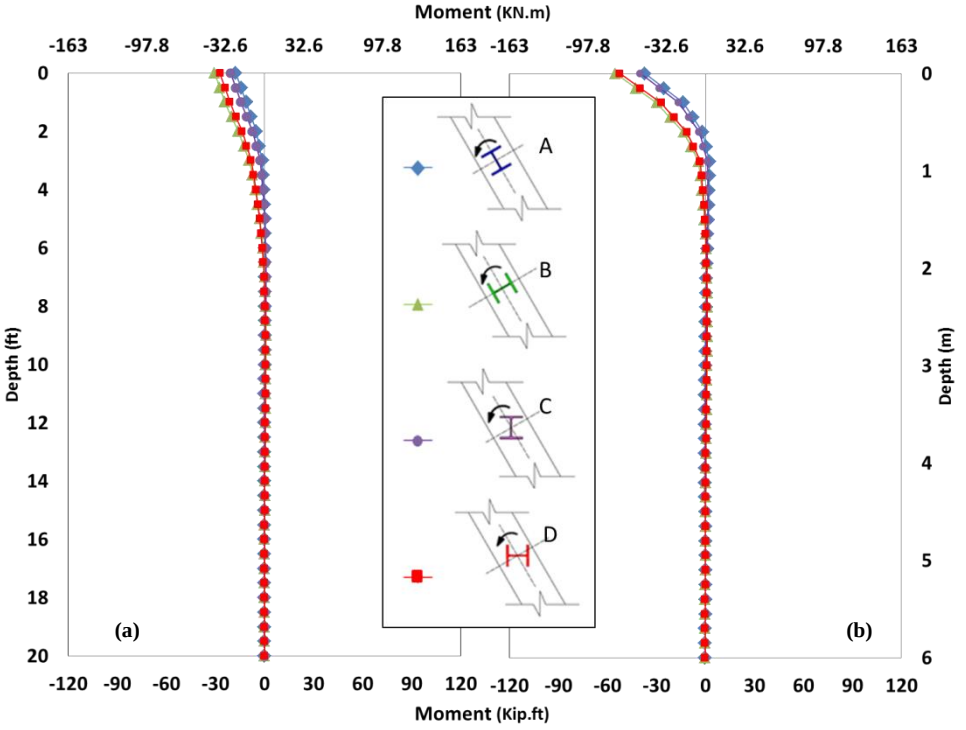

Figure 6-15: Moments in the Interior Piles about 1-1 Due to Dead Load and Decrease in Temperature (a) Pile 3 (b) Pile 4 (South Abutment)

The figures above show that orientations B and D (Table 6-1) moments are very close, and are typically larger than when piles are oriented in cases A and C (Table 6-1). This means that orienting the piles as in cases B and D, larger moments are generated in the piles for a given rotation and displacement. This result is reasonable since these two pile orientations cause the piles to bend mostly about the major principal axis. It was also concluded that the moments in the exterior piles are slightly larger than those occurring in interior piles. Moreover, moments from dead loads and temperature decrease are larger than from dead loads and temperature increase. This is a consequence of not only applying decrease in temperature that was larger in magnitude than increase in temperature, but also as a result of having restraint from soil behind the abutment for temperature increase but not for temperature decrease, when piles are the only source of abutment restraint. It can also be noticed that when applying decrease in temperature and dead load, the moment results at the top of piles 6, 5, and 4 are negative whereas they are positive at the top of piles 1, 2, and 3. This could be as a result of having a larger temperature effect since the applied decrease in temperature was much larger than increase in temperature. To understand the effect of temperature only on moment in piles, plots in Figures 6-16 to 6-18 illustrate moments at the south abutment caused by a temperature decrease (Figure 6-2). Similar plots for a temperature increase (Figure 6-1), and for north abutment piles are in Appendix E.

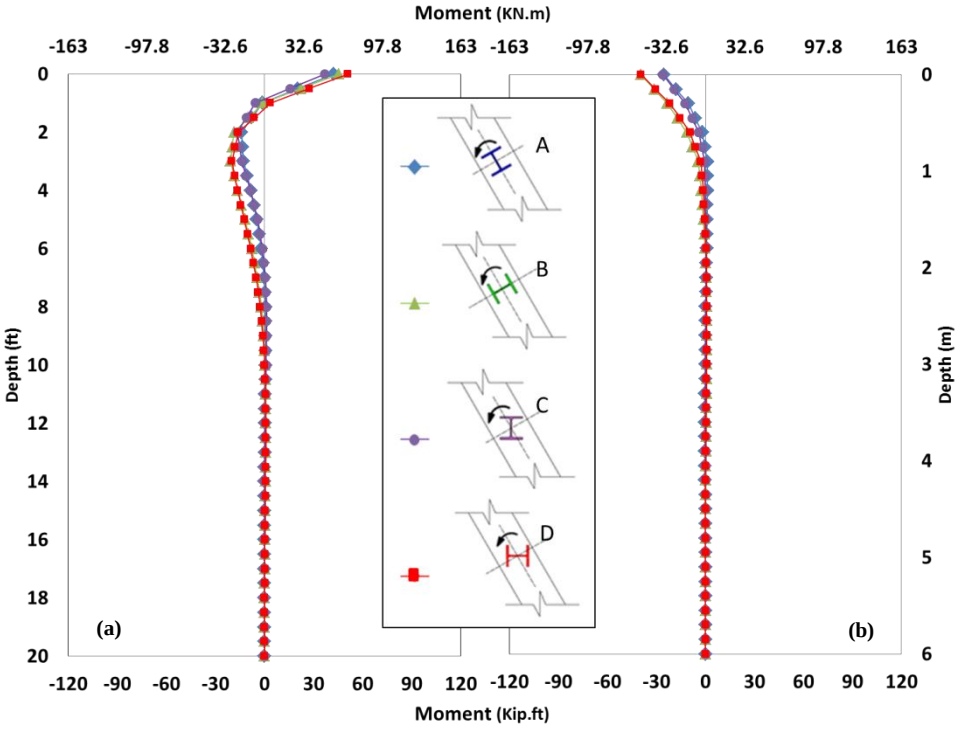

Figure 6-16: Moments in the Exterior Piles about 1-1 Due to Decrease in Temperature (a) Pile 1 (b) Pile 6 (South Abutment)

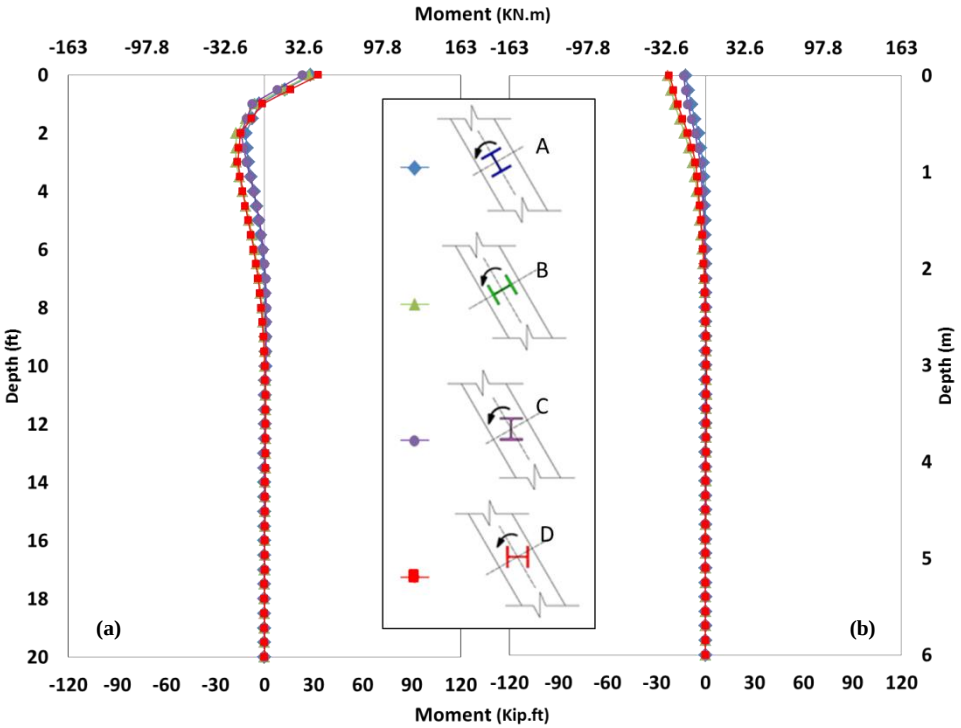

Figure 6-17: Moments in the Interior Piles about 1-1 Due to Decrease in Temperature (a) Pile 2 (b) Pile 5 (South Abutment)

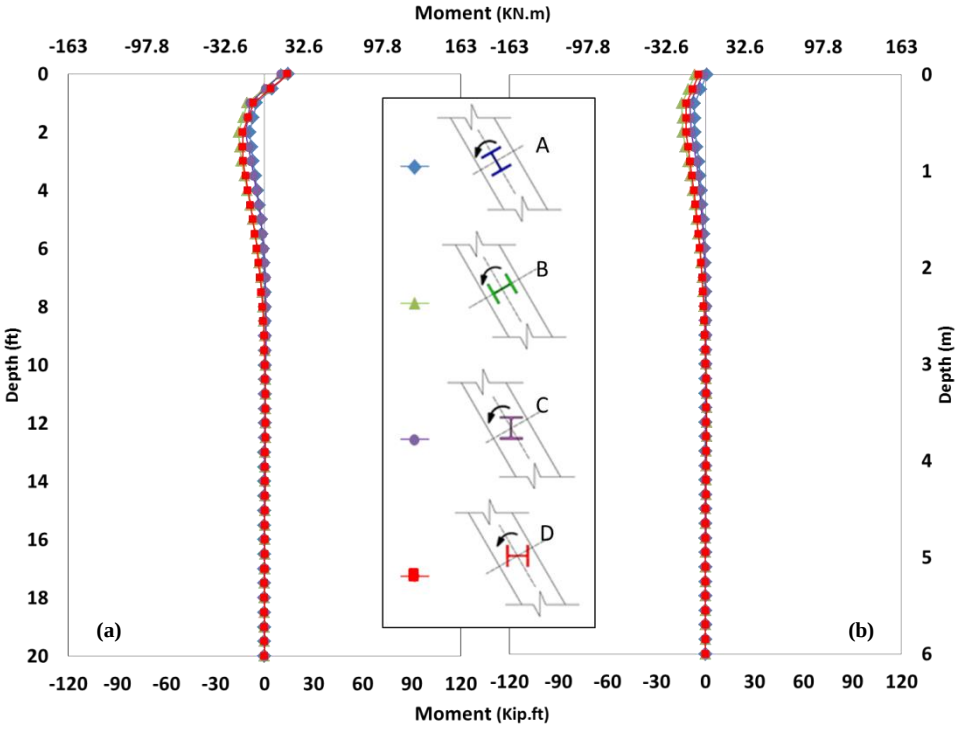

Figure 6-18: Moments in the Interior Piles about 1-1 Due to Decrease in Temperature (a) Pile 3 (b) Pile 4 (South Abutment)

The moment results plotted in Figures 6-16 to 6-18 show that when applying decrease in temperature only, the negative moments at the top of piles 5 and 6 due to applying dead loads and temperature decrease (Figures 6-13 to 6-15) have decreased. On the other hand, the piles that showed relatively small positive moments at their tops when applying dead loads and temperature decrease have showed larger positive moment when applying temperature decrease only. Hence, one can conclude that dead loads cause positive moments which will either add or subtract to moments due to temperature changes. It can also be concluded that in a skew IA bridge, the moment in piles could vary significantly and that the moments in piles located at the acute corners of the bridge are comparable and the same thing applies on those located at the obtuse corners.

The calculated moments about axis 2-2 were also studied in detail. As shown in Figures 6-19 to 6-21, applying dead loads and temperature increase resulted in

much smaller moments if compared to those calculated about axis 1-1. A similar observation is made when applying dead load and temperature decrease (Figures 6-22 to 6-24). Moments about axis 2-2 piles bend primarily about their minor principal axis for cases B and D, resulting in smaller values if compared to those resulted about 1-1 for orientations B and D.

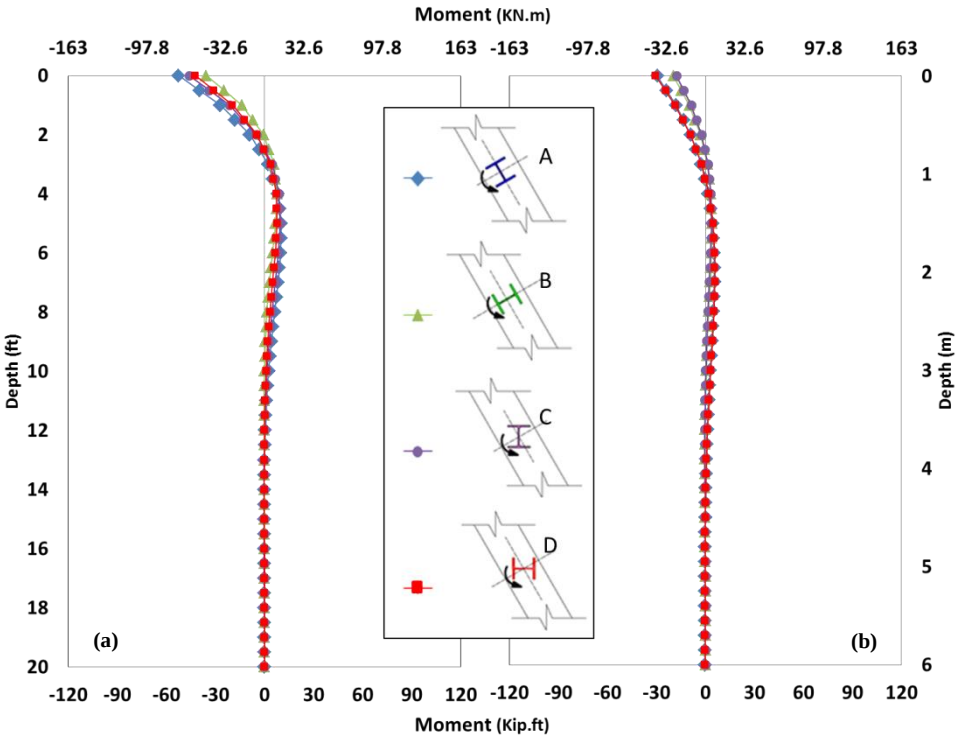

Figure 6-19: Moments in the Exterior Piles about 2-2 Due to Dead Load and Increase in Temperature (a) Pile 1 (b) Pile 6 (South Abutment)

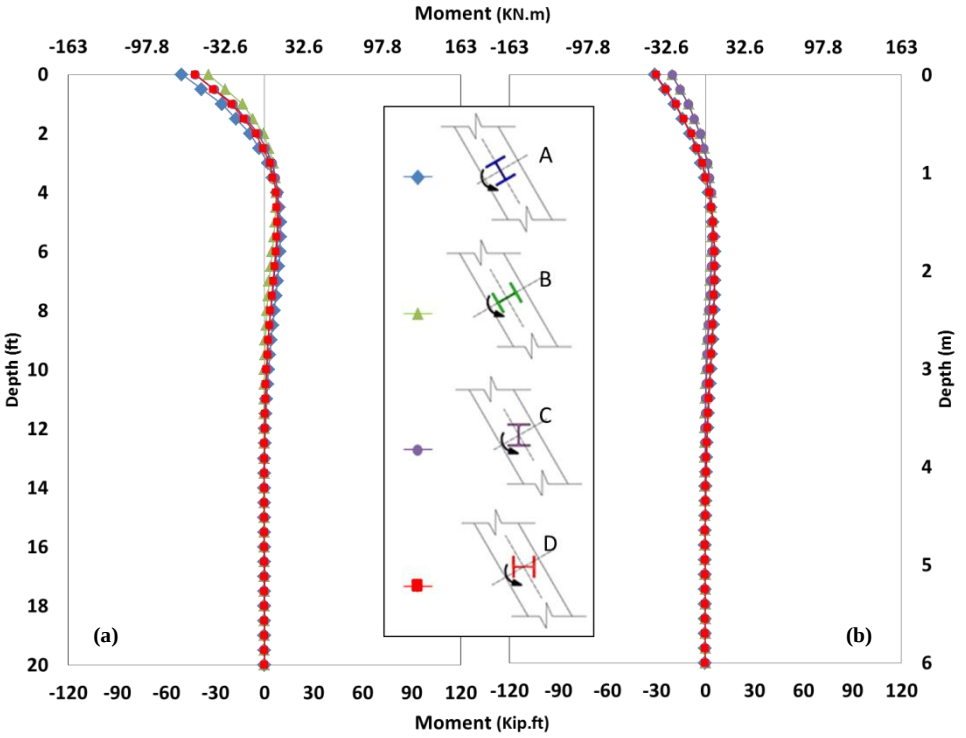

Figure 6-20: Moments in the Interior Piles about 2-2 Due to Dead Load and Increase in Temperature (a) Pile 2 (b) Pile 5 (South Abutment)

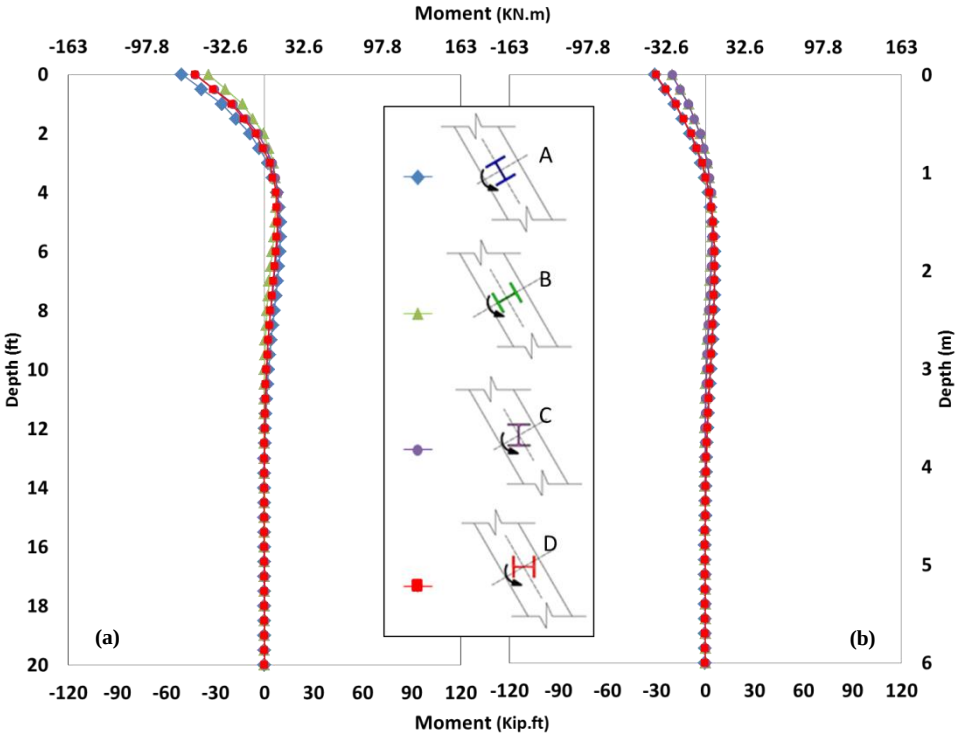

Figure 6-21: Moments in the Interior Piles about 2-2 Due to Dead Load and Increase in Temperature (a) Pile 3 (b) Pile 4 (South Abutment)

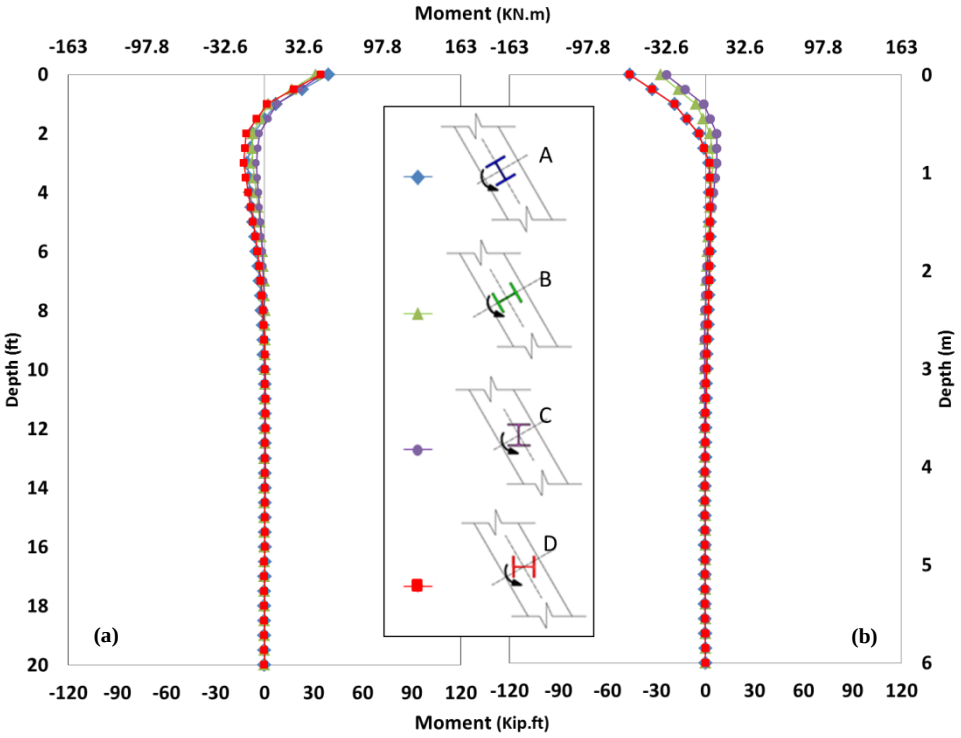

Figure 6-22: Moments in the Exterior Piles about 2-2 Due to Dead Load and Decrease in Temperature (a) Pile 1 (b) Pile 6 (South Abutment)

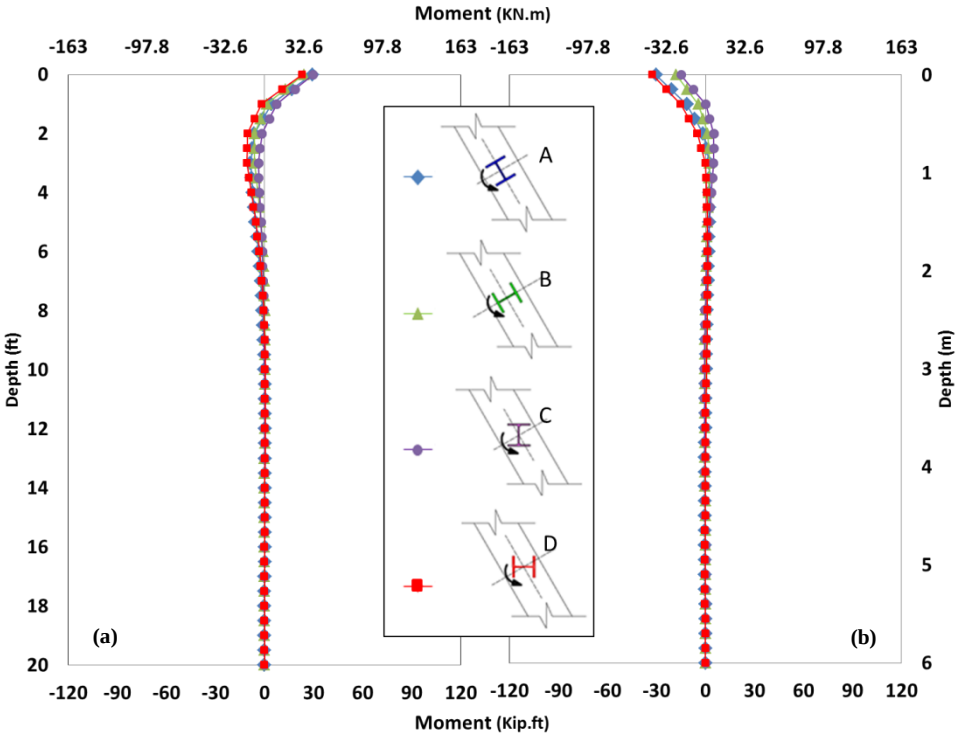

Figure 6-23: Moments in the Interior Piles about 2-2 Due to Dead Load and Decrease in Temperature (a) Pile 2 (b) Pile 5 (South Abutment)

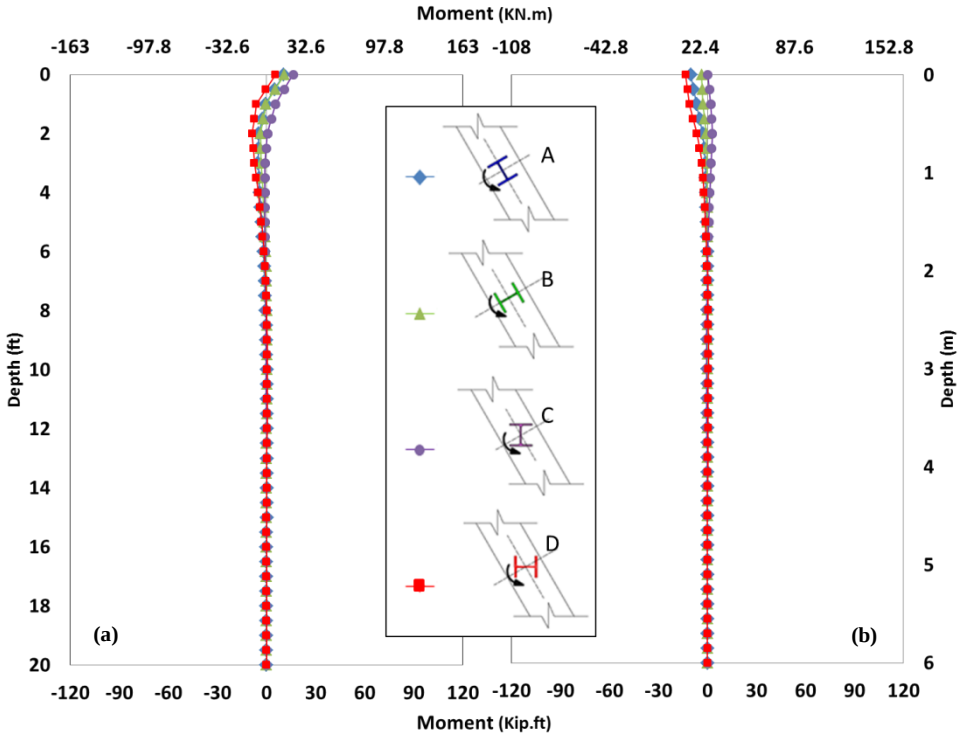

Figure 6-24: Moments in the Interior Piles about 2-2 Due to Dead Load and Decrease in Temperature (a) Pile 3 (b) Pile 4 (South Abutment)

From a design perspective, the ratio between moment demand and moment strength (capacity) is more important than moment magnitude to determine pile adequacy. The weak axis yield moment capacity of the piles used (HP 10x57) is 82 kip.ft (111 KN.m) whereas strong axis yield moment capacity of this shape is 245 kip.ft (332 KN.m). Figures 6-25 and 6-26 show the maximum moment demand-to-capacity ratios appeared in piles supporting the north and south abutments about their weak and strong original axes for each orientation when considering dead loads plus increase or decrease in temperature (Figures 6-1 and 6-2), respectively. The maximum major and minor axis moments occurred at the top of the piles. The ratios presented in these figures should be taken as qualitative measures to evaluate effects of pile orientation for design since load factors have not been included and the plastic moment capacity is not used in this comparison. Also, the interaction between axial force-moment strength has not been included in these calculations.

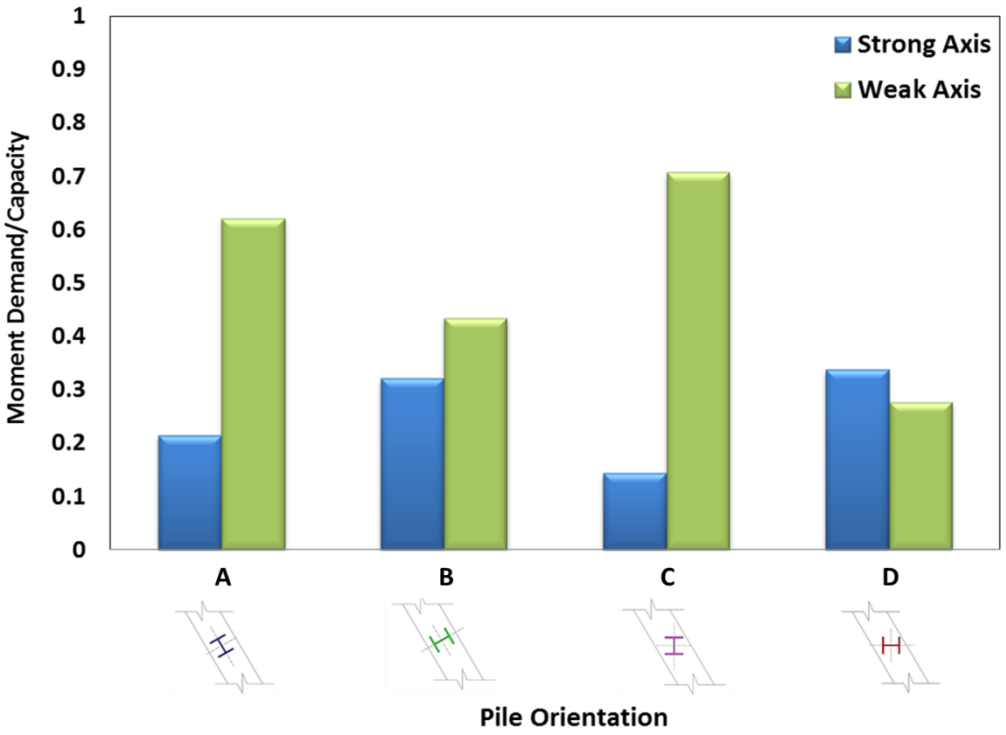

Figure 6-25: Moment Demand Capacity Ratio of the Four Orientations Due to Dead Loads and Increase in Temperature

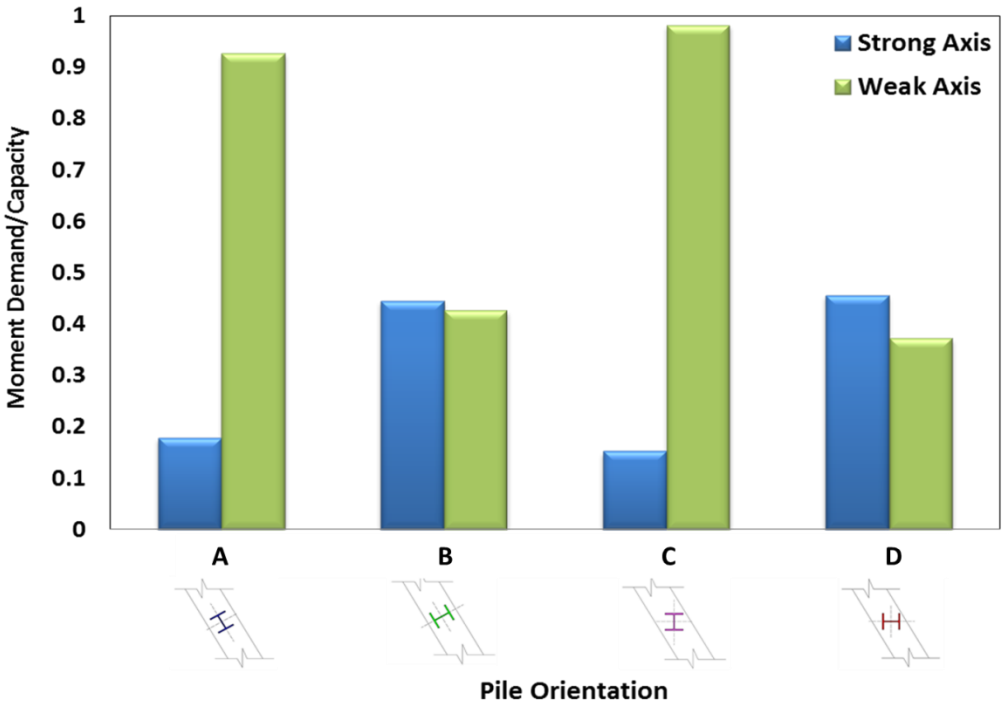

Figure 6-26: Moment Demand Capacity Ratio of the Four Orientations Due to Dead Loads and Decrease in Temperature

Plotting moment demand-to-capacity ratio (Figures 6-25 and 6-26) showed that although abutment displacement and rotation did not change due to different pile orientations, orientation has a significant effect on the possibility of reaching pile capacity. The results shown in Figures 6-25 and 6-26 indicate that orientations A and C resulted in higher ratios about the weak axis of piles in comparison to orientations B and D. This observation holds true when applying either an increase or a decrease in temperature in combination with dead loads. The maximum weak axis moment demand capacity ratio due to orientation C was higher by 5.5% in comparison orientation A which ratio is 0.927. The highest ratio between moment demand and capacity about the pile strong axis also correspond to orientations B and D. The maximum ratio about the strong axis, however, is only 0.45 and it corresponds to dead loads combined with temperature decrease. It can also be noted that orientations A and C result in small strong axis moment ratios and much larger weak axis moment ratios that represent 92 % and 98 % of the section capacity, respectively. Since the residual stresses are not accounted for in the FE model, it is possible that pile yielding may have occurred in the Brimfield Bridge owing to the fact that piles were oriented as in case A. Also, the maximum moment appeared in pile 6 at the south abutment, where abutment displacement readings showed permanent displacement toward the superstructure (shifting) indicating a possible pile yielding. However, the observed permanent displacement may also be caused by the effect of soil properties or other parameters. Orientations B and D result in relatively equal weak and strong axis moment ratios with maximum values not exceeding 46% of the section capacity. Therefore, for bridges that are subjected to the same conditions as the Brimfield Bridge and have similar dimensions, orienting the piles as in B and D can be advantageous, especially since the displacement and rotation results are not varying

with different orientations. On the other hand, since moment due to orientations A and C is less than yield, the design is still adequate, and as IAB problems previously reported included cracking of the abutment, a lower moment at the pile/abutment interface is beneficial, which means that one can also use orientations A and C if pile yield is accounted for in design equations as several states do.

6.5 Summary

In this chapter, four pile orientations were considered to examine the effect of orientation on the Brimfield Bridge model. The investigation included abutment displacement and rotation as well as bending moments in piles. It was concluded that in a bridge with similar properties as Brimfield Bridge and subjected to the same conditions, both abutment displacement and rotation are not affected significantly by pile orientation. Nevertheless, plotting weak and strong axes moment demand-to-capacity ratios for dead loads and temperature increase and decrease, showed that the moment ratios can vary significantly due to different pile orientations. The results indicate that orientations B and D (Table 6-1) lead to lower ratios about the strong and weak axes of the piles. Despite resulting in higher moments, orientations B or D might be better options in terms of pile orientation because of the lower moment ratios computed, yet when considering pile yield in the design, orientations A and C could be used due to smaller moments at the top of piles.

CHAPTER 7

SUMMARY AND CONCLUSIONS

7.1 Summary

In this thesis, the behavior of a prestressed concrete IAB with a 30-degree skew angle was investigated. The superstructure of the bridge (Brimfield Bridge) consists of the recently developed NEXT-F Beam section and includes an 8 in. (200 mm) cast in place concrete deck. A comprehensive calculation was conducted first considering all conditions the NEXT-F beams have undergone during construction including creep and prestress losses to explain the behavior of these beams during construction. The calculation results were then compared to corrected field data taken at different times after beam fabrication and during bridge construction.

Field data were also used to get a general understanding of the long term behavior of the bridge primarily due to thermal effects. A FE model was constructed and validated using field data taken during a live load test conducted shortly after the end of construction. The FE model was tuned by varying different parameters that were identified as affecting the results. These include soil properties of the backfill and around the piles, the temperature application method on the model, and the value of coefficient of thermal expansion assumed in the analyses. Finally, the effect of four different pile orientations on global bridge response and its influence on moments along the piles was studied to recommend an orientation that could be considered for design of this type of bridge. Based on the results from this research the conclusions and recommendations presented in the following section are drawn.

7.2 Conclusions and Recommendations

7.2.1 NEXT-F Beam Behavior during Construction

The following conclusions are drawn based on a comparison of calculated strains and measured strains during construction.

- The NEXT-F beam behavior was as anticipated during construction. Calculated strain approximate well to actual strain readings and follow the same trends. Strain was at different stages such as immediately after detensioning, while in the yard outside the plant, when installed on the abutments, and when casting the deck. In these calculations, the effect of prestress force release using AASHTO LRFD was investigated. Also, the moment generated in the beams due to different support conditions was taken into account. Creep effect was also included using Branson (1977). Linear elastic assumption was applied and Hook's law was used to determine strain from stress.
- The small differences observed between calculated strain and measured strains are attributed to shrinkage of concrete, which was not included in the calculations as well as errors embedded in the losses equations.
- The maximum compressive strain recorded and calculated captured at the time of de-tensioning represents 63 % of AASHTO LRFD 2010 limit. As anticipated, no tensile strain occurred during construction.

7.2.2 Behavior of the Bridge Based on Instrument Data

The following conclusions are drawn based on studying readings recorded by the instruments that were installed during construction in the bridge including strain gauges, crackmeters, and tiltmeters.

- A noticeable temperature variation within the depth of the superstructure was recorded. Temperature variations in the transverse direction of the bridge were also observed. These thermal gradients need to be accounted to capture the behavior of the bridge by means of FE models.
- Bridge contraction in the winter was larger in magnitude that bridge expansion during the summer.
- The displacements measured at both acute corners of the bridge are comparable. Similarly, displacements measured at the obtuse corners were of similar magnitude.
- Abutment displacements measured during the winter of the second year, were larger than those that occurred during the first year winter. This holds true at the west side and east side of the south and north abutment, respectively.
- The south abutment rotation during second year summer was larger than during the first year. The north abutment rotation during second year winter was larger in comparison with first year rotations measured during winter.
- The longitudinal strain readings in the deck were compressive throughout the 18 months of monitoring. This could be a result of creep and shrinkage of the concrete deck which led to contraction.
- Although strains in the deck were negative throughout the monitoring period, the variation in deck strains by season implies that the bridge expands in summer months and contracts during winter months.
- Comparing the strain readings at the top of beams 1, 2, and 3 to those taken at the deck suggest that both have the same trend yet different magnitudes. This is due to the fact that the deck above these beams was cast a year after, and still suffering of creep and shrinkage. The readings taken at the deck portion

above beams 4, 5, and 6 showed the same trend and much closer strain magnitude if compared to strains taken at top of these beams.

- The distribution of strains with depth confirms the assumption of composite action between deck and beams.
- Strain gauge readings at the bottom of the beams showed that during winter the bottom of the NEXT-F beams experience tensile stress and compressive stress during the summer. This behavior suggests that in the winter the bridge adopts a deformed shape that is concave upward as a result from thermal contraction. A concave downward deformed shape occurred during the summer, consistent with expansion of the bridge and the measured abutment movement.
- The sidewalk appears to act compositely with the deck on top of beam six. This is due to the higher strain readings captured at the bottom of the west stem of beam six.

7.2.3 Validation of the Finite Element Model of the Brimfield Bridge and Influence of Key Parameters

- Accounting for changes in soil properties behind abutments and piles constructed during phase I resulted in FE model values that closer approximated the measured response.
- The FE model results showed good agreement with strains measured during the live-load test, except for strains in beam 4 when investigating configuration 7 and beams 5 and 6 when examining configuration 8.
- Displacement and rotation readings were used to calibrate the FE model for long-term behavior of the bridge. The soil properties that were used for the

live-load test model worked well in to validate year one performance of the bridge during summer.

- During year 1, the top 3 ft (0.9 m) of the soil around piles were assumed to be frozen in winter. The FE model results better approximated measured abutment displacements and, especially, rotations when assuming stiffer soil at the top representing frozen soil condition.
- The method used to apply thermal changes on the model was found to influence model results significantly. Using the thermal variations measured across the transverse direction of the bridge and the depth of the superstructure provided the most accurate results compared with the measured values of abutment displacement and rotation
- Plausible different values of the coefficient of thermal expansion of concrete were used in different analyses. Using high values to correct field data resulted in deformed shapes that matched with the expected overall bridge deformation. These same values of the coefficient of thermal expansion improved FE model results when compared with measured data. In this study it was found that the a value of α of 6.5 με/°F (11.7 με/°C) gave the best correlation with data. As a result, all strain data were re-corrected for temperature using a value of α 6.5 με/°F (11.7 με/°C)
- Pile instrumentation would have been helpful to further verify the observations made on bridge performance.

7.2.4 Pile orientation

Four pile orientations were considered to examine the influence on bridge performance and recommend an orientation for a bridge similar to the Brimfield Bridge. The following conclusions and recommendations are made:

- Abutment displacements and rotations are not significantly affected by pile orientation. Bridge expansion and contraction are largely independent of pile orientation.
- Moments in piles due to orientations A and C (Table 6-1), which result from resisting the loads in the transverse and longitudinal directions of the abutment, were almost the same in most of the piles. The same observation was made in case of orientations B and D. However, not always this was the case.
- Both orientations A and C led to high weak axis moment (almost yielding) in piles which was caused by applying dead load and negative change in temperature.
- The orientations that gave the smallest ratio between moment demand and moment capacity were B and D. This conclusion is limited to bridges similar to the Brimfield Bridge and subjected to the similar loading conditions. However, when considering pile yield in the design, orientations A and C could be used due to smaller moments at the top of piles which can be beneficial in preventing pile/abutment interface from cracking.
- Pile 6 at the south abutment in Brimfield Bridge could have yielded in winter of year one. This was concluded through the ratio between moment demand and moment capacity of orientation A (same orientation used in the bridge) and due to the shifting in displacement occurred at this corner where pile 6 is located.

7.3 Future Study

Future studies to be conducted to determine the effect of pile orientation on bridges with different skew angles, length, and width. Also, studying IABs that

incorporate the recently developed NEXT F and D beam section would be a point of interest. Moreover, investigating the effect of changes in soil conditions and temperature during the successive years on the live load test results so that the bridge can be rated accordingly, then the results can be compared to those resulted from equations given by AASHTO LRFD 2010 so that modifications to these equations might be applied. Finally, continued monitoring of the bridge is essential to understand its behavior during successive years and to identify any major changes in behavior.

APPENDIX A

EXAMPLE OF STRAIN CALCULATION DURING CONSTRUCTION

Beam No.1

After 10 minute of detensioning Strain Calculations.

Section properties:

Self-weight= (142.4*1183.84/(12^3*10^3)= 0.097557 kips/in

(a) Gross Precast Section: A_g: 1183.84 in^2, I_g= 115935.66 in^4 , y_b= 19.547 in
(b) Initial Transformed Section: (i.e before 7 days)

E_{ci}= 33 K_1 $W_c^{1.5}$ $\sqrt{fci'}$ = 33* 1* $0.1424^{1.5}$ *10^3 * $\sqrt{8.472}$ = 5161.452 Ksi
Concrete weight = 142.4 Pcf.
E_p= 29000 Ksi → n= E_p/ E_{ci} → n= 5.62 → *(n-1)= 4.62

	Component	Modulus of Elasticity(Ksi)	Modular ratio, n	Area (in^2)	y_b	A*y_b	I_{cg}+ A*d^2
1	Beam	5161.452	1	1183.84	19.55	23144	116068.5
2	Upper Strands	29000	4.62	4	30	120	465.26
3	Bottom Strands	29000	4.62	32.1	5.5	176.44	6038.05
			Sum	**1219.9**	**19.215**	**23440.44**	**122571.8**

e=11.327 in, et=11 in

Losses Estimation

$\Delta fp_{SR} = \epsilon_{sh} E_p K_{id}$

ϵ_{sh}= K_s K_{hs} K_f K_{td}* 0.48*10^{-3}

K_{hs} = (2.00 – 0.014 H)= 2-0.014*61= 1.146 , Where H = 61

k_s = 1.45 – 0.13(V/S) ≥ 1.0 → 1.45- 0.13 * 3.94 = 0.937<1 → Use 1

$K_f = \frac{5}{1+fc'} \rightarrow \frac{5}{1+8.472} = 0.53$

$K_{td} = \frac{t}{61-4fc'+t}$, where t=0.0417 day → K_{td}=1.536*10^{-3}

ϵ_{sh}= 4.48*10^{-7}

$K_{id} = \frac{1}{1+\frac{Ep\ Aps}{Eci\ Ag}\left(1+\frac{Ag\ e^2}{Ig}\right)*\{1+0.7\Psi(ti,td)\}}$

Ψ_b= 1.9 K_s K_{hc} K_{td} $t_i^{-0.118}$

K_{hc} = (1.56 – 0.008 H)= 1.072

t_i= 0.868 day (age at transfer)

Ψ_b= 0.00318

$$K_{id}= \frac{1}{1+\frac{29000*7.812}{5161.452*1183.84}\left(1+\frac{1183.84*11.327^2}{115935.66}\right)*\{1+0.7*0.00318} = 0.923$$

Δf_{pSR}= 0.012 Ksi

$$\Delta f_{pcr}= \frac{Ep}{Eci}\ fcgp\ \Psi b(td,ti)Kid$$

f_{cgp}= P_i [1/A_t + e_t^2/I]- (Mg e)/It

Pi= 36* 45.290 = 1630.44 Kips

Mg= $Wl^2/8$ → Mg= 0.097557* $800.75^2/8$ = 7819.2 K.in

f_{cgp}=1630.44[(1/1219.9) + (11^2/122571.8)]-((7819.2 *11)/ 122571.8)

f_{cgp}=2.24 Ksi

$K_{td}= \frac{t}{61-4fc'+t}$, where t= $6.94*10^{-3}$ day → K_{td}=$2.6*10^{-4}$

Ψ_b= $5.4*10^{-4}$

$$K_{id}= \frac{1}{1+\frac{29000*7.812}{5161.452*1183.84}\left(1+\frac{1183.84*11^2}{115935.66}\right)*\{1+0.7*5.4*10-4\}} = 0.923$$

$$\Delta f_{pcr}=\frac{29000}{5161.452} * 2.24 * 4.94 * 10^{-4} * 0.923 = 0.0057\ Ksi$$

$$\Delta f_{pRL}= \frac{fpt}{Kl}\left(\frac{fpt}{fpy}-0.55\right)$$

f_{pt}= 1630.44/7.812 =208 Ksi, f_{py}= 243 Ksi

KL= 30 (Low Relaxation Strands)

Δf_{pRL}= 2.12 Ksi

Total loss = (2.12 +0.0057 +0.012)*10^3*7.812 = 16700 lb

Stress and Strain Calculations:

Stress at bottom :

Due to initial force and self-weight

$$\sigma_{b1}= -\frac{Pi}{At} - \frac{Pi*et*y}{It} + \frac{M*y}{It}$$

$$\sigma_{b1}= -\frac{1630440}{1219.9} - \frac{1630440\ *11*19.215}{122571.8} + \frac{7819200*19.215}{122571.8}$$

σ_b1= -2922.32psi

Due to Presstress losses

$$\sigma_b2= (\Delta f_{pRL}+ \Delta f_{pcr}+ \Delta f_{pSR})\frac{Aps}{Ag}\left(1+\frac{Ag\ eg\ yb}{Ig}\right)$$

$$\sigma_b2= (2.12 +0.0057 +0.0112)*10^3*\frac{7.812}{1183.84}\left(1 + \frac{1183.84*11.327*19.55}{115935.66}\right)=46 \text{ psi}$$

Total bottom stress= 46-2922.32=-2876.35 psi

$\epsilon_b = \frac{\sigma b}{Ec} \rightarrow \epsilon_b = \frac{-2876.32}{5161452} = -557.26*10^{-6}$

Strain due to Creep in concrete:

$Ct = (t^{0.6}/(d+t^{0.6})*Cu \rightarrow Ct = \frac{0.00694\text{^}0.6}{10+0.00694\text{^}0.6)}*0.8*0.8*2.35 = 0.00758$

$\text{Initial strain} = \frac{-Pi/Ag-(Pi*eg*yb)/Ig+(M*yb)/Ig}{Ec}$

$= \frac{-\frac{1630440}{1183.84}-\frac{1630440*11.327*19.55}{115935.66}+\frac{7819200*19.55}{115935.66}}{5161452} = -0.00061$

Creep strain= -0.00061* 0.0758= -4.6238*10^-6

Total Strain (bottom) =(-557.26*10^{-6}) – (4.6238*10^-6)= -562*10^{-6}

Stress at Top :

Due to initial force and self-weight

$\sigma_{t1} = -\frac{Pi}{At} + \frac{Pi*et*yt}{It} - \frac{M*y}{It}$

$\sigma_{t1} = -\frac{1630440}{1219.9} + \frac{1630440*11*12.785}{122571.8} - \frac{7819200*12.785}{122571.8}$

$\sigma_t 1 = -281.42$psi

Due to Presstress losses

$\sigma_t 2 = (\Delta fp_{RL} + \Delta fp_{cr} + \Delta fp_{SR})\frac{Aps}{Ag}(1+\frac{Ag\ eg\ yt}{Ig})$

$\sigma_t 2 = -(2.12 + 0.0057 + 0.012)*10^3*\frac{7.812}{1183.84}(1 + \frac{1183.84*11.327*12.453}{115935.66}) = -34.4$ psi

Total bottom stress= -34.4-281.42=-315.815 psi

$\epsilon_t = \frac{\sigma t}{Ec} \rightarrow \epsilon_b = \frac{-315.815}{5161452} = -6.12*10^{-6}$

Strain due to Creep in concrete:

$Ct = (t^{0.6}/(d+t^{0.6})*Cu \rightarrow Ct = \frac{0.00694\text{^}0.6}{10+0.00694\text{^}0.6)}*0.8*0.8*2.35 = 0.00758$

$\text{Initial strain} = \frac{-Pi/Ag-(Pi*eg*yb)/Ig+(M*yb)/Ig}{Ec}$

$= \frac{-\frac{1630440}{1183.84}-\frac{1630440*11.327*12.453}{115935.66}+\frac{7819200*12.453}{115935.66}}{5161452} = -4.52252*10^{-5}$

Creep strain= -4.52252*10^-5* 0.0758= -3.42964*10^-7

Total Strain (Top) =(-6.12*10^-6) – (3.42964*10^-7)= -6.153* 10^{-6}

APPENDIX B

INDIVIDUAL STRAIN GAUGES PLOTS

Figure B (1-60)-: Strain Vs. Time

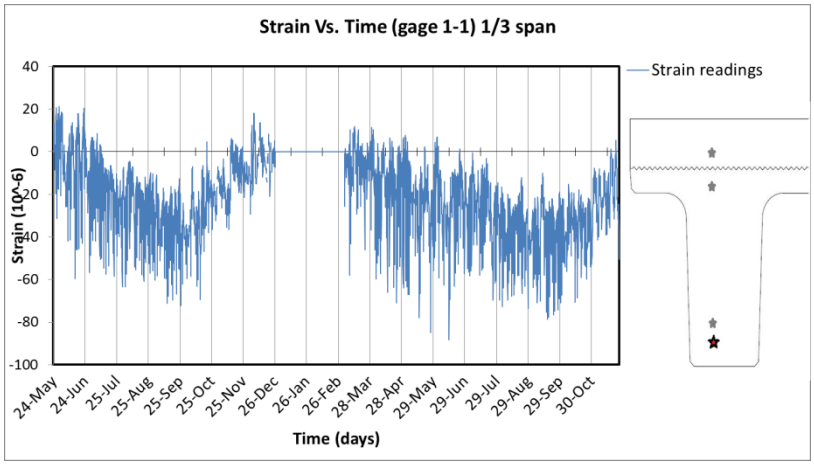

(1): Strain Vs. Time (gage 1-1)

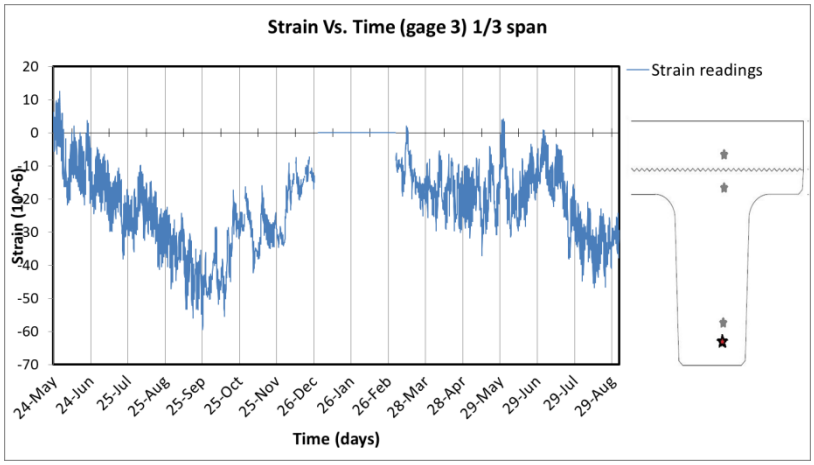

(2) : Strain Vs. Time (gage 1-3)

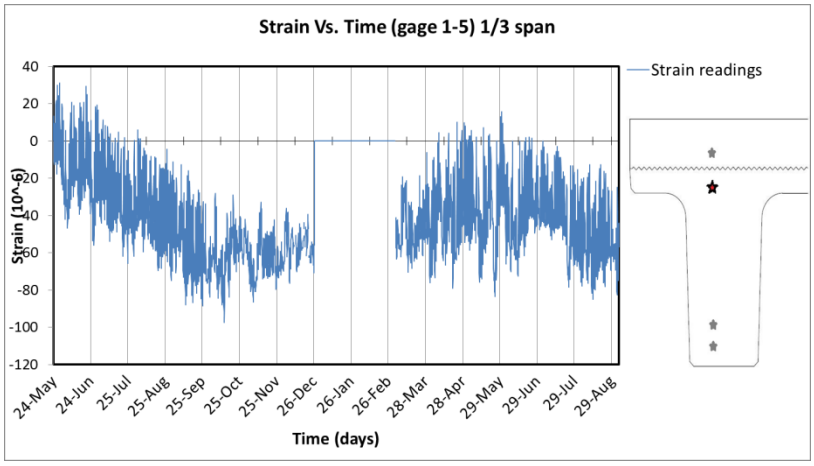

(3): Strain Vs. Time (gage 1-5)

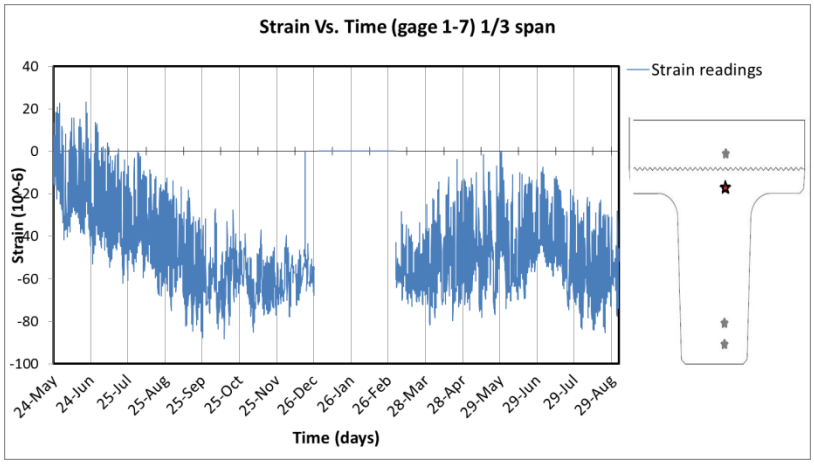

(4): Strain Vs. Time (gage 1-7)

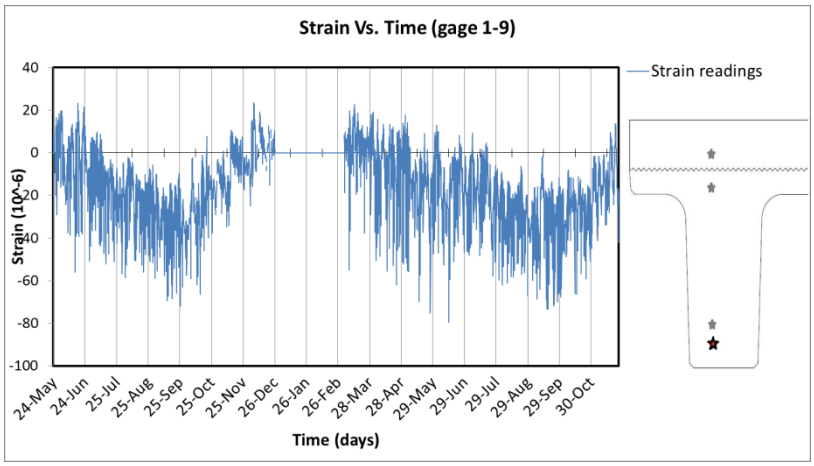

(5): Strain Vs. Time (gage 1-9)

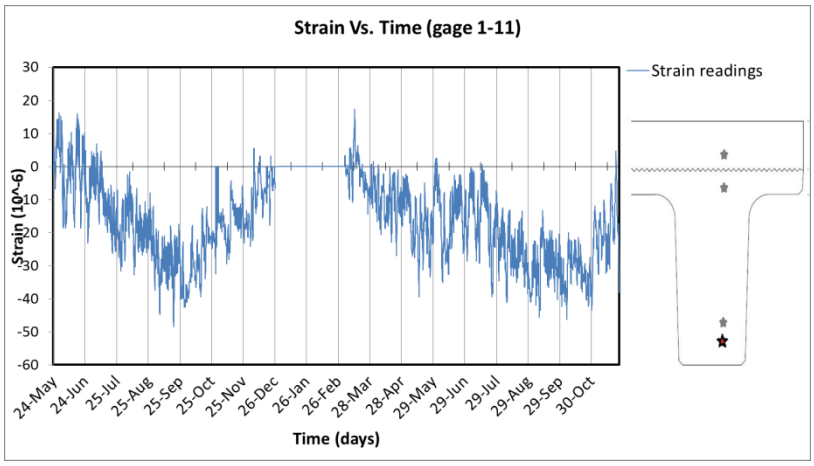

(6): Strain Vs. Time (gage 1-11)

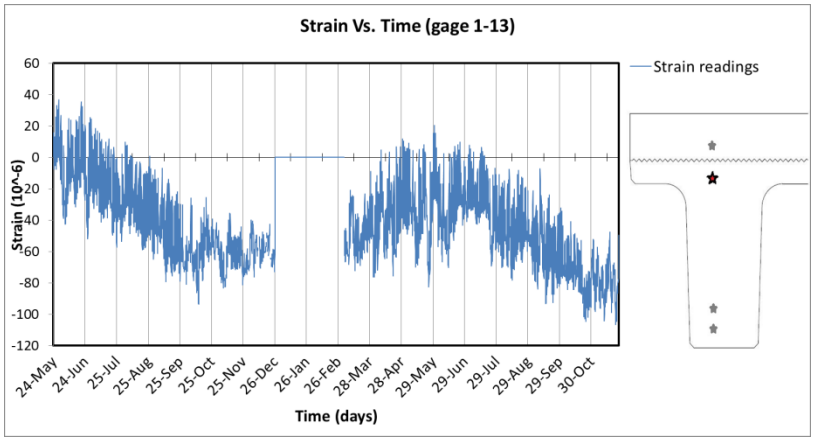

(7): Strain Vs. Time (gage 1-13)

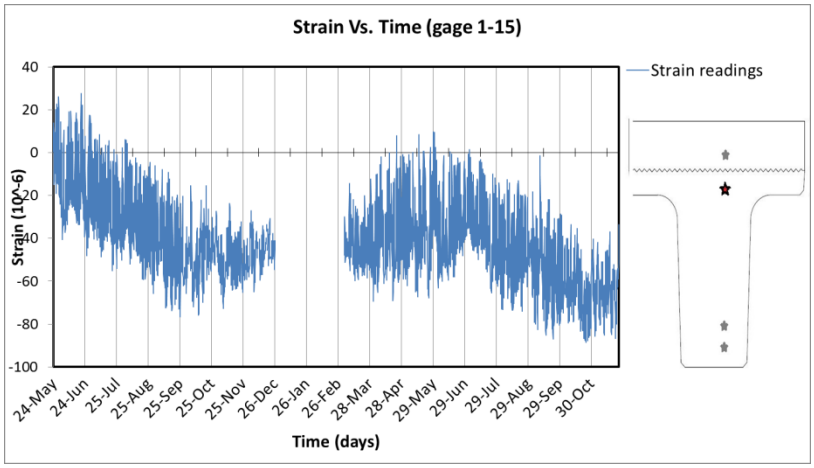

(8): Strain Vs. Time (gage 1-15)

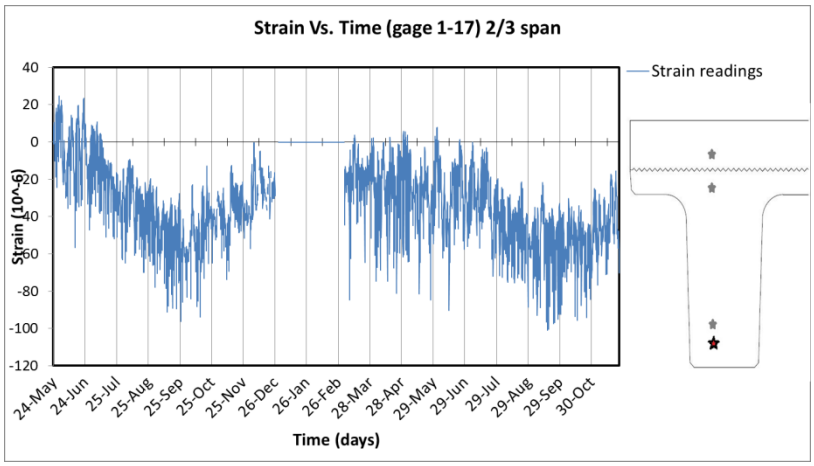

(9): Strain Vs. Time (gage 1-17)

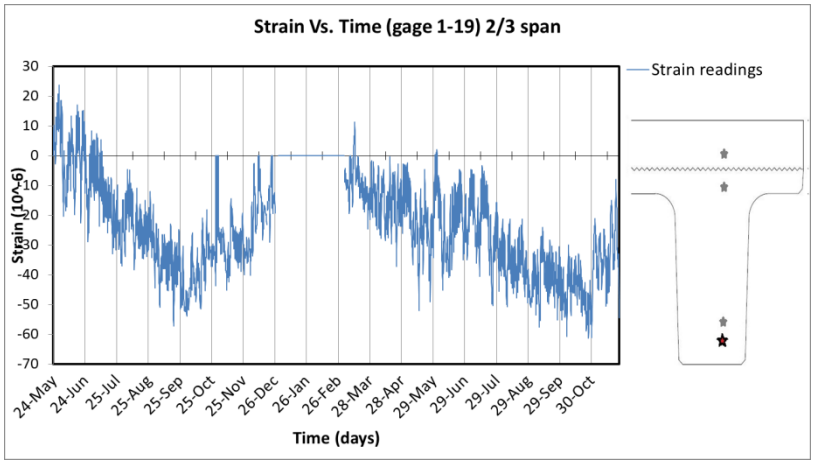

(10): Strain Vs. Time (gage 1-19)

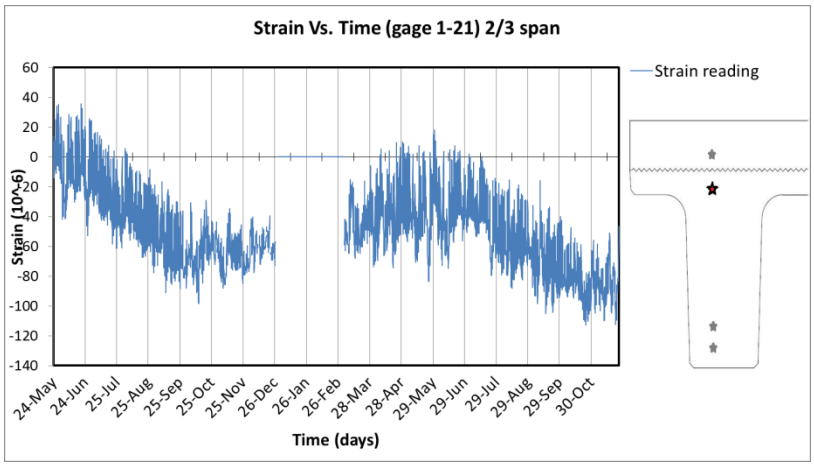

(11): Strain Vs. Time (gage 1-21)

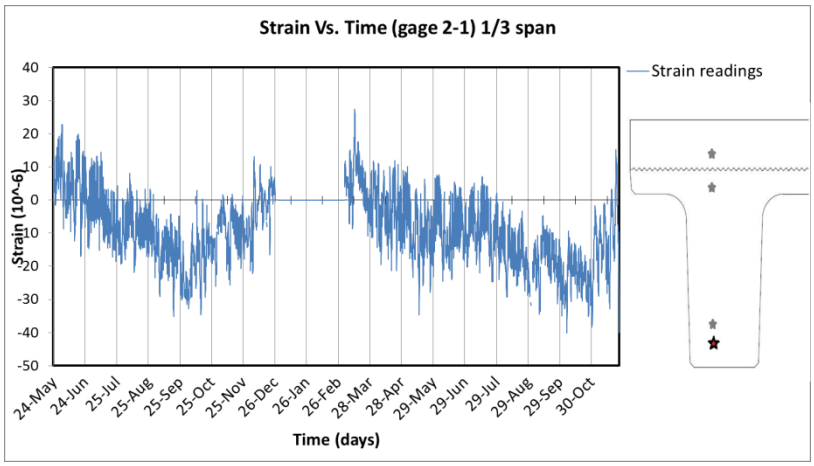

(12): Strain Vs. Time (gage 2-1)

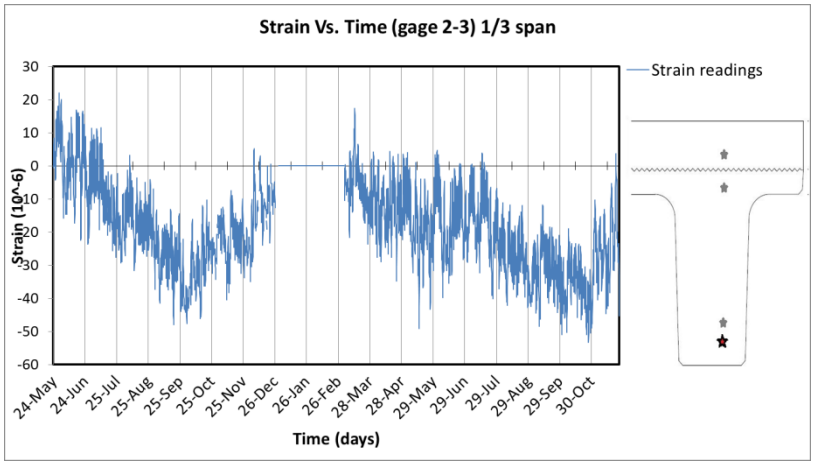

(13): Strain Vs. Time (gage 2-3)

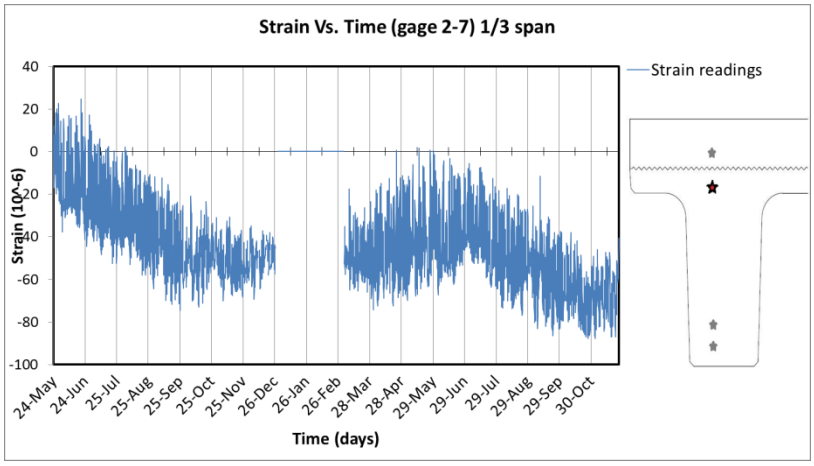

(14): Strain Vs. Time (gage 2-7)

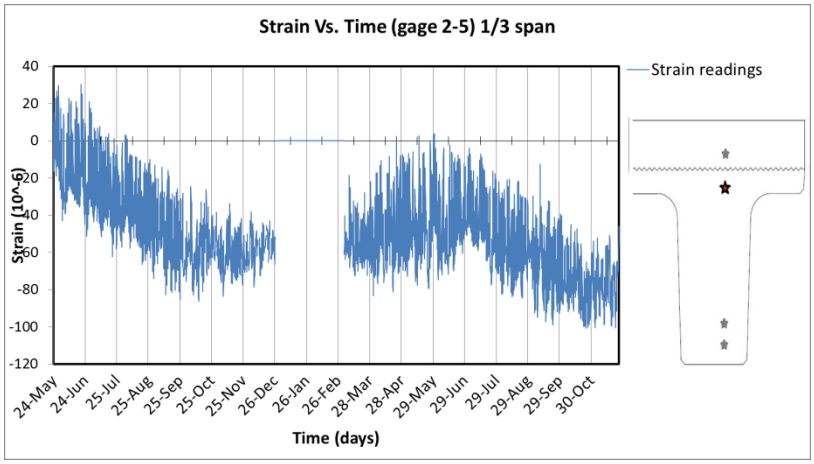

(15): Strain Vs. Time (gage 2-5)

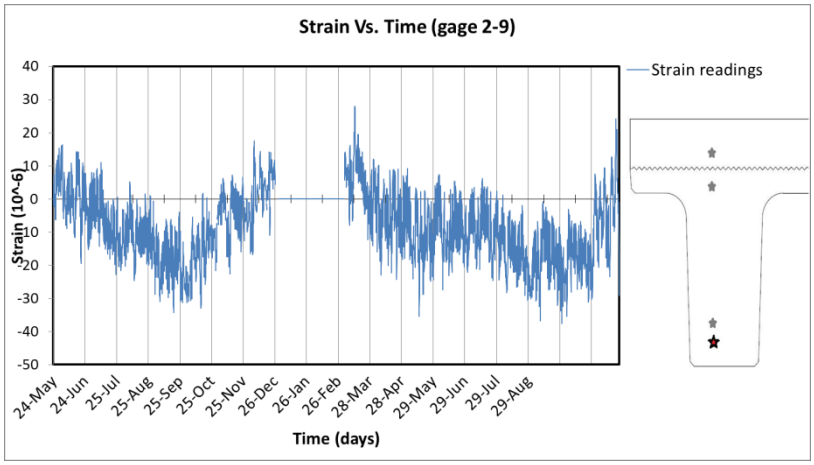

(16): Strain Vs. Time (gage 2-9)

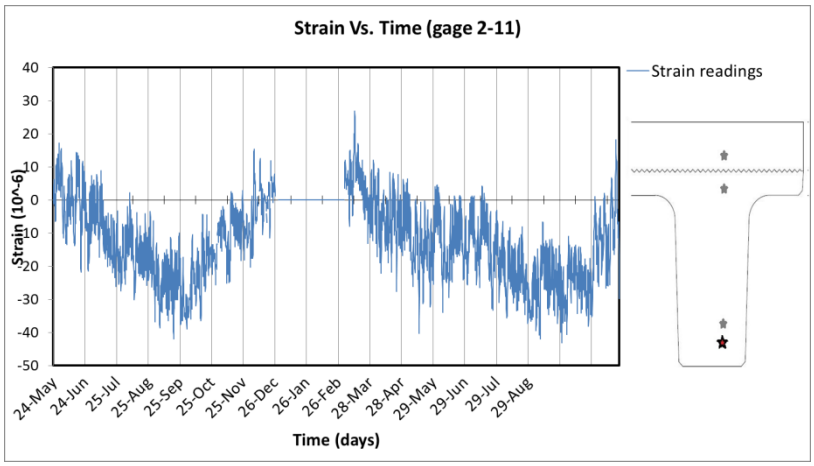

(17): Strain Vs. Time (gage 2-11)

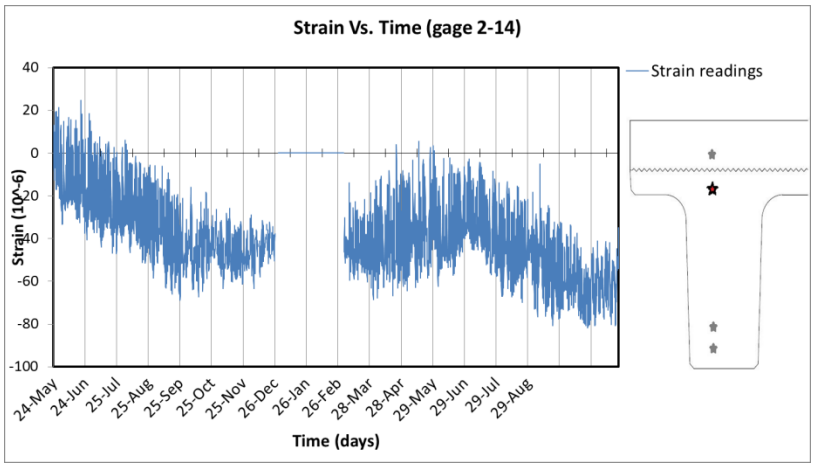

(18): Strain Vs. Time (gage 2-14)

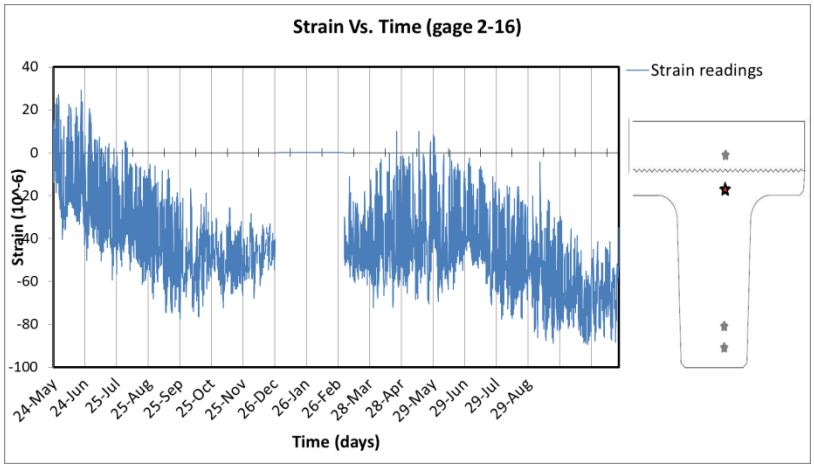

(19): Strain Vs. Time (gage 2-16)

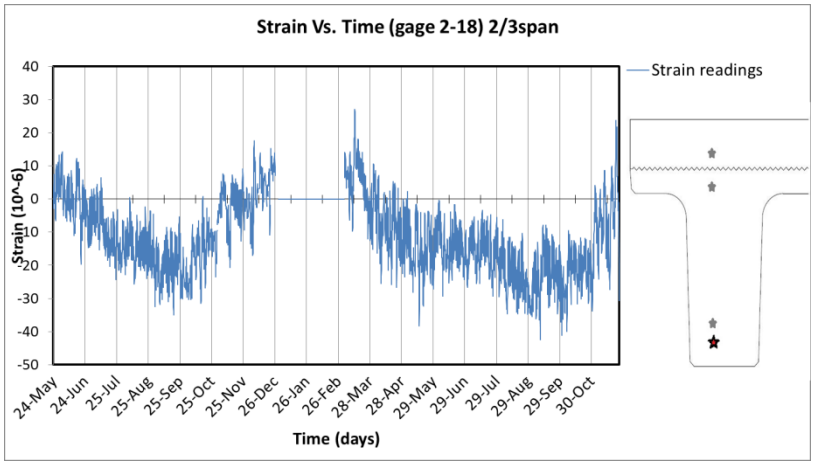

(20): Strain Vs. Time (gage 2-18)

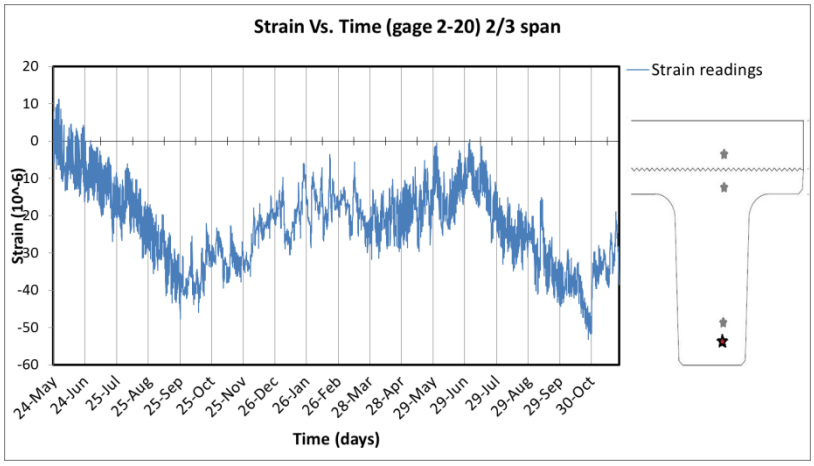

(21): Strain Vs. Time (gage 2-20)

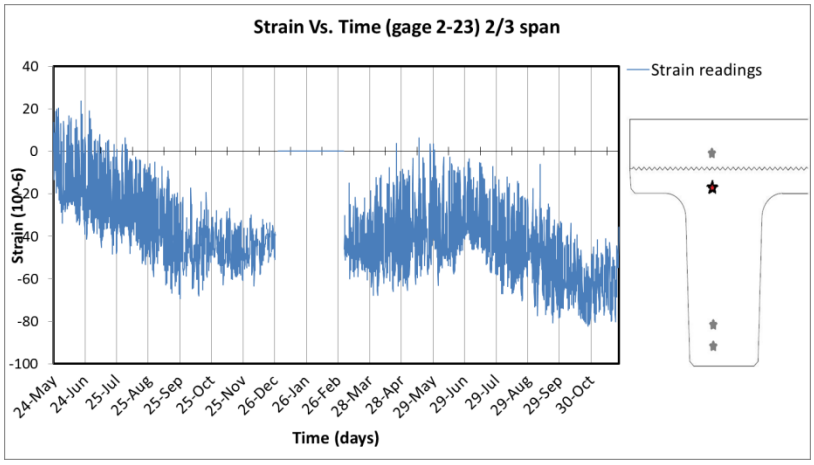

(22): Strain Vs. Time (gage 2-23)

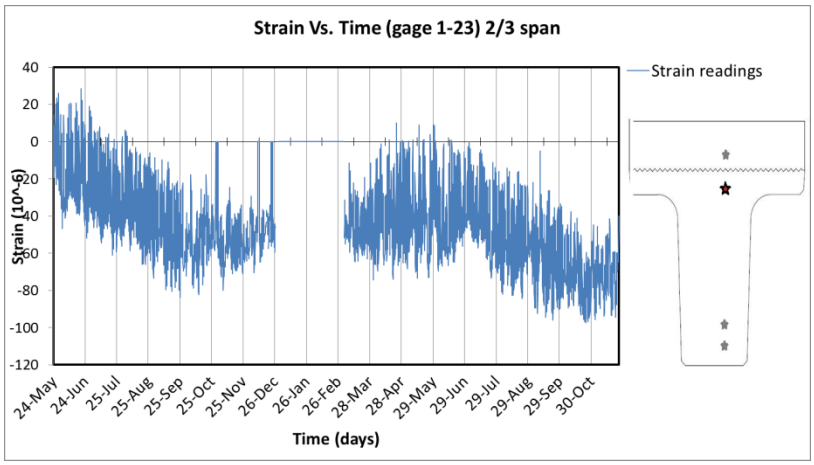

(23): Strain Vs. Time (gage 1-23)

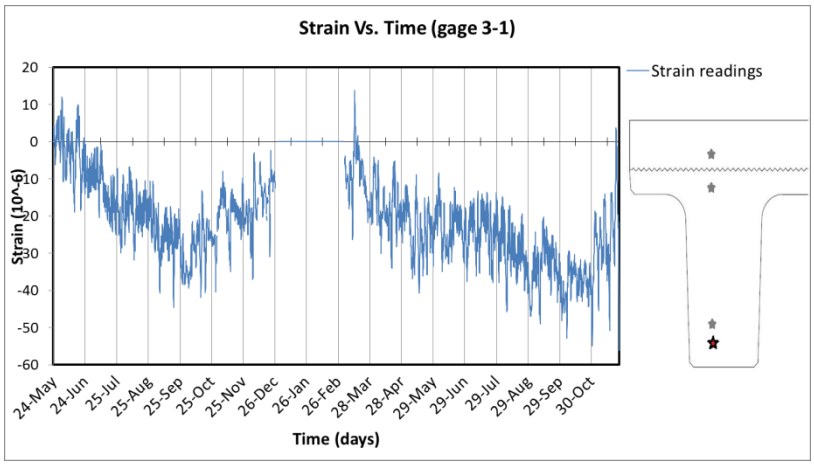

(24): Strain Vs. Time (gage 3-1)

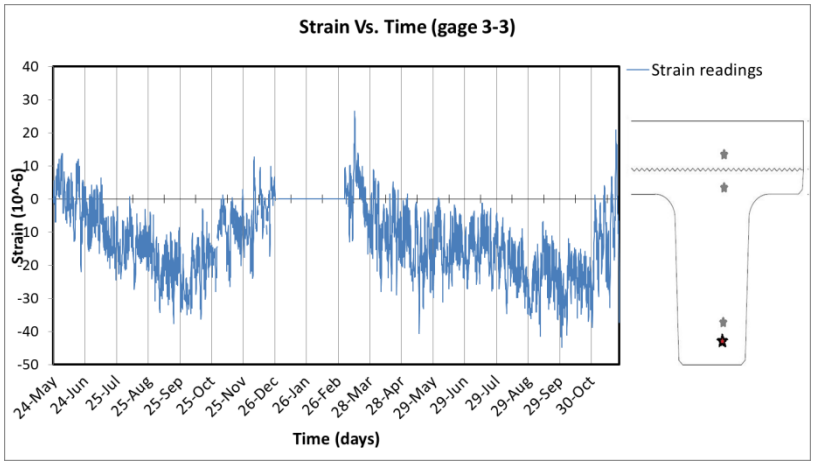

(25): Strain Vs. Time (gage 3-3)

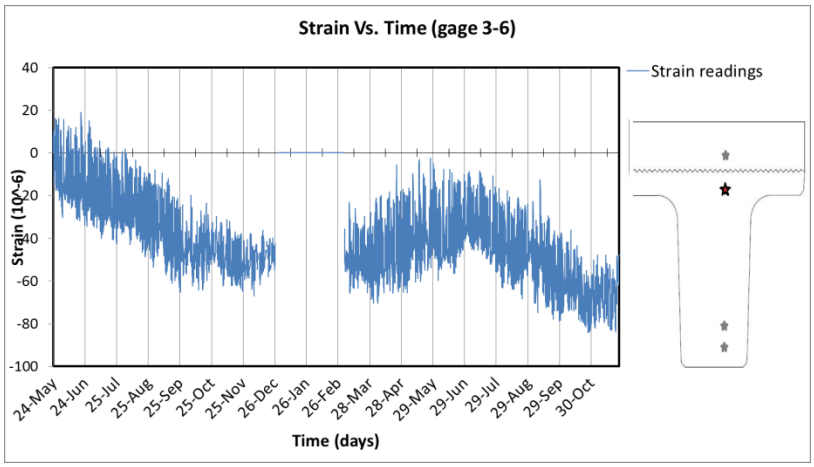

(26): Strain Vs. Time (gage 3-6)

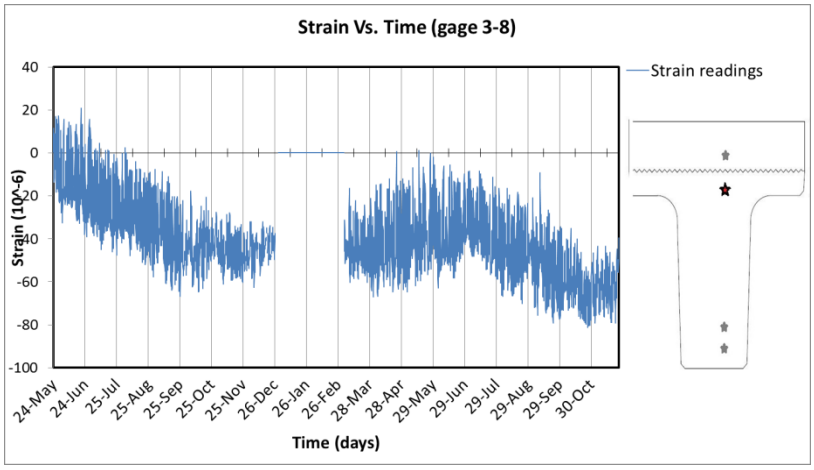

(27): Strain Vs. Time (gage 3-8)

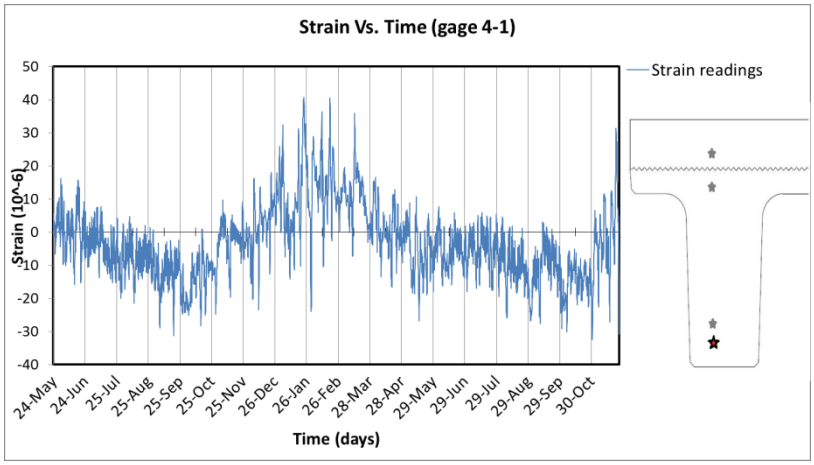

(28): Strain Vs. Time (gage 4-1)

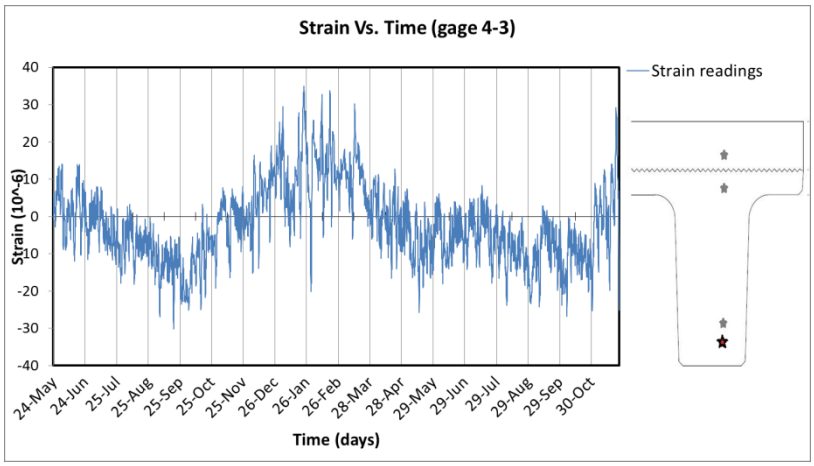

(29): Strain Vs. Time (gage 4-3)

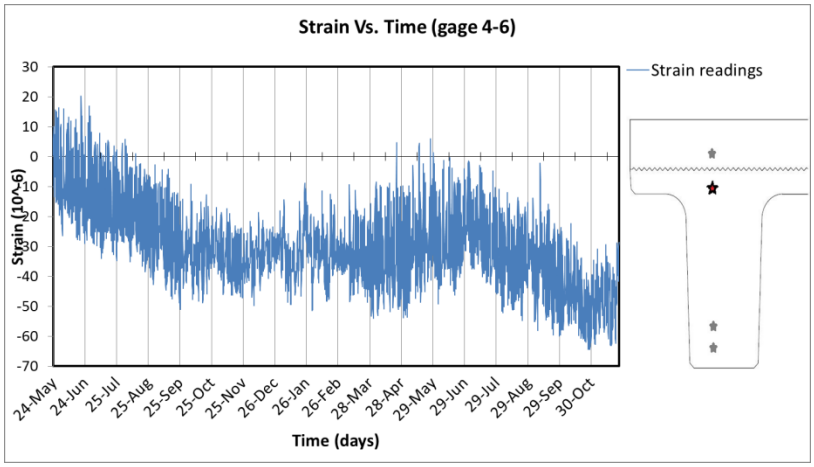

(30): Strain Vs. Time (gage 4-6)

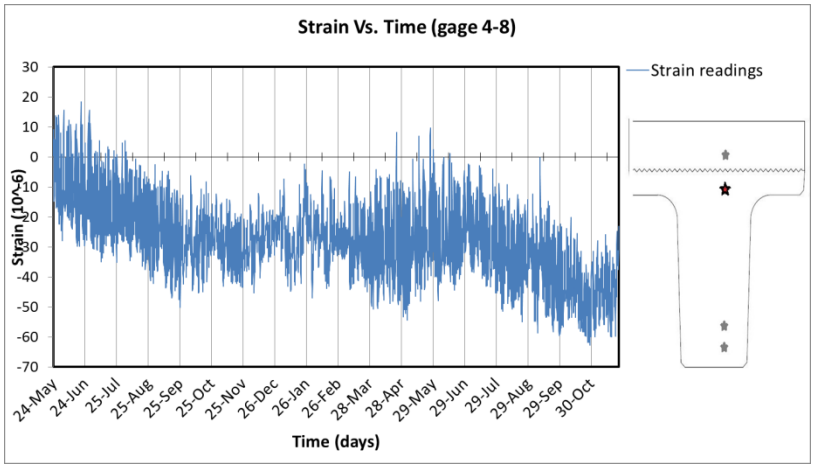

(31): Strain Vs. Time (gage 4-8)

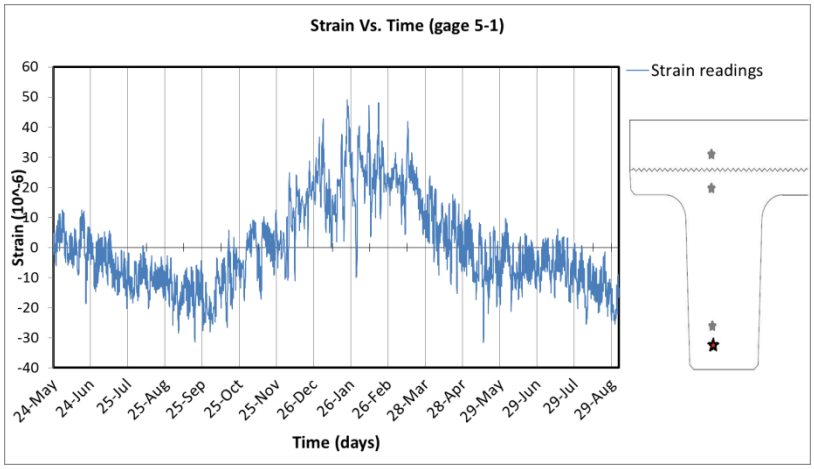

(32): Strain Vs. Time (gage 5-1)

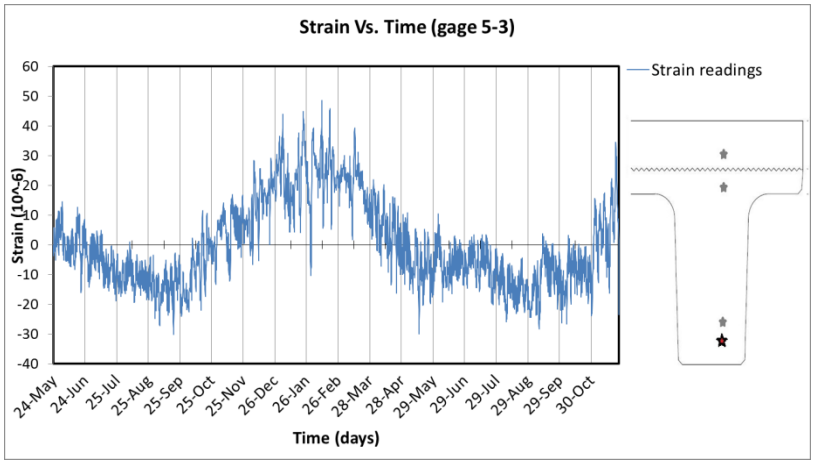

(33): Strain Vs. Time (gage 5-3)

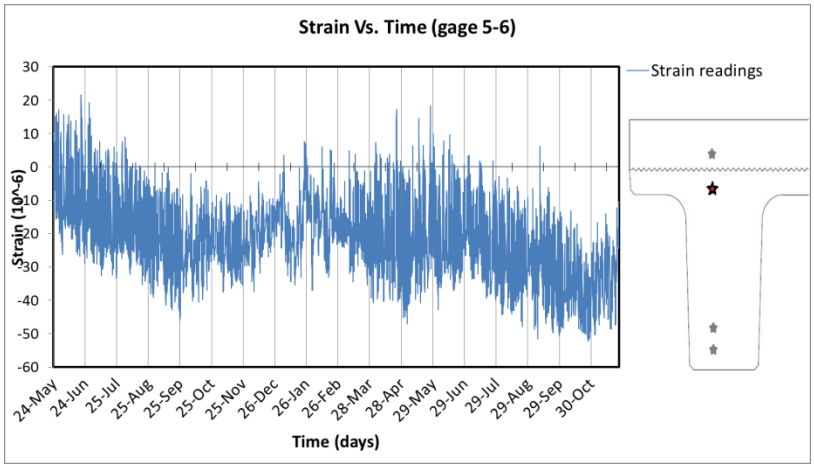

(34): Strain Vs. Time (gage 5-6)

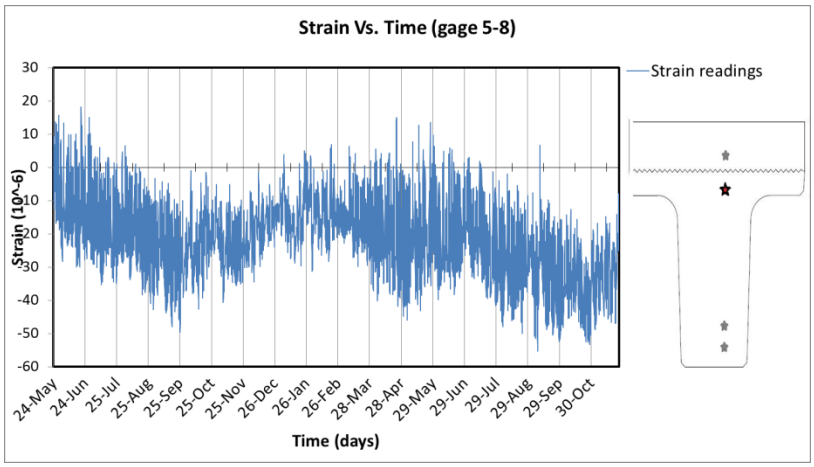

(35): Strain Vs. Time (gage 5-8)

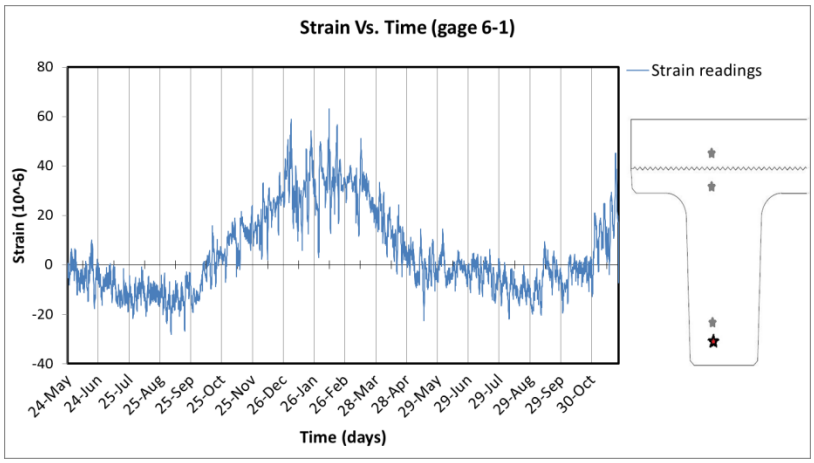

(36): Strain Vs. Time (gage 6-1)

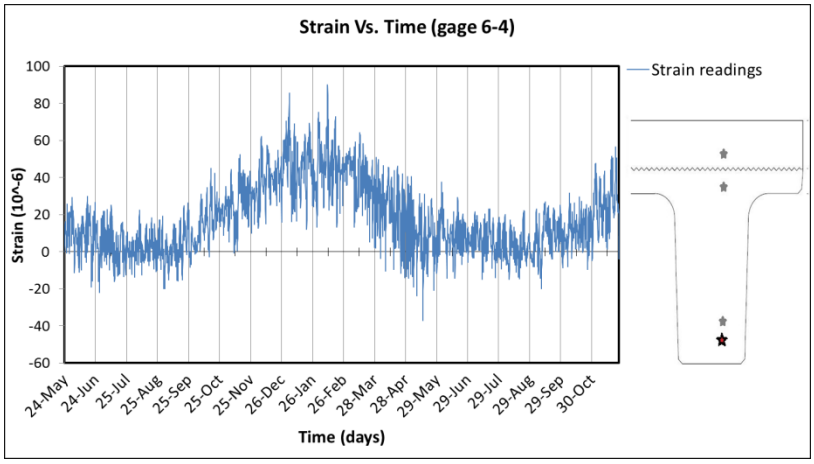

(37): Strain Vs. Time (gage 6-4)

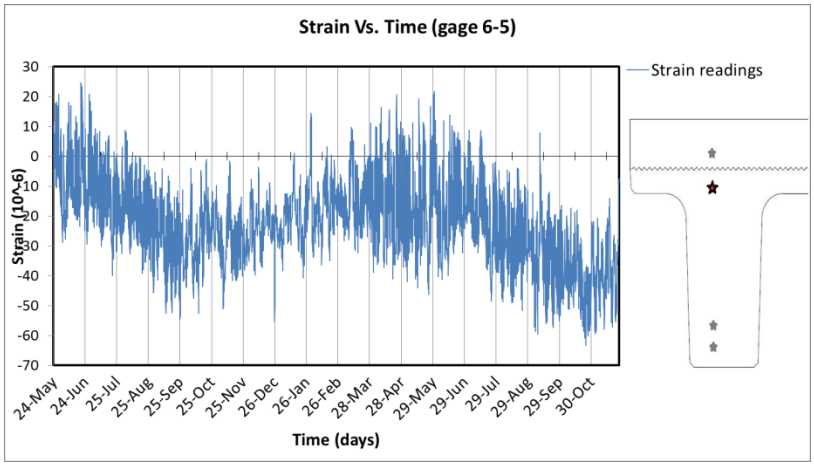

(38): Strain Vs. Time (gage 6-5)

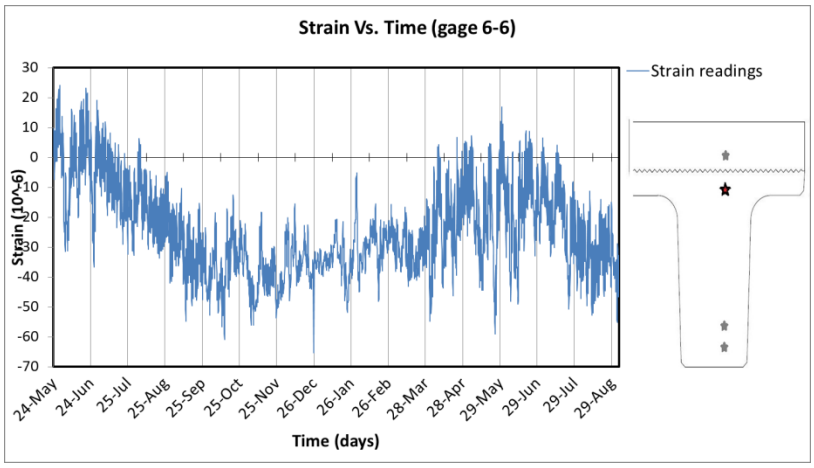

(39): Strain Vs. Time (gage 6-6)

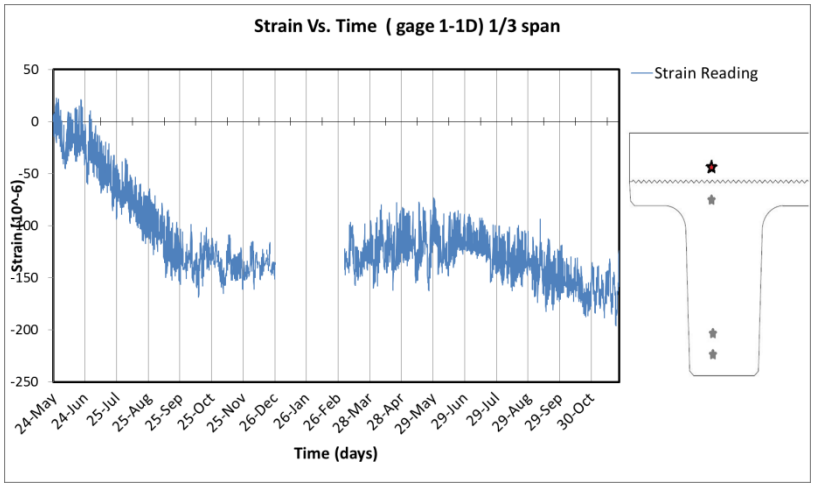

(40): Strain Vs. Time (gage 1-1D)

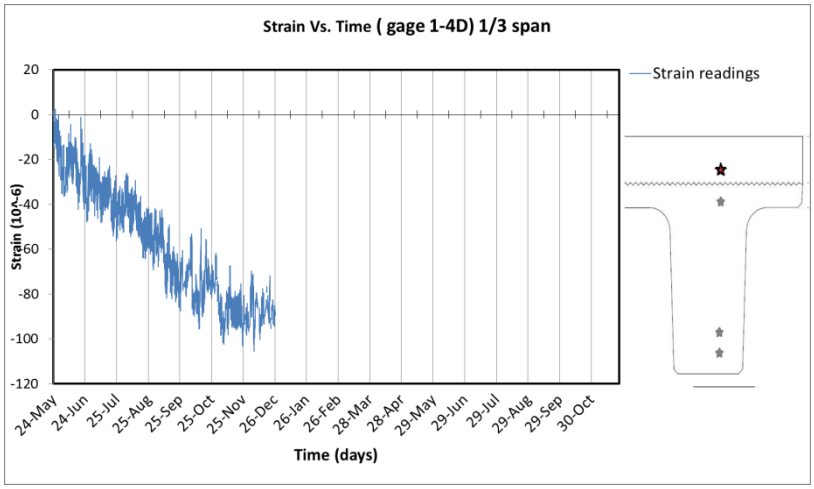

(41): Strain Vs. Time (gage 1-4D) 1/3 Span

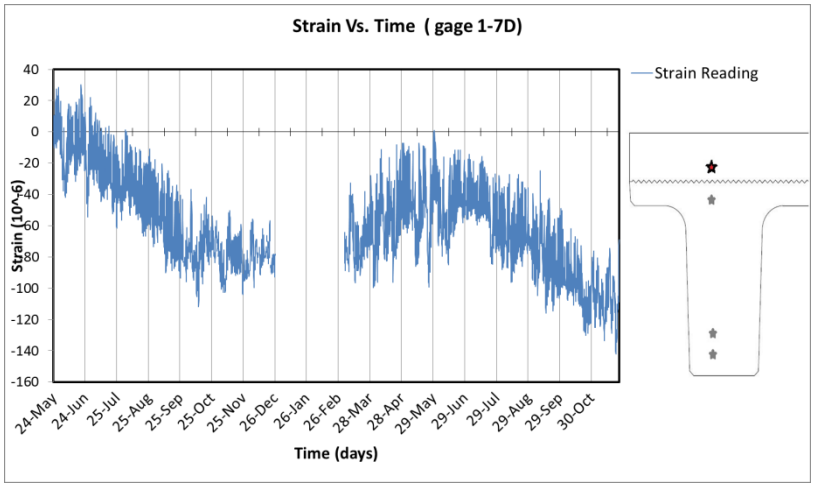

(42): Strain Vs. Time (gage 1-7D)

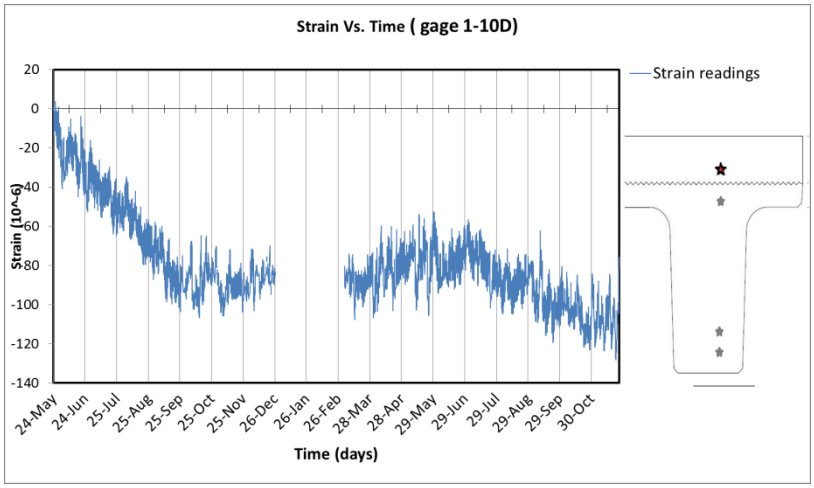

(43): Strain Vs. Time (gage 1-10D)

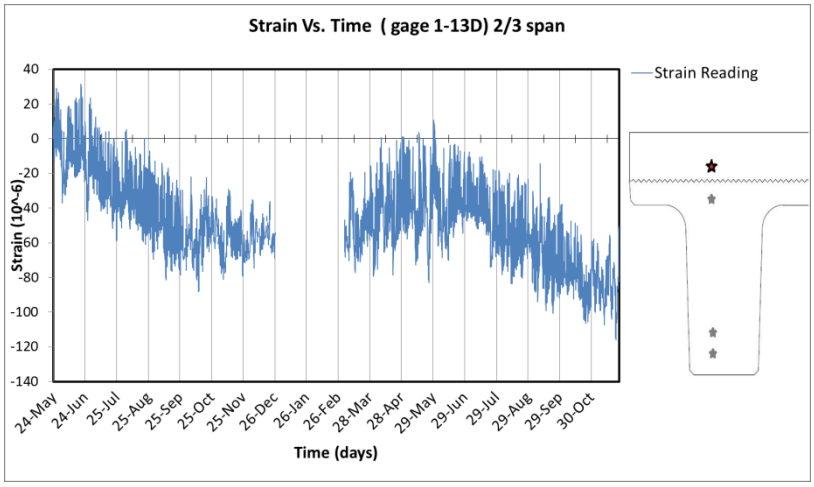

(44): Strain Vs. Time (gage 1-13D)

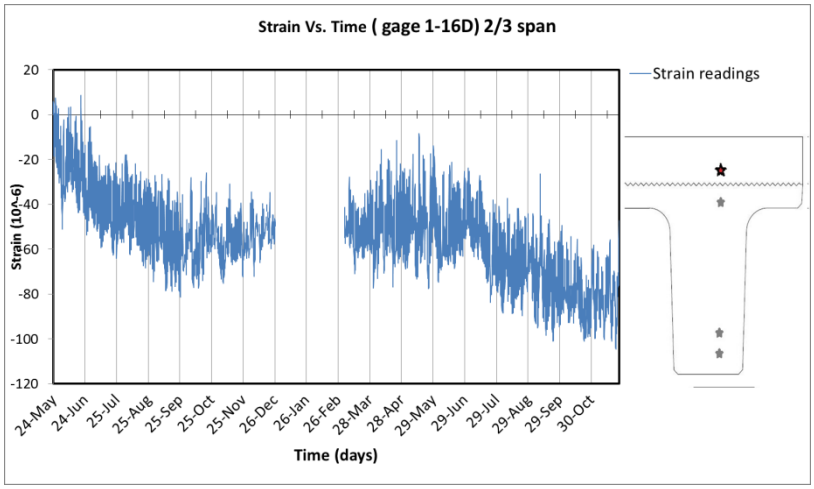

(45): Strain Vs. Time (gage 1-16D)

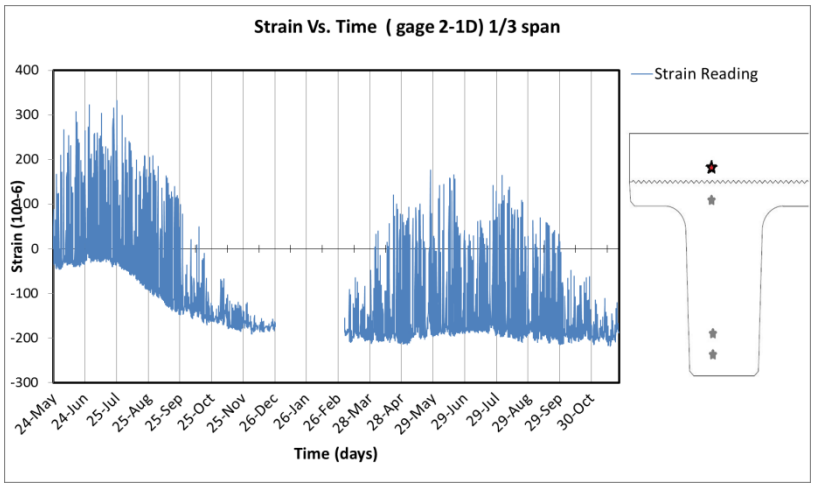

(46): Strain Vs. Time (gage 2-1D)

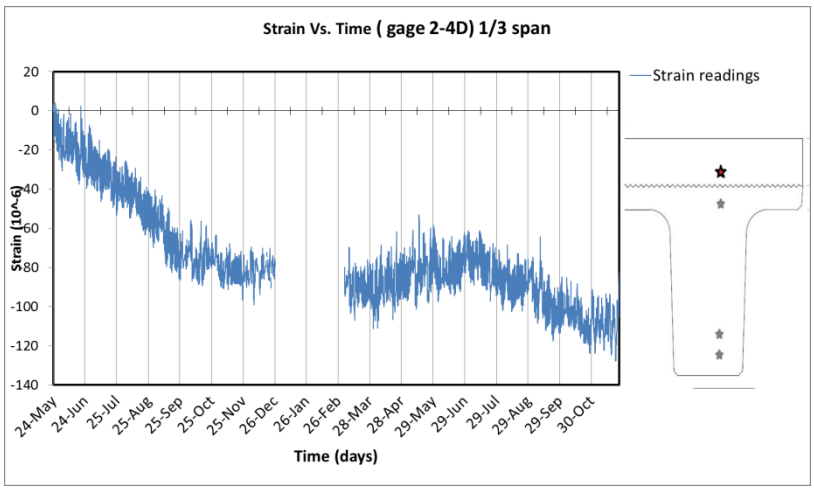

(47): Strain Vs. Time (gage 2-4D)

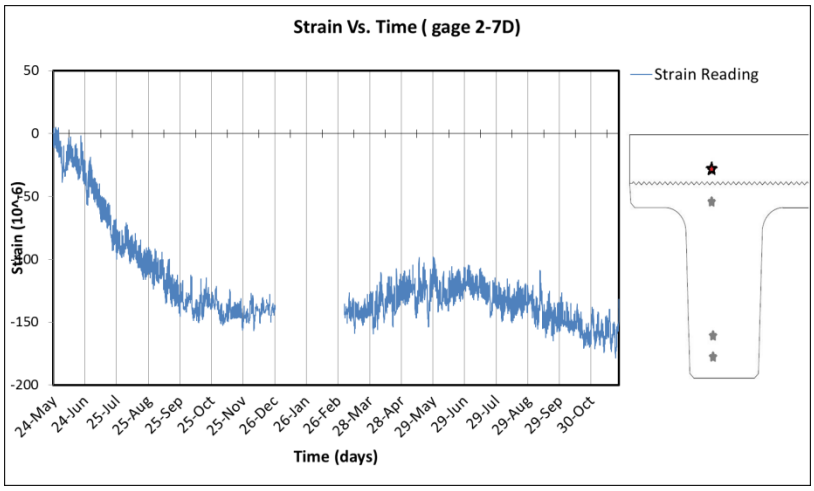

(48): Strain Vs. Time (gage 2-7D)

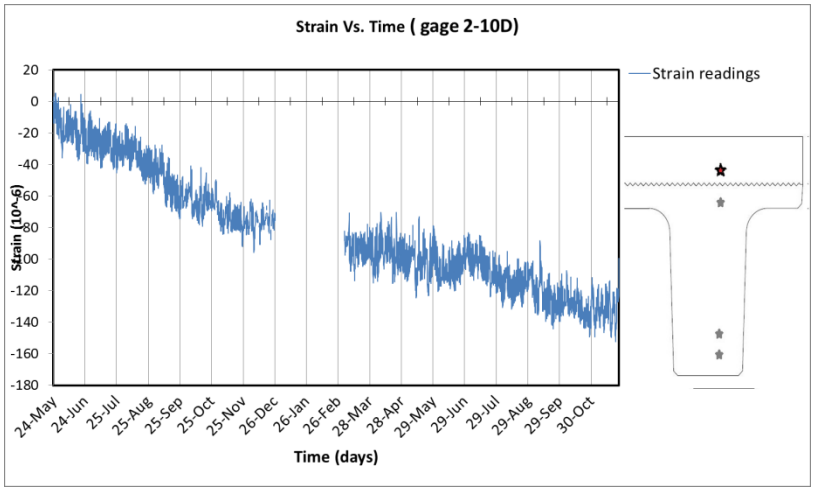

(49): Strain Vs. Time (gage 2-10D)

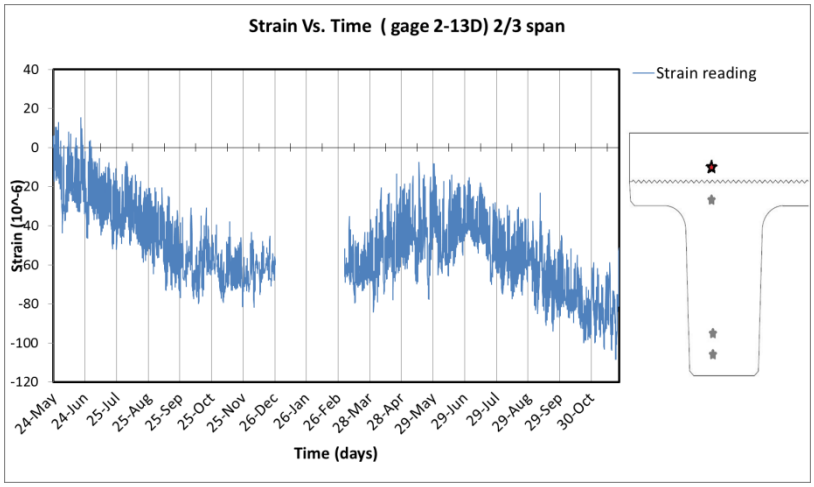

(50): Strain Vs. Time (gage 2-13D)

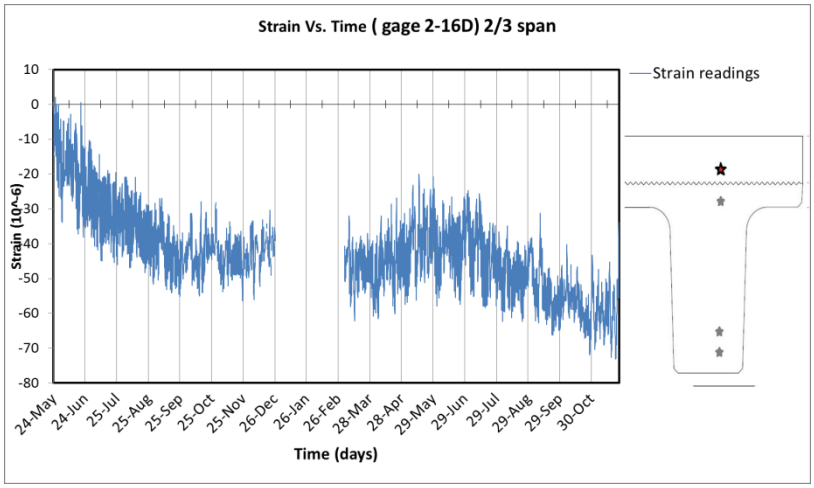

(51): Strain Vs. Time (gage 2-16D)

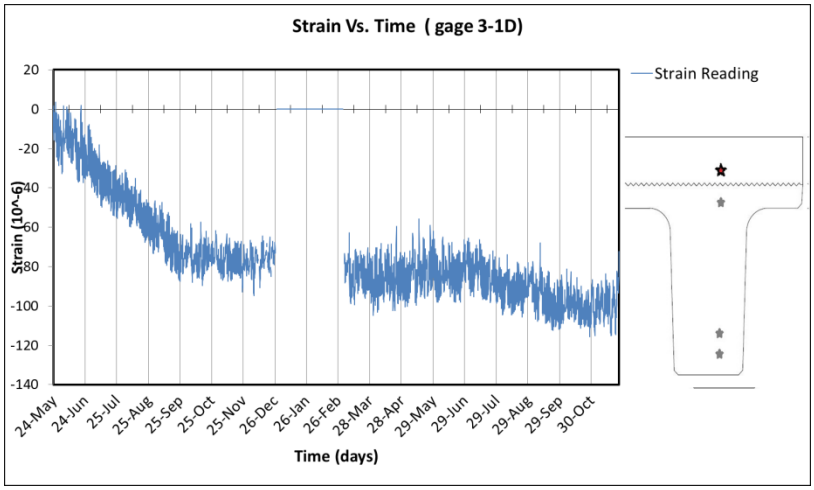

(52): Strain Vs. Time (gage 3-1D)

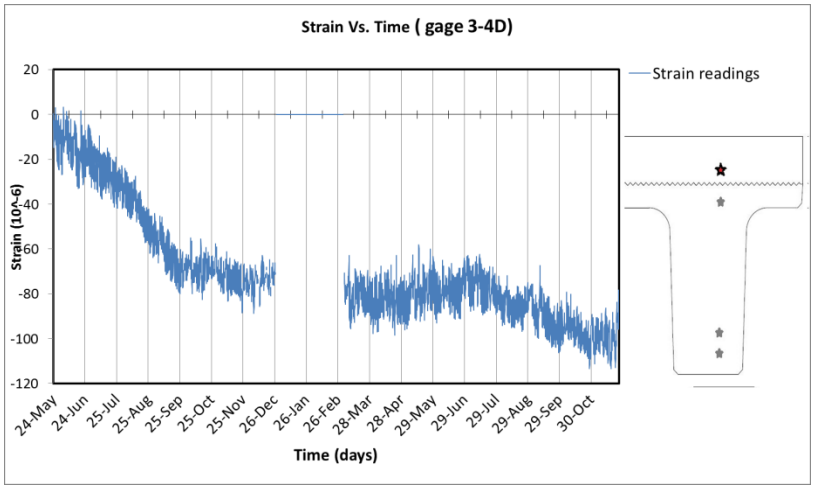

(53): Strain Vs. Time (gage 3-4D)

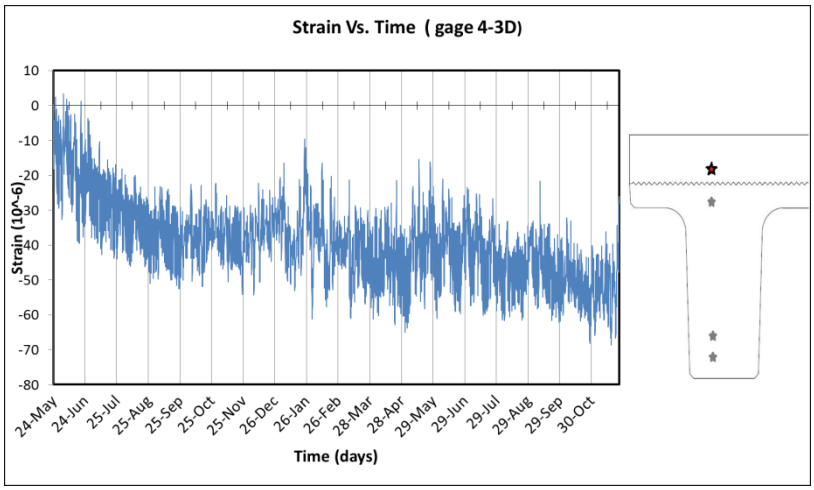

(54): Strain Vs. Time (gage 4-3D)

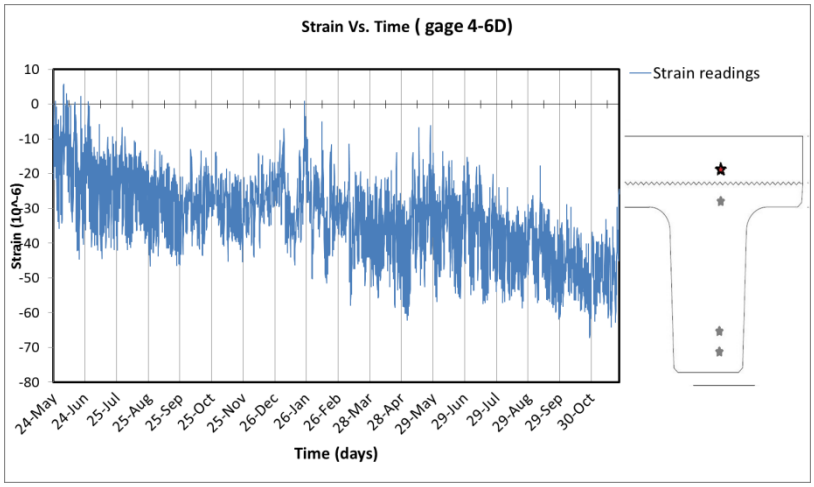

(55): Strain Vs. Time (gage 4-6D)

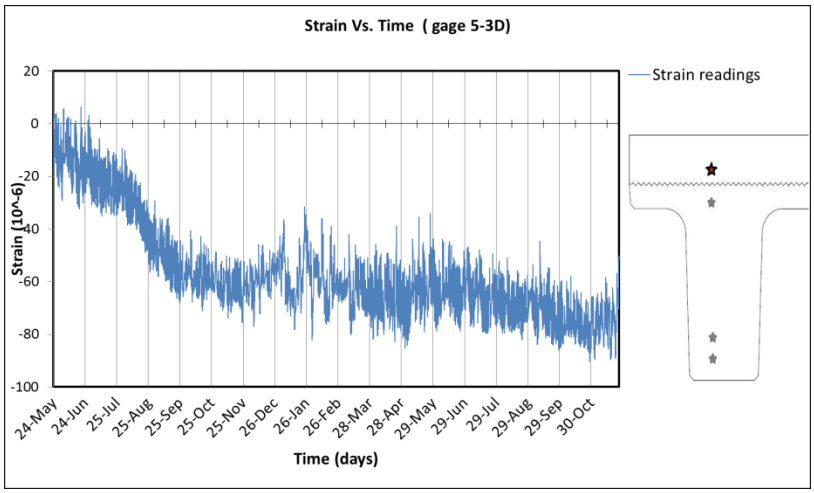

(56): Strain Vs. Time (gage 5-3D)

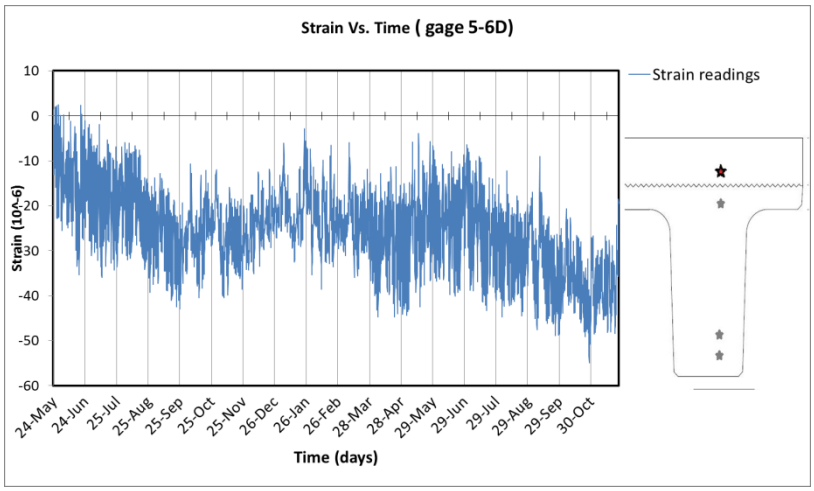

(57): Strain Vs. Time (gage 5-6D)

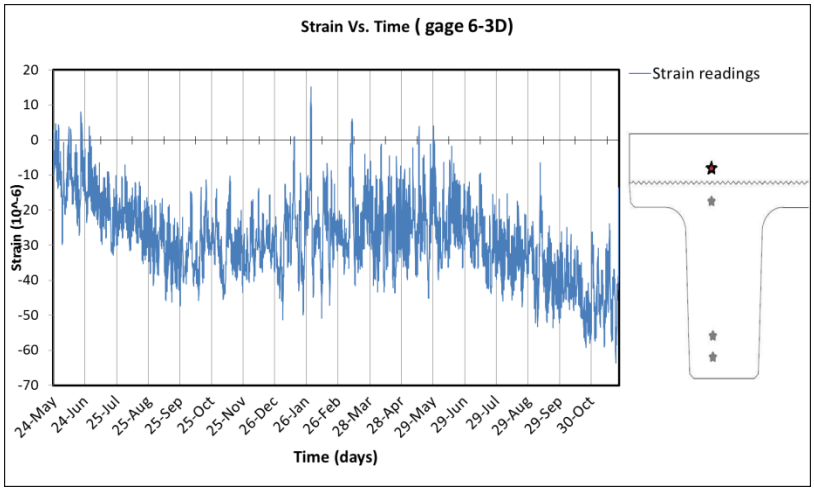

(58): Strain Vs. Time (gage 6-3D)

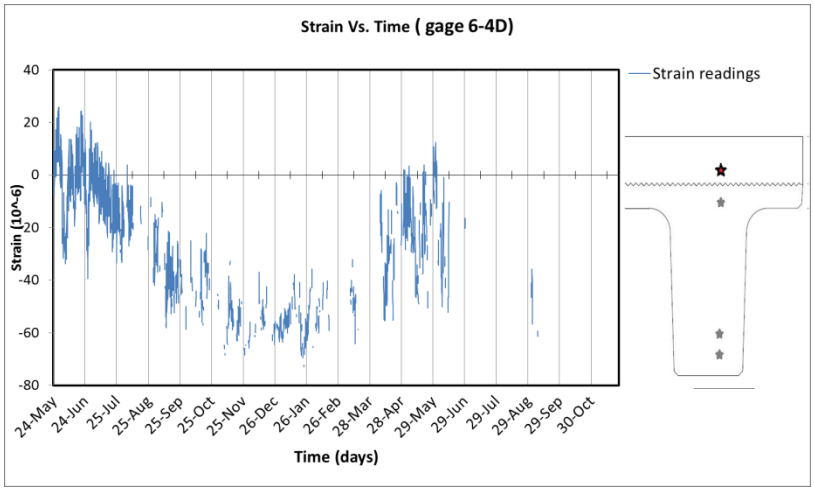

(59): Strain Vs. Time (gage 6-4D)

APPENDIX C

STRAIN DISTRIBUTION THROUGHOUT BEAMS DEPTH

DURING CONSTRUCTION

Figure C: Strain Distribution throughout The Beam Depth

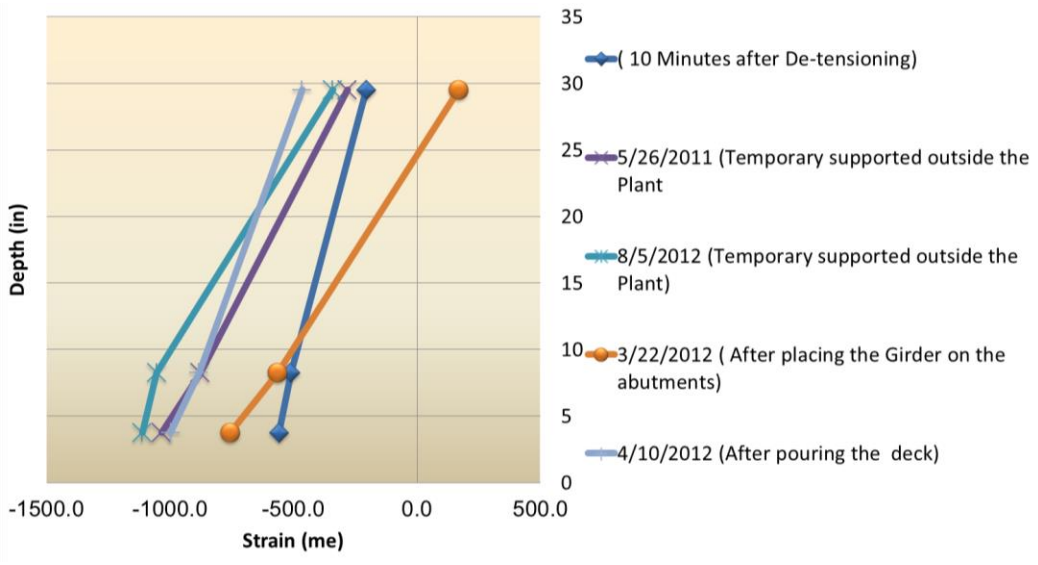

(1): Strain Distribution throughout The Beam Depth 1 (1/3- span)

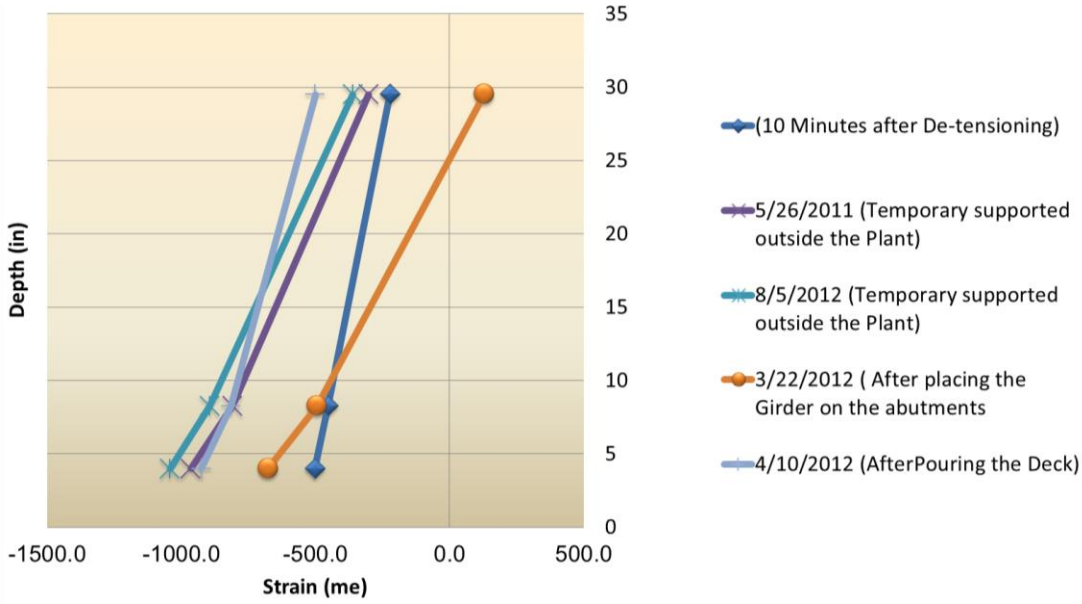

(2): Strain Distribution throughout The Beam Depth 1 (Mid- span)

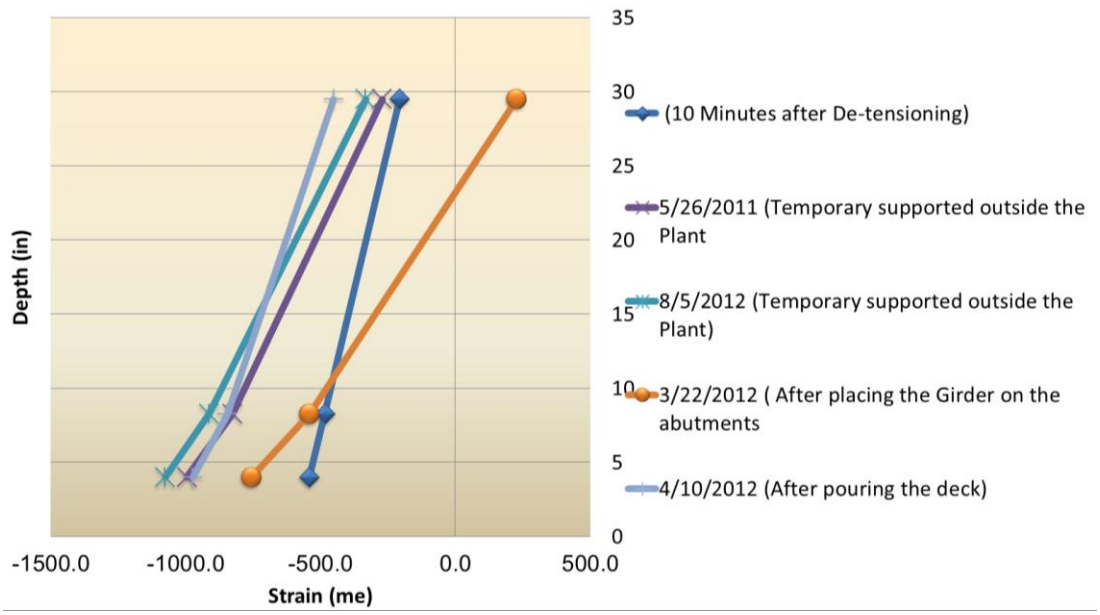

(3): Strain Distribution throughout The Beam Depth 1 (2/3- span)

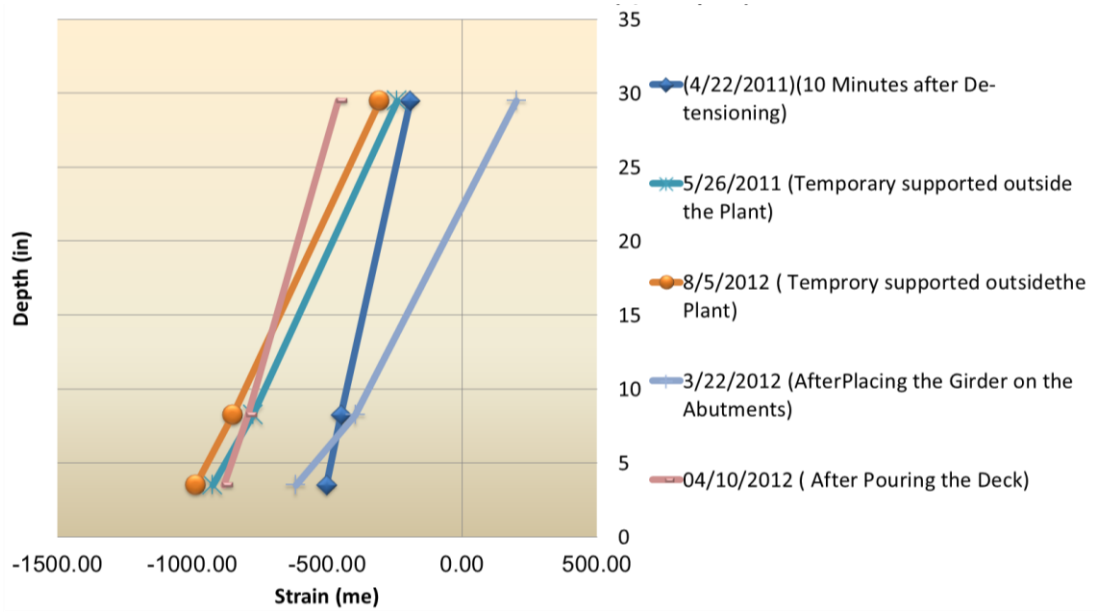

(4): Strain Distribution throughout The Beam Depth 2 (1/3- span)

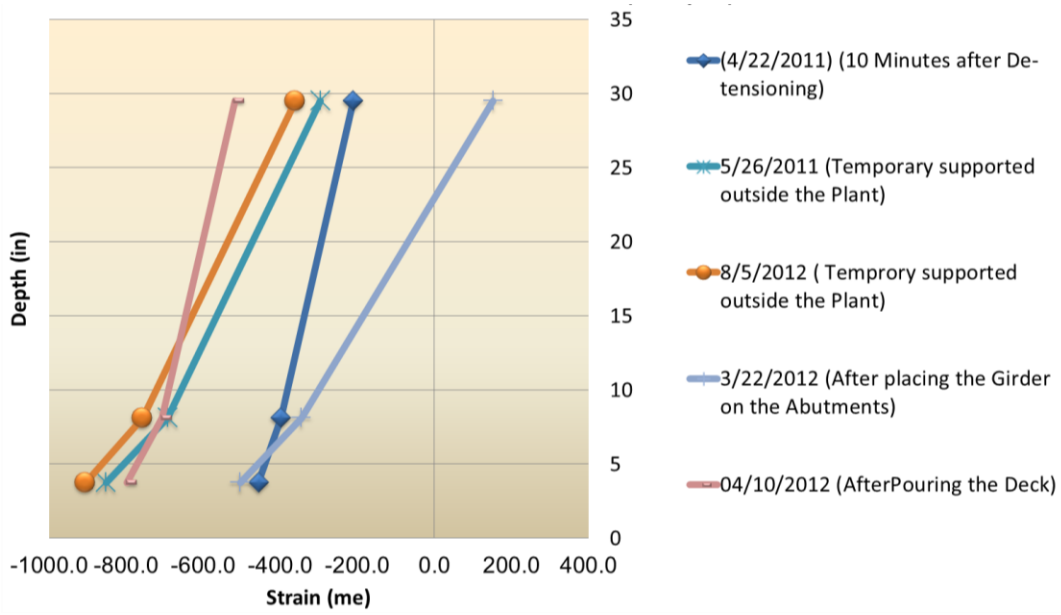

(5): Strain Distribution throughout The Beam Depth 2 (Mid- span)

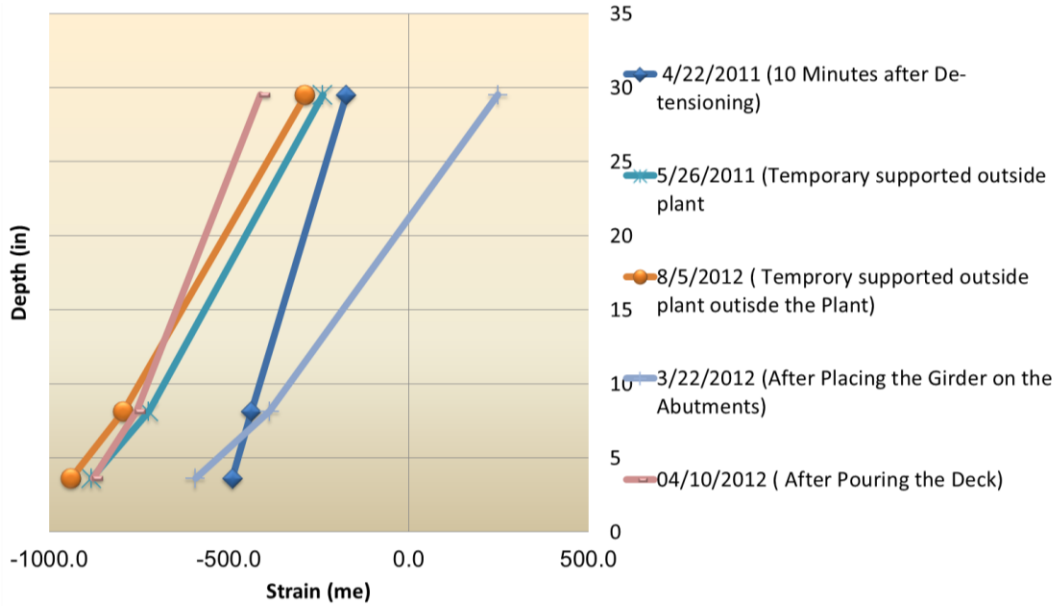

(6): Strain Distribution throughout The Beam Depth 2 (2/3- span)

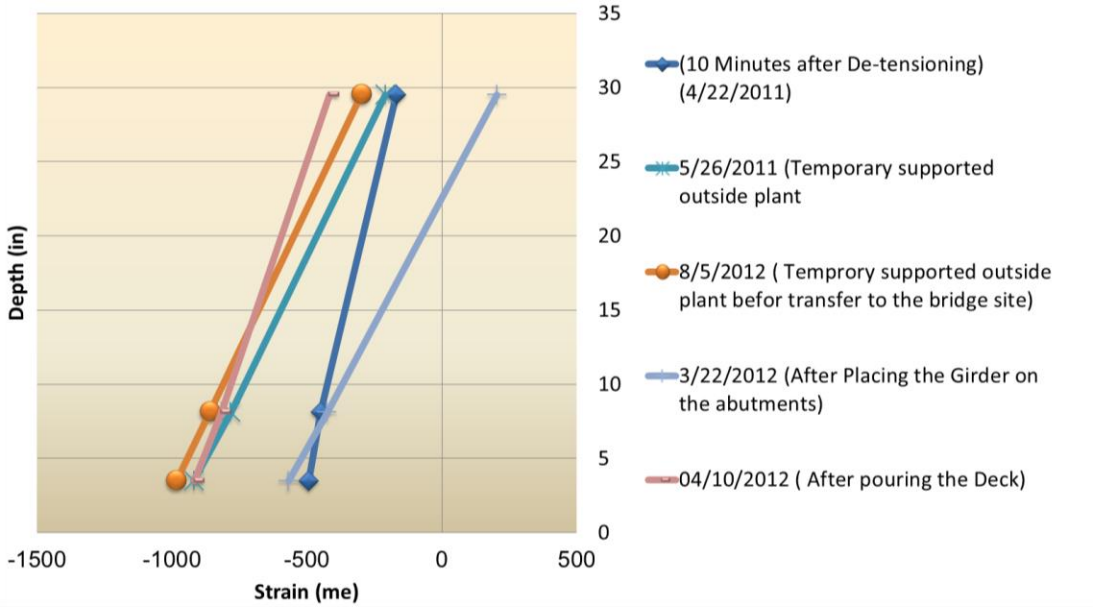

(7): Strain Distribution throughout The Beam Depth 3 (Mid- span)

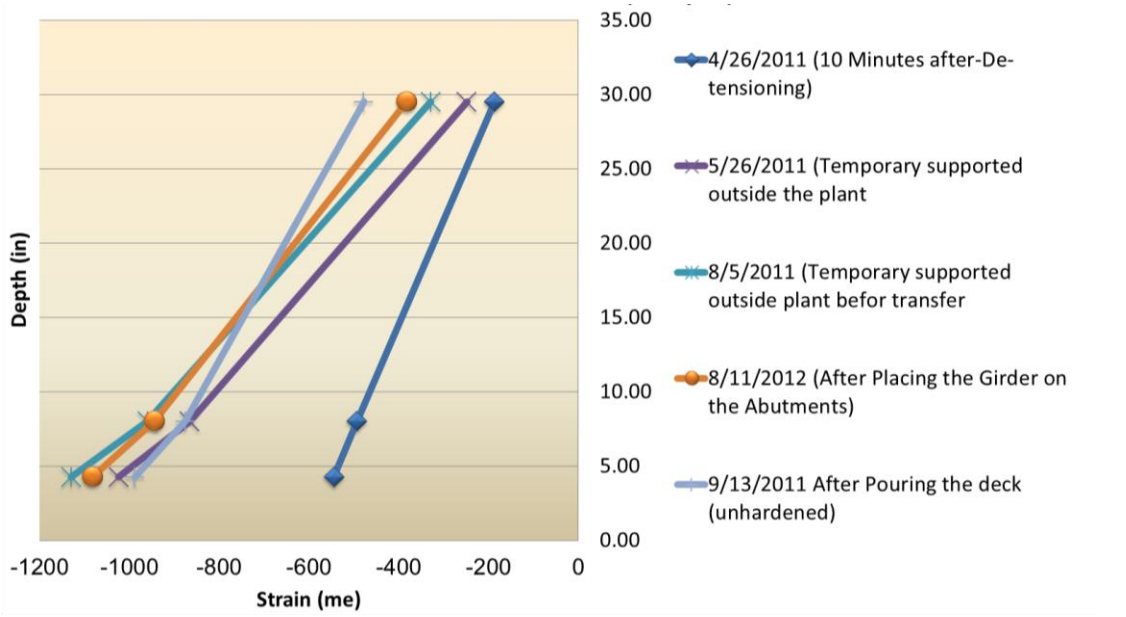

(8): Strain Distribution throughout The Beam Depth 4 (Mid - span)

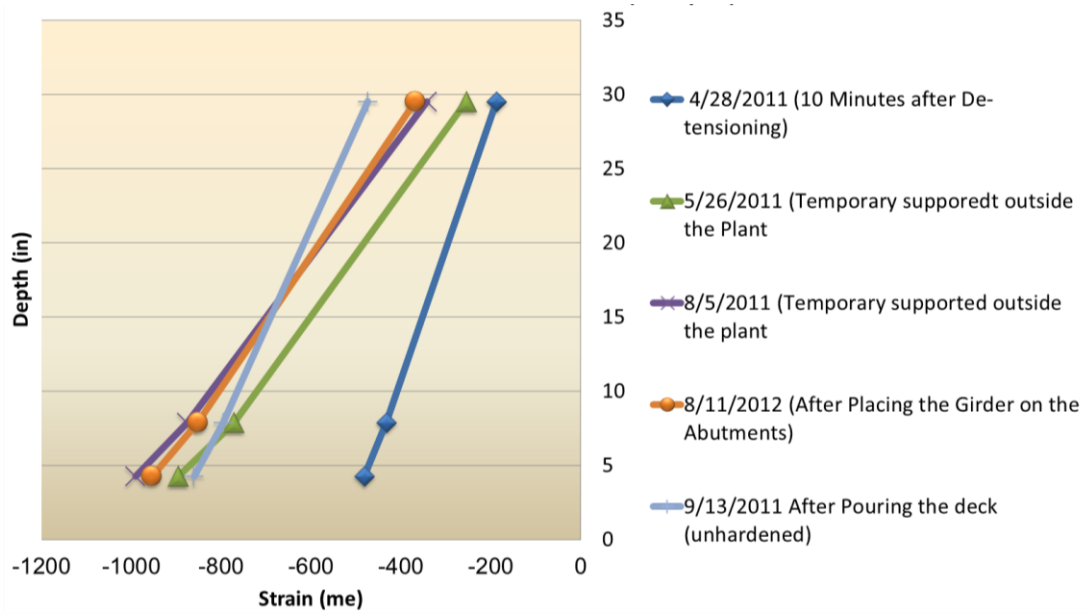

(9): Strain Distribution throughout The Beam Depth 5 (Mid - span)

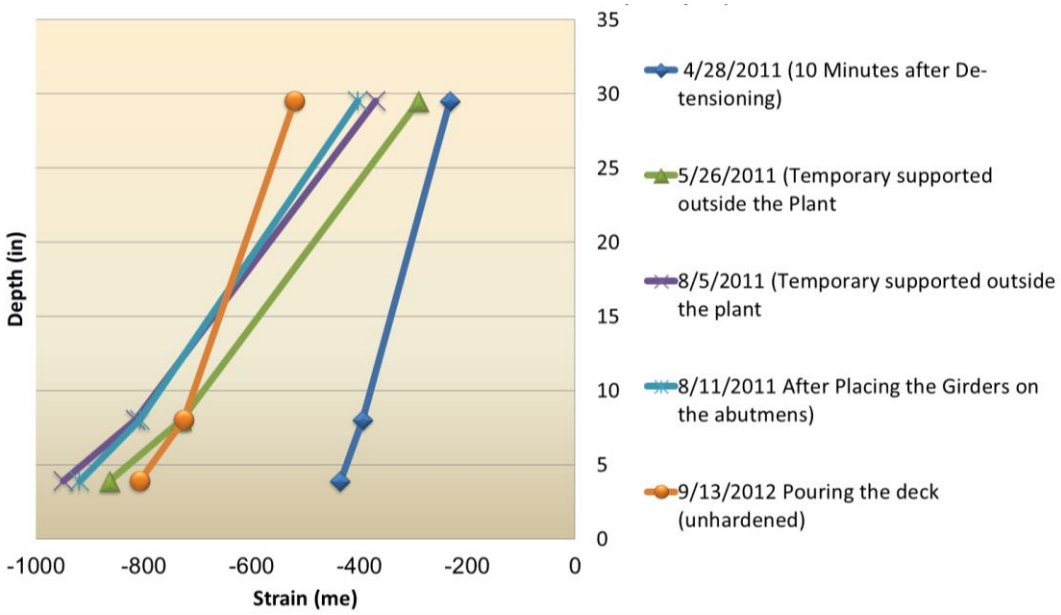

(10): Strain Distribution throughout The Beam Depth 6 (Mid - span)

APPENDIX D

PARAMETRIC ANALYSIS RESULTS

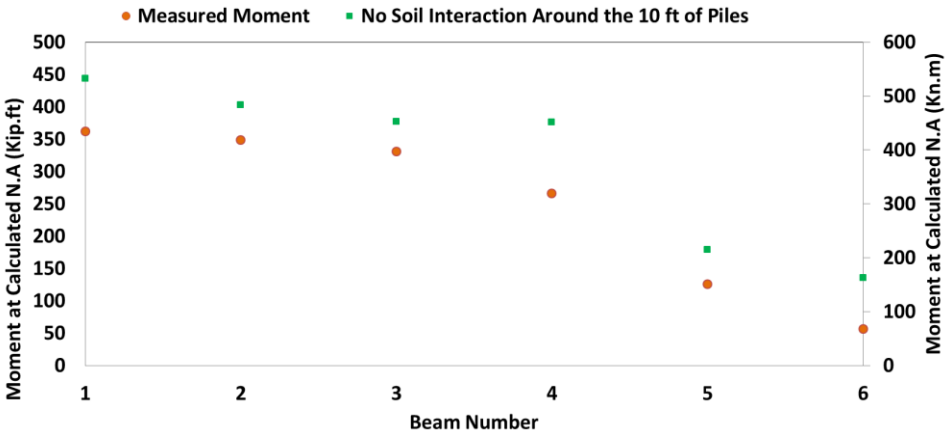

Figure D-1: Comparison between Field and FE Models Results for Configuration 7

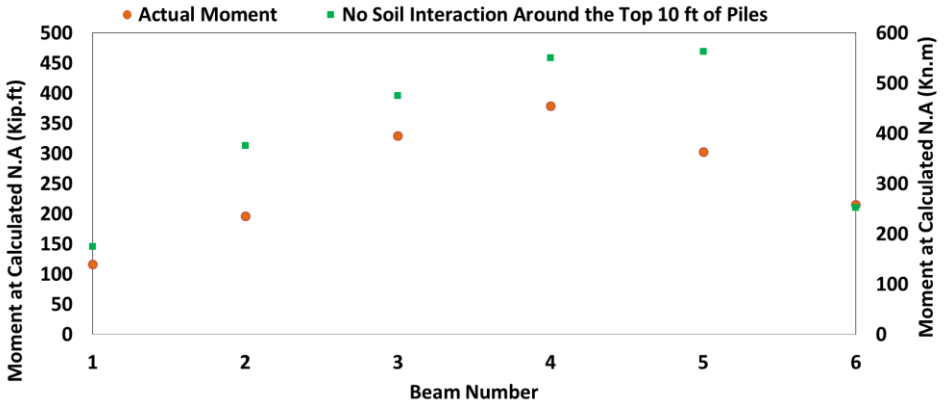

Figure D-2: Comparison between Field and FE Models Results for Configuration 8

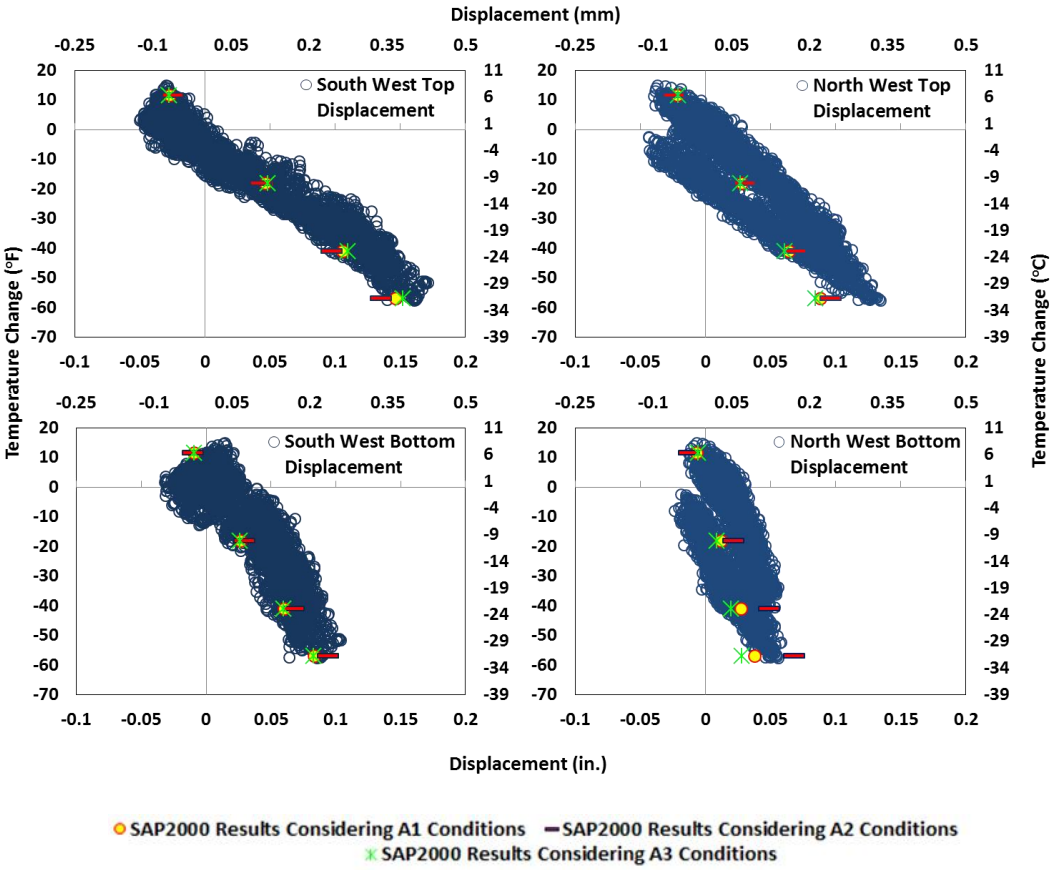

Figure D-3: Comparison among FE Model Displacement Results of Different Soil Conditions with Regards to Field Data

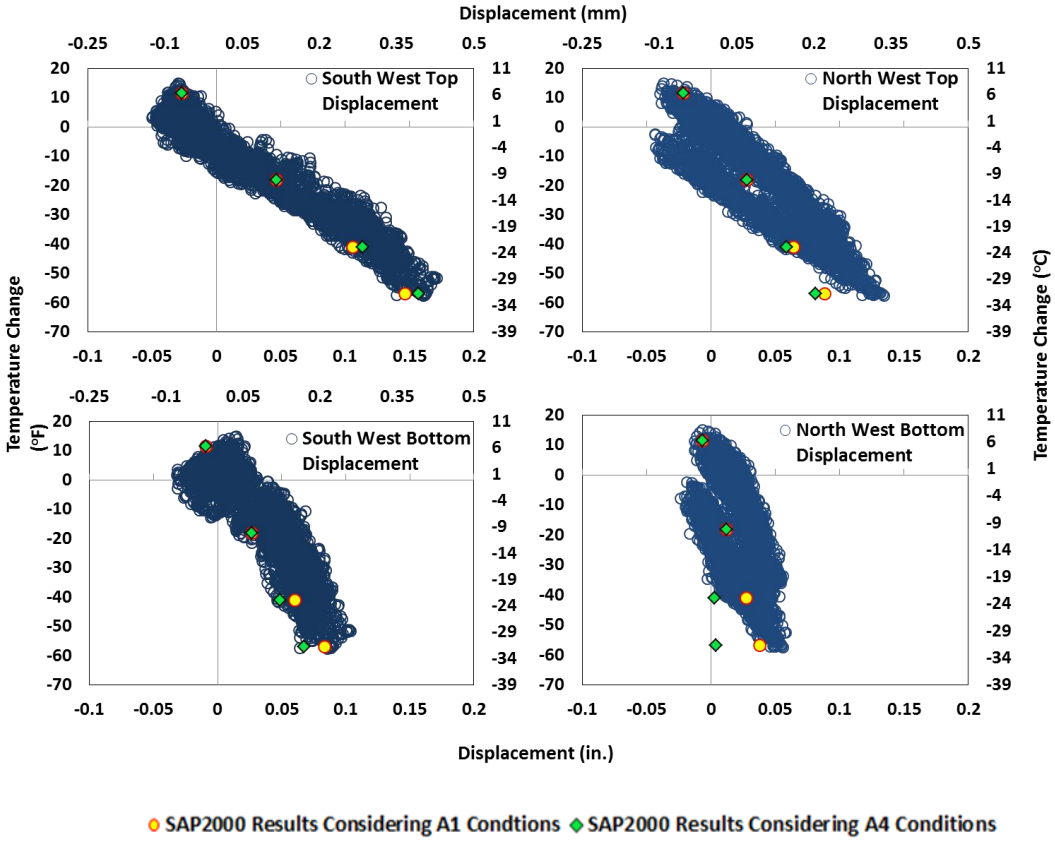

Figure D-4: Comparison among FE Model Displacement Results of Conditions A1 and A4 with Regards to Field Data

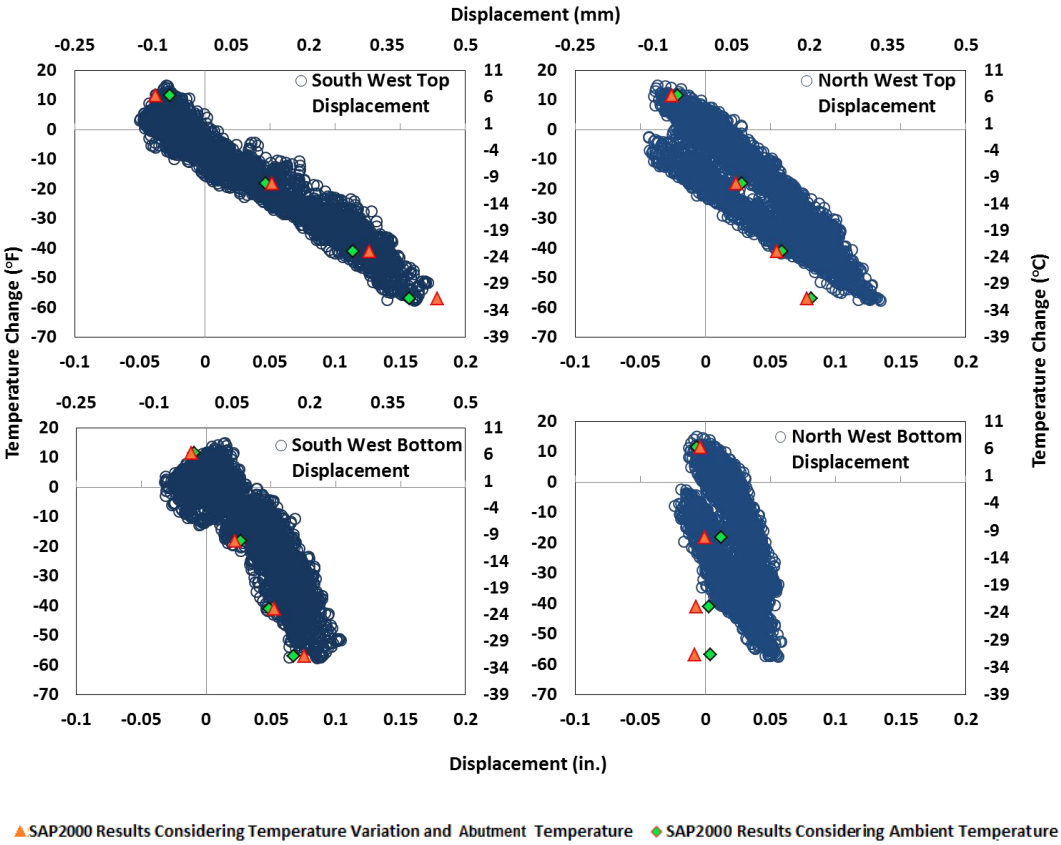

Figure D-5: Comparison between FE Model Displacement Results due to Different Ways in Applying Thermal Loads

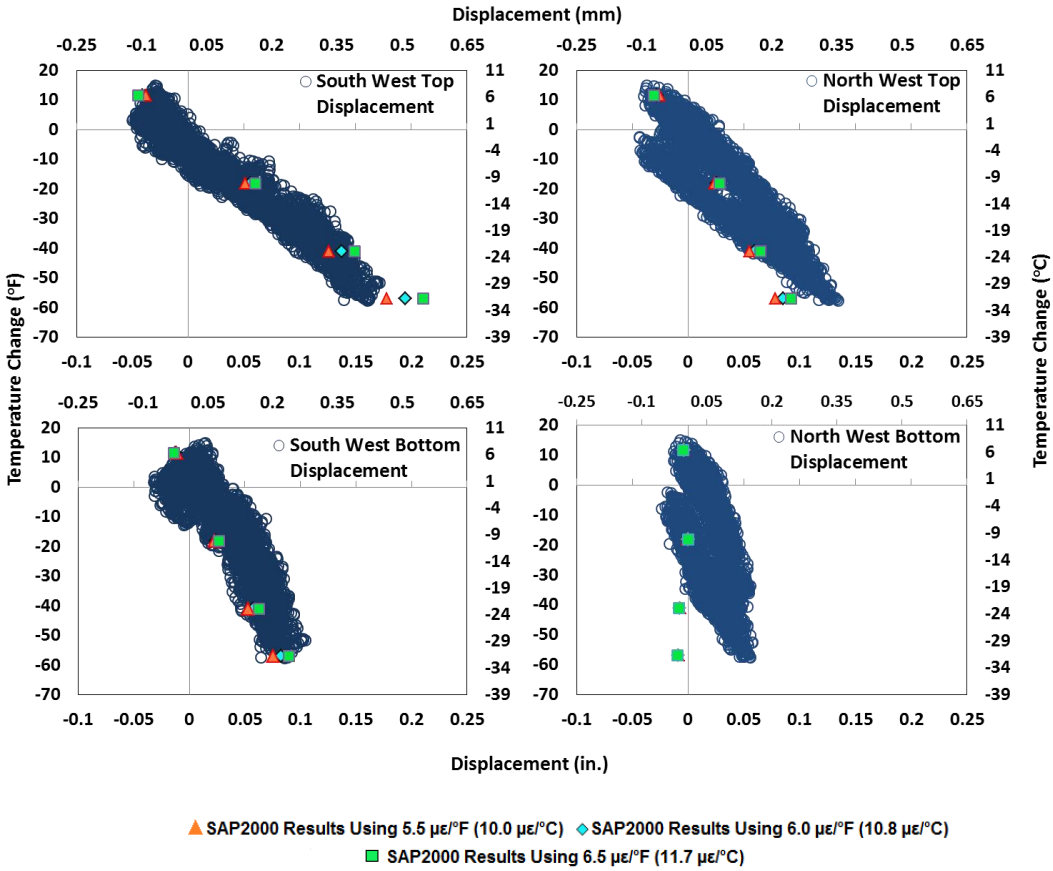

Figure D-6: Comparison among FE Model Displacement Results due to Using Different Coefficient of Thermal Expansion with Regards to Field Data

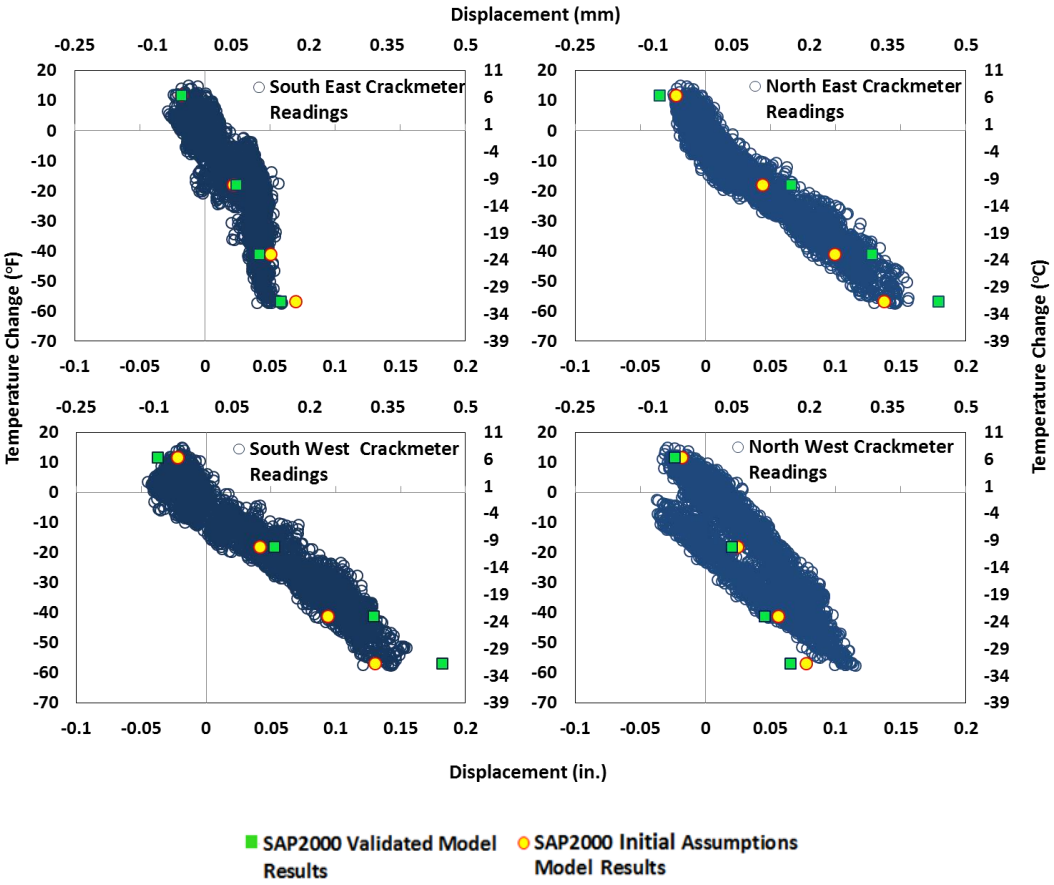

Figure D-7: Comparison between Initial Assumptions FE Model and The Final Calibrated FE Model Displacement Results with Regards to Field Data

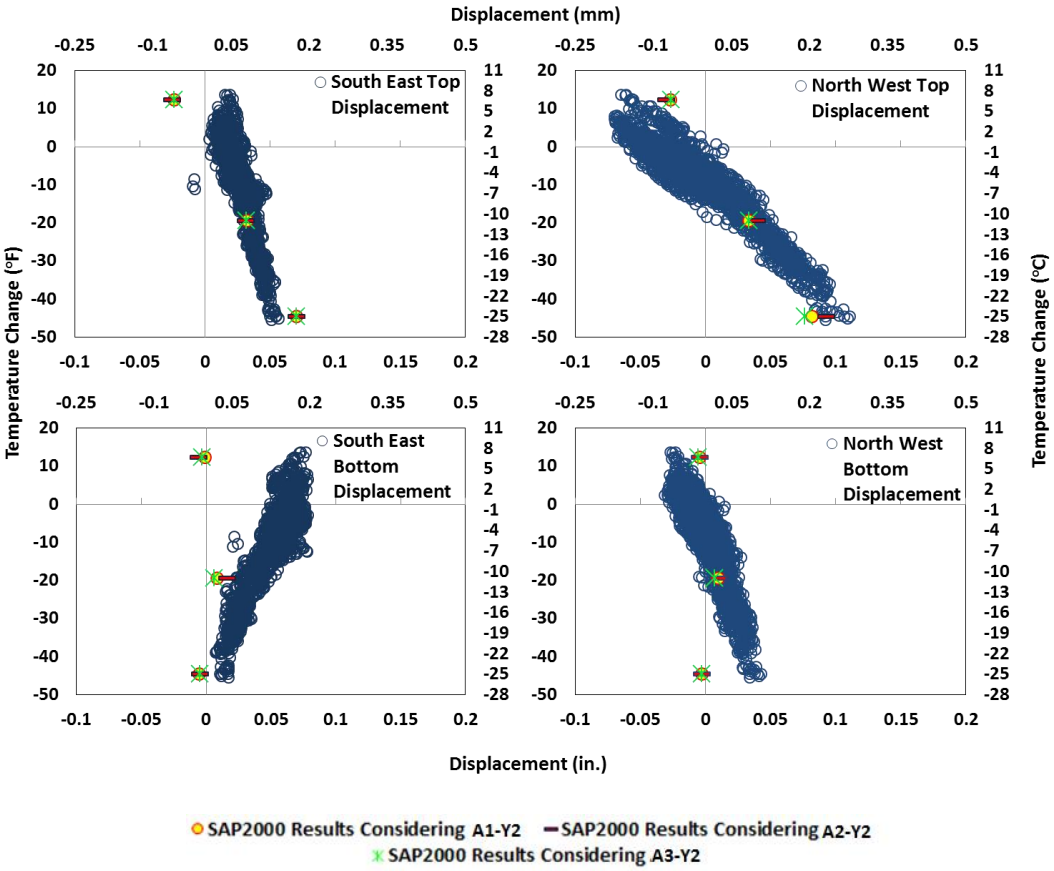

Figure D-8: Comparison among FE Model Displacement Results of Different Soil Conditions Considering no Frozen Soil in Winter with Regards to Field Data

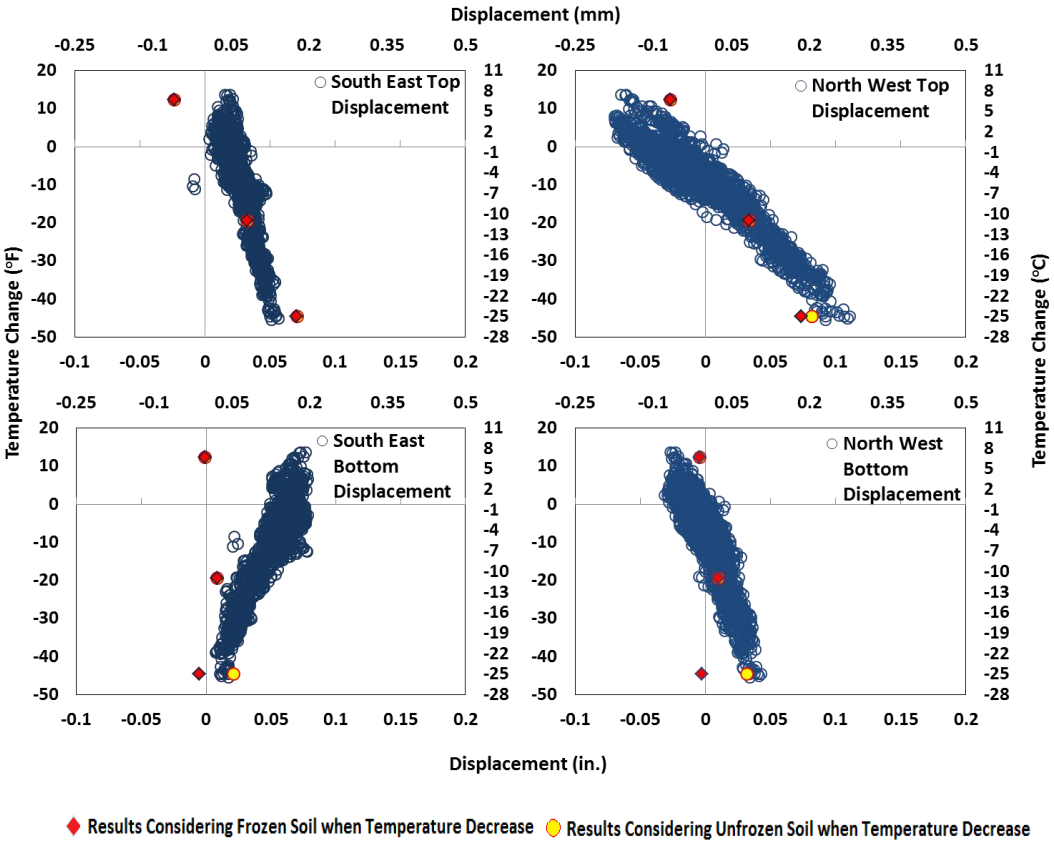

Figure D-9: Comparison between Displacement Results of Two FE Models One Considers Frozen Soil Condition in Winter and The Other Does not with Regards to Field Data

APPENDIX E

MOMENT IN PILES

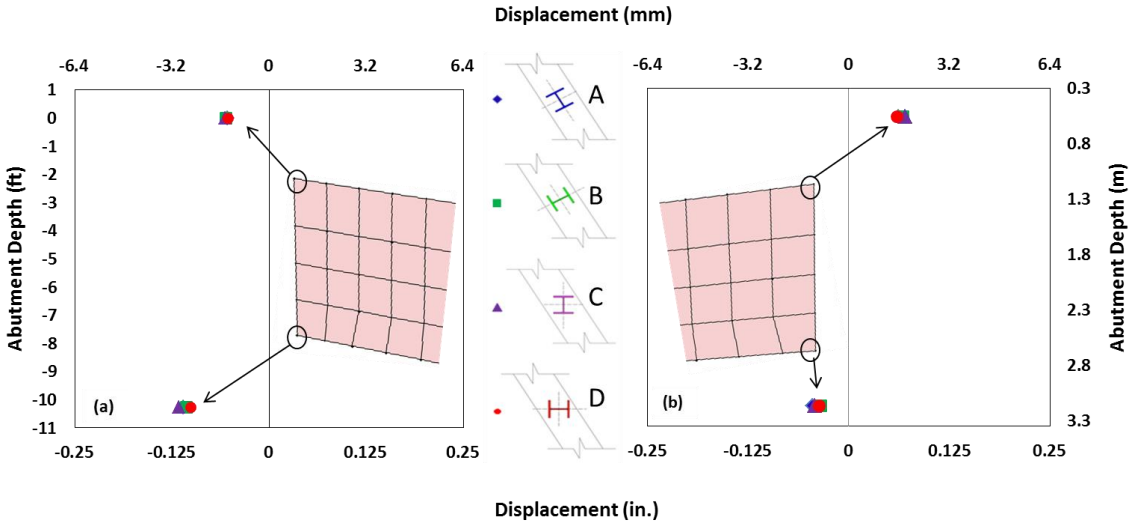

Figure E-1: Longitudinal Abutment Displacements from Different Pile Orientations: Temperature Increase and Dead Load (a) Obtuse Corner (b) Acute Corner (South Abutment) (North Abutment)

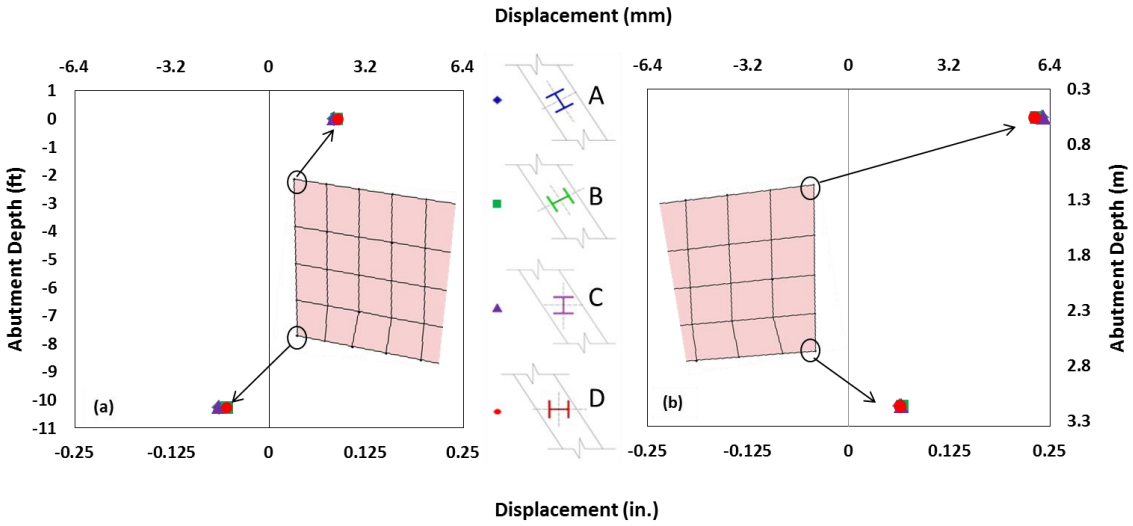

Figure E-2: Longitudinal Abutment Displacements from Different Pile Orientations: Temperature Decrease and Dead Load (a) Obtuse Corner (b) Acute Corner (North Abutment)

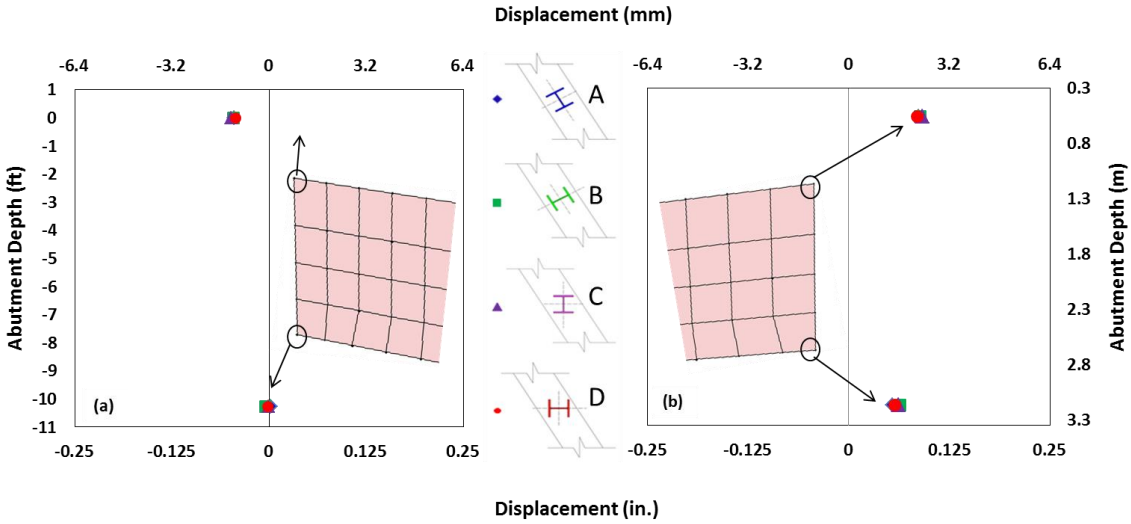

Figure E-3: Transverse Abutment Displacements from Different Pile Orientations: Temperature Increase and Dead Load (a) Obtuse Corner (b) Acute Corner (North Abutment)

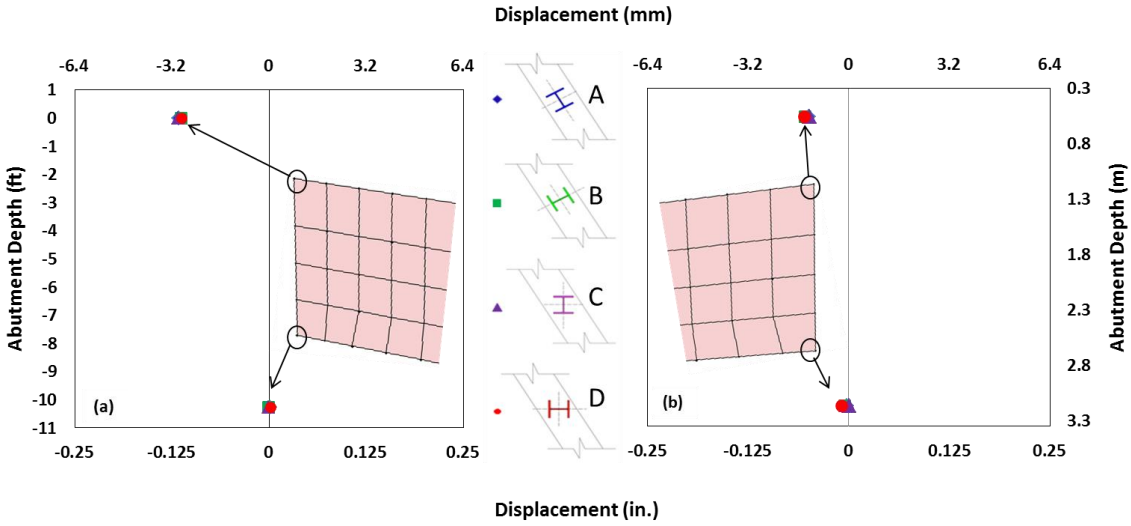

Figure E-4: Transverse Abutment Displacements from Different Pile Orientations: Temperature Decrease and Dead Load (a) Obtuse Corner (b) Acute Corner (North Abutment)

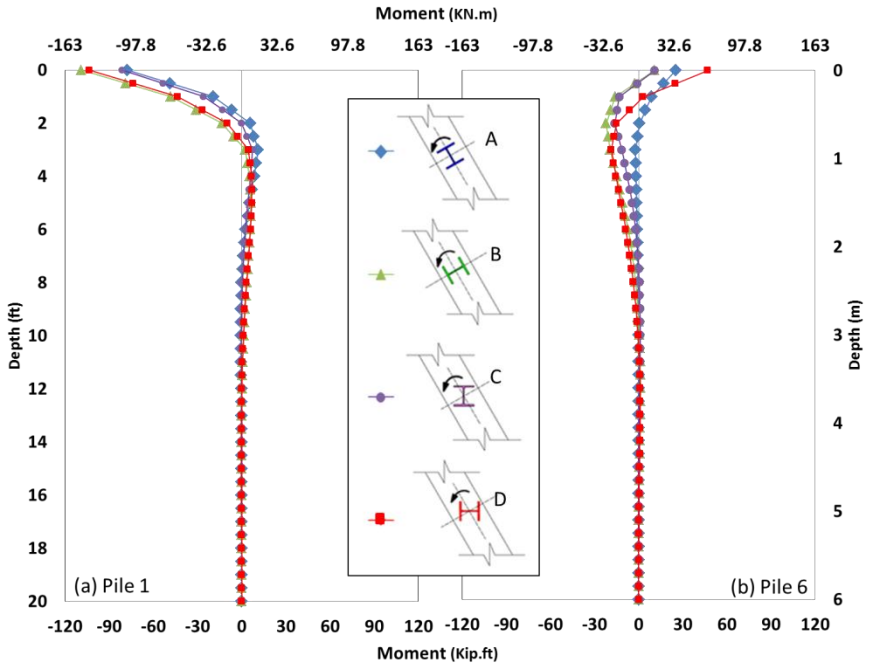

Figure E-5: Moments in the Exterior Piles about 1-1 Due to Dead Load and Decrease in Temperature (North Abutment)

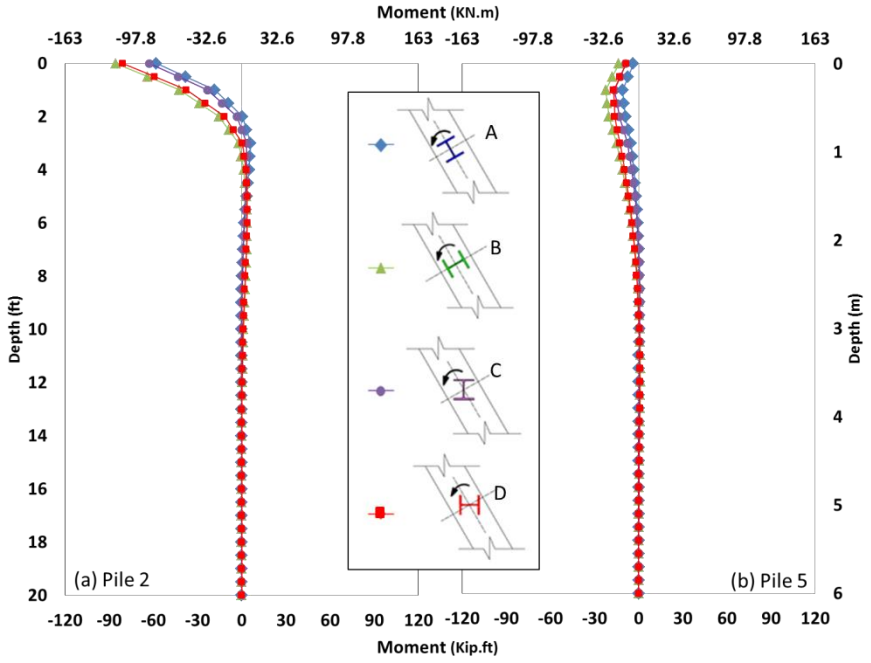

Figure E-6: Moments in the Interior Piles about 1-1 Due to Dead Load and Decrease in Temperature (North Abutment)

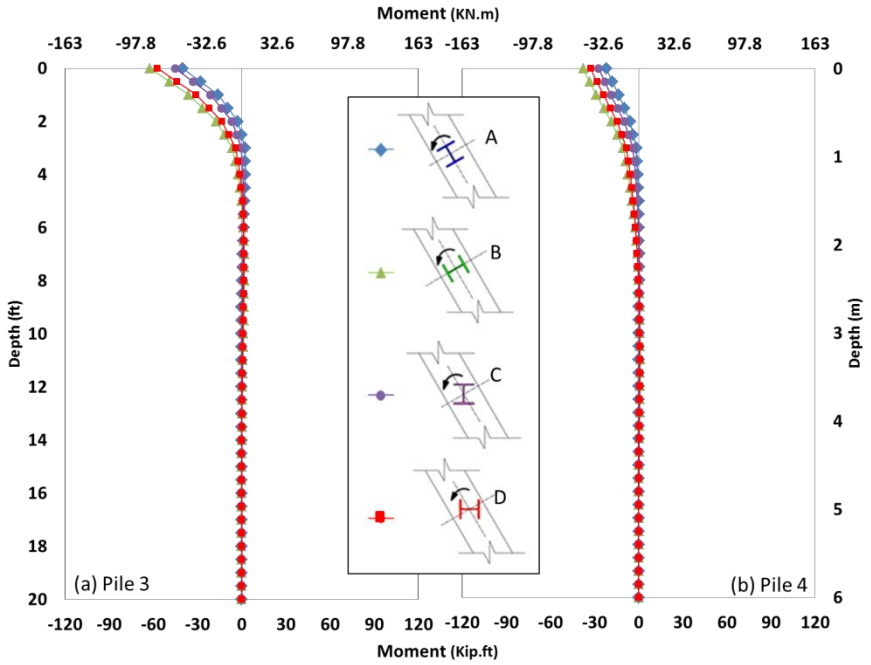

Figure E-7: Moments in the Interior Piles about 1-1 Due to Dead Load and Decrease in Temperature (North Abutment)

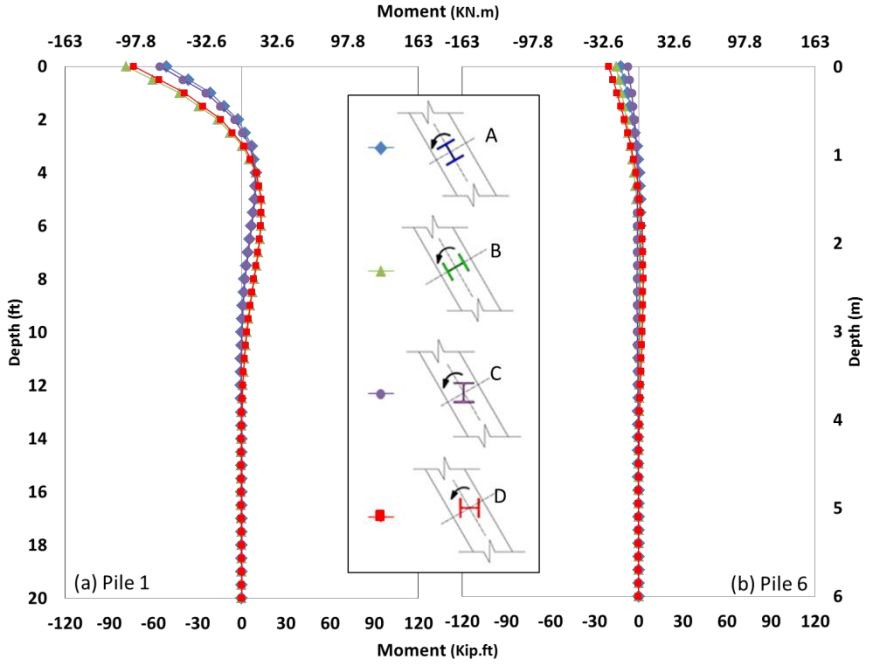

Figure E-8: Moments in the Exterior Piles about 1-1 Due to Dead Load and Increase in Temperature (North Abutment)

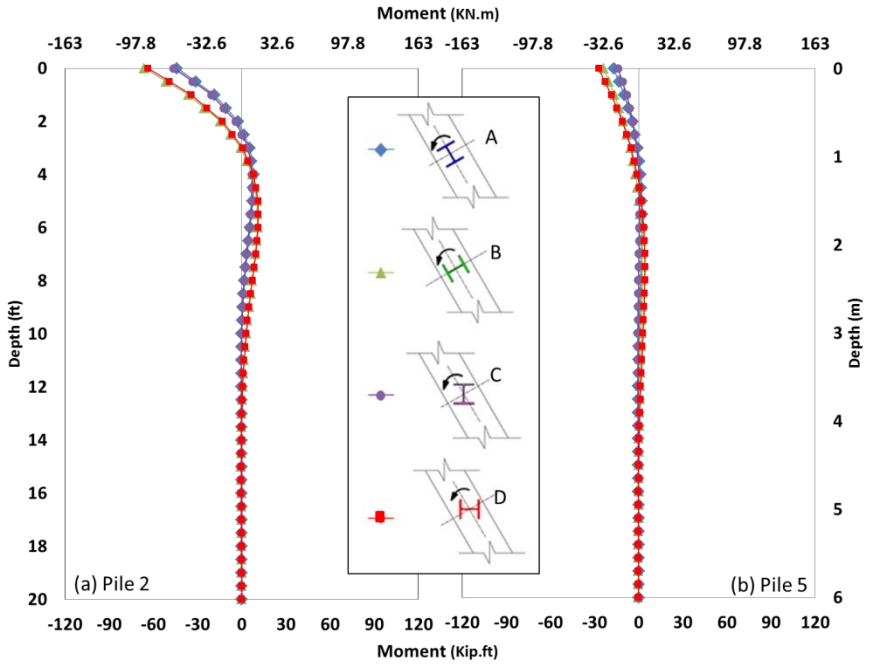

Figure E-9: Moments in the Interior Piles about 1-1 Due to Dead Load and Increase in Temperature (North Abutment)

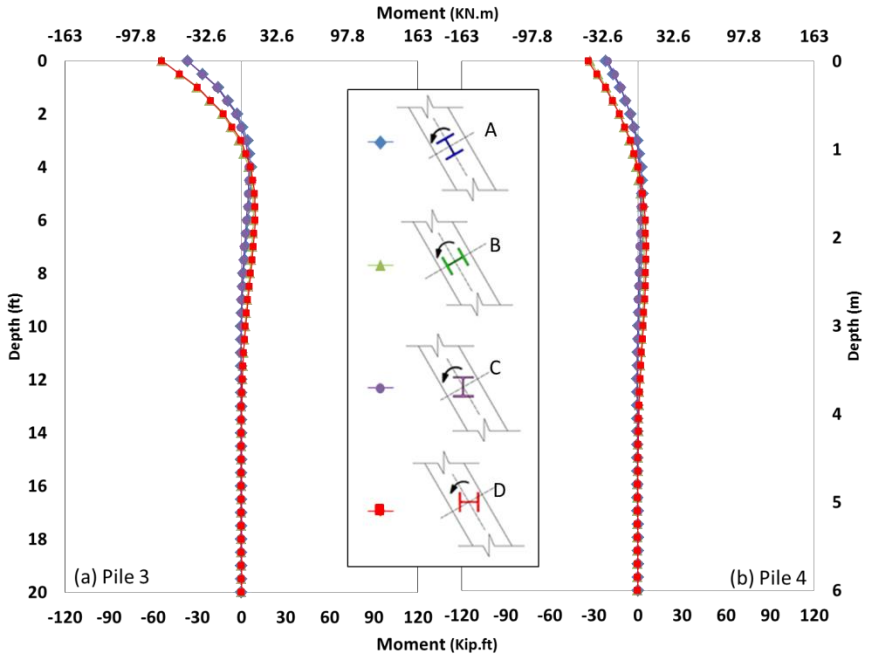

Figure E-10: Moments in the Interior Piles about 1-1 Due to Dead Load and Increase in Temperature (North Abutment)

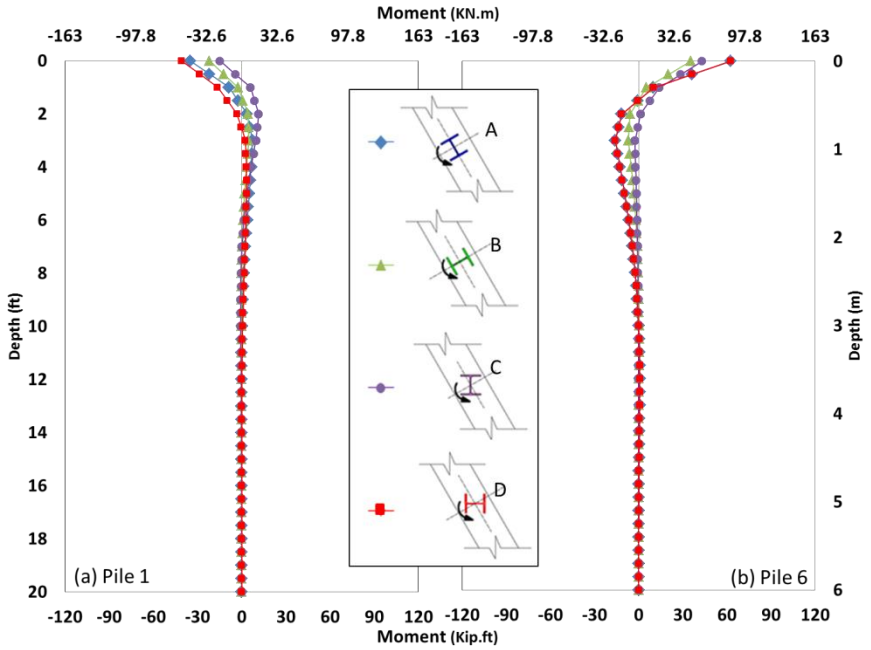

Figure E-11: Moments in the Exterior Piles about 2-2 Due to Dead Load and Decrease in Temperature (North Abutment)

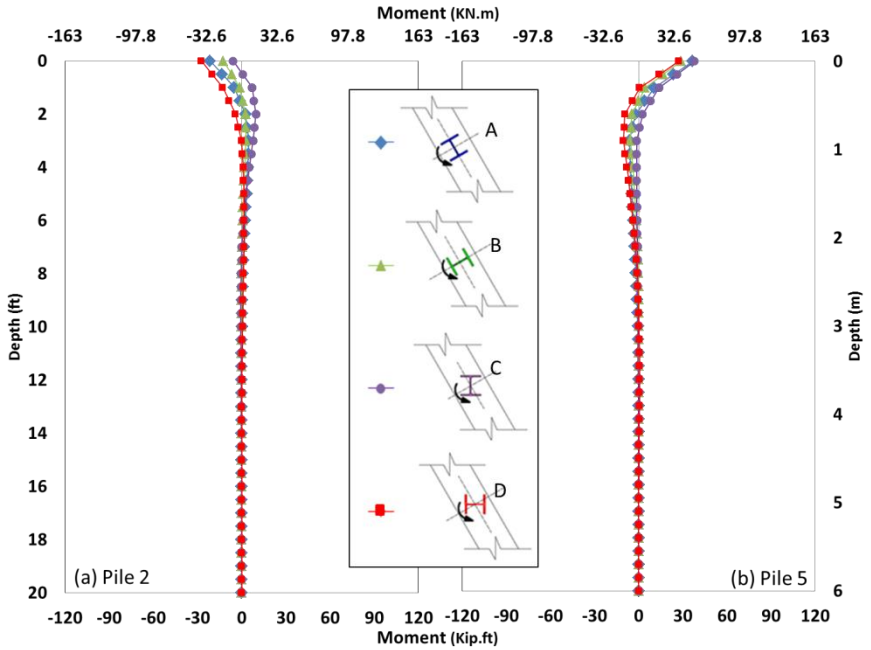

Figure E-12: Moments in the Interior Piles about 2-2 Due to Dead Load and Decrease in Temperature (North Abutment)

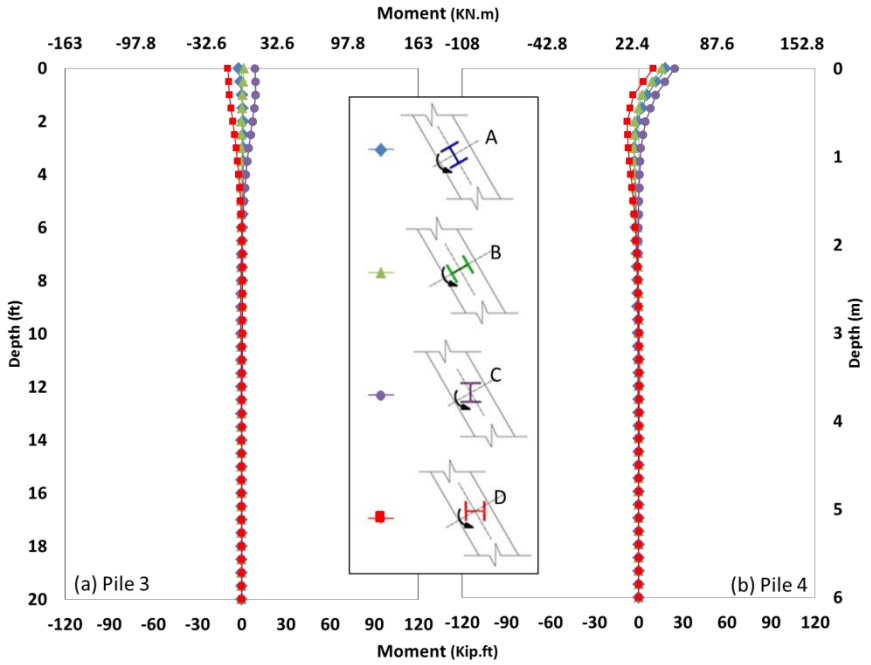

Figure E-13: Moments in the Interior Piles about 2-2 Due to Dead Load and Decrease in Temperature (North Abutment)

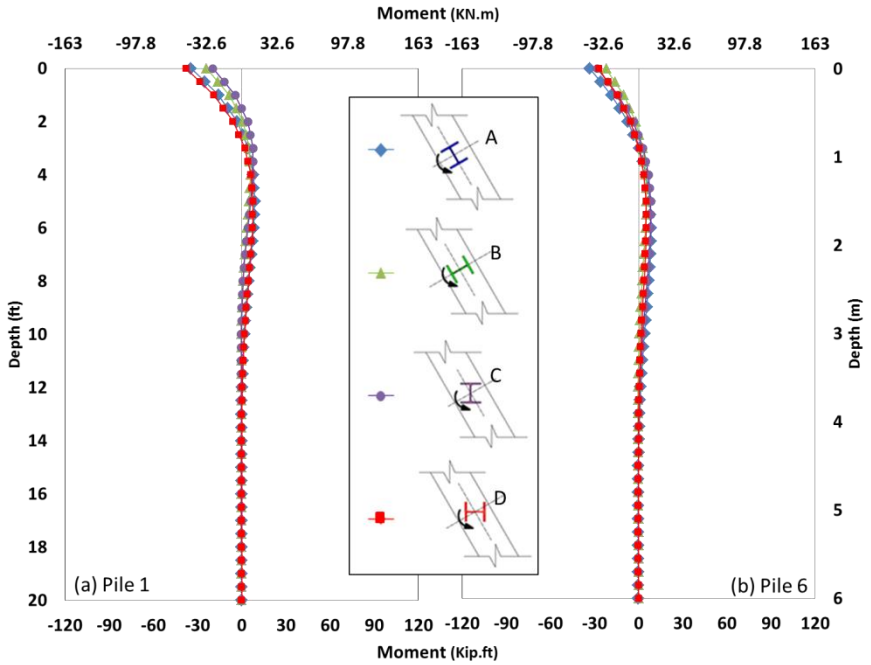

Figure E-14: Moments in the Exterior Piles about 2-2 Due to Dead Load and Increase in Temperature (North Abutment)

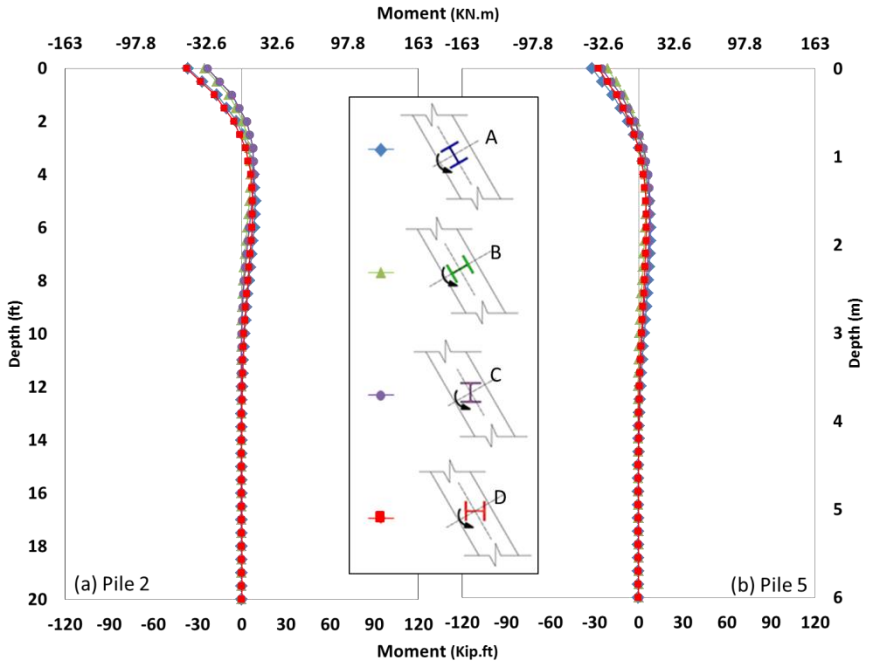

Figure E-15: Moments in the Interior Piles about 2-2 Due to Dead Load and Increase in Temperature (North Abutment)

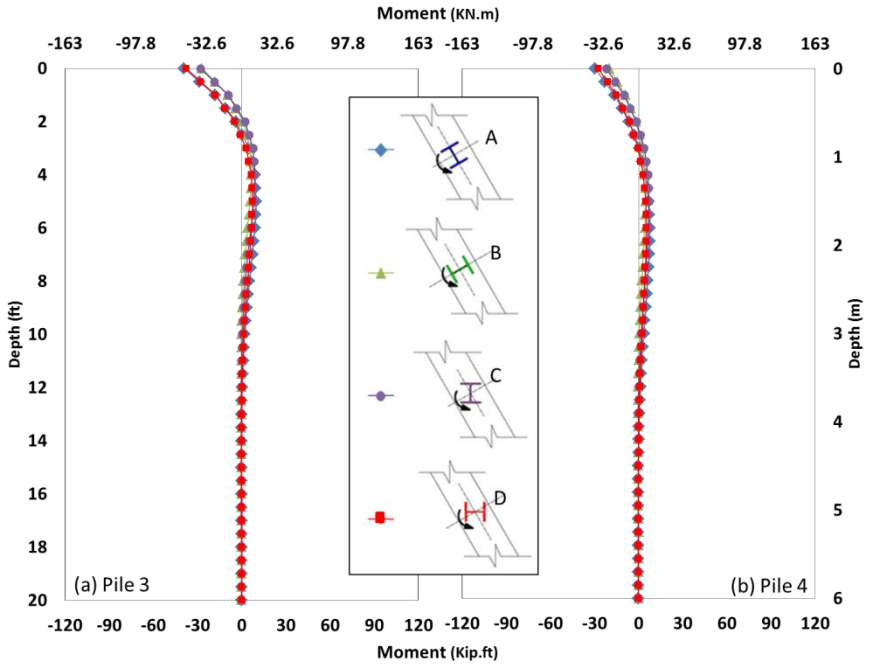

Figure E-16: Moments in the Interior Piles about 2-2 Due to Dead Load and Increase in Temperature (North Abutment)

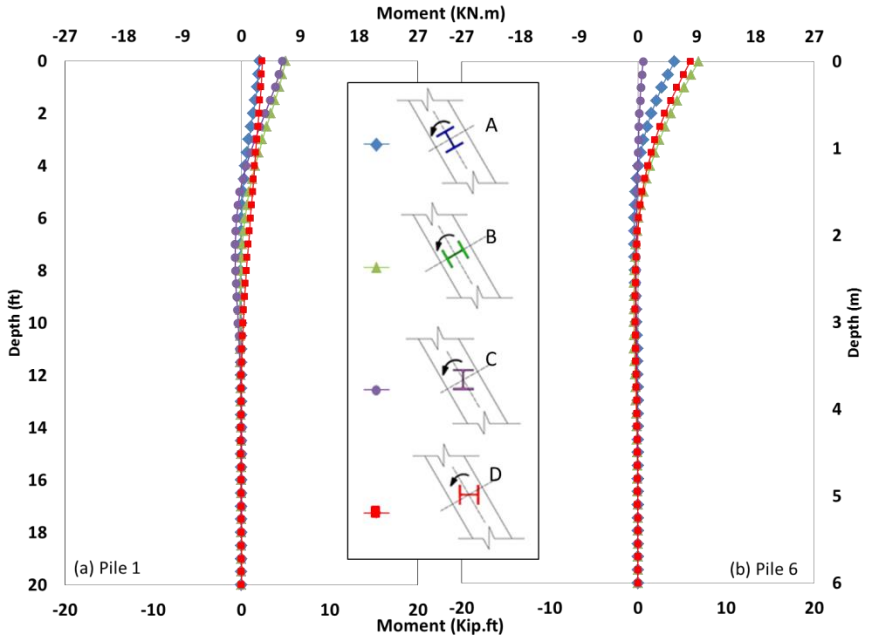

Figure E-17: Moments in the Exterior Piles about 1-1 Due to Increase in Temperature (South Abutment)

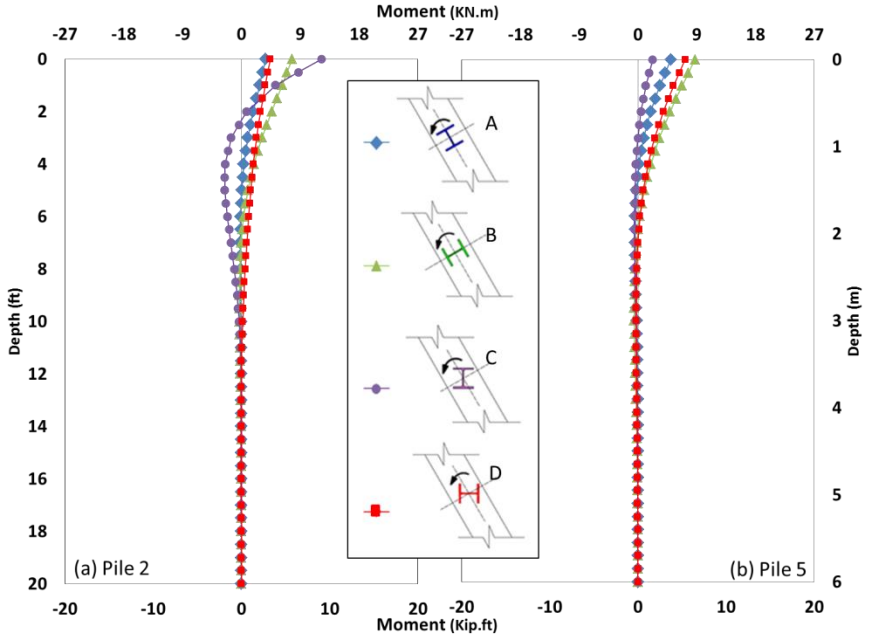

Figure E-18: Moments in the Interior Piles about 1-1 Due to Increase in Temperature (South Abutment)

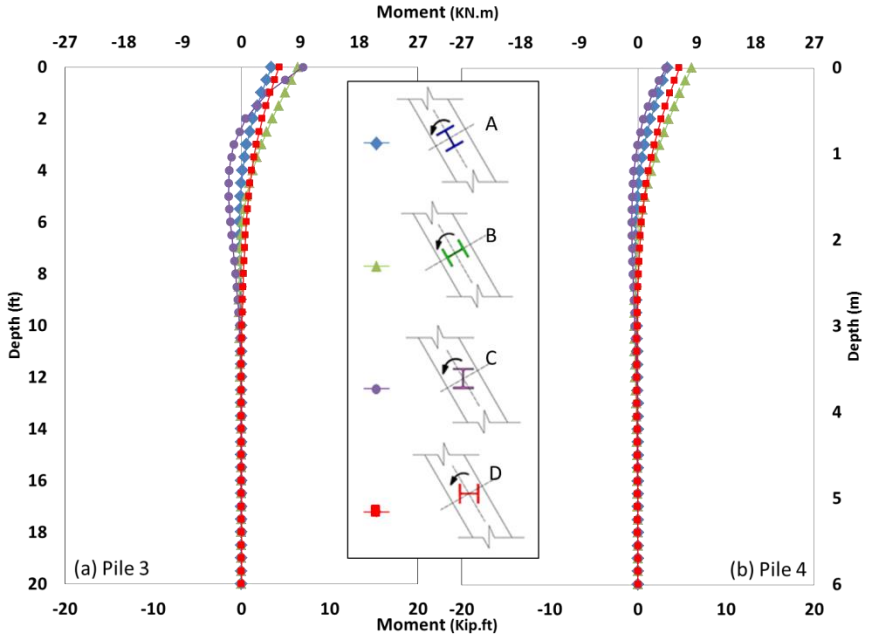

Figure E-19: Moments in the Interior Piles about 1-1 Due to Increase in Temperature (South Abutment)

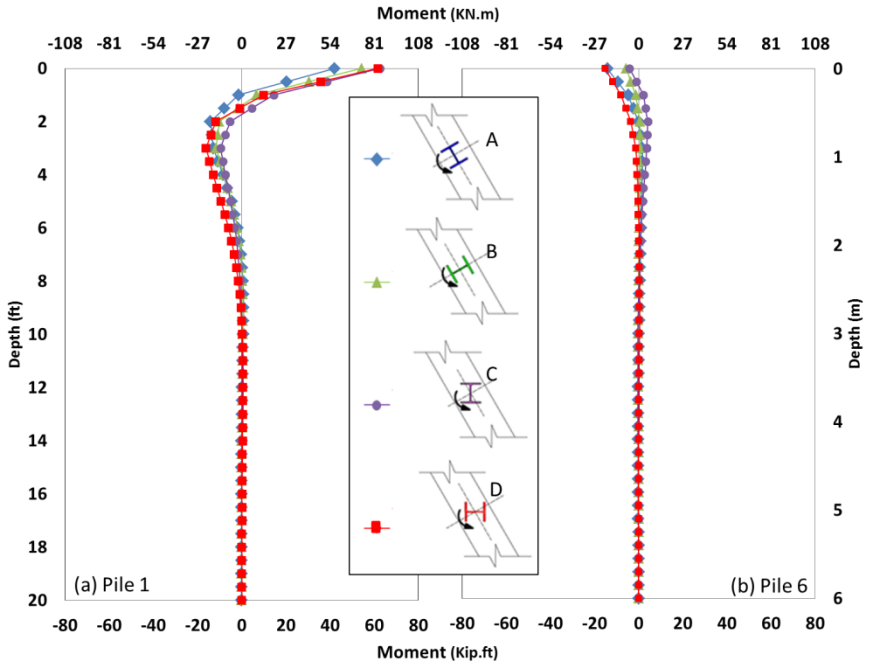

Figure E-20: Moments in the Exterior Piles about 2-2 Due to Decrease in Temperature (South Abutment)

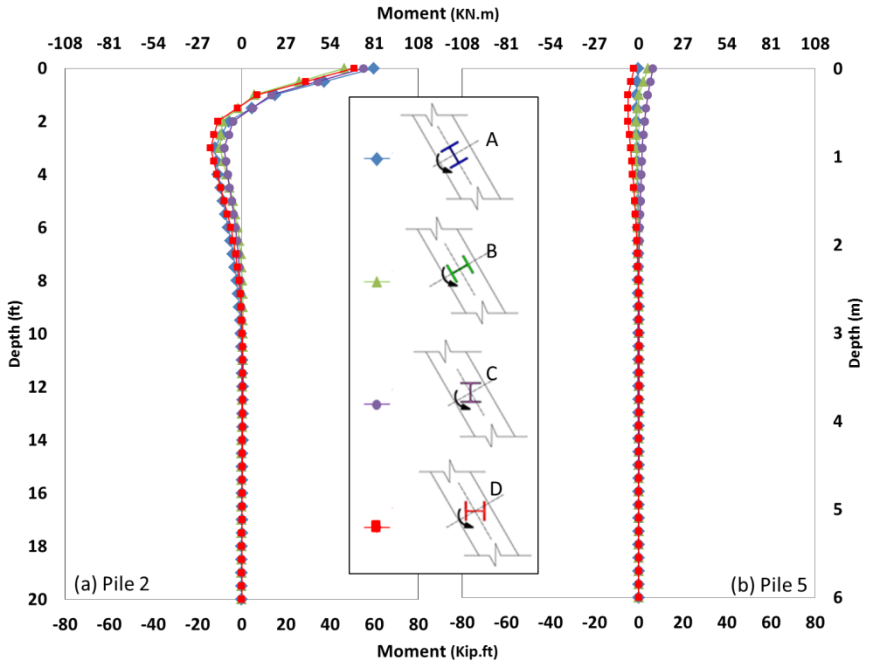

Figure E-21: Moments in the Interior Piles about 2-2 Due to Decrease in Temperature (South Abutment)

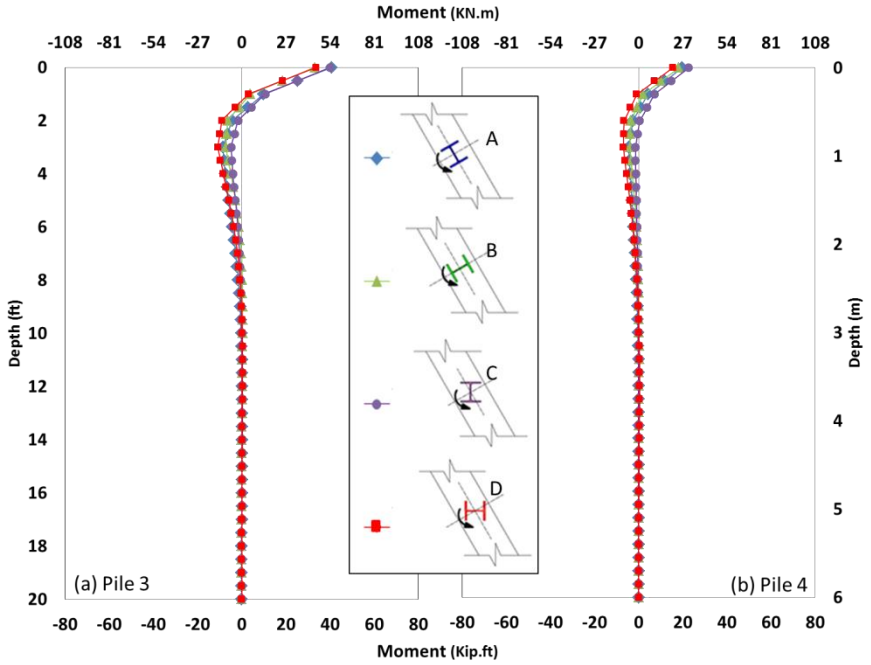

Figure E-22: Moments in the Interior Piles about 2-2 Due to Decrease in Temperature (South Abutment)

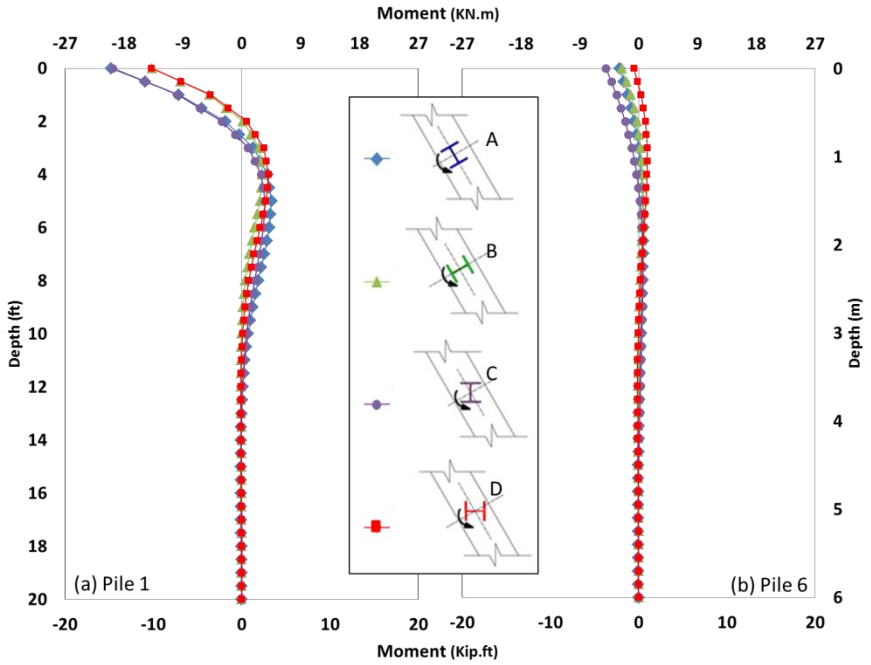

Figure E-23: Moments in the Exterior Piles about 2-2 Due to Increase in Temperature (South Abutment)

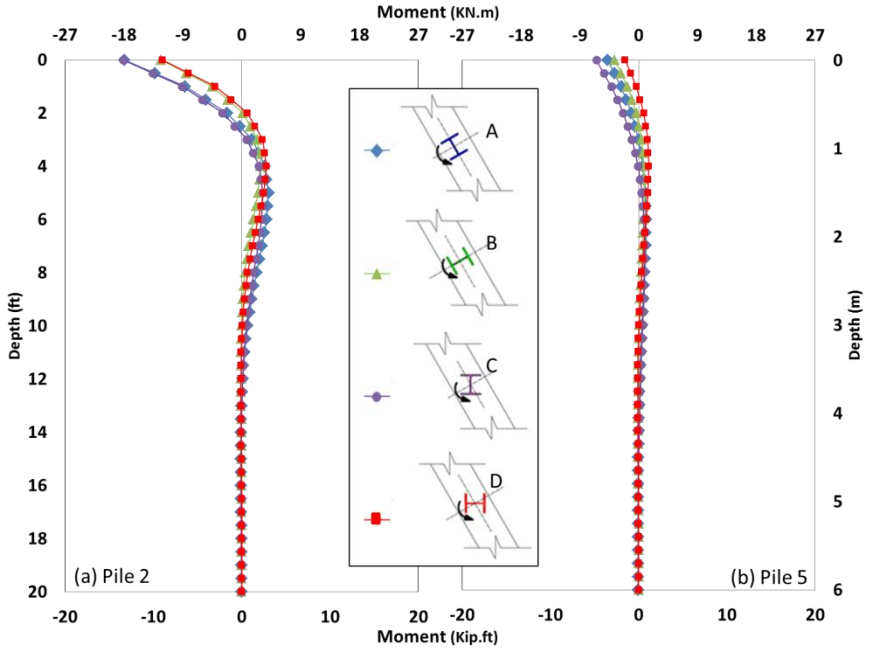

Figure E-24: Moments in the Interior Piles about 2-2 Due to Increase in Temperature (South Abutment)

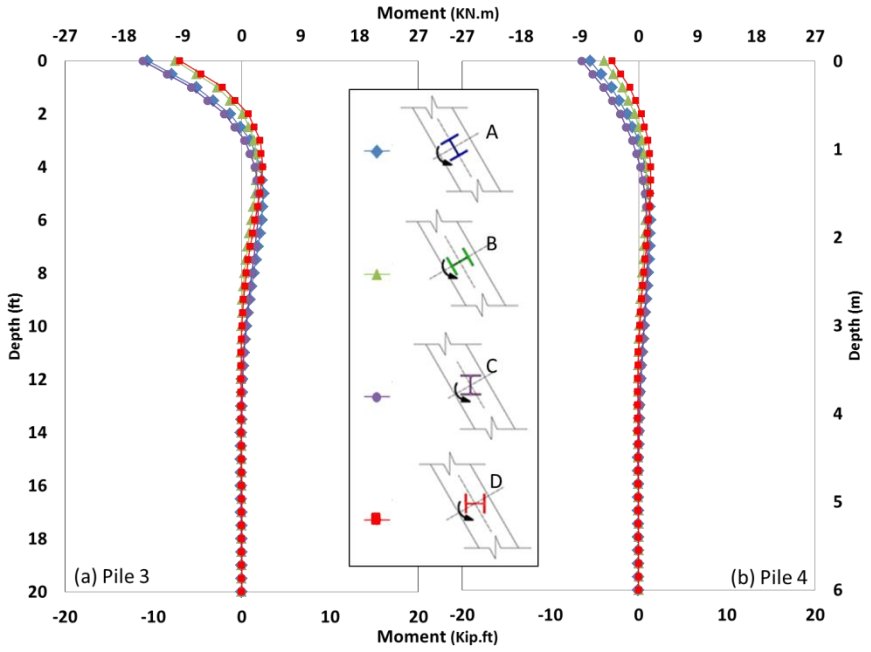

Figure E-25: Moments in the Interior Piles about 2-2 Due to Increase in Temperature (South Abutment)

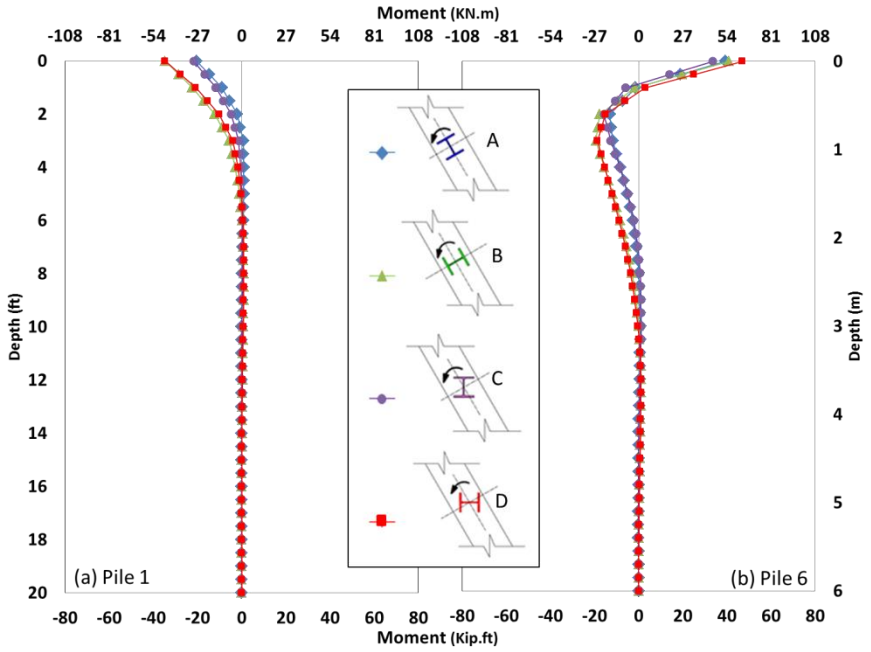

Figure E-26: Moments in the Exterior Piles about 1-1 Due to Decrease in Temperature (North Abutment)

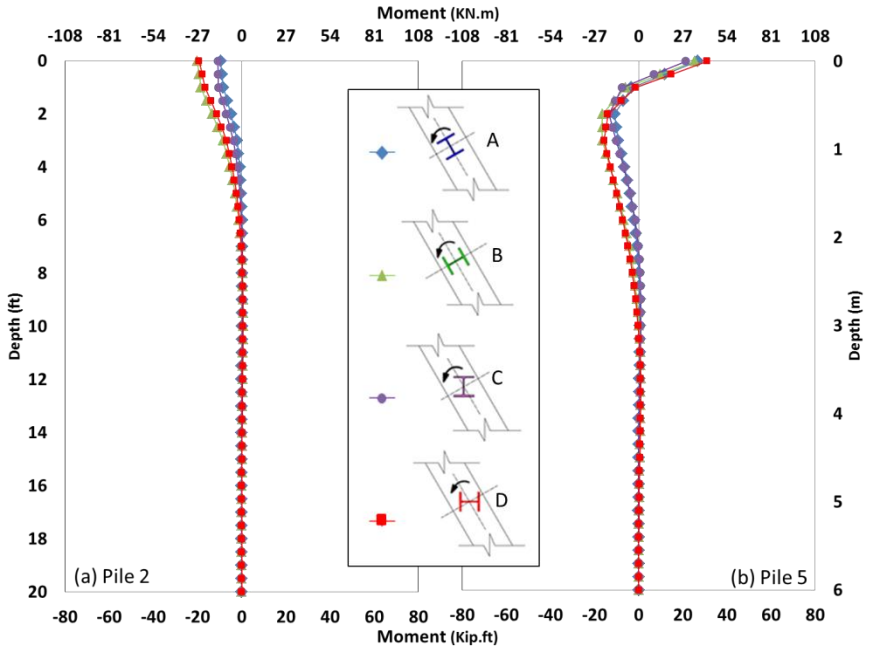

Figure E-27: Moments in the Interior Piles about 1-1 Due to Decrease in Temperature (North Abutment)

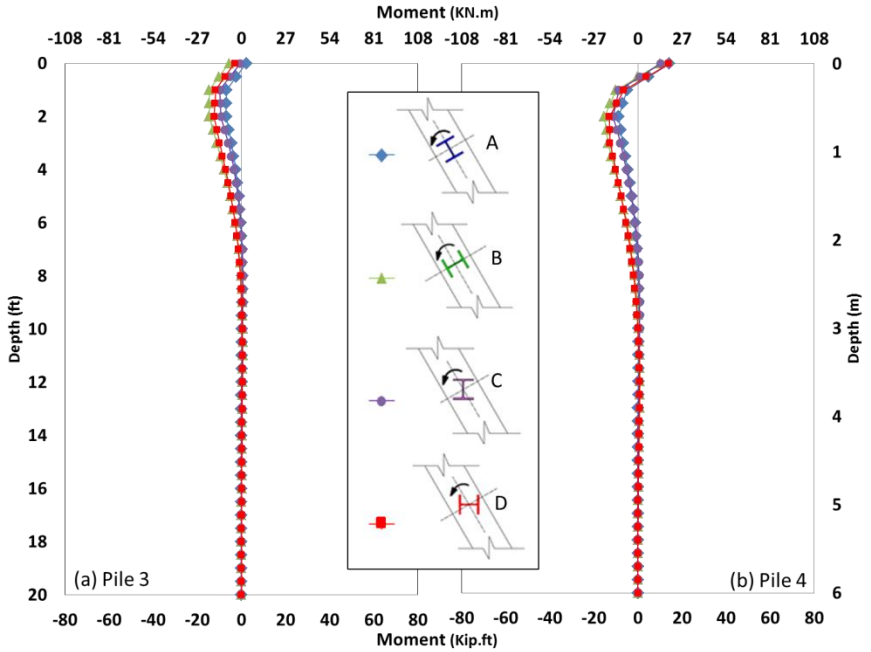

Figure E-28: Moments in the Interior Piles about 1-1 Due to Decrease in Temperature (North Abutment)

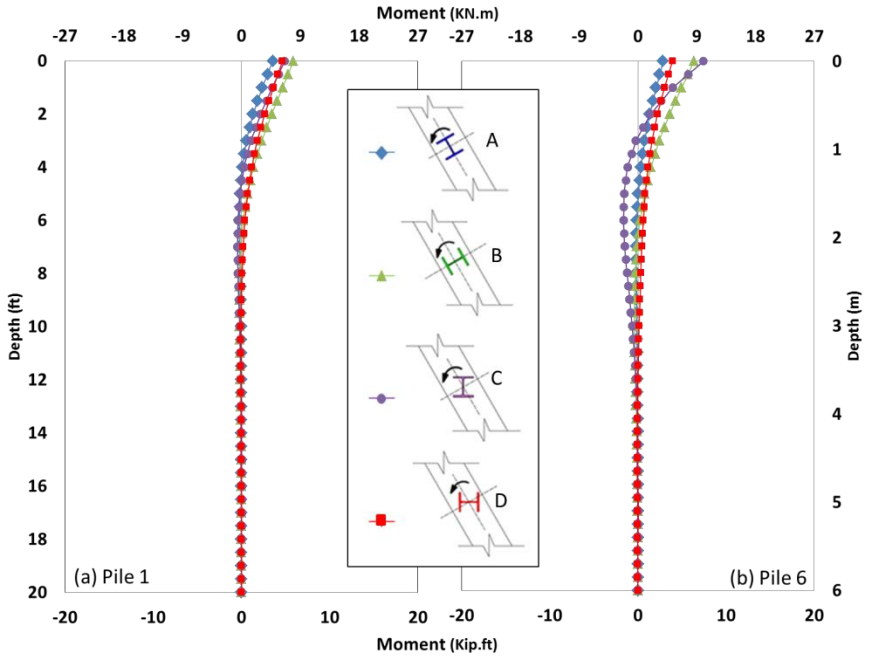

Figure E-29: Moments in the Exterior Piles about 1-1 Due to Increase in Temperature (North Abutment)

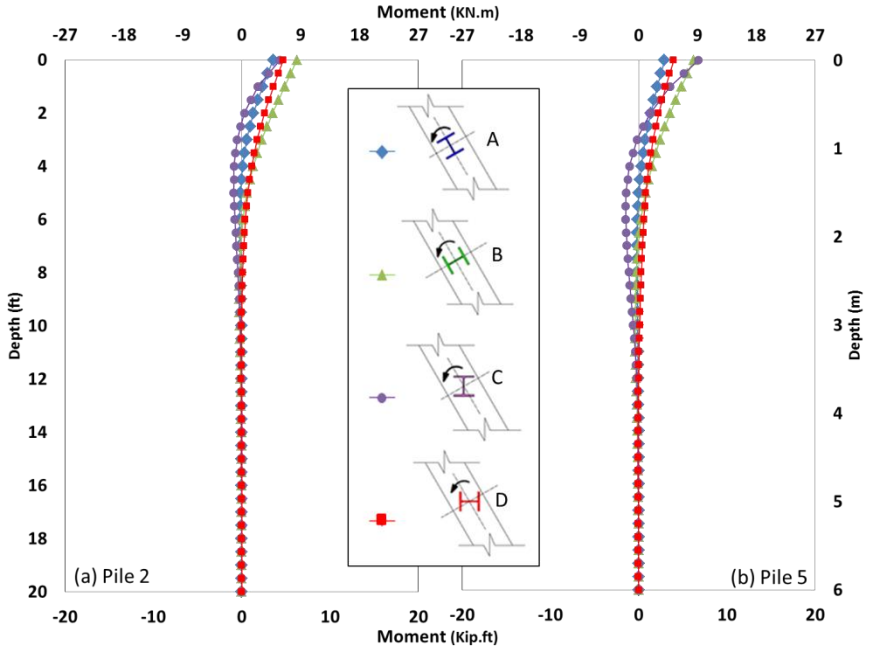

Figure E-30: Moments in the Interior Piles about 1-1 Due to Increase in Temperature (North Abutment)

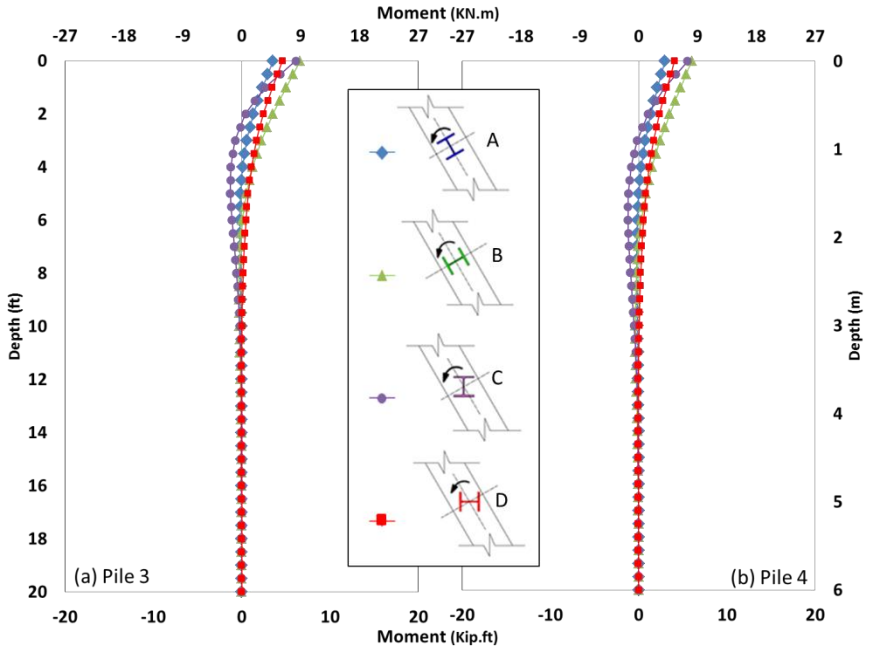

Figure E-31: Moments in the Interior Piles about 1-1 Due to Increase in Temperature (North Abutment)

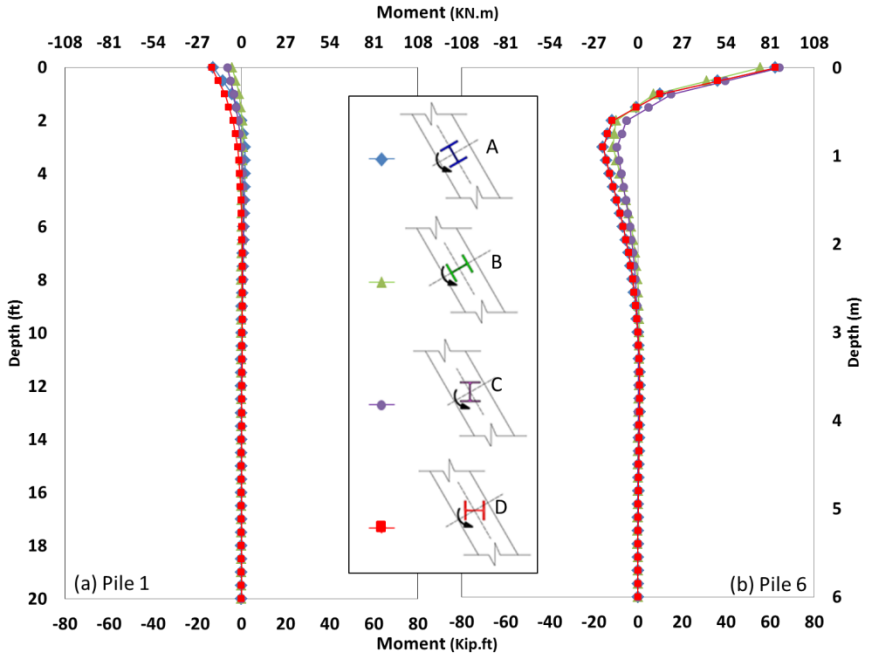

Figure E-32: Moments in the Exterior Piles about 2-2 Due to Decrease in Temperature (North Abutment)

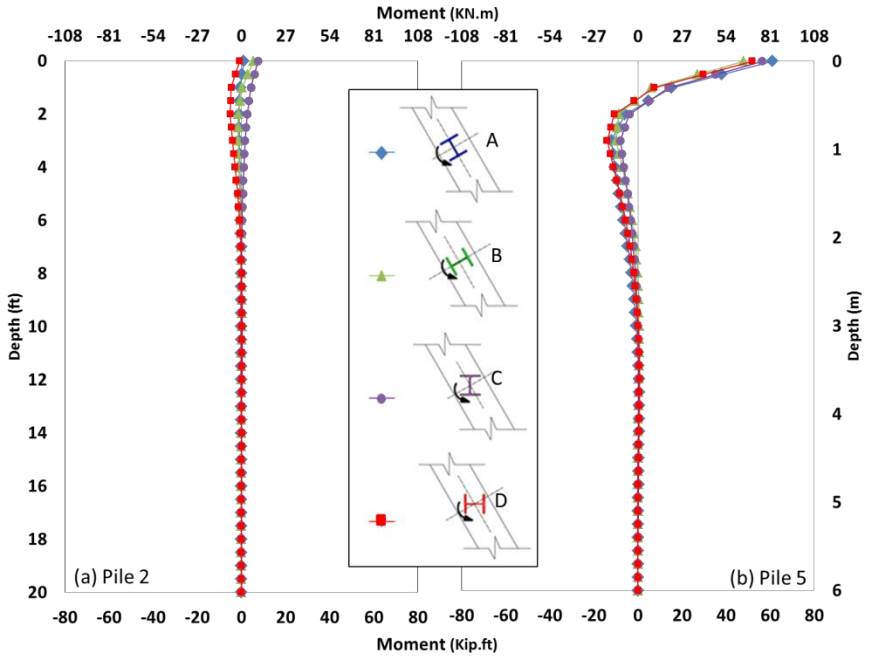

Figure E-33: Moments in the Interior Piles about 2-2 Due to Decrease in Temperature (North Abutment)

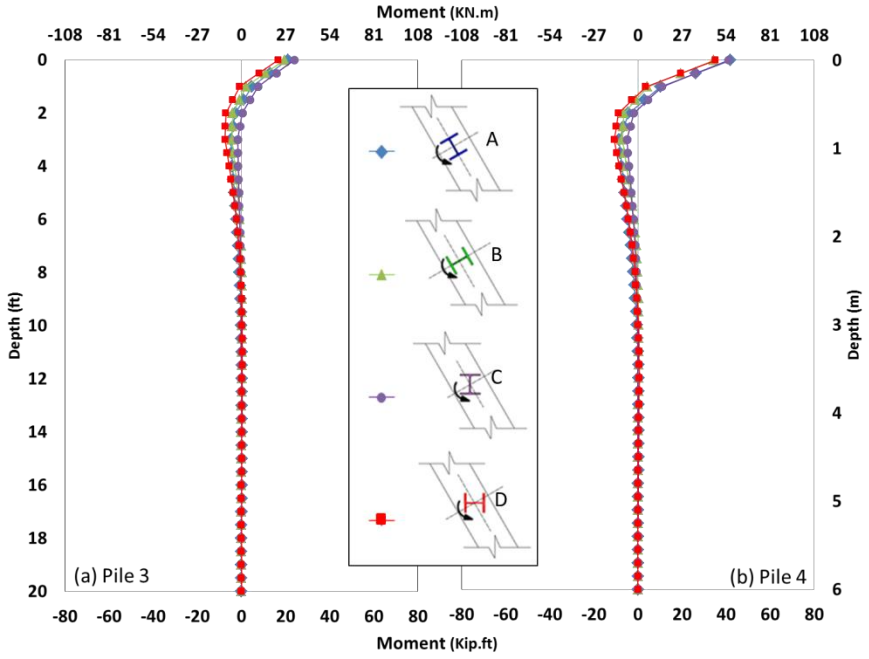

Figure E-34: Moments in the Interior Piles about 2-2 Due to Decrease in Temperature (North Abutment)

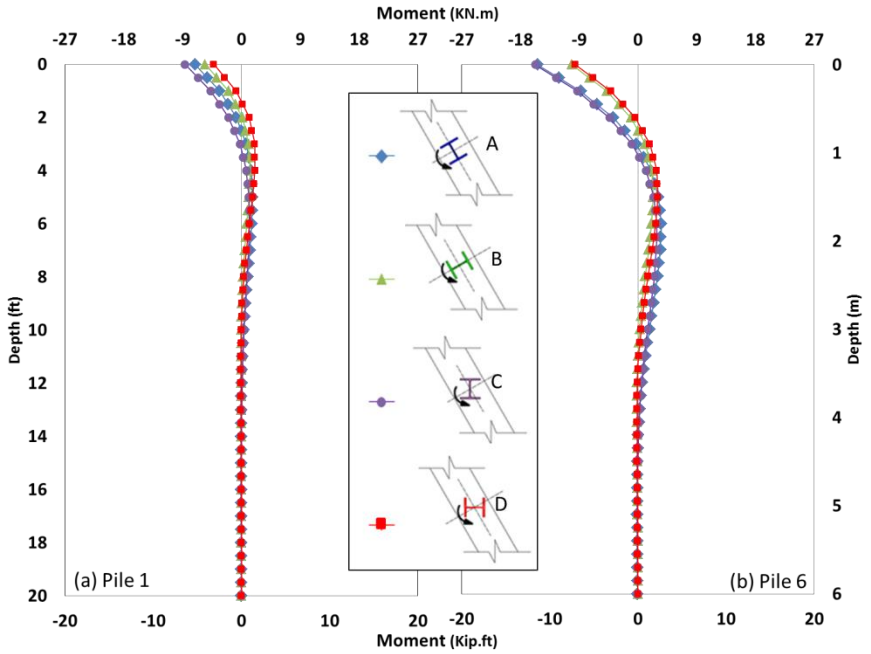

Figure E-35: Moments in the Exterior Piles about 2-2 Due to Increase in Temperature (North Abutment)

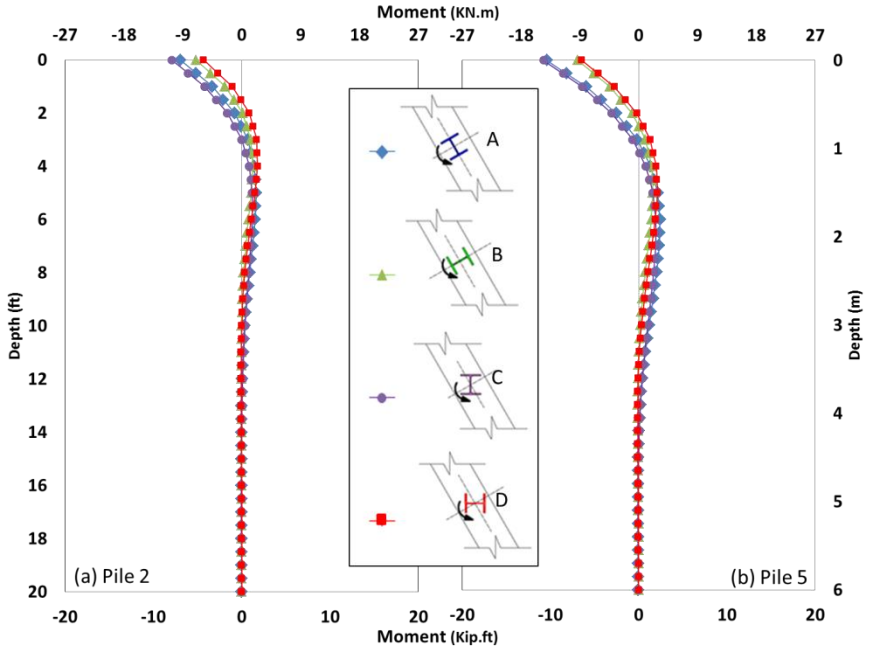

Figure E-36: Moments in the Interior Piles about 2-2 Due to Increase in Temperature (North Abutment)

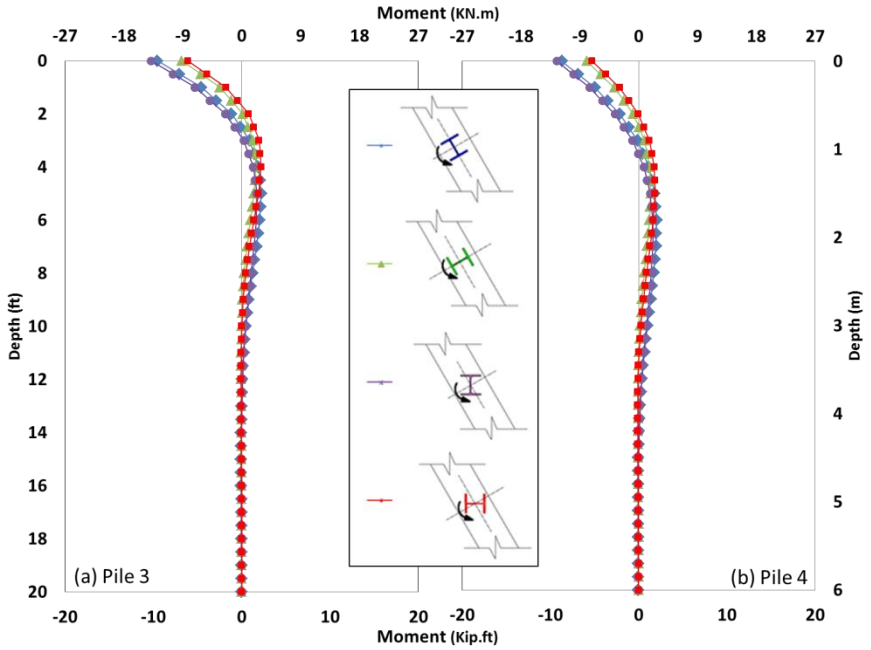

Figure E-37: Moments in the Interior Piles about 2-2 Due to Increase in Temperature (North Abutment)

REFERENCES

ACI Committee 209. *Prediction of Creep, Shrinkage, and Temperature Effects in Concrete Structures.* American Concrete Institute, 1997, 25.

American Petroleum Institute (API). "Recommended Practice for Planning, Designing and Constructing Fixed Offshore Platforms—Working Stress Design." Washington, D.C., 2005.

Arsoy, S., Barker, M., Duncan, J. *The Behavior of Integral Abutment Bridges.* Richmond, VA: FHWA, 1999, 33.

Barker, R., Duncan, J., Rojiani, K., Washington, P. *Manuals for The Design of Bridge Foundations.* R. M. Barker, J. M. Duncan, K. B. Rojiani, P. S., Washington, D.C.: National Cooperative Highway Research Program (NCHRP), 1991.

Bonczar, C., Civjan, S., Breña, S., and DeJong, J. *Behavior of Integral Abutment Bridges: Field Data and Computer Modeling.* Boston, MA: Office of Transportation Planning, 2005, 218.

Bransone, D. *Deformation of Concrete Structures.* McGrew-Hill, 1979.

Civjan, S., Bonczar, C., Breña, S., DeJong, J., and Crovo, D. "Integral Abutment Bridge Behavior: Parametric Analysis of a Massachusetts Bridge." *J. Bridge Eng.*, 2007: 64–71.

Comartin, C., Niewiarowski, R., Rojabn, C. *Seismic Evaluation And Retrofit of Concrete Buildings Volume 1.* Applied Technology Council (ATC), 1996.

Ericson, D. "Live load Distribution Behavior of the Brimfield Bridge." Amherst, MA, 2013.

Faraji, S., Ting, J., Crovo, D., Ernst, H. "Nonlinear Analysis Of Integral Bridges: Finite-Element Model." *Journal of Geotechnical And Geoenvironmental Engineering*, 2001: 454-461.

Frosch, R., Lovell, M. *Long-term Behavior of Integral Abutment Bridges.* FHWA, 2011, 168.

Gardner, L. "The First NEXT Beam Bridge." *PCI Journal*, 2013: 55-62.

Gazetas, G. "Formulas and Charts for Impedances of Surface and Embedded Foundations." *Journal of Geotechnical Engineering*, 1991: 1363-1381.

GeoKomn. "Instruction Manual Model 4200/4202/4204/4210." Lebanon, NH, 2010.

Hassiotis, S., Roman, E. "A survey of Current Issues on the Use of Integral Abutment Bridges." *Bridge Structures*, 2005: 81-101.

Kalayci, E. *Analysis of Curved Integral Abutment Bridges.* Amherst, MA, 2010.

Kim, W. and Laman, J. "Seven-Year Field Monitoring of Four Integral Abutment Bridges." *J. Perform. Constr. Facil.*, 2012: 54-64.

Lam, I., Martin, I. *Seismic Design of Highway Bridge Foundations Volume II.* FHWA, 1986, 181.

Massachusetts Highway Department. *MassHighway Bridge Manual Guidlines.* Boston, MA, 2005.

Najib, R., Amde, A. "Effect of Pile Orientation in Skewed Integral Abutment Bridges." *IBC*, 2010.

Olson, S., Holloway, K., Buenker, J., Long, J., LaFave, J. *Thermal Behavior of IDOT Integral Abutment Bridges and Proposed Design Modifications.* Springfield, IL: FHWA, 2013, 63.

Precast/Prestressed Concrete Institute Northeast. *Gidelines for Northeast Extreme Tee Beam (NEXT Beam) 1st Edition.* Belmont, MA, 2012.

Seed, H., Wong, R., Idriss, I., and Tokimatsu, K. "Moduli and Damping Factors Dynamic Analyses of Cohesionless Soils." *J. Geotech. Engrg.*, 1986: 1016–1032.

Selezneva. O., Hallenbeck, M. *Long-Term Pavement Performance Pavement Loading User Guide (LTPP PLUG).* McLean, VA: FHWA, 2013, 98.

Singh, A. (2012). EVALUATION OF LIVE-LOAD DISTRIBUTION FACTORS (LLDFs) OF NEXT BEAM BRIDGES. Amhers, MA. *Evaluation of Live-Load Distribution Factors (LLDFs) of NEXT Beam Bridges.* Amherst, MA, 2012.

Thompson, Theodore. *Passive earth pressures behind integral bridge abutments.* Amherst, MA: University of Massachusetts Amherst, ProQuest, UMI, 1999.

VTrans, Integral Abutment Committee. *Integral Abutment Bridge Design Guidelines Second Edition* . Montpelier, Vermont, 2008.

William, G., Shoukry, S., Riad, M. "Study of Thermal Stresses in Skewed Integral Abutment Steel Girder Bridges." *International Association for Bridge and Structural Engineering* (IABSE), 2012: 308-317.